CUTTING THROUGH THE NOISE IN QUANTUM MATERIALS WITH ULTRASOUND

A Dissertation
Presented to the Faculty of the Graduate School
of Cornell University
in Partial Fulfillment of the Requirements for the Degree of
Doctor of Philosophy

by
Florian Theuss
August 2024

”Das Einfache durch das Zusammengesetzte, das Leichte durch das Schwierige erkären zu wollen, ist ein Unheil, das in dem ganzen Körper der Wissenschaft verteilt ist.”
Johann Wolfgang von Goethe,
Wilhelm Meisters Wanderjahre

”Attempting to explain the simple through the compound, the easy through the difficult, is an evil that is spread throughout the entire body of science.”
Johann Wolfgang von Goethe,
Wilhelm Meister’s Journeyman Years

CUTTING THROUGH THE NOISE IN QUANTUM MATERIALS WITH ULTRASOUND

Florian Theuss, Ph.D.
Cornell University 2024

Strong interactions between electrons are the foundation of a myriad of exciting phenomena in condensed matter physics. In this thesis, we investigated two such cases—topological antiferromagnetism in Mn_3X ($X = Ge, Sn$), and unconventional superconductivity in UTe_2—by measuring their elastic moduli via the resonant ultrasound spectroscopy and pulse-echo ultrasound techniques.

Our measurements in Mn_3X find exceptionally large magnetoelastic coupling in the high-temperature antiferromagnetic state in both compounds, indicated by large derivatives of the Néel temperature with respect to hydrostatic pressure: (39 ± 3) K/GPa in Mn_3Ge and (14.3 ± 2.0) K/GPa in Mn_3Sn. Our measurements also helped identify the antiferomagnetic phase in these compounds as a piezomagnetic phase, rare behavior in which the total magnetization depends linearly on applied strain.

From our pulse-echo ultrasound measurements in UTe_2, we conclude that its superconducting order parameter has only one component which is the same between samples showing one and two superconducting transitions. Our data further suggests that the order parameter transforms as the B_{2u} irreducible representation of the D_{2h} point group. Comparing RUS and pulse-echo ultrasound data, as well as considering high-energy X-ray diffraction microscopy data, we speculate that the origin of the two transitions seen in some samples of UTe_2 is due to structural inhomogeneity in these samples.

BIOGRAPHICAL SKETCH

Florian Theuss was born in 1996 in Heilbronn, Germany. He finished high school at the Werner-von-Siemens Gymnasium in Regensburg in 2014 as valedictorian and began his undergraduate studies in physics at Heidelberg University in Heidelberg, Germany in the same year. Florian finished his undergraduate degree in 2017, with his Bachelor's thesis in the group of Jan Pawlowski, working on functional renormalization in quantum field theory. It was during this time that he discovered one of the most intriguing concepts permeating all fields of physics: the idea that knowledge of the microscopic details of a physical system is not required to identify measurable quantities. This concept, that he first encountered during his study of high energy theory, is what inspired his passion for condensed matter physics, where it was originally discovered.

Florian then continued his education with a two-year Master's program at Heidelberg University. However, with support from a Fulbright Travel Award and a travel grant from the Cornell Club Germany, he spent the first of these two years at Cornell University, participating in an exchange program. It was during this time, studying unusual superconducting patterns on micro-structured devices in the group of Katja Nowack, that he developed an interest in experimental physics. Upon returning to Heidelberg University for his Master's thesis, he delved into the origin of multiferroicity in one-dimensional spin chains using electron spin resonance under the supervision of Rüdiger Klingeler.

Subsequently, Florian returned to Cornell University in 2019, where he pursued his PhD in experimental condensed matter physics under the guidance of Brad Ramshaw. His research continued to focus on correlated phases and emergent phenomena in quantum materials using ultrasound, and also included advancing existing ultrasound techniques.

ACKNOWLEDGEMENTS

Completing a PhD is of course impossible without a tremendous amount of help and support from a variety of people, and I am extremely grateful to each and every one of them. Here, I want to acknowledge some of the most important influences I've had over the last several years, but could never attempt to make this a complete list.

First, I want to thank my supervisor Brad Ramshaw for his mentorship, which made my time at Cornell a wonderful experience. He managed to provide me with the perfect balance between hands-on guidance and the freedom to carry out my own experiments and make my own mistakes. After all, I would not have become the independent researcher I am today, without the enthusiasm and clarity with which Brad approaches physics. I am glad to have found an advisor with whom I could also form a genuine friendship, which I hope to maintain in the future.

In addition, I would also like to thank all former and current members of the Ramshaw group that I've had the pleasure to work with over the years. Sayak, Yawen, Patrick, Avi, Gaël, Sahas, and Yifei have all contributed to a great atmosphere in our shared office, where helping and supporting each other was the norm. I was fortunate to arrive at the Ramshaw lab when all basic instrumentation had just been set up by existing graduate students. Without Sayak and Patrick, who built and taught me about the resonant ultrasound spectroscopy and pulse-echo ultrasound setups in the lab, none of my experiments would have been possible. Patrick and Avi also deserve all of the credit in developing our sputtered thin-film shear transducers, which were crucial to a large part of the research presented in this thesis. Developing our fitting algorithm would have not been possible without Avi, who is solely responsible for the entire mathematical framework of the forward calculation, and Gaël, who was tremendously helpful in writing the fitting procedure. I would like to further thank Gaël for significantly improving the culture in our group, for example by introducing daily group lunches. I am also grateful to Gaël for his guidance on how to navigate the academic world. Without him, I would not have been able to make as many friends across different institutions, or organize a student seminar at Cornell, just to name a few examples.

Besides the Ramshaw group, I want to thank all of our collaborators, particularly Johnpierre Paglione and his group, who provided us with many samples and intriguing discussions. He was also kind enough to invite me to multiple talks throughout our collaboration. I am also extremely grateful to Katja Nowack for giving me a project during the last summer of my exchange at Cornell. Most faculty members would not have given an exchange student as much of their time as Katja did for me. Without her, I would not have found my way to experimental condensed matter physics.

Navigating physics and research was hard enough without administrative issues on top. This is why I want to thank the entirety of the administrative support staff in the physics department and LASSP. In particular, it has been a pleasure working with Meredith Collins, who helped me organize a student seminar at Cornell. Besides administrative help, most of my work would not have been possible without the technical expertise of the professional machine shop at LASSP, or the Cornell Institute of Biotechnology Imaging Facility. Teresa Porri, the staff scientist responsible for the CT-scans, is probably one of

the nicest, most responsive and professional instrumentation managers I have had the pleasure to work with.

Since spending five years only in the lab would drive anyone crazy, I'm grateful to all my friends for providing continuous relief. I will never forget the many memories made with Saba, Alen, Chris, Kripa, Maya, and Sam from intramural soccer adventures, evenings playing pool, nights out, wine tours, and relaxed football Sundays. I am also grateful for a large group of friends I made playing volleyball, including but not limited to Josh, Steven, and Zexi.

I am of course very thankful for having my wife Megan with me for almost the entire duration of my PhD. We met when I was an exchange student, and she was a senior at Cornell. I am sure she wasn't anticipating living in Ithaca for another five years, and I am extremely appreciative of the sacrifices she made for us. While it may seem that the rest of my family played a smaller role in my life during the last few years, they were living an Atlantic ocean away after all, this could not be further from the truth. I can't thank my brothers, but most of all my parents enough, for continuously supporting me, even though I'm sure it is not always easy for them.

TABLE OF CONTENTS

LIST OF TABLES

LIST OF FIGURES

CHAPTER 1

INTRODUCTION

The phenomenon of collective or emergent behavior is one of the most captivating aspects of condensed matter physics. This concept suggests that when many electrons in a solid interact with each other, they cannot be described by the behavior of their individual constituents alone. Instead, entirely new behavior emerges. This principle is particularly intriguing because it encompasses emergent particles such as Majorana fermions and Weyl fermions that are essential to our understanding of particle physics but are explicitly excluded from the Standard Model. Emergent behavior often arises when electrons interact strongly with each other and form correlated, ordered phases characterized by broken symmetries. These broken symmetries, like broken rotational symmetry in ferromagnets or broken gauge symmetry in superconductors, are central to understanding the interactions between electrons in solids and permeate almost all fields of modern science. Identifying such correlated symmetry-breaking states, including characterizing which symmetry is broken, is a challenging yet crucial task.

A common set of probes in condensed matter physics aimed at addressing this issue include the measurements of susceptibilities. A susceptibility measures the response of the sample to a small externally applied perturbation. Examples are heat capacity as the response to temperature perturbations, magnetic susceptibility as the response to externally applied magnetic fields, or optical probes measuring the response to electromagnetic fields. The key challenge is to find a susceptibility which is different in the ordered state compared to the disordered state. For that to happen, the externally applied perturbation must couple to the broken symmetry of the ordered phase. Magnetic susceptibilities, for example, are ideal for probing magnetically ordered states: disordered spins can easily be tilted with external magnetic fields, whereas ordered spins, like in a ferromagnet, are stiff and respond in a qualitatively different way to a magnetic perturbations. Finding the right perturbation one needs to apply is not always as straightforward, however. URu_2Si_2 [1] is a prominent example, where even after intense research for almost four decades and even though an arsenal of experimental and theoretical techniques has been applied, the symmetry of the order parameter of its hidden order phase is still a mystery.

In this thesis we use resonant ultrasound spectroscopy (RUS) and pulse-echo ultrasound techniques to measure the elastic moduli of quantum materials. Elastic moduli are strain susceptibilities, i.e. they measure the response of the sample to strain. They are particularly well suited to detect ordered phases and the associated broken symmetries, because several strains, coupling to different broken symmetry states, exist. This fundamental property of strain makes ulrasound a powerful technique to probe which symmetry is broken at a thermodynamic phase transitions and to detect novel or rare correlated states, inaccessible with other techniques. Practical advantages of ultrasound techniques are that they can be performed in extreme environments like ultra-low temperatures (i.e. in dilution refrigerators), or extremely high magnetic fields, including pulsed fields. Ultrasound measurements, for example, were crucial in determining orbital quadrupolar ordering in UPd_3 [2], or nematic order in iron arsenide superconductors [3].

For certain correlated phases, it is possible that no single external perturbation couples to the broken symmetry in the ordered state, but multiple perturbations need to be applied simultaneously. One example is the piezomagnetic state [4], in which the total magnetization depends linearly on applied strain, akin to electric fields in piezoelectric materials. In these materials, external magnetic fields combined with certain strains couple to the ordered state. While theoretically straightforward, piezomagnetic phases are exceptionally rare and difficult to detect. As part of this thesis (see chapter 6), we investigated Mn_3X (X = Ge, Sn), a family of topological antiferromagnets, which are suggested to exhibit a piezomagnetic phase around 400 K. We performed both RUS and pulse-echo ultrasound measurements to measure the elastic moduli of Mn_3X in zero and finite applied magnetic field, respectively. For both techniques, we had to build new measurement setups, which were able to withstand temperatures of up to about 450 K.

The second symmetry-breaking correlated phase investigated in this thesis is superconductivity (see chapter 5). Superconductivity was first discovered in mercury in 1911 by Heike Kamerlingh Onnes [5], but since then myriad superconducting materials have been found (see Figure 1.1). In a superconductor, the electrons of a metal form a coherent state, meaning that all wavefunctions of the individual electrons acquire the same phase. This coherence leads to exotic properties like zero electrical resistance or the Meissner effect. It also means that the $U(1)$ gauge symmetry present for free electrons is broken, which is the defining characteristic for a superconducting state.

A different picture for the emergence of superconductivity is that due to an effective attractive interaction, electrons form *Cooper pairs*, leading to a gap in the quasiparticle spectrum. Depending on the type of interaction, these Cooper pairs can break rotational symmetries of a lattice, in addition to $U(1)$ gauge symmetry. This rotational symmetry breaking of Cooper pairs is often characterized by the angular momentum of the pair wavefunction (similar to atomic orbitals). For example, a spatially isotropic interaction between electrons often leads to s-wave Cooper pairs with zero angular momentum, whereas ferromagnetic or anti-ferromagnetic interactions can lead to Cooper pairs with angular momenta one (p-wave Cooper pairs) or two (d-wave Cooper pairs), respectively [8]. Knowing which rotational symmetry is broken in the superconducting state can therefore give critical insight into the microscopic pairing mechanism responsible for the formation of superconductivity.

Even though knowledge of the rotational symmetry of the superconducting order parameter is a key ingredient to our understanding of superconductivity, we have only been able to unambiguously determine which symmetry is broken for a few select compounds. Examples are s-wave BCS superconductors and the d-wave cuprates [9]. Counterexam-

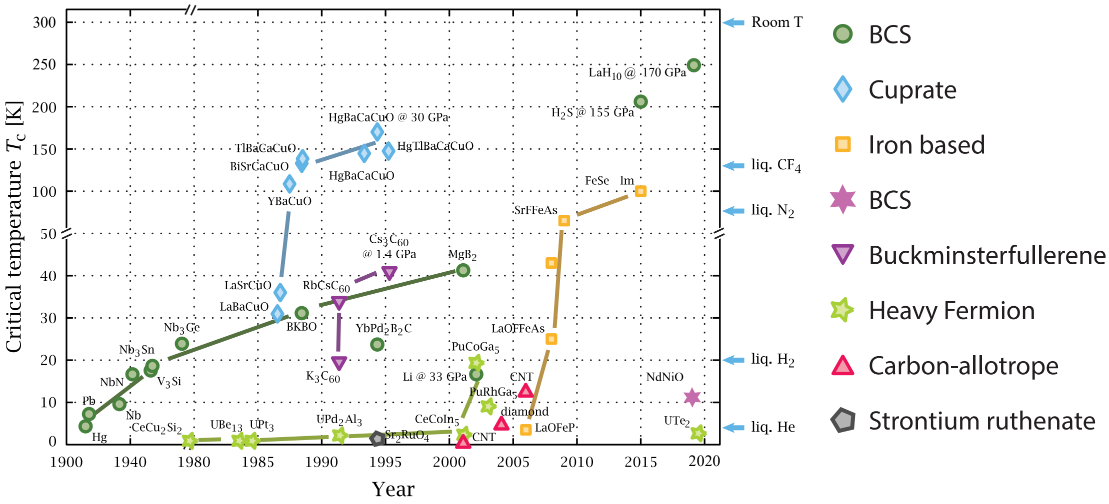

Figure 1.1: **Timeline of superconductors.** Superconducting materials are plotted according to their critical temperatures and the year they were discovered. Different symbols and colors group different families of superconductors. In this thesis, we investigated UTe_2, which was discovered in 2019 with $T_c \approx 2$ K. Figure adapted from [6, 7].

ples like Sr_2RuO_4 exist, however, where even after decades of research with an arsenal of different techniques and the existence of ultra-clean samples, the broken symmetry of its superconducting state is still unknown [10, 11].

Ultrasound has a long history of applications in superconductivity research. Measuring the exponential decay of the ultrasonic attenuation in the superconducting state, for example, provided one of the early confirmations of BCS theory [12]. Ultrasound has also been extensively employed in heavy-Fermion superconductors. One example is UPt_3, where ultrasound measurements were critical in determining that this material is one of very few superconductors which exhibit multiple intrinsic superconducting phases as a function of temperature (at zero magnetic field and ambient pressure) [13]. In chapter 5 of this thesis, we present our ultrasound studies on UTe_2, a different heavy-Fermion superconductor, in which some samples show multiple superconducting phases. Our measurements imply that the multiple superconducting transition in UTe_2 are of extrinsic origin, however. They also help identify which rotational symmetry is broken in the superconducting state.

We started our investigations into superconductivity in UTe_2 with resonant ultrasound spectroscopy measurements. Since these samples were small and brittle, and polishing uranium-based compounds can bear health hazards, we were not able to prepare our RUS samples into rectangular prisms, which is what is commonly done for RUS experiments. Therefore, in order to perform these measurements and analyze our data, we developed a new algorithm which fits elastic moduli to RUS spectra of irregularly-shaped samples (see chapter 4). This new analysis procedure requires 3D models of our samples, which we obtained via nano-CT scans at the Cornell Institute of Biotechnology. With our new fitting algorithm, we were able to obtain fits for two of the three RUS samples we measured. We assume that our fitting process did not work for one of these samples because it contained too much structural inhomogeneity and/or its shape had too many irregularities. The other two samples, however, give fit results consistent with each other, as well as with pulse-echo ultrasound measurements we performed later. In order to extract the temperature dependence of the elastic tensor of UTe_2 through T_c, we then measured the temperature dependencies of over 100 resonances for both samples. Unfortunately, neither decomposition was reliable enough on the required relative scale of 10^{-5} for us to make unambiguous statements about the superconducting order parameter in UTe_2.

This uncertainty in our RUS decompositions is why we performed additional pulse-echo ultrasound measurements. Since a jump in a shear modulus at T_c is what determines the dimensionality of the superconducting order parameter, we measured all shear moduli in samples of UTe_2 which feature one and two superconducting transitions (we measured three samples in total). The main finding of our measurements is the absence of a jump in any shear modulus. Since a statement about the absence of a feature is always only as good as the resolution of the data, a large focus of our efforts was to reduce noise in our measurements. The high-resolution data presented in this thesis was only possible due to the development of thin-film shear transducers in our lab (see chapter 3), which only finished after we had already started our RUS measurements. Almost all of the credit for this development belongs to Patrick Hollister and Avi Shragai in the Ramshaw Lab (see [14] for the PhD thesis of Patrick, detailing the development process).

Comparing our RUS and pulse-echo ultrasound data, as well as additional X-ray diffraction microscopy data we took in the earliest stages of our RUS endeavors, we believe that the lack of order-10^{-5} reliability of the elastic moduli obtained with RUS is due to structural inhomogeneity in the samples, rather than inherent to our newly developed fitting algorithm.

In the following thesis, we first introduce the notion of groups and representations in the context of condensed matter theory, in particular their connection to elasticity and second order phase transitions, with a focus on superconductivity (chapter 2). We then continue to explain the fundamental principles of resonant ultrasound spectroscopy and pulse-echo ultrasound measurements, as well as give details about their experimental setups (chapter 3). In chapter 4, we present our new procedure to fit RUS spectra of irregularly-shaped samples, before discussing our ultrasound measurements of UTe_2 (chapter 5) and Mn_3X (chapter 6). We conclude this thesis in chapter 7 by summarizing our main results and outlining future experiments which could help solve outstanding puzzles in both systems.

CHAPTER 2

BACKGROUND: SYMMETRY IN SOLID STATE SYSTEMS

Symmetry is an essential ingredient to most modern fields of science. It is, however, nowhere more prevalent than in condensed matter physics, describing the properties of solids. Solids are characterized by the periodic arrangement of atoms in a lattice, breaking the continuous translational and rotational symmetries present in free space, which is a key feature distinguishing them from fluids and gases (where both continuous symmetries are still present; see Figure 2.1).

From the definition of a Bravais lattice [15, Chapter 4] as an *infinite array of discrete points with an arrangement and orientation that appears exactly the same, from whichever of the points the array is viewed*, it becomes clear that the lattices formed in solids (only) obey discrete symmetries, rather than the continuous symmetries of free space (see Figure 2.1).

These discrete symmetries characterizing each lattice are formally described by *space groups*. Space groups contain all rigid symmetry transformations taking the lattice into itself (i.e. the lattice is *invariant* under these transformations). These transformations include translations by a lattice vector, as well as certain rotations, reflections, and inversions. As it turns out, besides translations, it is enough to consider rotations, reflections, and inversions which leave at least one point of the lattice fixed [15, Chapter 7]. The collection of these latter symmetry operations form a subgroup of the full space group, the *point group*.

In order to be able to discuss the consequences symmetry properties of solids have on their physical properties, it is helpful to first review some basic aspects of group theory and representations (section 2.1). We will then go over specific characteristics of point groups (section 2.2). More details on groups in general, as well as point groups can be found in Appendix A and Appendix B, respectively. We subsequently discuss elasticity (section 2.3) and superconductivity (section 2.4) in solids with a focus on symmetry related aspects.

2.1 Introduction to Groups and Representations

The goal of this chapter is to give an intuitive understanding of groups and representations, in particular how they are relevant to our topic of symmetry transformations. It is based

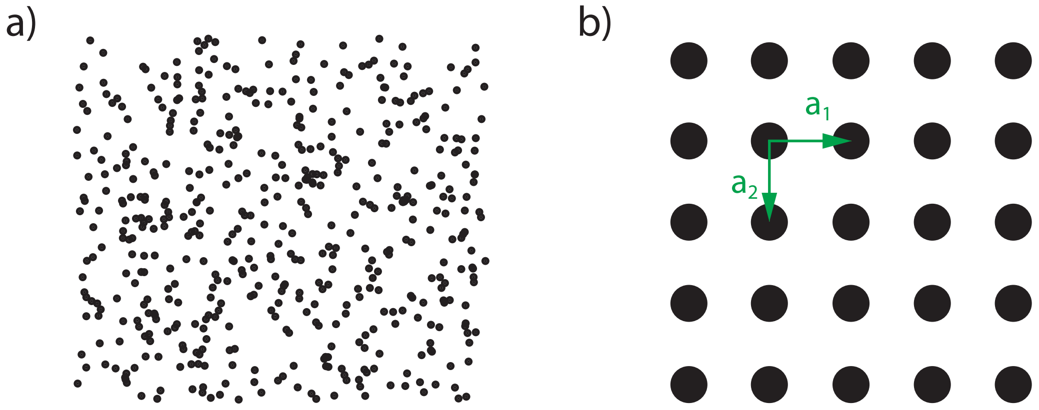

Figure 2.1: **Broken symmetries in solids.** a) A free 2D gas represented by a collection of random points. It is described by its average particle density $n(\mathbf{r}) = n$, which as a function of space $\mathbf{r}$ possesses continuous translational and rotational symmetry. b) Illustration of a two-dimensional square lattice. The lattice exhibits discrete translational symmetry by the lattice vectors $\vec{a}_1$ and $\vec{a}_2$. It is additionally characterized by 4-fold rotational symmetry.

on [16, Chapters 12 and 13], unless noted otherwise. For a more formal approach, the reader is referred to one of the many textbooks on group theory for condensed matter physicists, see for example [17]. A short introduction and definitions of relevant terms and properties are also given in Appendix A.

Symmetry Groups. Symmetry operations leave a system unchanged or transform it into an equivalent configuration. Consider the set G of all such symmetry operations g_1, g_2, ... leaving an object invariant. Since the system will remain unchanged after any one of these transformations, it will still remain fixed after a second consecutively applied symmetry operation. The product of two symmetry operations is therefore also part of G. This set must also contain a unit element, since per definition it leaves the original object unchanged. Furthermore, consider an individual symmetry transformation g_i. Since it transforms the system into itself, a potential inverse element g_i^{-1} must also leave the system invariant. It is therefore also a symmetry transformation and is part of the original set g_1, g_2, ... Explicit constructions of symmetry operations are always functions, making associativity an inherent feature. Based on these properties above, we have demonstrated that the set of all symmetry transformations leaving a particular object unchanged is indeed a group.

The group describing transformations of crystal lattices is called the space group and includes discrete translations, rotations, and reflections (more in section 2.2). Space groups are in general not abelian, since translations and rotations don't usually commute.

Representations. Groups and their elements are usually defined in a quite abstract way and explicit forms depend on the function the element acts on. Consider for example rotations. We can express rotations as 2×2 matrices when acting on two-dimensional vectors, 3×3 matrices when acting on three-dimensional vectors, and so on. These explicit matrices for particular rotations are part of different *representations* of the rotations group.

Let us discuss the definition of a representation a little more carefully. First, consider the effect of group transformations on some function f_1. By applying all transformations of the group G, we obtain n new functions, where n is the order of the group. We can expect that while some of these functions may be linearly dependent, a subset of $d \leq n$ functions f_1, f_2, ..., f_m are linearly independent. Thus, the function obtained by applying an arbitrary transformation g from G to one of the functions f_i will be a linear combination of all linearly independent f_i $(i = 1, ..., d)$, i.e.

$$g f_i = \sum_{j=1}^{d} G_{ji} f_j, \tag{2.1}$$

where the constants G_{ij} correspond to the group element g. The full matrix G_{ij} is called the *matrix* of the transformation g. The full set of matrices of all the elements in a group is called a *representation* of the group. The set of linearly independent functions f_i $(i = 1, ..., d)$ with respect to which these matrices are defined is called the *basis* of the representation, and the number d of these functions is called the *dimension* of the representation. In the special case of an *irreducible* representation, every basis function can be accessed by applying some group element on a linear combination of all other basis functions.

A nice example illustrating this concept of irreducible representations are angular momentum states in free space. Free space (or any spherically symmetric system) is characterized by continuous rotational symmetry in three dimensions (the group $SO(3)$)[1], which allows us to describe eigenstates by their total angular momentum. To each angular momentum j correspond $2j+1$ eigenstates with the same energy. Each of these eigenstates is described by the component of the angular momentum m $(-j <= m <= j)$. For example, three states exist with total angular momentum $j = 1$. They have $m = -1, 0, 1$. Under rotations, angular momentum is conserved, such that an angular momentum state described by j and m can only be transformed into linear combinations of the same total angular momentum j. The set of states characterized by the same angular momentum j thus form the basis of a $2j+1$ dimensional irreducible representation of the rotation group $SO(3)$: a s-wave state with angular momentum zero transforms as a one-dimensional representation, p-wave states with angular momentum one (and $m = -1, 0, -1$) transform as a three-dimensional representation, etc.

---

[1] As we will discuss in section 2.2, solids are characterized by discrete, rather than continuous symmetries. However, most of the features of representations and groups illustrated by this example are valid for discrete and continuous symmetry groups.

The *direct product* of two irreducible representations is generated by forming all possible products of their respective basis functions. The new set of functions forms a basis of a new representation, which is in general reducible. However, any reducible representation can be decomposed into several irreducible representations.

The concept of direct products is again nicely illustrated using the example of angular momentum states in free space. In particular, the direct product of spin-$\frac{1}{2}$ states is an example which is often discussed in quantum mechanics classes (even though not in terms of group theory). A spin-$\frac{1}{2}$ state transforms as a two-dimensional representation of the rotation group in free space ($SO(3)$). A basis for the two-dimensional representation is given by up ($|S_z = 1/2\rangle$) and down ($|S_z = -1/2\rangle$) states. The direct product of this representation with itself gives the following states: $|1/2, 1/2\rangle$, $|-1/2, -1/2\rangle$, $|-1/2, 1/2\rangle$, $|1/2, -1/2\rangle$. As mentioned above, these can be divided into symmetric and antisymmetric sets of product states, each forming their own representation. The antisymmetric product is given by $\frac{1}{2}\left(|1/2, -1/2\rangle - |-1/2, 1/2\rangle\right)$. It forms the one-dimensional $s = 0$ representation of the rotation group. The symmetric product states are given by $|1/2, 1/2\rangle$, $|-1/2, -1/2\rangle$, and $\frac{1}{2}\left(|1/2, -1/2\rangle + |-1/2, 1/2\rangle\right)$, forming the three-dimensional $s = 1$ representation of $SO(3)$.

All irreducible representations of point groups (see section 2.2) are *real*, meaning all matrices representing the group transformations are real. The direct product of a real representation with itself always contains the identity representation. Combined with the fact that the product of any two one-dimensional irreducible representations is also one-dimensional, we have that any product of a real one-dimensional representation with itself is always identical to the identity representation. Only if the dimension of the irreducible representation is greater than one can the direct product with itself contain irreducible representations other than the identity representation.

2.2 Point Groups

Before discussing details of point group symmetries, we want to clarify a few terms often used in the context of crystallography: atoms in solids form regular patterns according to their *crystal lattice*. This crystal lattice consists of the *unit cell* (sometimes called *basis*) which is periodically repeated along integer multiples of the unit cell vectors. The pattern solely described by the unit cell vectors is the *Bravais lattice*. The Bravais lattice is identical to the crystal lattice if the unit cell consists of only one atom.

The symmetry properties of crystal lattices are described by their space group. A space group consists of discrete translational symmetry of the lattice along the lattice vectors, and of the *point group*. The latter describes the relation between the lattice vectors (i.e. the symmetry of the Bravais lattice) as well as the symmetries of the unit cell itself. Point groups contain symmetry operations which leave at least one point of the lattice fixed. These operations include, discrete n-fold rotation axes, reflections off

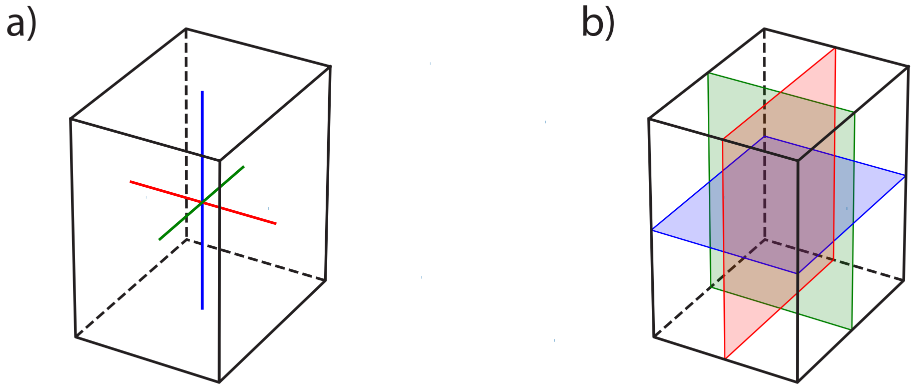

Figure 2.2: **$\mathbf{D_{2h}}$ symmetry operations.** Shown are the 2-fold rotation axes a) and mirror planes b) in an orthorhombic lattice.

planes, discrete rotations followed by reflections off planes perpendicular to the rotation axes, and inversion about the center of symmetry.

A point group can only contain the above operations in a way such that all axes or planes of symmetry intersect in at least one point. Otherwise, successive application of symmetry operations can violate the requirement that one point needs to remain fixed at all times.

There are a total of 32 point groups describing the symmetries of crystal lattices[2]. Comprehensive lists can be found for example in [15, 16], or at this website created by Gernot Katzer [18]. Here we will discuss the orthorhombic (D_{2h}) and hexagonal (D_{6h}) point groups, since they are most relevant to the materials studied in this thesis (D_{2h} for chapter 5 and D_{6h} for chapter 6). More details, including a more general treatment of the D_{nh} and O_h point groups, are given in Appendix B.

Orthorhombic $\mathbf{D_{2h}}$. The symmetries of orthorhombic lattices (see Figure 2.2) are described by three orthogonal 2-fold rotation axes and 3 mirror planes. Each mirror plane is perpendicular to one of the rotation axes. The remaining symmetry element is inversion about the center of the rectangular prism.

Hexagonal $\mathbf{D_{6h}}$. The symmetry operations in hexagonal lattices (see Figure 2.3) include one 6-fold rotation axis (blue), as well as six 2-fold rotation axes perpendicular to it. Out of the six 2-fold rotation axes, only two are non-equivalent (red and green). The rest can be obtained by rotating one of these axes by 60° about the z-axis. The 6-fold rotation axis is also a rotary-reflection axis. There are also seven mirror planes. One is

---

[2] There are, however, only 7 point groups describing Bravais lattices. The remaining 25 can be obtained by considering unit cells which lower the symmetry of the Bravais lattice.

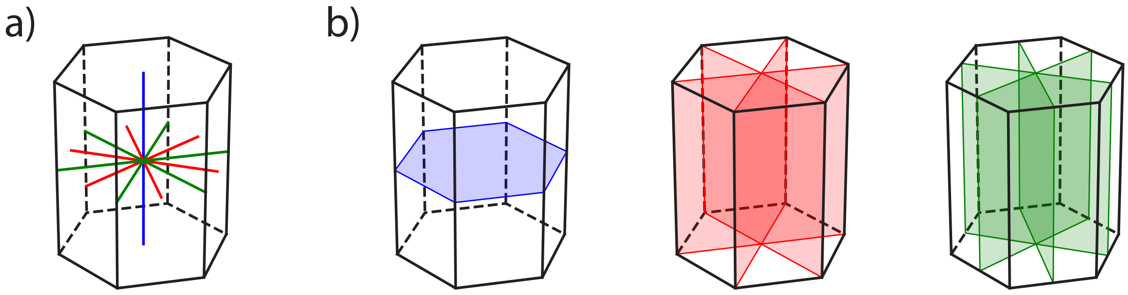

Figure 2.3: **$\mathbf{D_{6h}}$ symmetry operations.** a) shows the rotational symmetry axes. It includes one 6-fold (blue) and six 2-fold (red and green) axes. Axes in the same color are equivalent. b) shows all mirror planes in D_{6h}. Mirror planes with the same color are equivalent.

perpendicular to the 6-fold rotation axis, the remaining six are perpendicular to the 2-fold rotation axes. Again, among those there are only two inequivalent mirror planes. The remaining symmetry element is inversion about the center of the hexagonal prism.

Multiplication Tables. Properties of irreducible representations are tabulated in their character and multiplication tables (see Appendix A for a more detailed introduction of characters and multiplications of irreducible representations). Describing how to find all irreducible representations of a point group extends beyond the scope of this thesis, but the procedures that are used, as well as tabulated properties of many point groups can be found in [16–18]. Here, we give the multiplication tables of the hexagonal D_{6h} (Table 2.1) and orthorhombic D_{2h} (Table 2.2) point groups. Character tables for both point groups are given in Appendix B.

Irreducible representations are conventionally labelled according to Mulliken symbols [19], where A and B are one-dimensional representations, and E[3] and T are two- and three-dimensional representations, respectively. A representations are further symmetric under rotations around the principle axis (often chosen to be the z axis). Subscripts g (u)[4] characterize representations which are even (odd) under inversion.

Since direct products commute, only the upper half of the multiplication tables are populated. Square brackets in the multiplication tables (e.g. $E_{1g} \otimes E_{1g} = A_{1g} \oplus [A_{2g}] \oplus E_{2g}$ for D_{6h} in Table 2.1) refer to the antisymmetric combination of basis functions according to Equation A.3. The multiplication tables (Table 2.1 and Table 2.2) also demonstrate what we have found earlier: the direct product of an irreducible representation with itself (the diagonal elements in the multiplication tables) always contains the identity representation (commonly referred to as A_g or A_{1g}). And only if the dimension of the

---

[3] E stands for ***entartet***, which means degenerate in German.

[4] g stands for ***gerade*** and u for ***ungerade***, which means even and odd in German.

	A_{1g}	A_{2g}	B_{1g}	B_{2g}	E_{1g}	E_{2g}	A_{1u}	A_{2u}	B_{1u}	B_{2u}	E_{1u}	E_{2u}
A_{1g}	A_{1g}	A_{2g}	B_{1g}	B_{2g}	E_{1g}	E_{2g}	A_{1u}	A_{2u}	B_{1u}	B_{2u}	E_{1u}	E_{2u}
A_{2g}		A_{1g}	B_{2g}	B_{1g}	E_{1g}	E_{2g}	A_{2u}	A_{1u}	B_{2u}	B_{1u}	E_{1u}	E_{2u}
B_{1g}			A_{1g}	A_{2g}	E_{2g}	E_{1g}	B_{1u}	B_{2u}	A_{1u}	A_{2u}	E_{2u}	E_{1u}
B_{2g}				A_{1g}	E_{2g}	E_{1g}	B_{2u}	B_{1u}	A_{2u}	A_{1u}	E_{2u}	E_{1u}
E_{1g}					$A_{1g} \oplus [A_{2g}] \oplus E_{2g}$	$B_{1g} \oplus B_{2g} \oplus E_{1g}$	E_{1u}	E_{1u}	E_{2u}	E_{2u}	$A_{1u} \oplus A_{2u} \oplus E_{2u}$	$B_{1u} \oplus B_{2u} \oplus E_{1u}$
E_{2g}						$A_{1g} \oplus [A_{2g}] \oplus E_{2g}$	E_{2u}	E_{2u}	E_{1u}	E_{1u}	$B_{1u} \oplus B_{2u} \oplus E_{1u}$	$A_{1u} \oplus A_{2u} \oplus E_{2u}$
A_{1u}							A_{1g}	A_{2g}	B_{1g}	B_{2g}	E_{1g}	E_{2g}
A_{2u}								A_{1g}	B_{2g}	B_{1g}	E_{1g}	E_{2g}
B_{1u}									A_{1g}	A_{2g}	E_{2g}	E_{1g}
B_{2u}										A_{1g}	E_{2g}	E_{1g}
E_{1u}											$A_{1g} \oplus [A_{2g}] \oplus E_{2g}$	$B_{1g} \oplus B_{2g} \oplus E_{1g}$
E_{2u}												$A_{1g} \oplus [A_{2g}] \oplus E_{2g}$
basis functions	z^2, $x^2 + y^2$	R_z			$\{R_x, R_y\}$ $\{xz, yz\}$	$\{x^2 - y^2, xy\}$		z			$\{x, y\}$	
strains	ϵ_{zz}, $\epsilon_{xx}^2 + \epsilon_{yy}^2$				$\{2\epsilon_{xz}, 2\epsilon_{yz}\}$	$\{\epsilon_{xx} - \epsilon_{yy}, 2\epsilon_{xy}\}$						

Table 2.1: **$\mathbf{D_{6h}}$ multiplication table.** The multiplication table shows how the product of two irreducible representations of the D_{6h} point group can be decomposed into irreducible representations. Additionally, the basis functions (up to second order polynomials or rotations) of certain irreducible representations are given. Linear combinations of strain forming bases of irreducible representations are also given where applicable. Table adapted from [20].

irreducible representation is two or higher does the product with itself contain additional irreducible representations besides A_g.

	A_g	B_{1g}	B_{2g}	B_{3g}	A_u	B_{1u}	B_{2u}	B_{3u}
A_g	A_g	B_{1g}	B_{2g}	B_{3g}	A_u	B_{1u}	B_{2u}	B_{3u}
B_{1g}		A_g	B_{3g}	B_{2g}	B_{1u}	A_u	B_{3u}	B_{2u}
B_{2g}			A_g	B_{1g}	B_{2u}	B_{3u}	A_u	B_{1u}
B_{3g}				A_g	B_{3u}	B_{2u}	B_{1u}	A_u
A_u					A_g	B_{1g}	B_{2g}	B_{3g}
B_{1u}						A_g	B_{3g}	B_{2g}
B_{2u}							A_g	B_{1g}
B_{3u}								A_g
basis functions	x^2, y^2, z^2	R_z xy	R_y xz	R_x yz		z	y	x
strains	ϵ_{xx}, ϵ_{yy}, ϵ_{zz}	$2\epsilon_{xy}$	$2\epsilon_{xz}$	$2\epsilon_{yz}$				

Table 2.2: **$\mathbf{D_{2h}}$ multiplication table.** The multiplication table shows how the product of two irreducible representations of the D_{2h} point group can be decomposed into irreducible representations. Additionally, polynomials up to second order, rotations, and linear combinations of strain which form bases for certain irreducible representations are given. Table adapted from [20].

2.3 Elasticity in Solids

2.3.1 Elastic Tensors in Crystal Lattices

The elastic tensor c_{ijkl} is defined as the proportionality constant between stress σ_{ij} and strain ϵ_{ij} according to Hooke's law:

$$\sigma_{ij} = \sum_{k,l=1}^{3} c_{ijkl}\epsilon_{kl}. \tag{2.2}$$

Stress and strain are symmetric tensors [21, Chapter 1]

$$\boldsymbol{\epsilon} = \begin{pmatrix} \epsilon_{xx} & \epsilon_{xy} & \epsilon_{xz} \\ \epsilon_{xy} & \epsilon_{yy} & \epsilon_{yz} \\ \epsilon_{xz} & \epsilon_{yz} & \epsilon_{zz} \end{pmatrix}, \quad \boldsymbol{\sigma} = \begin{pmatrix} \sigma_{xx} & \sigma_{xy} & \sigma_{xz} \\ \sigma_{xy} & \sigma_{yy} & \sigma_{yz} \\ \sigma_{xz} & \sigma_{yz} & \sigma_{zz} \end{pmatrix}, \tag{2.3}$$

such that there are only 21 independent elements in the elastic tensor and 6 independent elements in σ_{ij} and ϵ_{ij}. We can therefore rewrite the stress and strain tensors into a 6-dimensional vector and the elastic tensor into a 6 × 6 matrix, using the *Voigt notation*. Equation 2.2 then becomes

$$\begin{pmatrix} \sigma_{xx} \\ \sigma_{yy} \\ \sigma_{zz} \\ 2\sigma_{yz} \\ 2\sigma_{xz} \\ 2\sigma_{xy} \end{pmatrix} = \begin{pmatrix} c_{11} & c_{12} & c_{13} & c_{14} & c_{15} & c_{16} \\ c_{12} & c_{22} & c_{23} & c_{24} & c_{25} & c_{26} \\ c_{13} & c_{23} & c_{33} & c_{34} & c_{35} & c_{36} \\ c_{14} & c_{24} & c_{34} & c_{44} & c_{45} & c_{46} \\ c_{15} & c_{25} & c_{35} & c_{45} & c_{55} & c_{56} \\ c_{16} & c_{26} & c_{36} & c_{46} & c_{56} & c_{66} \end{pmatrix} \begin{pmatrix} \epsilon_{xx} \\ \epsilon_{yy} \\ \epsilon_{zz} \\ 2\epsilon_{yz} \\ 2\epsilon_{xz} \\ 2\epsilon_{xy} \end{pmatrix}. \tag{2.4}$$

The number of independent elements in the elastic tensor—the *elastic moduli*—is further reduced in crystal environments of higher symmetry. An extensive treatment of the elastic tensor in all Bravais lattices can be found in [21, Chapter 1, Section 10]. Here, we give those for orthorhombic (D_{2h} point group; 9 independent elastic moduli) and hexagonal (D_{6h} point group; 5 independent elastic moduli) as they are most relevant for the subsequent chapters 5 and 6:

$$\mathbf{c}_{D_{2h}} = \begin{pmatrix} c_{11} & c_{12} & c_{13} & 0 & 0 & 0 \\ c_{12} & c_{22} & c_{23} & 0 & 0 & 0 \\ c_{13} & c_{23} & c_{33} & 0 & 0 & 0 \\ 0 & 0 & 0 & c_{44} & 0 & 0 \\ 0 & 0 & 0 & 0 & c_{55} & 0 \\ 0 & 0 & 0 & 0 & 0 & c_{66} \end{pmatrix}, \quad \mathbf{c}_{D_{6h}} = \begin{pmatrix} c_{11} & c_{12} & c_{13} & 0 & 0 & 0 \\ c_{12} & c_{11} & c_{13} & 0 & 0 & 0 \\ c_{13} & c_{13} & c_{33} & 0 & 0 & 0 \\ 0 & 0 & 0 & c_{44} & 0 & 0 \\ 0 & 0 & 0 & 0 & c_{44} & 0 \\ 0 & 0 & 0 & 0 & 0 & \frac{c_{11}-c_{12}}{2} \end{pmatrix}. \tag{2.5}$$

2.3.2 Elastic Free Energy

In order to analyze the elastic behavior of solids at thermodynamic phase transitions (as is done in subsection 2.3.3 and is relevant for the successive chapters of this thesis), we need to know the free energy of a strained solid. Two considerations play a role here: one is that the free energy has to be invariant under any symmetry transformations of the solid (i.e. it transforms as the identity representation of the relevant point group), meaning each individual term must be invariant. Secondly, the free energy must be in a minimum in thermodynamic equilibrium. It is thus required to have a minimum for vanishing strain and we arrive at the elastic free energy[5]

$$\begin{aligned} \mathcal{F}_{el} &= \frac{1}{2}\epsilon_{ij} c_{ijkl} \epsilon_{kl} && (2.6) \\ &= \frac{1}{2}\epsilon_i c_{ij} \epsilon_j , && (2.7) \end{aligned}$$

where we have switched to Voigt notation (see Equation 2.4) in the second line.

Since the free energy—and thus all its individual terms—is required to be invariant under all symmetry operations, it is helpful to discuss the symmetry properties of deformations. In particular, we can ask how the individual elements of the strain tensor transform under operations of the relevant point group. Or in other words: Which linear combinations of strain form bases for irreducible representations?

In order to find the irreducible representations formed by the elements of the strain tensor, it is helpful to visualize deformations $\vec{u}\,(\vec{x})$ related to certain strains. The strain tensor is defined from deformations as [21]

$$\epsilon_{ij} = \frac{1}{2}\left(\frac{\partial u_i}{\partial x_j} + \frac{\partial u_j}{\partial x_i}\right) . \tag{2.8}$$

Let us consider for example the strain $\epsilon_{xx} + \epsilon_{yy}$, which is equal to the strain tensor

$$\boldsymbol{\epsilon}^{(xx+yy)} = \begin{pmatrix} 1 & 0 & 0 \\ 0 & 1 & 0 \\ 0 & 0 & 0 \end{pmatrix} . \tag{2.9}$$

The simplest deformation vector resulting in this strain is $\vec{u}^{(xx+yy)} = (x, y, 0)$. A streamline plot of this deformation vector is shown in Figure 2.4a. The same figure also contains a color plot of the polynomial x^2+y^2. We can see that both $\vec{u}^{(xx+yy)}$ and x^2+y^2 exhibit the same symmetry properties. Further, considering the example of the D_{6h} point group, in which the polynomial x^2+y^2 forms a one-dimensional A_{1g} irreducible representation (see Table 2.1), we can conclude that the linear combination of xx- and yy-strains $(\epsilon_{xx}+\epsilon_{yy})$ transforms as the A_{1g} irreducible representation of the D_{6h} point group.

---

[5] In principle, certain terms linear in strain are still allowed based on these considerations. They include terms linear in compressional strains (i.e. strains invariant under point group transformations) and linear in temperature. However, since all of our measurements are performed in thermal equilibrium (i.e. we measure the isothermal elastic moduli), this term is zero.

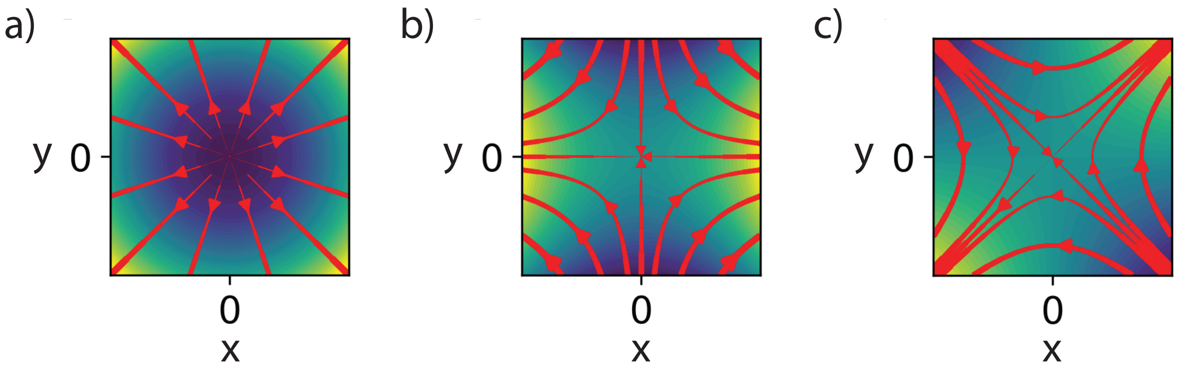

Figure 2.4: **Symmetry properties of strains.** Shown are color plots of the polynomials x^2+y^2 (a), x^2-y^2 (b), and xy (c), overlaid by streamline plots of the deformation vectors $\vec{u}^{(xx+yy)} = (x, y, 0)$ (a), $\vec{u}^{(xx-yy)} = (x, -y, 0)$ (b), and $\vec{u}^{(xy)} = (y, x, 0)$ (c). The thickness of the lines is proportional to the magnitude of the plotted vectors.

Other examples shown in Figure 2.4 are $\epsilon_{xx} - \epsilon_{yy}$ caused by $\vec{u}^{(xx-yy)} = (x, -y, 0)$, which has the same symmetry properties as the polynomial $x^2 - y^2$, and ϵ_{xy} caused by $\vec{u}^{(xy)} = (y, x, 0)$, which has the same symmetry properties as the polynomial xy. A similar analysis can be done for the remaining elements of the strain tensor, resulting in ϵ_{zz}, ϵ_{xz}, and ϵ_{yz} having the same properties under point group symmetry transformations as the polynomials z^2, xz, and yz, respectively. Knowing the polynomial functions which form bases of irreducible representations, it is then straightforward to find the correct linear combinations of strains transforming according to those same irreducible representations. This is done for the D_{6h} and D_{2h} point groups in the bottom rows of Table 2.1 and Table 2.2. A general observation is that strain always transforms as even representations, i.e. strain is always even under inversion.

We can now rewrite the elastic free energy in Equation 2.6 in terms of strains transforming as irreducible representations, done here for the D_{6h} and D_{2h} point groups

$$\begin{aligned}\mathcal{F}_{el}^{D_{6h}} =& \frac{1}{2}\Big(c_{A_{1g},1}\epsilon_{A_{1g},1}^2 + c_{A_{1g},2}\epsilon_{A_{1g},2}^2 + 2c_{A_{1g},3}\epsilon_{A_{1g},1}\epsilon_{A_{1g},2} \\ & + c_{E_{1g}}\left|\epsilon_{E_{1g}}\right|^2 + c_{E_{2g}}\left|\epsilon_{E_{2g}}\right|^2\Big), \end{aligned} \tag{2.10}$$

$$\begin{aligned}\mathcal{F}_{el}^{D_{2h}} =& \frac{1}{2}\big(c_{Ag,1}\varepsilon_{Ag,1}^2 + c_{Ag,2}\varepsilon_{Ag,2}^2 + c_{Ag,3}\varepsilon_{Ag,3}^2 + 2c_{Ag,4}\varepsilon_{Ag,1}\varepsilon_{Ag,2} \\ & + 2c_{Ag,5}\varepsilon_{Ag,1}\varepsilon_{Ag,3} + 2c_{Ag,6}\varepsilon_{Ag,2}\varepsilon_{Ag,3} + c_{B3g}\varepsilon_{B3g}^2 + c_{B2g}\varepsilon_{B2g}^2 + c_{B2g}\varepsilon_{B2g}^2\big). \end{aligned} \tag{2.11}$$

Here, the subscript now refers to the irreducible representation describing the transformation behavior of the relevant strains. We have used the following notation for the D_{6h}

point group

$$\begin{aligned}\epsilon_{A_{1g},1}, \epsilon_{A_{1g},2} &= \epsilon_{xx} + \epsilon_{yy}, \epsilon_{zz}, \quad (2.12)\\ \epsilon_{E_{1g}}, \epsilon_{E_{2g}} &= \left\{2\epsilon_{xz}, 2\epsilon_{yz}\right\}, \left\{\epsilon_{xx} - \epsilon_{yy}, 2\epsilon_{xy}\right\},\\ c_{A_{1g},1}, c_{A_{1g},2}, c_{A_{1g},3} &= \frac{c_{11} + c_{12}}{2}, c_{33}, c_{13}, \quad (2.13)\\ c_{E_{1g}}, c_{E_{2g}} &= c_{44}, \frac{c_{11} - c_{12}}{2},\end{aligned}$$

and for the D_{2h} point group

$$\begin{aligned}\epsilon_{A_g,1}, \epsilon_{A_g,2}, \epsilon_{A_g,3} &= \epsilon_{xx}, \epsilon_{yy}, \epsilon_{zz}, \quad (2.14)\\ \epsilon_{B_{1g}}, \epsilon_{B_{2g}}, \epsilon_{B_{3g}} &= 2\epsilon_{yz}, 2\epsilon_{xz}, 2\epsilon_{xy},\\ c_{A_g,1}, c_{A_g,2}, c_{A_g,3}, c_{A_g,4}, c_{A_g,5}, c_{A_g,6} &= c_{11}, c_{22}, c_{33}, c_{12}, c_{13}, c_{23}, \quad (2.15)\\ c_{B_{1g}}, c_{B_{2g}}, c_{B_{2g}} &= c_{66}, c_{55}, c_{44}.\end{aligned}$$

From this analysis, we can define *compressional strains* as symmetry conserving, i.e. A_{1g}, strains, whereas *shear strains* break the symmetry of the point group and transform as an irreducible representation different from the identity representation. Note that the elastic moduli are also labelled with an irreducible representation in their subscript. However, all elastic moduli are scalars (i.e. invariant under any symmetry operation), this label is only to make clear which is the corresponding strain.

2.3.3 The Elastic Tensor at Second Order Phase Transitions

After discussing the free energy of a deformed solid, the next step is to analyze the effect of a second order phase transition on the elastic tensor. This section mainly follows [22–24].

The Ginzburg-Landau free energy of a second order phase transition described by an order parameter η is given by

$$\mathcal{F}_{OP} = \frac{1}{2}a\eta^2 + \frac{1}{4}b\eta^4, \tag{2.16}$$

where $a = \alpha\left(T - T_c\right)$, and α and b are real, positive constants. Since any representation can be decomposed into direct sums of irreducible representations, let us assume for simplicity that η transforms according to an irreducible representation of the point group describing the free energy. The above free energy is always allowed by symmetry, since the product of any irreducible representation with itself always contains the identity representation. Terms cubic in the order parameter are in principle allowed for certain irreducible representations and point groups (for example for the E_{2g} representation in the D_{6h} point group), but lead to first order rather than second order phase transitions.

The order parameter η is in general allowed to transform as any of the irreducible representations of the given point group, including multidimensional ones (for example

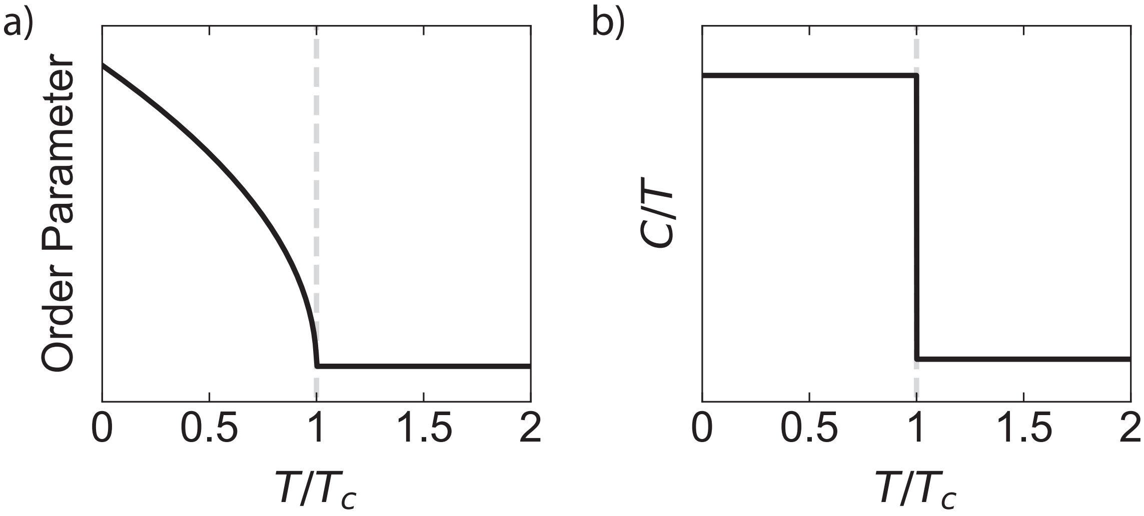

Figure 2.5: **Second order phase transition.** Temperature dependence of the order parameter amplitude (a) and the specific heat C/T (b) at a second order phase transition.

E_{1g} or E_{2g} in D_{6h}). In that case the order parameter is often parametrized as $\eta = (\eta_x, \eta_y)$, and it is important to keep in mind that η^2 and η^4 in Equation 2.16 refer to the direct product of the irreducible representation. That means, η^2 is not only $\eta_x^2 + \eta_y^2$, but also includes terms like $\eta_x^2 - \eta_y^2$, or $\eta_x \eta_y$. All such combinations which transform as the identity representation are then allowed to appear in the free energy.

The order parameter in the above free energy is zero above the critical temperature T_c and is proportional to $\sqrt{T_c - T}$ below (see Figure 2.5a). One of the most common ways to measure phase transitions is to measure the specific heat divided by temperature C/T, which shows a step discontinuity (i.e. a jump) at T_c (Figure 2.5b). This step is always a step up (i.e. C/T is larger for $T < T_c$).

We now introduce additional terms into the free energy, which couple the order parameter and strain

$$\mathcal{F}_{coupling} = \gamma \eta^n \epsilon_\Gamma^m, \tag{2.17}$$

where γ is a real constant and Γ refers to the irreducible representation of the strain (see for example Equation 2.12 or Equation 2.14). Of course, the above product is only allowed to be present in the free energy is the direct product of the irreducible representations of the order parameter and strain transform as the identity transformation (if the direct product contains more than one irreducible representation, only the specific combinations of η and ϵ forming the identity representation are allowed). Below, we discuss the effects of a coupling between strain ϵ_Γ and order parameter η up to second order in both on the corresponding elastic modulus c_Γ (they are summarized in Figure 2.6):

- $\boldsymbol{\eta\epsilon_\Gamma}$: This term linear in both order parameter and strain leads to a divergence $\propto \frac{1}{T-T_c}$ of the corresponding elastic modulus c_Γ. This product is only allowed if η

and ϵ_Γ transform according to the same irreducible representation. This behavior is analogous to the divergence of the magnetic susceptibility in a ferromagnet close to the phase transition.

- $\boldsymbol{\eta\epsilon_\Gamma^2}$: This term linear in order parameter and quadratic in strain can be interpreted as a correction to the elastic moduli in Equation 2.10 or Equation 2.11. Above T_c, the order parameter is zero and the normal state elastic modulus is unaffected. Below T_c, c_Γ shows an additional component proportional to $\sqrt{T_c - T}$. When considering this term it is important to note that the direct product of strain with itself can only form symmetric combinations. E.g. even though in D_{6h}, $E_{2g} \otimes E_{2g} = A_{1g} \oplus [A_{2g}] \oplus E_{2g}$ (where the square brackets denote the antisymmetric product; see Table 2.1), if we are considering strain as the object transforming as the E_{2g} representation, only the A_{1g} and E_{2g} representations are be accessible.
- $\boldsymbol{\eta^2\epsilon_\Gamma}$: This term quadratic in order parameter η and linear in strain ϵ_Γ will lead to a jump in the elastic modulus c_Γ at T_c. The size of this jump δc is related to the jump in the specific heat $\Delta C/T$ through Ehrenfest relations:

  $$\delta c_\Gamma = -\frac{\Delta C}{T}\left(\frac{dT_c}{d\epsilon_\Gamma}\right)^2. \tag{2.18}$$

  This term is always allowed for compressional strains (i.e. strains transforming as A_{1g}), since the direct product of an irreducible representation with itself always contains the identity representation (i.e. η^2 will always contain the A_{1g} representation). If and only if the dimension of the irreducible representation of the order parameter is greater than one can the direct product with itself contain other irreducible representations, besides A_{1g}. From this follows that for shear strains, this term linear in strain and quadratic in order parameter (and the resulting jump of the elastic modulus at T_c) is only possible for order parameters with multidimensional representations.
- $\boldsymbol{\eta^2\epsilon_\Gamma^2}$: This term quadratic in both strain and order parameter is always allowed for any representation of ϵ_Γ or η and leads to a change in slope (a *kink*) of the respective elastic modulus c_Γ at T_c.

We have so far restricted our discussion to point group symmetries. However, other symmetry operations exist under which solids (and consequently their free energy) are invariant. They include for example time-reversal symmetry (TRS), discrete translational symmetry, or gauge symmetry. All strains transform as the identity representation under all of these symmetry transformations, however, order parameters in general do not. Magnetic order parameters, for example, generally break TRS. In that case, out of the four coupling terms discussed above, only those in which η appears in in even powers are allowed by symmetry. The same holds for superconducting order parameters (gauge symmetry) and charge density waves (translational symmetry).

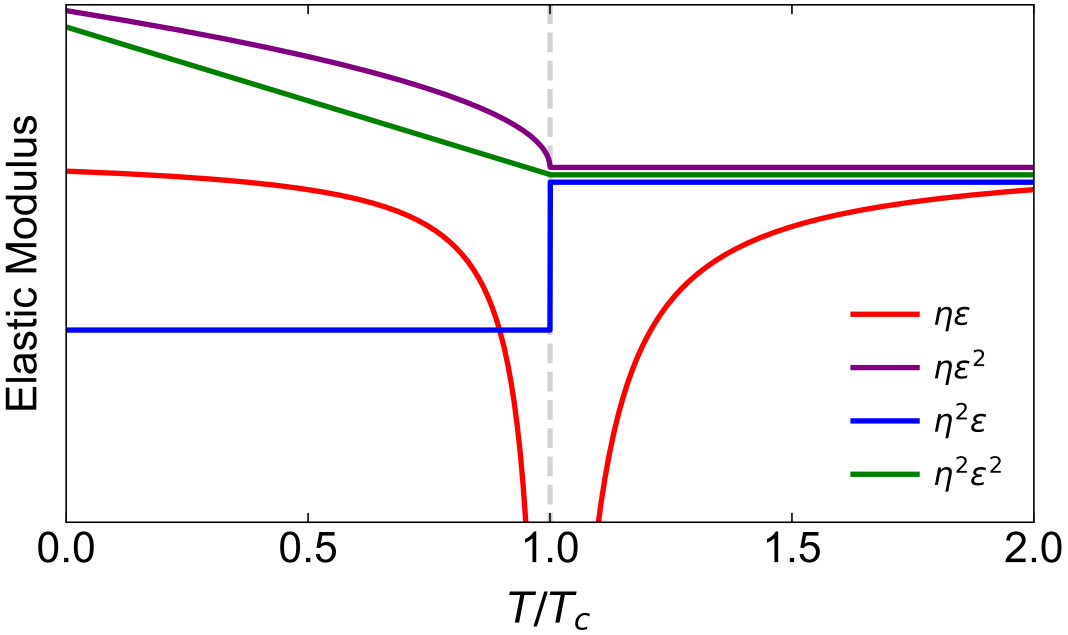

Figure 2.6: **Elastic moduli at 2$^{\text{nd}}$ order phase transitions.** Temperature dependence of elastic moduli at a second order phase transition for various couplings between strain and the order parameter.

2.4 Superconductivity

In 1908, Heike Kamerlingh Onnes first managed to liquefy helium, opening an entire new realm of low temperature physics. This achievement earned him the Nobel prize in 1913, *for his investigations on the properties of matter at low temperatures which led, inter alia, to the production of liquid helium* [25]. Three years later, enabled by his discovery, Onnes observed a vanishing resistivity in mercury below about 4.2 K [5]. With that discovery, mercury was the first measured superconductor. Besides zero resistivity, superconductors also exhibit the Meißner (or Meißner–Ochsenfeld) effect, which is the complete expulsion of constant applied magnetic fields when cooled through their superconducting transitions. Note that this effect is distinct from the expulsion of a magnetic field which is turned on when the sample is inside the superconducting state (this magnetic field expulsion can be explained solely on the basis of perfect conduction). However, it took almost half a decade and many failed attempts [26] until 1957, when Bardeen, Cooper, and Schrieffer (BCS) developed a microscopic theory of superconductivity [27].

2.4.1 Conventional Superconductivity

BCS theory describes conventional superconductivity where an attractive interaction between electrons causes the formation of Cooper pairs. The development of this state of Cooper pairs opens a gap at the Fermi surface, which is at the heart of the abovementioned measurable properties of superconductors [28, 29]. It can be described by the pairing Hamiltonian

$$\mathcal{H} = \sum_{\vec{k},s} \xi_{\vec{k}} c^{\dagger}_{\vec{k}s} c_{\vec{k}s} + g \sum_{\vec{k},\vec{k}'} c^{\dagger}_{\vec{k},\uparrow} c^{\dagger}_{-\vec{k},\downarrow} c_{-\vec{k}',\downarrow} c_{\vec{k}',\uparrow}, \tag{2.19}$$

where $c_{\vec{k},s}$ ($c^{\dagger}_{\vec{k},s}$) annihilates (creates) an electron with momentum $\vec{k}$ and spin s. The first term is the electron band structure $\epsilon_{\vec{k}}$ of the metal with respect to the chemical potential μ: $\xi_{\vec{k}} = \epsilon_{\vec{k}} - \mu$. The second term describes the attractive interaction between two particles of opposite spin and momentum, with a constant scattering matrix element $g < 0$. g is assumed to be momentum independent, which originates from an attractive contact interaction $U(\vec{r}, \vec{r}') = g\delta(\vec{r} - \vec{r}')$ in real space. The latter is motivated by the very short range of electron-phonon interactions, which are the attractive interaction mechanism at the base of BCS theory. The variational ground state to this Hamiltonian given by BCS is

$$|\Phi_{\mathrm{BCS}}\rangle = \prod_{\vec{k}} \left\{ u_{\vec{k}} + v_{\vec{k}} c^{\dagger}_{\vec{k},\uparrow} c^{\dagger}_{-\vec{k},\downarrow} \right\} |\mathrm{vac}\rangle, \tag{2.20}$$

where $|\mathrm{vac}\rangle$ is the vacuum and $\left|u_{\vec{k}}\right|^2 + \left|v_{\vec{k}}\right|^2 = 1$. It describes a coherent state of pairs of electrons with opposite spin and momentum (i.e. *Cooper pairs*). Using the intuition given by this Cooper pair ground state, we can alternatively define the mean field

$$b_{\vec{k}} = \langle c_{-\vec{k},\downarrow} c_{\vec{k},\uparrow} \rangle, \tag{2.21}$$

which connects states that differ by two electrons. $b_{\vec{k}}$ can be interpreted as the *pair wavefunction* of Cooper pairs in momentum space. The expectation value is given by $\langle A \rangle = \mathrm{tr}\left[\exp(-\beta\mathcal{H}) A\right] / \mathrm{tr}\left[\exp(-\beta\mathcal{H})\right]$, and $\beta = 1/k_B T$ is the inverse temperature. Substituting Equation 2.21 into the Hamiltonian (Equation 2.19) and ignoring terms quadratic in $\left(c_{-\vec{k},\downarrow} c_{\vec{k},\uparrow} - b_{\vec{k}}\right)$, the Hamiltonian becomes

$$\mathcal{H} = \sum_{\vec{k},s} \xi_{\vec{k}} c^{\dagger}_{\vec{k}s} c_{\vec{k}s} - \sum_{\vec{k}} \left(\Delta^* c_{-\vec{k},\downarrow} c_{\vec{k},\uparrow} + \Delta c^{\dagger}_{\vec{k},\uparrow} c^{\dagger}_{-\vec{k},\downarrow} \right) - \Delta^* b_{\vec{k}}. \tag{2.22}$$

Here we have defined $\Delta = -g \sum_{\vec{k}} b_{\vec{k}}$. We can then diagonalize the above mean field Hamiltonian by using the Bogoliubov transformation

$$c_{\vec{k},\uparrow} = u^*_{\vec{k}} \gamma_{\vec{k}1} + v_{\vec{k}} \gamma^{\dagger}_{\vec{k}2}, \tag{2.23}$$

$$c^{\dagger}_{-\vec{k},\downarrow} = -v^*_{\vec{k}} \gamma_{\vec{k}1} + u_{\vec{k}} \gamma^{\dagger}_{\vec{k}2}. \tag{2.24}$$

$\gamma_{\vec{k}1}$ contains both $c_{\vec{k}\uparrow}$ and $c^{\dagger}_{-\vec{k}\downarrow}$, i.e. it takes part in destroying an electron with momentum $\vec{k}$ and spin ↑ or creating an electron with momentum $-\vec{k}$ and spin ↓. Either way, it reduces the total momentum by $\vec{k}$ and the spin component S_z by $\hbar/2$, i.e. it acts as an electron-like quasiparticle. $\gamma_{\vec{k}2}$, on the other hand, increases the total momentum and S_z, i.e. it acts as a hole-like quasiparticle. The functions $u_{\vec{k}}$ and $v_{\vec{k}}$ are identical to those in Equation 2.20 and we have again that $\left|u_{\vec{k}}\right|^2 + \left|v_{\vec{k}}\right|^2 = 1$. Using this transformation, the Hamiltonian reads

$$\mathcal{H} = \sum_{\vec{k}} \left(\xi_{\vec{k}} - E_{\vec{k}} + \Delta b_{\vec{k}}\right) + \sum_{\vec{k}} E_{\vec{k}} \left(\gamma^{\dagger}_{\vec{k}1}\gamma_{\vec{k}1} + \gamma^{\dagger}_{\vec{k}2}\gamma_{\vec{k}2}\right), \tag{2.25}$$

where $E_{\vec{k}} = \pm\sqrt{\xi^2_{\vec{k}} + \Delta^2}$ is the Bogoliubov quasiparticle energy. $\sum_{\vec{k}} \left(\xi_{\vec{k}} - E_{\vec{k}} + \Delta b_{\vec{k}}\right) \approx -\frac{1}{2}N_0 \left|\Delta\right|^2$ is *condensation energy*, i.e. the energy gain due to the formation of the Cooper pair ground state (N_0 is the density of states at the Fermi level). In summary, the attractive interaction g in Equation 2.19 leads to a Fermi surface instability where electron-like ($\gamma_{\vec{k}1}$) and hole-like ($\gamma_{\vec{k}2}$) quasiparticles hybridize and a gap of 2Δ opens up.

In the above treatment, the definition of the pair wavefunction $b_{\vec{k}} = \langle c_{-\vec{k},\downarrow} c_{\vec{k},\uparrow}\rangle$ is only appropriate because we expect the ground state to be a coherent superposition of many-body states with Cooper pairs $\left(\vec{k}\uparrow, -\vec{k}\downarrow\right)$ (i.e. Equation 2.20). Only in this ground state is the expectation value in $b_{\vec{k}}$ non-zero, as opposed to normal metals, where it averages to zero. This is also why $b_{\vec{k}}$ is a possible choice of order parameter. Just as appropriate, since it possesses the same symmetry properties, is the use of the gap function Δ as the order parameter.

2.4.2 Symmetry Considerations

Let us now consider the symmetry properties of the superconducting order parameter. As mentioned above, point group symmetries are not the only transformations which leave the free energy invariant. The full symmetry group respected by the free energy is given by [30]

$$G = G_0 \times U(1) \times T. \tag{2.26}$$

T represents time-reversal, $U(1)$ is the group of global gauge transformations, and G_0 contains space group symmetries as well as spin rotations. In this thesis, however, we are only investigating point group symmetry breaking superconducting order parameters which are translationally invariant. Notably, under $U(1)$ gauge transformations the superconducting order parameter develops a global phase $b_{\vec{k}} \to b_{\vec{k}}e^{i\phi}$ (or equivalently for Δ), and under time reversal $b_{\vec{k}}$ (Δ) changes to its complex conjugate $b^*_{\vec{k}}$ (Δ^*). Since the superconducting order parameter is in general a complex function, we cannot make any generally applicable comments about its representation under time-reversal symmetry. We are eventually interested in how superconducting order parameters and strain couple in the free energy. Since strain breaks neither $U(1)$ gauge symmetry nor time-reversal symmetry, a superconducting order parameter can only ever appear in even powers when coupling to strain. In particular, products of the order parameter with itself have to be formed in a way such that it transforms as the identity transformations under $U(1)$ and T. We revisit this argument in subsection 2.4.5, when explicitly analyzing elastic moduli at superconducting phase transitions. Here, the consequence is that when discussing symmetry properties of superconducting order parameters, we focus solely on the point group and spin rotation symmetries in G_0.

In the case of small spin-orbit coupling[6], G_0 can be decomposed into

$$G_0 = G_c \times SO(3), \tag{2.27}$$

where $SO(3)$ is the group of continuous rotations in three dimensions describing spin rotations, and G_c is the point group of the crystal lattice describing orbital symmetries[7]. In this case, where orbital and spin rotations are independent of each other, we can parametrize the pair wavefunction of Cooper pairs as the product of an orbital f and spin χ part

$$\Psi(\vec{r}, s; \vec{r}', s') = f\left(\vec{r} - \vec{r}'\right) \chi\left(s, s'\right). \tag{2.28}$$

The basis of BSC theory of conventional superconductivity (see subsection 2.4.1) was very short-ranged phonon-mediated interactions between quasiparticles. It was modeled as a contact interaction $g\delta\left(\vec{r} - \vec{r}'\right)$. That is, two quasiparticles only interact with each other, if there is a finite probability for both to exist at the same place. Following from the Pauli exclusion principle, the pair wavefunction can then only include pairs of opposite spins, and the spin part $\chi\left(s, s'\right)$ must behave like a spin singlet. Additionally, the orbital part in Equation 2.28 must be heavily peaked at $\vec{r} - \vec{r}' = 0$, and it can only depend on the distance between to particles, but not on the direction of $\vec{r} - \vec{r}'$, i.e. $f = f\left(|\vec{r} - \vec{r}'|\right)$. Thus, f transforms as the identity representation of the point group G_c. Often times, angular momentum states, i.e. the irreducible representations of free space, are used to describe the spatial symmetries of a superconducting order parameter. In this language, the order parameter of a conventional superconductor transforms as an s-wave state. The spin-singlet nature of χ, and identity representation of f are the defining features of conventional superconductors. Their order parameter only breaks $U(1)$ gauge symmetry, but does not further reduce the symmetry of the lattice.

Since the form of the pair wavefunction in Equation 2.28 is purely based on the requirement of small spin-orbit coupling, some of the above considerations can be generalized to unconventional superconductors (see more on unconventional superconductors in subsection 2.4.3). Because the pair wavefunction describes a state with two electron-like quasiparticles, it must acquire a minus sign when exchanging particles, i.e.

$$\Psi(\vec{r}, s; \vec{r}', s') = -\Psi(\vec{r}', s'; \vec{r}, s). \tag{2.29}$$

---

[6] In subsection 2.4.4 we treat the case of strong spin-orbit coupling, where orbital and spin rotations are not independent and need to be considered together.

[7] In general, G_c is the full space group of the lattice. However, since we are only investigating translationally invariant superconducting order parameters in this thesis, it is sufficient to consider the point group symmetries.

It follows that either $\chi\left(s,s'\right)=-\chi\left(s',s\right)$, or $f\left(\vec{r}-\vec{r}'\right)=-f\left(\vec{r}'-\vec{r}\right)$. Notably, exchanging particles has the same effect on f as inversion (i.e. $\vec{r}\rightarrow-\vec{r}$), such that the two possible scenarios are:

1. The orbital part of the pair wavefunction is even under inversion (i.e. it has even parity) and the spin part is odd under particle exchange.
2. The orbital part of the pair wavefunction is odd under inversion (i.e. it has odd parity) and the spin part is even under particle exchange.

Since the pair wavefunction describes two spins, the only possibilities for χ are a spin-singlet state (i.e. $S=0$) which is odd under particle exchange, or a spin-triplet state (i.e. $S=1$, $S_z=-1,0,1$) which is even under particle exchange (see discussion on angular momentum irreducible representations in three dimensions earlier). In the case of small spin orbit coupling, the terms *spin singlet* and *even parity* (or *spin triplet* and *odd parity*) are therefore often used interchangeably.

As mentioned above, in the context superconducting order parameter symmetries, the effects of the crystal lattice are often ignored and order parameters are classified according to their angular momentum (i.e. irreducible representations of the three-dimensional rotation group in free space), instead of according to irreducible representations of the point group of the lattice. Even angular momentum states (e.g. s, d, g, ...) are even under inversion, whereas odd angular momentum states (e.g. p, f, ...) are odd under inversion. Spin-singlet superconductors are therefore s-, d-, g-, ... wave superconductors and spin-triplet superconductors are p-, $f-$, ... wave superconductors.

While the classification of superconductors according to angular momentum is not entirely correct in a crystal lattice, where irreducible representations of the relevant point group should be used to classify order parameters, it is helpful to gain some physical intuition. Certain irreducible representations can still be assigned angular momentum and the above parity argument still holds. For example, the three-dimensional p-wave representation $\{p_x,p_y,p_z\}$ in free space splits into one one-dimensional representation $\{p_z\}$ (A_{2u}) and one two-dimensional representation $\{p_x,p_y\}$ (E_u) in a tetragonal lattice (D_{4h}). While angular momentum is not a good quantum number anymore to distinguish between these two irreducible representations, both can be assigned angular momentum $J=1$, and both representations are odd under inversion (just like the p-wave $J=1$ state in $SO(3)$).

2.4.3 Unconventional Superconductivity

The s-wave character of conventional BCS superconductivity follows directly from an attractive interaction at $\vec{r}-\vec{r}'=0$[8]. Such an interaction is possible if attractive phonon-

---

[8] Note that an attractive interaction described by $\delta(\vec{r}-\vec{r}')$ is, however, not the only way to achieve s-wave superconductivity.

mediated interactions are dominant over repulsive Coulomb interactions. For strongly correlated electron systems, however, repulsive Coulomb interaction dominates at $\vec{r}-\vec{r}'=0$. Unconventional superconductors get around this repulsive interaction by forming higher angular momentum pair wavefunctions (i.e. p, d, f, g, ...), which have zero probability of both quasiparticles being at the same place. Thus, unconventional superconductors usually have non-zero angular momentum Cooper pairs, or equivalently, their order parameter transforms as a non-trivial representation of the relevant point group. Several different interaction mechanisms have been shown to mediate unconventional superconductivity, including ferro- and antiferrmagnetic fluctuations [8].

In this section, following [10, 29, 31], we discuss basic properties of unconventional superconductors. For this purpose, it is not necessary to assume any particular pairing interaction. It is enough to introduce a general (attractive) scattering matrix element $V_{\vec{k},\vec{k}';s_1s_2s_3s_4}$ into the BCS pairing Hamiltonian in Equation 2.19:

$$\mathcal{H} = \sum_{\vec{k},s} \xi_{\vec{k}} c^\dagger_{\vec{k}s} c_{\vec{k}s} + \frac{1}{2} \sum_{\vec{k},\vec{k}'} \sum_{s_1,s_2,s_3,s_4} V_{\vec{k},\vec{k}';s_1s_2s_3s_4} c^\dagger_{\vec{k},s_1} c^\dagger_{-\vec{k},s_2} c_{-\vec{k}',s_3} c_{\vec{k}',s_4}. \tag{2.30}$$

In analogy to the conventional case, we can define the mean field

$$b_{\vec{k},ss'} = \langle c_{-\vec{k}s} c_{\vec{k}s'} \rangle \,. \tag{2.31}$$

Ignoring terms quadratic in deviations from $b_{\vec{k},ss'}$ results in

$$\mathcal{H} = \sum_{\vec{k},s} \xi_{\vec{k}} c^\dagger_{\vec{k}s} c_{\vec{k}s} - \frac{1}{2} \sum_{\vec{k},s_1,s_2} \left(\Delta_{\vec{k},s_1s_2} c^\dagger_{\vec{k},s_1} c^\dagger_{-\vec{k},s_2} + \Delta^*_{\vec{k},s_1s_2} c_{\vec{k},s_1} c_{-\vec{k}',s_2} \right) + K, \tag{2.32}$$

where $K = -\frac{1}{2} \sum_{\vec{k},\vec{k}'} \sum_{s_1,s_2,s_3,s_4} V_{\vec{k},\vec{k}';s_1s_2s_3s_4} \langle c^\dagger_{\vec{k}s_1} c^\dagger_{-\vec{k}s_2} \rangle \langle c_{-\vec{k}'s_3} c_{\vec{k}'s_4} \rangle$. The gap functions are defined as

$$\Delta_{\vec{k},ss'} = - \sum_{\vec{k}',s_3s_4} V_{\vec{k},\vec{k}';ss's_3s_4} b_{\vec{k}',s_3s_4}, \tag{2.33}$$

$$\Delta^*_{\vec{k},ss'} = - \sum_{\vec{k}',s_1s_2} V_{\vec{k}',\vec{k};s_1s_2s's} b^*_{\vec{k}',s_1s_2}, \tag{2.34}$$

such that the total generalized gap function is now a complex 2 × 2 matrix

$$\hat{\Delta}_{\vec{k}} = \begin{pmatrix} \Delta_{\vec{k},\uparrow\uparrow} & \Delta_{\vec{k},\uparrow\downarrow} \\ \Delta_{\vec{k},\downarrow\uparrow} & \Delta_{\vec{k},\downarrow\downarrow} \end{pmatrix} . \tag{2.35}$$

In this notation, spin-singlet pairing can be described by a single (even parity) gap function $\Delta^0_{\vec{k}} = \Delta^0_{-\vec{k}}$ such that

$$\hat{\Delta}^{singlet}_{\vec{k}} = \begin{pmatrix} 0 & \Delta^0_{\vec{k}} \\ -\Delta^0_{\vec{k}} & 0 \end{pmatrix} . \tag{2.36}$$

Using this singlet gap function and diagonalizing the Hamiltonian in Equation 2.32 yields the quasiparticle spectrum

$$E_{\vec{k}}^{singlet} = \pm\sqrt{\xi_{\vec{k}}^2 + \left|\Delta_{\vec{k}}^0\right|^2}, \tag{2.37}$$

analogous to the conventional case with the only difference that the quasiparticle gap $\Delta_{\vec{k}}^0$ is allowed to be momentum dependent here. For weak spin-orbit coupling, we can again separate the gap function into a spin and an orbital part, where the spin part transforms as a singlet state and the orbital part transforms as even angular momentum states (in free space) or as even irreducible representations of a point group (in a crystal lattice).

In the case of spin-triplet pairing, the gap matrix has three independent elements ($\Delta_{\vec{k},\uparrow\downarrow} = \Delta_{\vec{k},\downarrow\uparrow}$) and can be represented by a three-dimensional (odd parity) complex vector in spin space $\mathbf{d}(\vec{k}) = d_x(\vec{k})\mathbf{x} + d_y(\vec{k})\mathbf{y} + d_z(\vec{k})\mathbf{z}$[9], where the following basis is chosen:

$$\begin{aligned}
\mathbf{x} &= \frac{1}{\sqrt{2}}\left(-\left|\uparrow\uparrow\right\rangle + \left|\downarrow\downarrow\right\rangle\right) = \left|S_x = 0\right\rangle, \\
\mathbf{y} &= \frac{1}{\sqrt{2}}\left(\left|\uparrow\uparrow\right\rangle + \left|\downarrow\downarrow\right\rangle\right) = \left|S_y = 0\right\rangle, \\
\mathbf{z} &= \frac{1}{\sqrt{2}}\left(\left|\uparrow\downarrow\right\rangle + \left|\downarrow\uparrow\right\rangle\right) = \left|S_z = 0\right\rangle.
\end{aligned} \tag{2.38}$$

In this basis, the gap matrix reads

$$\hat{\Delta}_{\vec{k}}^{triplet} = \begin{pmatrix} -d_x + id_y & d_z \\ d_z & d_x + id_y \end{pmatrix}. \tag{2.39}$$

Diagonalizing the Hamiltonian Equation 2.32 with this gap matrix results in the following quasiparticle spectrum:

$$E_{\vec{k}}^{triplet} = \pm\sqrt{\xi_{\vec{k}}^2 + \Delta_{\vec{k}}^2}, \tag{2.40}$$

$$\Delta_{\vec{k}} = \sqrt{\mathbf{d}\cdot\mathbf{d}^* \pm |\mathbf{d}\times\mathbf{d}^*|}. \tag{2.41}$$

From this Equation 2.40 we can distinguish two qualitatively different cases: the first case is $|\mathbf{d}\times\mathbf{d}^*| = 0$. Superconducting states with this **d**-vector are called *unitary*. *Non-unitary* pairing is then described by $|\mathbf{d}\times\mathbf{d}^*| \neq 0$. For non-unitary superconductors, two different gaps appear in the quasiparticle spectrum, i.e. ↑↑ and ↓↓ Cooper pairs have different gaps. **d**-vectors of non-unitary states are not time-reversal invariant. Instead, time-reversal (which transforms **d** into $\mathbf{d}^*$) leads to a rotation of the **d**-vector in spin space, such that **d** and $\mathbf{d}^*$ are not parallel.

For weak spin-orbit coupling, and similarly to the cases of conventional or unconventional spin-singlet superconductivity, we can again separate the orbital and spin symmetry properties of the spin-triplet pairing wavefunction, or equivalently the **d**-vector. As

---

[9] Here the vector **d** is denoted by a bold letter to emphasize its vector nature in spin space and distinguish it from vectors in orbital/momentum space denoted as $\vec{k}$.

mentioned above, **d** transforms as a vector in spin-space. That is, it transforms as a three-dimensional representation of continuous rotations in three dimensions ($SO(3)$), i.e. the $J = 1$ representation or spin-triplet state. Orbital symmetry operations (i.e. continuous rotations in free space or point group elements in a lattice) act on **d** through its momentum dependence, i.e. a symmetry transformation g acts as $g\mathbf{d}(\vec{k}) = \mathbf{d}(g\vec{k})$. Therefore, when categorizing the **d**-vector into irreducible representations (or angular momentum states), each component of **d** can be analyzed independently.

2.4.4 Strong Spin-Orbit Coupling

In the discussion of the symmetry properties of the superconducting gap function (or the **d**-vector) in the sections above, we have always assumed weak spin-orbit coupling. In that case we were able to independently analyze its behavior under spin rotations and point group transformations. In many strongly correlated electron systems, e.g. in many heavy-fermion superconductors, spin-orbit coupling is strong, however, and the pair wavefunction cannot be separated into a spin and orbital part. Below, we will discuss this case of strong spin-orbit coupling, following [30].

For any transformation of the point group of the lattice involving rotations, the rotation has to be carried out on the orbital *and* spin coordinates of the order parameter. The full symmetry group of the free energy reduces from Equation 2.26 and Equation 2.27 to

$$G = G_c \times U(1) \times T. \tag{2.42}$$

As a consequence, we cannot characterize the transformation of the spin coordinates according to continuous rotations in three dimensions anymore, but need to view them in the context the point group of the lattice. Thus, the language of spin-singlet and spin-triplet, which referred to the $J = 0$ and $J = 1$ irreducible representations of rotations in three-dimensions, is not appropriate anymore. Rather, for an order parameter transforming according to the irreducible representation Γ_{orbit} when transformations are applied to the orbital coordinates and according to Γ_{spin} when applied to the spin coordinates, the correct transformation behavior of the order parameter is characterized by the representation given by the direct product $\Gamma_{orbit} \otimes \Gamma_{spin}$.

First, let us consider what used to be spin-singlet states. Spin-singlet Cooper pairs in the weak spin-orbit limit were characterized by vanishing angular momentum. In the strong spin-orbit limit, this property is now equivalent to a pair wavefunction isotropic under point group rotations applied to the spin coordinates. That is, Γ_{spin} is the identity representation of the point group $\Gamma_{spin} = A_g$ (A_g is the identity representation in D_{2h}, but may be denoted differently in other point groups). Therefore, $\Gamma_{orbit} \otimes \Gamma_{spin} = \Gamma_{orbit} \otimes A_g = \Gamma_{orbit}$ and only the irreducible representation formed by symmetry transformations of the orbital coordinates need to be considered. We can thus treat the point group symmetry properties of the order parameter in the strong spin-orbit limit identically to those in the weak spin-orbit limit. Importantly, the gap function can still be described by one

Irr. Rep. (basis)	A_u ($k_xk_yk_z$)	B_{1u} (k_z)	B_{2u} (k_y)	B_{3u} (k_x)
B_{1g} ($\mathbf{z}$)	B_{1u}	A_u	B_{3u}	B_{2u}
B_{2g} ($\mathbf{y}$)	B_{2u}	B_{3u}	A_u	B_{1u}
B_{3g} ($\mathbf{x}$)	B_{3u}	B_{2u}	B_{1u}	A_u

Table 2.3: **$\mathbf{D_{2h}}$ triplet order parameters.** Shown is the part of the multiplication table of the D_{2h} point group relevant to an odd parity superconducting order parameter in the strong spin-orbit limit. B_{3g}, B_{2g}, B_{1g} are possible irreducible representations for Γ_{spin}, and A_u, B_{1u}, B_{2u}, B_{3u} are possible irreducible representations for Γ_{orbit}.

complex number $\Delta_{\vec{k}}$, with even parity $\Delta_{\vec{k}} = \Delta_{-\vec{k}}$, such that the only possible irreducible representations are even under inversion.

For spin-triplet states, it is important to remember that the **d**-vector was constructed in a way such that it transforms as a vector under spin rotations. In the context of point groups, this means that **d** transforms as a pseudo-vector, i.e. it transforms as a vector under rotations, but is even under inversion. Therefore, the basis vectors **x**, **y**, and **z** (see Equation 2.38) have the same symmetry properties (and therefore transform according to the same irreducible representations) as the rotations R_x, R_y, and R_z, respectively (see Table 2.1 and Table 2.2 for irreducible representations of rotations in D_{2h} and D_{6h}). While the exact irreducible representations vary for different point groups, they are always even under inversion and since the **d**-vector still requires $\mathbf{d}(\vec{k}) = -\mathbf{d}(-\vec{k})$, any possible irreducible representation Γ_{orbit} has to be odd under inversion, such that the direct product $\Gamma_{orbit} \otimes \Gamma_{spin}$ has odd parity.

Since we are discussing superconductivity in the heavy-fermion, spin-triplet superconductor UTe$_2$ with orthorhombic (i.e. D_{2h}) crystal structure in chapter 5, let us expand here on the possible irreducible representations of the superconducting order parameter, as well as the associated **d**-vector and quasiparticle gap. In D_{2h}, the rotations R_x, R_y, R_z, and therefore also the **d**-vector basis states **x**, **y**, **z** transform as the irreducible representations B_{3g}, B_{2g}, B_{1g}, respectively (see Table 2.2). Since Γ_{orbit} needs to be odd under inversion, the only possibilities are A_u, B_{1u}, B_{2u}, and B_{3u}. Possible irreducible representations of **d** are then given by all direct products between these representations. The relevant part of the multiplication table for D_{2h} (see Table 2.2 for the full table) is shown in Table 2.3. We can distinguish four different irreducible representations (A_u, B_{1u}, B_{2u}, B_{3u}), each of which are obtained by three different combinations of Γ_{spin} and Γ_{orbit}. The irreducible representations, along with the possible basis functions are

$$A_u : k_z\mathbf{z},\ \ k_y\mathbf{y}, k_x\mathbf{x} \tag{2.43}$$

$$B_{1u} : k_xk_yk_z\mathbf{z},\ \ k_x\mathbf{y}, k_y\mathbf{x}, \tag{2.44}$$

$$B_{2u} : k_x\mathbf{z},\ \ k_xk_yk_z\mathbf{y}, k_z\mathbf{x}, \tag{2.45}$$

$$B_{3u} : k_y\mathbf{z},\ \ k_z\mathbf{y}, k_xk_yk_z\mathbf{x}. \tag{2.46}$$

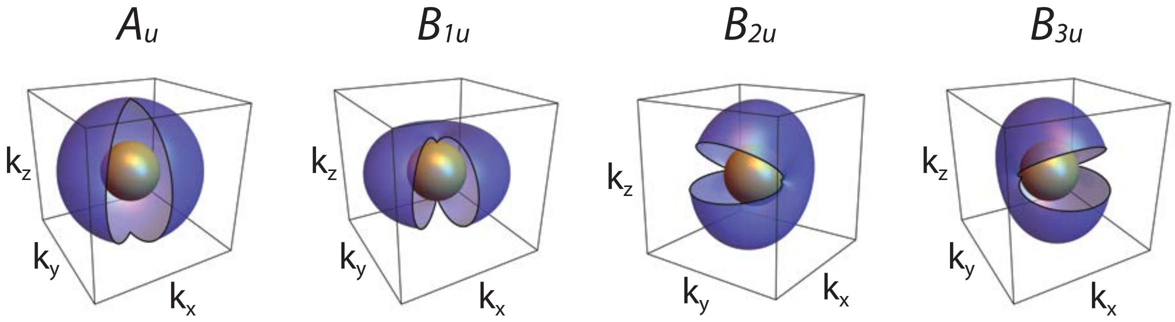

Figure 2.7: **Odd parity quasiparticle gaps in $\mathbf{D_{2h}}$.** Quasiparticle gaps of the odd parity superconducting states $\Delta_{\vec{k}}^{A_u}$, $\Delta_{\vec{k}}^{B1u}$, $\Delta_{\vec{k}}^{B2u}$, $\Delta_{\vec{k}}^{B3u}$ (from left to right) in the strong-spin orbit limit are plotted on a spherical Fermi surface. The magnitude of the gap is proportional to the distance between the Fermi surface (gray surface) and the surface plotted in blue. We have used $\alpha = \beta = \gamma$.

The corresponding **d**-vectors are then given by linear combinations of the three possible basis functions for each irreducible representation

$$\mathbf{d}_{A_u} = \{\alpha k_x, \beta k_y, \gamma k_z\}\,, \tag{2.47}$$
$$\mathbf{d}_{B_{1u}} = \{\alpha k_y, \beta k_x, \gamma k_x k_y k_z\}\,, \tag{2.48}$$
$$\mathbf{d}_{B_{2u}} = \{\alpha k_z, \beta k_x k_y k_z, \gamma k_x\}\,, \tag{2.49}$$
$$\mathbf{d}_{B_{3u}} = \{\alpha k_x k_y k_z, \beta k_z, \gamma k_y\}\,, \tag{2.50}$$

where α, β, and γ are independent, real constants. According to Equation 2.40, these **d**-vectors lead to the following momentum dependencies of the quasiparticle gap,

$$\Delta_{\vec{k}}^{A_u} = \sqrt{(\alpha k_x)^2 + (\beta k_y)^2 + (\gamma k_z)^2}, \tag{2.51}$$
$$\Delta_{\vec{k}}^{B_{1u}} = \sqrt{(\alpha k_y)^2 + (\beta k_x)^2}, \tag{2.52}$$
$$\Delta_{\vec{k}}^{B_{2u}} = \sqrt{(\alpha k_z)^2 + (\gamma k_x)^2}, \tag{2.53}$$
$$\Delta_{\vec{k}}^{B_{3u}} = \sqrt{(\beta k_z)^2 + (\gamma k_y)^2}, \tag{2.54}$$

where we have only included terms linear in k_i. $\Delta_{\vec{k}}^{A_u}$ is fully gapped everywhere on the Fermi surface, $\Delta_{\vec{k}}^{B_{1u}}$ has nodes along k_z (i.e. $k_x = k_y = 0$), $\Delta_{\vec{k}}^{B_{2u}}$ has nodes along k_y (i.e. $k_x = k_z = 0$), and $\Delta_{\vec{k}}^{B_{3u}}$ has nodes along k_x (i.e. $k_y = k_z = 0$) (see Figure 2.7).

2.4.5 Identifying Pairing Symmetries with Strain

The microscopic theory of any superconductor is based on detailed knowledge of its attractive interaction matrix. However, no one single experiment to date is equipped to unambiguously determine this pairing interaction. However, measuring elastic moduli through the superconducting phase transition can reveal essential information about the point group symmetry of the order parameter. Knowing the irreducible representation of the superconducting order parameter can in turn give crucial information about the microscopic pairing mechanism. s-wave superconductors, for example, are usually caused by phonon mediated interactions, whereas p-wave (d-wave) order parameters are often associated with ferromagnetic (antiferromagnetic) interactions [8]. Furthermore, a superconducting order parameter can only break time-reversal symmetry if it transforms as a multidimensional representation of the point group, and in two-dimensional systems, multidimensional representations of the order parameter are required for topological superconductivity [32].

In subsection 2.3.3 we have already discussed the behavior of elastic moduli at second order phase transitions based on how the corresponding strain couples to the order parameter. Thus, measuring all elastic moduli (corresponding to strains transforming as different irreducible representations of the point group) and analyzing their behavior across the critical temperature T_c allows us to learn about the irreducible representation of the order parameter itself. Here, we want to give a physical interpretation on how elastic moduli are affected by superconductivity. In general, it is important to remember that superconducting order parameters break $U(1)$ gauge symmetry, whereas no strain does. Since the free energy is required to be invariant under global gauge transformations, the only coupling terms allowed between strain ϵ_Γ and the superconducting order parameter η are even powers in η. Up to second order in both, the possible coupling terms are $\eta^2\epsilon_\Gamma$ and $\eta^2\epsilon_\Gamma^2$, where Γ labels the irreducible representation of the strain.

First, let us consider one-dimensional superconducting order parameters (i.e. order parameters transforming as one-dimensional irreducible representations of the point group). Since superconducting order parameters are complex valued, a one-dimensional order parameter can be parametrized by two independent real numbers, an amplitude η_0 and a phase ϕ: $\eta = \eta_0 e^{i\phi}$. However, due to $U(1)$ gauge invariance of the free energy, only the amplitude η_0 is physically relevant. Possible terms coupling η_0 and strain are $\eta_0^2\epsilon_\Gamma$ and $\eta_0^2\epsilon_\Gamma^2$. Since η transforms as a one-dimensional representation, $\eta^2 = \eta_0^2$ transforms as the identity representation (e.g. A_g in D_{2h}). Thus, the coupling term quadratic in order parameter and linear in strain is only allowed for compressional strains, where $\Gamma = A_g$, but not for shear strains (which break the symmetry of the lattice). The term quadratic in both order parameter and strain is allowed for all strains, since $\Gamma \otimes \Gamma$ always contains the identity representation.

From a more physically intuitive perspective, note that η_0^2 is proportional to the superfluid density. Since compressional strains change the volume of the Fermi surface, we can expect them to couple linearly to the superfluid density, and linearly modulate the superconducting gap amplitude. Shear strains, on the other hand, change the shape of the Fermi surface, but leave its volume fixed. Therefore, they do not couple to the superfluid density (at least linearly). And since the superfluid density (or equivalently the gap amplitude) is the only free parameter for a one-dimensional superconducting order parameter, shear strains do not modulate the superconducting gap. In summary, only compressional elastic moduli are allowed to jump at a superconducting phase transition with a one-dimensional order parameter, all elastic moduli are allowed to have a kink at T_c (see Figure 2.8).

Two-dimensional superconducting order parameters can be described by two amplitudes and two phases $\boldsymbol{\eta} = \left\{\eta_x e^{i\phi_x}, \eta_y e^{i\phi_y}\right\}$. However, global gauge invariance of the free energy reduces the free parameters to three and only the relative phase $\phi = \phi_y - \phi_x$ between the two components is physically relevant. The order parameter is often parametrized with a total amplitude η_0, a relative amplitude θ, and a relative phase ϕ, such that $\boldsymbol{\eta} = \eta_0 \left\{\cos\theta, e^{i\phi}\sin\theta\right\}$. Similarly to the one-dimensional case, we can form the term $\eta_0^2 \epsilon_{A_g}$ in the free energy, where compressional strains couple linearly to the superfluid density and modulate the superconducting gap amplitude. However, since the order parameter transforms as a two-dimensional irreducible representation, the direct product with itself can also contain irreducible representations other than the identity representation. Thus, coupling terms which couple shear strains linearly to the square of the order parameter are also allowed for certain representations of order parameter and shear strain.

Approaching the same problem from a more physically intuitive picture, the additional degrees of freedom of a two-dimensional superconducting order parameter (i.e. its relative amplitude and phase) make it possible to modulate not only the total amplitude of the gap, but also its shape. Shear strains, changing the shape of the Fermi surface, can therefore directly couple to the shape of the superconducting gap. A famous example is the coupling of a p-wave superconducting order parameter $\boldsymbol{\eta}_p = \left\{\eta_{p_x}, \eta_{p_y}\right\}$ (E_u irreducible representation) to the shear strain $\epsilon_{xy}+\epsilon_{yx}$ (B_{1g} irreducible representation) in a tetragonal crystal (D_{4h}): $(\epsilon_{xy} + \epsilon_{yx}) \left(\eta_{p_x}\eta^*_{p_y} + \eta^*_{p_x}\eta_{p_y}\right) = (\epsilon_{xy} + \epsilon_{yx})\, \eta_0^2 \sin(2\theta)\cos(\phi)$. The particular coupling term is called the *phase mode* of the order parameter, since it couples the relative phase ϕ to strain. This particular coupling term leads to a jump in the shear elastic modulus $c_{B_{1g}} = c_{66}$ at T_c.

Equivalently to the case of a one-dimensional superconducting order parameter, coupling terms quadratic in order parameter and strain are always allowed for all strains. Thus, for a two component order parameter all compressional moduli and certain shear moduli are allowed to show a jump at T_c, all elastic moduli are allowed to have a kink (see Figure 2.8).

The two cases of one- and two-dimensional irreducible representations of the superconducting order parameter are summarized in Figure 2.8, with the examples of an s-wave gap (representing one-dimensional representations) and a $p_x + ip_y$ gap function (representing two-dimensional representations). The shear strain is chosen to be $\epsilon_{xy}+\epsilon_{yx}$. From the figure, we can see that the identifying feature of a two-dimensional superconducting order parameter is a jump in a shear modulus. It is important to note that not all shear moduli will jump at T_c if the order parameter is two-dimensional. Without knowing the exact representation of the superconducting order parameter, we can only make the inverse statement, that *no* shear modulus is allowed to jump for a one-dimensional order

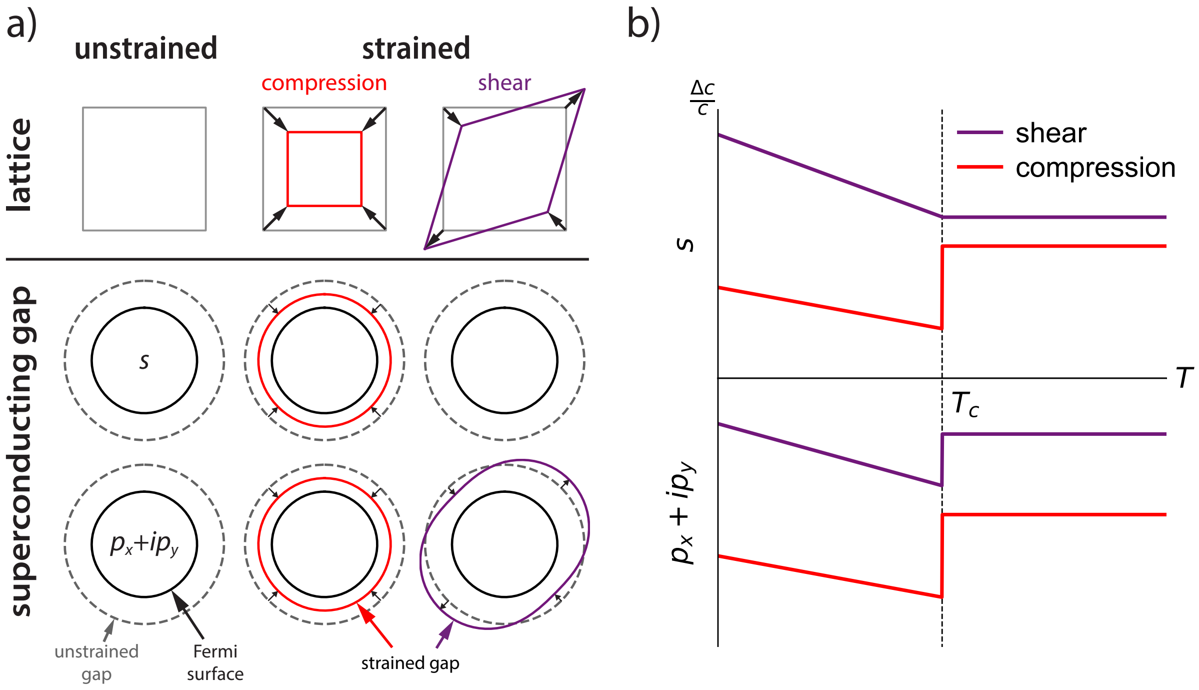

Figure 2.8: **The different effects of strain on one- and two-dimensional superconducting order parameters.** a) shows how the superconducting gaps of an s-wave and $p_x + ip_y$ order parameter are modulated by compression and shear strains. The superconducting gaps (gray dashed lines in the unstrained case and red/purple under compression/shear strains) are plotted on circular Fermi surfaces (black lines). b) shows the resulting behavior of compressional and shear elastic moduli at T_c for the different order parameters. Figure taken from [33].

parameter. In the two-dimensional case, jumps in *certain* shear moduli are allowed, but which ones will depend on the exact combination of irreducible representations of order parameter and strain. Therefore, only from measuring the collective behavior of all elastic moduli through the superconducting transition can we make conclusive statements about the symmetry/dimensionality of the irreducible representation of the supeconducting order parameter.

CHAPTER 3

EXPERIMENTAL TECHNIQUES AND ANALYSIS

In this thesis, we used resonant ultrasound spectroscopy (RUS) and pulse-echo ultrasound to measure the elastic moduli of solids. RUS measures the three-dimensional mechanical resonances of solids. Similar to a one-dimensional string whose resonance frequencies depend on its length, line density, and tension, resonance frequencies of three-dimensional solids depend on their shape, density, and elastic moduli. Measuring a set of resonance frequencies, along with the shape and density of a material, we can extract its elastic moduli.

Pulse-echo ultrasound is a time-of-flight experiment. A sound pulse is sent into the sample, travelling back and forth between the sample boundaries. From the dimensions of the sample and the travel time of the pulse, we can extract the material's sound velocity. In practice, however, we usually measure the relative change in sound velocity (instead of the absolute value) via the phase comparison method. With this method it is not required to know the sample dimensions, and a higher precision can be achieved.

The sound velocities v (as measured from pulse-echo ultrasound) are related to elastic moduli c (as measured from RUS) via the density ρ

$$v = \sqrt{\frac{c}{\rho}}, \tag{3.1}$$

where the measured sound velocity corresponds to different combinations of elastic moduli depending on the propagation and polarization directions of the excited sound pulse [34]. Both techniques have their advantages and disadvantages. Since RUS measures resonance frequencies, we can extract the full elastic tensor from one experiment on one sample. Pulse-echo ultrasound on the other hand typically only measures one elastic modulus per experiment. In order to measure the full elastic tensor, several samples have to be prepared, increasing the chance for systematic errors. However, due to the experimental setup required for RUS (further discussed in section 3.1), it is challenging to perform these measurements in large magnetic fields, especially if the sample is magnetic. Pulse-echo ultrasound, on the other hand, is a very robust technique in magnetic fields, even suited for experiments in pulsed magnets.

Below we give details on the physics behind these techniques, as well as experimental and numerical methods used to analyze the obtained data. Additional details can be found in the previous theses of Sayak Ghosh [24] (RUS) and Patrick Hollister [14] (pulse-echo ultrasound).

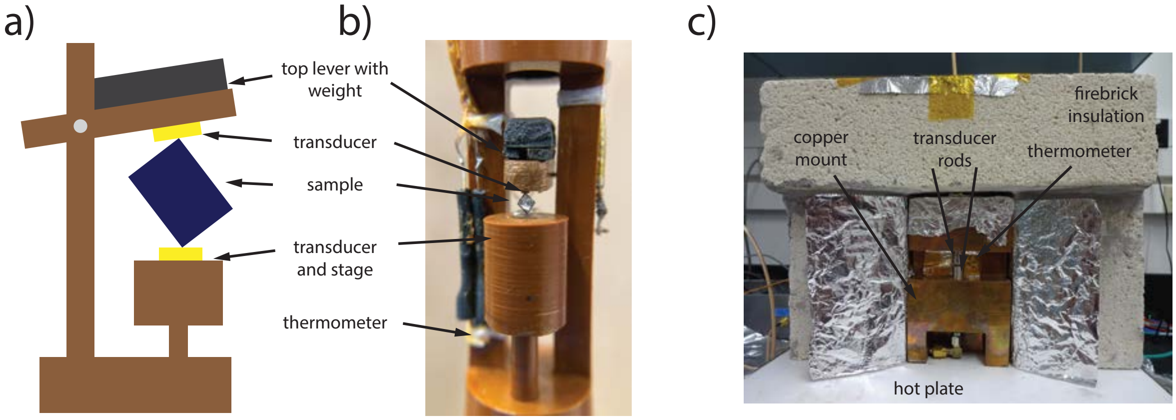

Figure 3.1: **RUS setup.** a) shows a schematic RUS setup. The sample (blue) is placed between two piezoelectric transducers (gold). b) shows a picture of our low temperature RUS setup. The sample is held between two piezoelectric transducers. The bottom transducer (barely visible due to the angle at which the picture is taken) is glued to a fixed stage, the top transducer is attached to a lever, which is additionally weighed down by a tungsten-epoxy mixture. c) is a picture of our high temperature RUS setup. The sample is held between two transducers, which are glued to transducer rods (the sample and transducers are not visible on the scale of the image). Both transducer rods are mounted in a copper mount on a hot plate, insulated with firebrick insulation. The temperature was measured with a platinum thermometer, here glued to the copper mount and protected by aluminum foil.

3.1 Resonant Ultrasound Spectroscopy

3.1.1 RUS Measurement Principle

In RUS, the sample is placed in weak mechanical contact between two piezoelectric transducers (see Figure 3.1). One of these transducers is driven at a certain frequency f, while the strain transmitted through the sample at the same frequency is detected at the opposite transducer. Stepping the drive frequency, we then measure the mechanical vibration spectrum of the sample. Mechanical resonances are harmonic oscillations of the lattice that produce a Lorentzian lineshape (see Figure 3.2).

The sample is usually mounted on its corners between the two transducers (see Figure 3.1 a), such that its vibrational behavior is accurately described by free boundary conditions. Its Lagrangian is then given by [35, 36]

$$\mathcal{L} = \frac{1}{2} \int \left(\sum_i \rho \dot{u}_i^2(\vec{x}) - \sum_{ijkl} c_{ijkl} \frac{\partial u_i(\vec{x})}{\partial x_j} \frac{\partial u_k(\vec{x})}{\partial x_l} \right) dV, \tag{3.2}$$

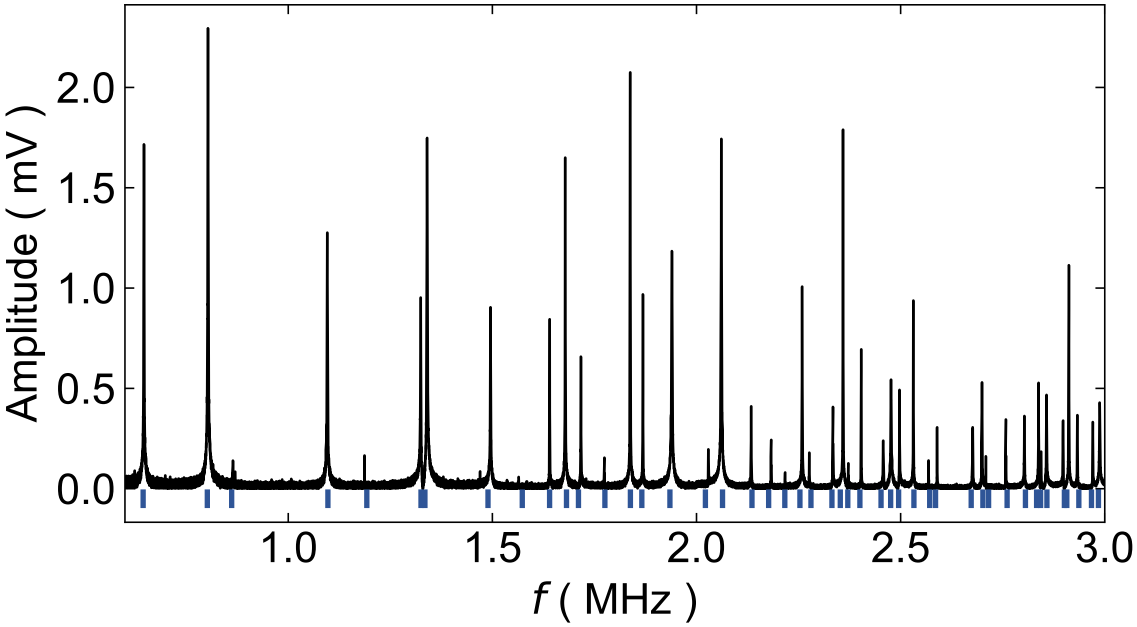

Figure 3.2: **RUS spectrum.** Typical RUS spectrum from about 0.6 to 3 MHz. Resonances given by Lorentzian peaks are specified by blue bars at the bottom of the plot.

where $\vec{u}(\vec{x})$ is the displacement field and $\dot{\vec{u}}$ its time derivative, ρ is the density, c_{ijkl} are the elastic moduli, and the integral is over the entire volume of the sample. Assuming a periodic time dependence of the displacement with frequency ω, i.e. $\vec{u}(\vec{x}, t) = e^{i\omega t}\vec{u}(\vec{x})$, the above Lagrangian leads to the elastic wave equation

$$\rho\omega^2 u_i + c_{ijkl}\frac{\partial^2 u_l}{\partial x_j \partial x_k} = 0. \tag{3.3}$$

Knowing the density, elastic moduli, and shape of a solid, solutions to this wave equation describe its mechanical resonance modes and resonance frequencies. This forward calculation is usually done by expanding the displacement vector in Cartesian polynomials [35, 36], which converts Equation 3.3 into a general eigenvalue problem. Solving the resulting eigenvalue problem commonly required the samples to have regular, i.e. cubic, spherical, ... shapes. However, as part of this thesis, we developed a new algorithm which enables the calculation of resonance spectra for irregularly shaped samples. We expand on the forward calculation for regularly and irregularly shaped samples in chapter 4. However, regardless of the method used for the forward calculation, the *backward* fitting process of elastic moduli to a measured resonance spectrum is done with a genetic algorithm global minimizer [37–39] (see subsection 3.1.3).

3.1.2 RUS Experimental Setup and Electronics

Two different RUS probes are used for measurements at low (see chapter 5) and high (see chapter 6) temperatures, respectively. Both setups, however, utilize the same room temperature electronics.

Low Temperature Setup An image of the low temperature RUS probe is shown in Figure 3.1 b. The apparatus is made out of PLAVIS Polyimide, a polymer know for its relatively small thermal expansion which reduces the possibility of the sample moving in the setup which would cause noise and discontinuities in the temperature dependence of the measured resonances. Additionally, PLAVIS attenuates sound very well, reducing the crosstalk between the transducers through the apparatus (instead of through the sample as desired), thus reducing a contribution to the background of the detected signal that has a lot of structure. The transducers are glued into the apparatus with a mixture of Loctite Stycast 2850FT epoxy and tungsten powder. The tungsten powder is added to increase the acoustic damping effect of the epoxy. Additionally, small alumina wear plates are glued to the face of the transducer which is in contact with the sample. They are added to decrease wear of the transducers, but we have also scratched small indents into the wear plates which add to secure the position of the sample. The sample is held in place by a post adjustable in the z direction at the bottom, and a freely movable lever at the top. A block of the stycast/tungsten mixture is added to the top of the lever to increase its weight and therefore the mechanical coupling between transducer and sample, leading to a higher signal-to-noise ratio. The transducers we used are 36° Y-cut lithium niobate crystals from Boston Piezo-Optics. They are 1.5 mm in diameter, with a fundamental frequency of 25 MHz ($\approx$ 0.1 mm thick), and gold electrodes on both sides with a fine lapped finish.

Low temperatures are achieved by dipping the RUS probe into a liquid helium bath. Pumping on the helium bath we achieve temperatures as low as 1.2 K. Since the sample is only in weak mechanical contact with the probe, thermal stability of the sample is a point of concern. To ensure good temperature control, the probe is built with two vacuum cans [23]. The inner can is filled with about 1 mbar of helium gas to ensure homogeneous thermalization. The outer can is filled with about 10^{-2} mbar to ensure good enough coupling to the liquid helium bath but still allow for temperature control by a heater (i.e. a coil of Alloy 294 (Advance) wire of about 100 Ω) on the RUS apparatus. Slow and controlled temperature sweeps are achieved by continuously pumping on the helium bath, such that we reach base temperature, and then slowly heating the sample with the heater on the RUS apparatus. The temperature is controlled with a Cryo-con Model 22C temperature controller.

High Temperature Setup An image of the high temperature RUS setup is shown in Figure 3.1 c. Its main components are a copper block (which holds the transducer

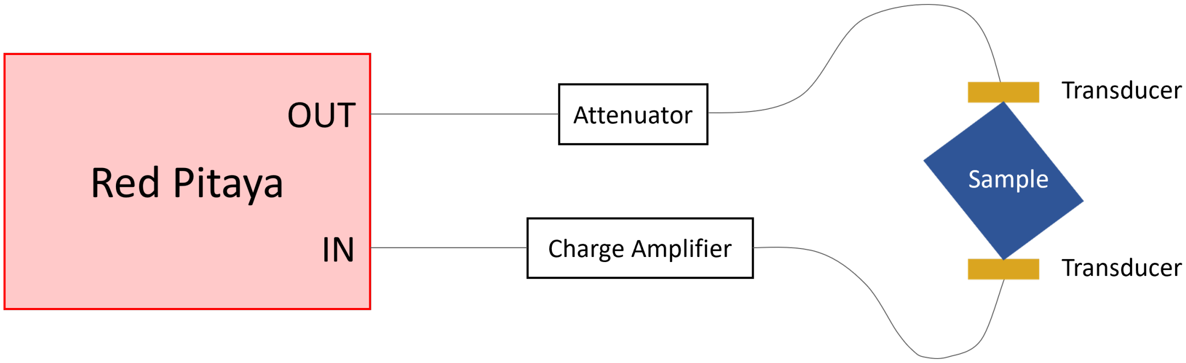

Figure 3.3: **RUS measurement circuit.** Sketch of the measurement electronics for a typical RUS experiment. A continuous AC drive signal with amplitude of about 1 V is generated by the RedPitaya and then attenuated before exciting the transducer. Sound transmitted through the sample is detected by a second transducer. The signal generated this way is amplified with a charge amplifier and recorded at the RedPitaya.

rods) encapsulated with firebrick insulation. This setup is then placed on a hot-plate for temperature control. Vertical holes are cut into the copper fixture to hold transducer rods (silver cylinders in Figure 3.1 c), while allowing for free motion of the top transducer rod along the z axis. The sample is held in place between the two transducers by the weight of the top transducer rod.

The transducer rods each consist of a stainless steel tube with an outer diameter of about 8 mm and a wall thickness of 0.8 mm. The transducers are glued into the tubes with ceramic epoxy (Cotronics Resbond 940 Fast Setting Adhesive). The transducers we used are 36° Y-cut lithium niobate transducers from Boston Piezo-Optics. They are 5 mm in diameter and 0.5 mm thick, with gold tab coax electrodes with a fine lapped finish.

Measurement Electronics The main control logic of our RUS experiment is a Red Pitaya StemLab 125 field programmable gate array (FPGA). It outputs a continuous sine wave at frequency f with an amplitude of 1 V. This signal is sent through a Mini-Circuit K1-VAT+ fixed attenuator (the chosen attenuation ranges from 0 dB to 30 dB) and to one of the transducers touching the sample. The strain wave excited at this transducer is then transmitted through the sample and reaches the opposite transducer where it induces an AC voltage at the drive frequency f. This signal is amplified through a charge amplifier (designed by Alamo Creek Engineering [36]) and recorded by the Red Pitaya (see Figure 3.3 for a sketch of the described circuit). The recorded data is then processed with a digital lock-in such that we obtain both the amplitude and phase of the signal. Importantly, this is an FPGA based program, implemented directly on the Red Pitaya [36, 40] such that we can utilize the full 125 MSPS sampling rate of the Red Pitaya. The data at each frequency is averaged for 1 ms. The RedPitaya in combination with our RUS apparatus and transducers results in an accessible frequency range from about 0.5 to 6 MHz.

For measurements on the high temperature setup, no attenuation of the 1 V output signal of the RedPitaya is used. Assuming a piezoelectric constant for $LiNbO_3$ of roughly $2 \times 10^{-11}\ \frac{\mathrm{C}}{\mathrm{N}}$ [41, 42], and the transducer thickness of 0.5 mm, we can estimate that the excited transducer produces strain of about 4×10^{-8}. For low temperature measurements, however, a non-zero attenuation is necessary. Otherwise, too much power is sent to the transducer heating the sample. The attenuation we used for many of the experiments on UTe_2 was 30 dB. This reduces the amplitude of the output signal from 1 V to 0.03 V. We also use thinner transducers in our low-temperature setup, with a thickness of 0.1 mm. Using the same piezoelectric constant as above, we then estimate the strain at the driving transducer to be about 6×10^{-9}.

3.1.3 Fitting Elastic Moduli

Fitting elastic moduli to a set of measured resonance frequencies is done by minimizing the root mean square (RMS) of the difference between experimentally measured resonance frequencies f_i^{exp} and calculated resonance frequencies f_i^{calc}

$$\mathrm{RMS} = \frac{1}{\sqrt{N}} \sqrt{\sum_{i=1}^{N} \left(\frac{f_i^{\mathrm{calc}} - f_i^{\mathrm{exp}}}{f_i^{\mathrm{calc}}} \right)^2}, \tag{3.4}$$

where N is the number of measured resonances. Defining this target function, and therefore also the entire fitting procedure, is independent of the forward solver chosen to calculate resonance frequencies from a given set of elastic moduli (see chapter 4). This RMS is in general a complicated function of elastic moduli with several local minima (see Figure 3.4). The existence of more than one local minimum in the RMS landscape prevents us from using local fitting methods like least squares or other gradient based algorithms. Rather, we need to employ a global minimizer. Several global minimization algorithms exist. For our purpose of fitting RUS spectra, a genetic algorithm global minimzer has proven to be a successful approach [39]. While it is not as fast or efficient as other methods, it is one of the most flexible and robust algorithms. We implement a genetic algorithm via *scipy.optimize.differential_evolution* in Python. Its working principle is as follows [37, 38, 43]:

1. **Generation of *parent sets*:** Generate M random parent sets of elastic moduli x_i^{parent}, $i \in [1, 2, ..., M]$. Every x_i is a vector where its elements are the independent elastic moduli of the material to be fitted. All elastic moduli are initialized within bounds specified at the beginning of the fit. We then calculate the resonance spectra and resulting RMS for each parent set, M in total. We call the set of elastic moduli with the smallest RMS x^{best}.
2. **Generation of *mutated sets*:** Create a mutated set of elastic moduli x_i^{mut} for each parent set x_i^{parent} according to

$$x_i^{\mathrm{mut}} = x^{\mathrm{best}} + \epsilon \left(x_j^{\mathrm{parent}} + x_k^{\mathrm{parent}} \right), \tag{3.5}$$

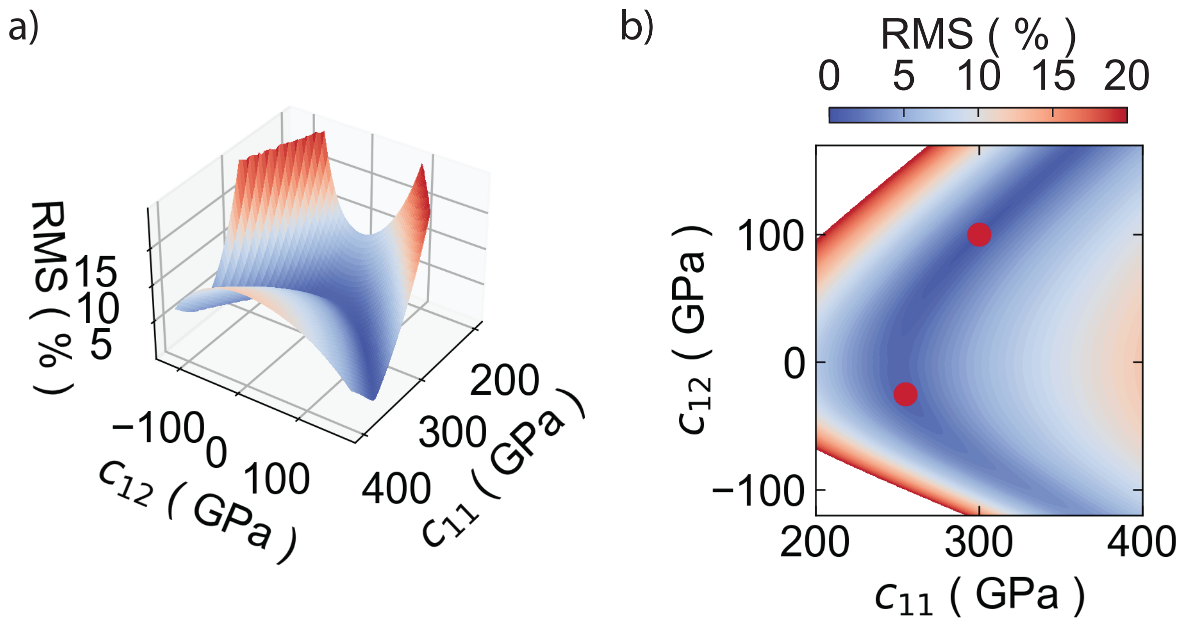

Figure 3.4: **RMS landscape.** Shown is the RMS of a simulated cubic crystal as a function of c_{11} and c_{22}. a) is a 3D surface plot, b) is a 2D color plot. Both panels use the same color map indicating the value of the RMS in %. The *measured* resonance frequencies are simulated for a cubic system with $c_{11} = 300$ GPa, $c_{12} = 100$ GPa, and $c_{44} = 120$ GPa in the shape of a rectangular parallelepiped with dimensions $(1.5 \times 2 \times 3)$ mm^3. We can see that the RMS is highly non-trivial as a function of c_{11} and c_{12}. Multiple local minima are marked with red circles in panel b).

where $j, k \in [1, M]$ are random indices. $\epsilon \in [0, 2]$ is the mutation parameter ensuring a controlled perturbation of x^{best}.

3. **Generation of *trial sets*:** Trial sets x_i^{trial} are then generated from both parent and mutated sets. Here, each component j of a given trial set x_i^{trial} is constructed as

$$x_{i,j}^{trial} = \begin{cases} x_{i,j}^{mut} & \text{if } rand(j) \leq p \text{ or } j = d \\ x_{i,j}^{parent} & \text{if } rand(j) > p \end{cases}, \tag{3.6}$$

where d is the number of independent elastic moduli, and $rand(j)$ is a random number between 0 and 1, different for each component $j = 1, \ldots, d$. $p \in [0, 1]$ is the crossover probability. p can be changed to optimize the fit performance and is not set by any physical parameter.

4. **Generation of new parent sets:** Lastly, we compare the original parent sets to their corresponding trial sets. For each $i = 1, \ldots, M$ we chose either x_i^{parent} or x_i^{trial} based on which has the smaller RMS as the new parent set for the next generation of the genetic algorithm. Therefore, we end up with another collection of M new parent sets of elastic moduli.

5. **Convergence:** Steps 2, 3, and 4 are then repeated until the standard deviation of all RMS values of a given generation falls below a tolerance defined as: tol·mean(RMS), where tol is a predetermined value and mean(RMS) is the average RMS value for the generation. Once this convergence criterium is reached, the fit is considered to have converged and the fit result is the set of elastic moduli of the last generation with the lowest RMS.
6. **Polishing:** The fit result obtained with the above genetic algorithm is then used as a starting point for a gradient descent fit, which further improves the quality of our fits.

Some of the default parameters we use for our genetic algorithm fits are a population size of $M = 15 \cdot n$, where n is the number of elastic moduli, a mutation parameter $\epsilon = 0.7$, a crossover probability $p = 0.9$, and a convergence tolerance $\text{tol} = 10^{-3}$.

A detail we need to consider for the fitting process is the concept of missing resonances. The idea is that when measuring an RUS spectrum, different resonances appear with different amplitudes. If the amplitude of a resonance f_j^{exp} drops below the noise of our setup, the compiled list of experimental resonance frequencies f_i^{exp} will be missing said resonance f_j^{exp}. In that case, every term in the RMS in Equation 3.4 for $i \geq j$ will be affected, and the final RMS will be artificially high. To avoid this scenario, our fitting code contains an additional parameter *maximum number of missing resonances* m_{max}. For every set of elastic moduli x_i we then calculate $N + m_{max}$ resonances, where N is again the number of measured resonances. Next we assign each of the N experimental resonances f_i^{exp} to one calculated resonance f_k^{calc}, ignoring the remaining m_{max} unpaired frequencies in f_i^{calc}. The pairing with the lowest RMS is considered to be the correct one. This assignment of experimental to calculated resonance frequencies is done in Python with *scipy.optimize.linear_sum_assignment*.

Good fit results empirically have an RMS between 0.1 and 0.5 %. However, within this range, the robustness of the resulting elastic moduli with the number of experimental resonances included in the fit is a better indicator of fit quality than the actual RMS. Due to the complicated RMS landscape, it is recommended to have many more resonances than independent elastic moduli. In this thesis, we have used 70 resonances for a cubic system (3 elastic moduli), over 80 for a hexagonal system (6 elastic moduli), and over 100 resonances for an orthorhombic system (9 elastic moduli).

Lastly, we discuss uncertainties from our RUS fits. A statistical uncertainty is determined by individually varying each elastic modulus from the best fit and finding the value at which the RMS has increased by 2 % [36, 44]. These uncertainties are generally on the order of 0.1 to 1 GPa. We have additionally identified three sources of systematic uncertainties which are of similar magnitude [43]: the first source is identified as small deviations of our RUS setup from the model of a nearly-free oscillator. A small shift in resonance frequencies is observable depending on how the sample is mounted in the apparatus, mainly caused by the weight of the setup on the sample. The resulting uncertainty in elastic moduli therefore heavily depends on the used setup. For the high temperature setup, the top transducer rod keeping the sample in place weighs about 5 g and uncertainties are about 2 GPa. For the low temperature setup, the top lever pushing on the sample weighs about 0.5 g and the resulting uncertainties are on the order of 0.5 GPa. A second source of systematic uncertainties are uncertainties in the alignment of the crystal axes to the macroscopic sample shape. A misalignment of 1 degree leads to an uncertainty of roughly 0.1 to 1 GPa. A third source of systematic uncertainty is given by an uncertainty in the sample densities. An uncertainty of 1 % in the sample density leads to an uncertainty of 1 % in all elastic moduli.

3.1.4 Temperature Dependence

In the section above, we have discussed how we fit elastic moduli to a set of measured resonance frequencies. All sources of uncertainty to this fit contribute about 1 GPa, which is a relative error of about 1 % (most elastic moduli are between 50 and 100 GPa). Features in the relative change of elastic moduli with temperature at second order phase transitions, however, can be as small as 10^{-5}. In order to obtain a temperature dependence of the elastic moduli, it is therefore not viable to run the above fit procedure at several temperature steps.

However, the required resolution can be achieved with the following procedure [23, 39]: Besides the absolute elastic moduli, we can also obtain the derivatives of each resonance frequency with respect to each elastic modulim from an RUS fit. In particular, from the elastic wave equation in Equation 3.3 we know that the resonances ω_i^2 are linear in the elastic moduli, such that

$$\alpha_{i\mu} \equiv \frac{\partial \ln \omega_i^2}{\partial \ln c_\mu} = 2\frac{\partial \omega_i}{\partial c_\mu}\frac{c_\mu}{\omega_i}, \tag{3.7}$$

is constant as a function of elastic moduli. From this definition follows that

$$\mathrm{d}\ln \omega_i^2 = \sum_\mu \alpha_{i\mu}\mathrm{d}\ln c_\mu, \tag{3.8}$$

$$\Leftrightarrow \quad 2\frac{\mathrm{d}\omega_i}{\omega_i} = \sum_\mu \alpha_{i\mu}\frac{\mathrm{d}c_\mu}{c_\mu}. \tag{3.9}$$

Discretizing this relation and replacing $f = \omega/2\pi$, we find

$$2\frac{\Delta f_i}{f_i} = \sum_\mu \alpha_{i\mu}\frac{\Delta c_\mu}{c_\mu}, \tag{3.10}$$

where $\frac{\Delta f_i}{f_i} = \frac{f_i(T)-f_i(T_0)}{f_i(T_0)}$, $\frac{\Delta c_\mu}{c_\mu} = \frac{c_\mu(T)-c_\mu(T_0)}{c_\mu(T_0)}$, and T_0 is the reference temperature at which the measurement started. Thus, by performing one fit and measuring the relative change in resonance frequencies as a function of temperature, we obtain the relative change in elastic moduli by solving the set of linear equations in Equation 3.10. For the $\alpha_{i\mu}$

coefficients we have the sum rule $\sum_\mu \alpha_{i\mu} = 1$, when summing over all elastic moduli (see Appendix C).

In the above analysis, we assume the coefficients $\alpha_{i\mu}$ to be temperature independent. They represent the amount of how much of the elastic modulus c_μ is contained in the resonance f_i and are mostly determined by the macroscopic shape of the sample. If the temperature range of interest is not too large and the fit is performed at a temperature close to it, changes in sample shape are insignificant and the assumption of temperature independent $\alpha_{i\mu}$ is appropriate.

While we recommend about 80 to 100 resonance frequencies for a reliable RUS fit, the temperature dependencies of only roughly 20 resonances (for a hexagonal system with five independent elastic moduli) are required for the decomposition into elastic moduli.

3.1.5 Sample Preparation and Requirements

Our RUS setups have a frequency range from about 0.5 to 6 MHz and for a good fit we need to measure about 50 to 100 resonances. For a sample with elastic moduli on the order of 100 GPa to have this many resonance frequencies in the accessible frequency range, it needs to be about $(1 \times 1 \times 1)$ mm^3 large. Depending on the exact elastic moduli, however, sizes between 0.5 mm and 3 mm are possible.

Samples within this size range are commonly prepared by polishing (using Thor Labs diamond lapping films with grid size of roughly 1 μm) them into rectangular parallelepipeds with appropriate side lengths. While not generally required, it is easiest if the crystallographic axes are aligned with the sides of the parallelepiped. As we will discuss in chapter 4, we have developed an algorithm to fit elastic moduli to irregularly shaped samples. However, for these samples, similar shape requirements apply. The closer the shape of an irregularly shaped sample is to a rectangular parallelepiped, the higher chances of a successful fit become. In particular, samples with large aspect ratios should be avoided.

3.2 Pulse-Echo Ultrasound

3.2.1 Pulse-Echo Measurement Principle

In pulse-echo ultrasound, a piezoelectric transducer is directly attached to the face of the sample. This transducer is used to send a sound wave at frequency f into the sample, as well as to detect the sound wave again every time it travels back to the transducer. These successive measurements result in an *echo pattern* similar to the one sketched in Figure 3.5. While the sound wave is travelling through the sample, it will continuously

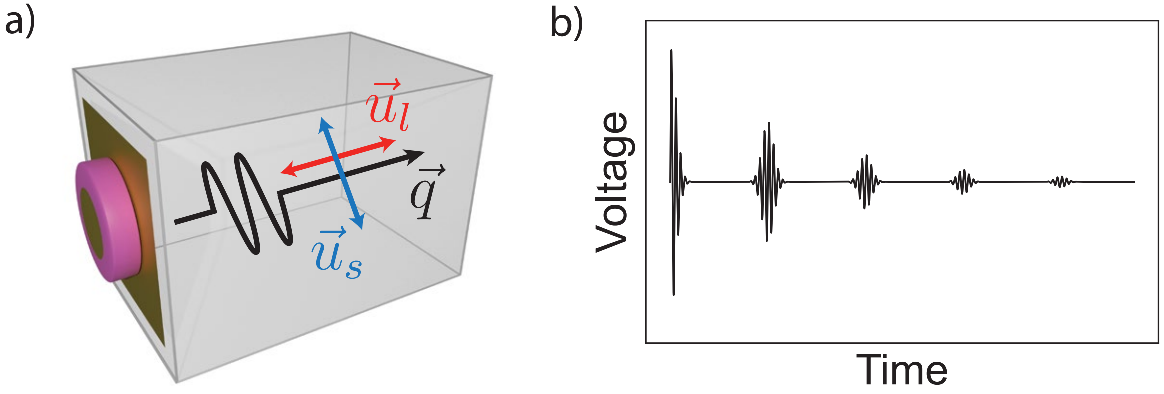

Figure 3.5: **Pulse-echo sketch.** a) shows the sketch of a sample with a transducer consisting of two gold electrodes and a piezoelectric (purple). The excited sound wave propagates perpendicular to the face to which the transducer is attached. Longitudinal (shear) transducers create sound waves with polarization vectors parallel (perpendicular) to the propagation vector, i.e. they produce longitudinal $\vec{u}_l$ (shear $\vec{u}_s$) sound modes. b) shows a simulated pulse echo signal. Voltage echoes are measured across the transducer every time the sound waves comes back to it, creating an echo pattern. Dissipation of the sound wave inside the sample leads to an exponential envelope of measured the echo pattern.

dissipate energy due to phonon-phonon, phonon-electron, and phonon-impurity scattering [45, 46], resulting in an exponential envelope of the measured echoes (see Figure 3.5).

Knowing the time between two echoes and the thickness of the sample we can determine the sound velocity. However, since measurements of the positions of the individual echoes are usually limited to a resolution of about 1 %, this method is not precise enough to measure discontinuities at phase transitions on the order of 10^{-5} in the relative change of the speed of sound. To get around this limitation, the *phase comparison* method is used to directly measure $\Delta v/v$. Here, we consider the phase difference ϕ between two echoes, which is given by

$$\phi = 2\pi \frac{t}{T}, \tag{3.11}$$

where t is the time between echoes and $T = 1/f$ is the period of the sound wave. t is given by $n2d/v$, where d is the thickness of the sample and n is an integer (the factor of 2 comes from the fact that the sound wave has to travel the width sample twice to come back to the transducer). Equation 3.11 then becomes

$$\phi = \frac{4\pi n d f}{v}, \tag{3.12}$$

such that we have for the relative phase change

$$\frac{\Delta\phi}{\phi} = -\frac{\Delta v}{v} + \frac{\Delta d}{d} + \frac{\Delta f}{f}. \tag{3.13}$$

For most of our measurements, the change in sample thickness can be neglected, and our measurements are performed at constant frequency such that we have for the relative change in sound velocity

$$\frac{\Delta v}{v} = -\frac{\Delta \phi}{\phi} \tag{3.14}$$

$$\Leftrightarrow \frac{\Delta c}{c} = -2\frac{\Delta \phi}{\phi}, \tag{3.15}$$

where in the second line, we have used Equation 3.1 to convert the relative change in sound velocity to a relative change in elastic modulus. Using this phase comparison method, we are able to obtain a precision of better than 10^{-6} in $\Delta c/c$.

Which elastic modulus is measured depends on the propagation and polarization direction of the sound wave. For a deeper anlysis, we start again from the elastic wave equation in Equation 3.3. However, this time we are assuming a plane wave form of the sound wave [15, Chapter 22] (instead of only assuming a periodic time dependence of the deformation like we did for the RUS case)

$$\vec{u}(t, \vec{r}) = u\hat{\varepsilon}e^{i(\omega t - \vec{q}\cdot\vec{r})}, \tag{3.16}$$

where $\omega = 2\pi f$, $\hat{\varepsilon}$ is the unit polarization vector, and $\vec{q}$ is the propagation vector of the sound wave. Plugging this solution to the deformation into the elastic wave equation, we get

$$\rho\omega^2\hat{\varepsilon}_i - c_{ijkl}q_j q_k \hat{\varepsilon}_l = 0. \tag{3.17}$$

Rewriting the propagation vector as its magnitude q and direction $\hat{q}$, $\vec{q} = q\hat{q}$, Equation 3.17 can be rewritten as [34]

$$\omega^2/q^2\hat{\varepsilon}_i = \left(c_{ijkl}\hat{q}_j\hat{q}_k/\rho\right)\hat{\varepsilon}_l, \tag{3.18}$$

which is an eigenvalue equation for the matrix $c_{ijkl}\hat{q}_j\hat{q}_k/\rho$. The three eigenvectors are the orthogonal polarization vectors, with eigenvalues $v^2 \equiv \omega^2/q^2$. Therefore, for any given sound propagation direction, three different sound velocities (or equivalently elastic moduli) can be measured: one is a longitudinal sound mode with the polarization parallel to the propagation, and two are transverse or shear sound modes with the polarization perpendicular to the propagation direction.

In practice, the propagation direction is perpendicular to the face to which the transducer is attached. The polarization is then determined by the type of transducer that is used: longitudinal transducers for longitudinal sound waves or shear transducers for transverse sound waves (see Figure 3.5). Table 3.1 shows a few combinations of propagation $\hat{q}$ and polarization $\hat{\varepsilon}$ vectors and the measured elastic moduli for point groups D_{2h} and D_{4h}.

While the sound wave travels through the sample it dissipates energy due to several phonon scattering processes. This leads to an exponential envelope of the echo pattern $Ae^{-t\tau}$ (see Figure 3.5 b). The attenuation coefficient τ is commonly converted to an attenuation as a function of distance, rather than time, through the sound velocity $\alpha =$

$\hat{q}$	$\hat{\varepsilon}$	$c^{D_{2h}}$	$c^{D_{6h}}$
[100]	[100]	c_{11}	c_{11}
	[010]	c_{66}	$\frac{c_{11}-c_{12}}{2}$
	[001]	c_{55}	c_{44}
[010]	[100]	c_{66}	$\frac{c_{11}-c_{12}}{2}$
	[010]	c_{22}	c_{11}
	[001]	c_{44}	c_{44}
[001]	[100]	c_{55}	c_{44}
	[010]	c_{44}	c_{44}
	[001]	c_{33}	c_{33}

Table 3.1: **Pulse echo sound velocity.** The measured elastic moduli for the D_{2h} and D_{6h} point groups are shown for sound waves with propagation direction $\hat{q}$ and polarization vector $\hat{\varepsilon}$.

τ/v. In SI units, where t is given in seconds and v in $\frac{\text{m}}{\text{s}}$, the unit of the sound attenuation is usually given in *Neper per meter* Np/m. The Neper is a logarithmic unit, similar to a decibel, with the difference that Nepers use the natural logarithm, whereas decibels use base-10 logarithms. The measured sound attenuation is affected by various scattering mechanisms, such as phonon-electron, phonon-phonon, or phonon-impurity scattering. It is very well suited to investigate dynamical effects in metals [47–49], superconductors [50–52], at second order phase transitions in general [22, 53], and many more. However, we do not discuss sound attenuation in detail here. The interested reader is referred to the references mentioned above as well as [46].

3.2.2 Piezoelectric Transducers

Piezoelectric transducers are the main component of a pulse-echo ultrasound setup. They consist of a piezoelectric sandwiched by a bottom and top electrode. For our measurements on Mn_3X (see chapter 6), we used Z-cut (41° X-cut) lithium niobate crystals with gold electrodes from Boston Piezo-Optics for longitudinal (shear) transducers. Their thickness amounts to a natural frequency of roughly 30 MHz. These transducers can then be operated at odd harmonics of their fundamental frequencies, and typical pulse-echo frequencies are on the order of 100 MHz (corresponding to a wavelength of 50 μm, assuming a sound velocity of 5000 m/s). These transducers are attached to the sample with AngströmBond AB 9110 LV room temperature cure epoxy. In order to access the bottom electrode of the transducer once it is glued to the sample, we sputter a thin ($\approx$ 100 nm) film of platinum on the sample before attaching the transducer (see Figure 3.6 a). The deposition of this platinum film is only necessary for insulating samples, however. For metallic samples, electrical access to the bottom electrode can be achieved through the sample. Notably, in both cases, a thin layer of AngströmBond between the sample and

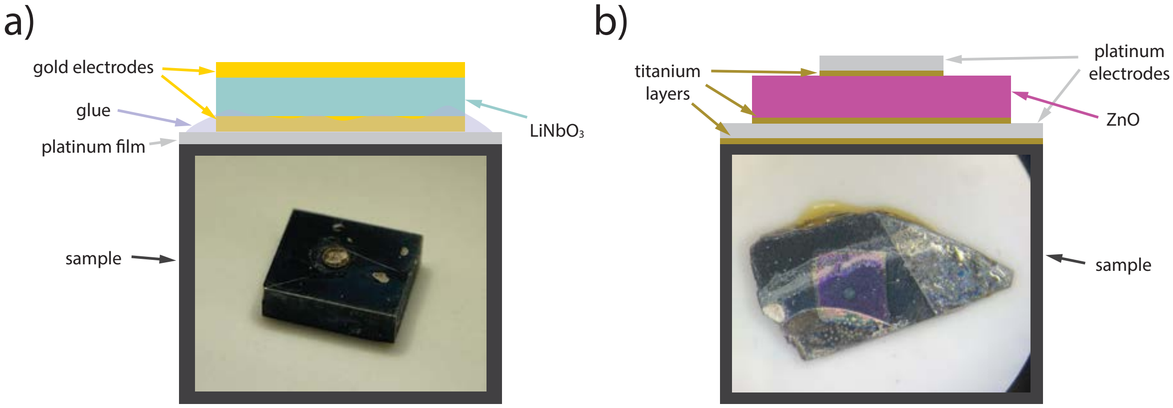

Figure 3.6: **Pulse-echo transducers.** a) image of a $LiNbO_3$ transducer on a Mn_3Ge sample and schematic of the transducer setup. The transducer ($LiNbO_3$ in light green surrounded by gold electrodes) is glued to the sample (dark gray) which is coated with a thin platinum layer (silver). b) image of a thin-film ZnO transducer on a UTe_2 sample and schematic of the transducer setup. The transducer consists of ZnO (purple) as the dielectric and platinum (silver) electrodes. Thin titanium films (bronze) are deposited between each transducer layer.

the transducer prevents direct electrical contact. However, at the RF frequencies used for pulse-echo ultrasound, capacitive coupling between the metallic sample surface (or the platinum film) and the bottom electrode is sufficient.

For measurements on UTe_2, we sputtered thin-film piezoelectric transducers directly on the sample. Here, bottom and top electrodes are platinum (100 nm), the piezoelectric is zinc oxide (ZnO) (1.5 μm), and a thin layer of titanium (8 nm) is deposited between each transducer layer to increase adhesion (see Figure 3.6). Sputtering of ZnO is achieved by RF sputtering with a ZnO target. The exact details of the sputtering recipes were developed by Patrick Hollister and Avi Shragai in the Ramshaw lab and a comprehensive discussion can be found in Patrick's PhD thesis [14]. Longitudinal transducers are produced by mounting the sample roughly in the center of the sample stage in the sputtering chamber and enabling the rotation of the sample stage during the sputtering process. Shear transducers, on the other hand, can be generated by mounting the sample on the edge of the sample stage, as far away from the ZnO target as possible. Rotation of the sample stage is then disabled during the sputtering process and the resulting polarization of the shear transducer is along the shortest line drawn between the target and the sample. Notably, shear transducers created this way exhibit both a shear *and* a longitudinal response (see Figure 3.7). These transducers have a bandwidth from about 500 Mhz to a few GHz (1 GHz corresponds to a wavelength of 5 μm, assuming a sound velocity of 5000 $\frac{\mathrm{m}}{\mathrm{s}}$).

The development of thin-film ZnO transducers has increased the accessible frequency range by almost a factor of 10. The higher frequency allows us to send shorter sound waves into the sample, decreasing interference effects from overlapping echoes and enabling

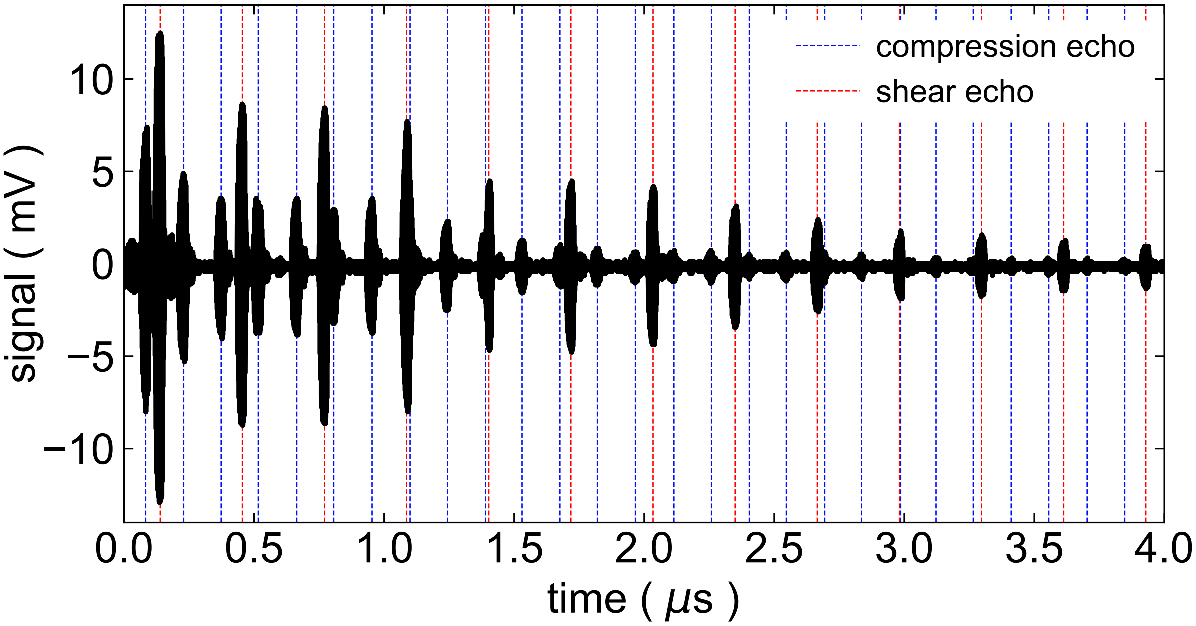

Figure 3.7: **ZnO transducer mixed longitudinal/shear response.** Shown is a raw pulse-echo signal from a ZnO shear transducer on UTe_2 (with a crystal structure belonging to the D_{2h} point group). The transducer is attached to the sample such that the propagation direction of the generated sound wave is along [010] and the polarization of its shear component is along [100]. The pulse train exhibits two distinct echo patterns: a fast echo pattern marked by blue vertical lines which corresponds to longitudinal sound with elastic modulus c_{22} (excited by the longitudinal response of the transducer), and a slow echo pattern marked by red vertical lines which corresponds to shear sound with elastic modulus c_{66} (excited by the shear response of the transducer). Figure adapted from [33].

the measurements of thinner samples. Furthermore, whereas $LiNbO_3$ transducers were only functional at discrete frequency values (i.e. odd harmonics of their fundamental frequency), ZnO transducers can be operated almost continuously withing the accessible bandwidth. The direct deposition of the ZnO transducers on the sample, rather than the use of glue as for $LiNbO_3$ transducers, has additionally significantly increased the signal-to-noise ratio of our pulse-echo signal (see Figure 3.8).

3.2.3 Pulse-Echo Experimental Setup and Electronics

Experimental Setup Samples with transducers are mounted at the end of different probes for pulse-echo measurements at high temperatures for Mn_3X (chapter 6) and low temperatures for UTe_2 (chapter 5).

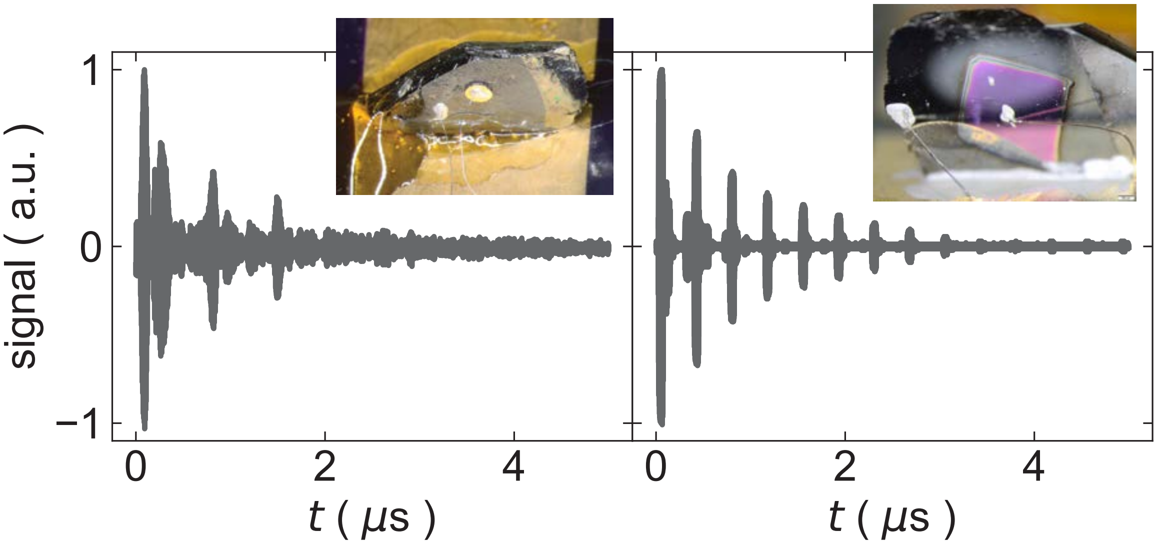

Figure 3.8: **$LiNbO_3$ vs ZnO transducer comparison.** Raw pulse-echo signals of c_{44} on a piece of UTe_2 measured with a $LiNbO_3$ (left panel) and ZnO (right panel) transducer. A significant increase of signal to noise can be observed from $LiNbO_3$ to ZnO. Both measurements were performed on the same sample. However, the sample has been further polished and thinned down after measurements with the $LiNbO_3$ transducer and before measurements with the ZnO transducer.

For measurements at high temperatures (see Figure 3.9 a), the sample and a platinum thermometer are glued to the face of a copper disk. The temperature is controlled with a heater wire wrapped around the side of the disk. A coaxial cable and wires for the thermometer are fed through the disk and heat sunk to a copper post. Short wires are glued on the sample with silver paint and soldered to the end of the coaxial cable. The entire mount is the successively encapsulated by a copper heat shield and a brass can. The probe was inserted into an Oxford Instruments variable temperature insert (VTI) in an Oxford Instruments 20 Tesla superconducting magnet system. During the measurement, we continuously pumped on the sample space to ensure high vacuum. For this purpose, both the heat shield and brass can were designed with openings to enable low pressures through the VTI sample space.

For measurements at low temperatures, the sample and a Cernox thermometer are glued to a PCB (see Figure 3.9). Thin (25 μm) silver wire is used to make contact to ground and voltage pads on the PCB, which are connected to a MMCX coaxial connector. The PCB is then glued to a copper mounting bracket which can be screwed to the end of a standard probe for a Oxford Instruments Heliox ^{3}He refrigerator.

Measurement Electronics A schematic of our pulse-echo ultrasound measurement electronics cuircut is shown in Figure 3.10. Short ($\approx 20-80$ ns) radiofrequency bursts with carrier frequencies between 100 MHz and 2.5 GHz are generated with a Tektronix TSG

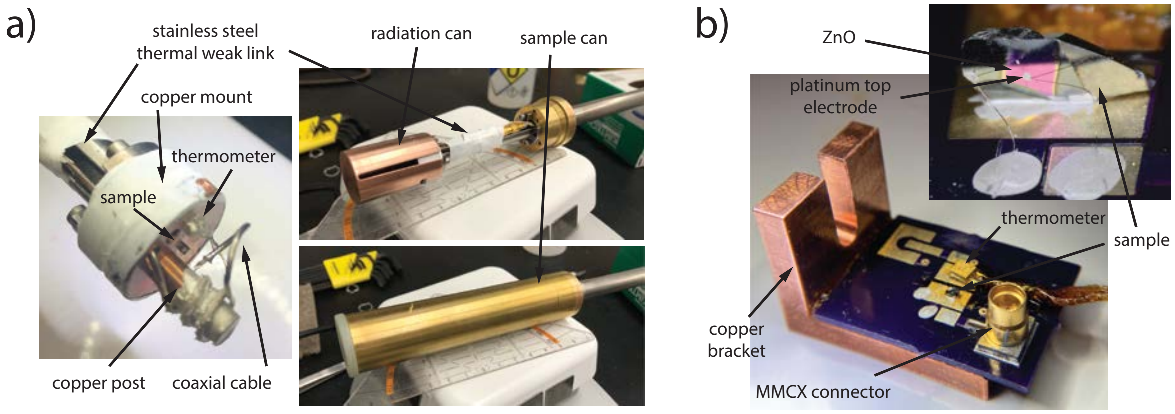

Figure 3.9: **Pulse-echo ultrasound setup.** Images of the pulse-echo ultrasound probes for high-temperature (a) and low-temperature (b) measurements.

4106A RF generator, modulated by a Tektronix AFG 31052 arbitrary function generator. The generated signal is then amplified by a Mini-Circuits ZHL-42W+ power amplifier (on average about +35 dB gain; powered by a Bel Fuse HC15-3-AG AC DC converter), sent through a series of Mini-Circuits ZFSWA2-63DR+ switches controlled by the same Tektronix AFG 31052 arbitrary function generator, and a Mini-Circuits SHP-150+ high pass filter (133-1000 MHz) before it reaches the transducer. Here, a sound wave is generated which travels through the sample and is then detected with the same transducer, where it creates a measurable voltage burst. This signal travels back through the high pass filter and to the switch array, where it is now directed through a Mini-Cuircuts ZX60-P103LN+ low noise amplifier, another Mini-Circuits SHP-150+ high pass filter (133-1000 MHz), and finally to the Tektronix MSO64 oscilloscope, where it is recorded.

Additional, optional elements in the above circuit include another Mini-Cuircuts ZX60-P103LN+ low noise amplifier immediately before the high pass filter leading up to the oscilloscope, and a Mini-Circuits VAT-X+ fixed attenuator between the high pass filter and the sample. The latter leads to less reflection of the RF signal at the transducer.

Typically, output powers of the RF generator between -20 and 0 dB (i.e. $0.01-1$ mW) are used, which are amplified to about $0.03 - 3$ W[1] after a gain of 35 dB at the power amplifier. Assuming that none of this power is reflected at the transducer, this corresponds to a voltage of about $1 - 10$ V across the transducer. Taking into account a thickness of 1.5 μm of our ZnO transducers and a piezoelectric constant of roughly 10 $\frac{\mathrm{pm}}{\mathrm{V}}$ [54], we can estimate the strain generated at the transducer to be on the order of 10^{-5} to 10^{-6}.

---

[1] It is important to note that we are not actually sending $0.03 - 3$ W of power to the transducer. $0.03 - 3$ W is the power if we were continuously exciting the transducer. However, we only excite short sound pulses that are about 100 ns wide with a repetition rate of 10 kHz, such that the actual power sent to the transducer is $0.03 - 3$ mW.

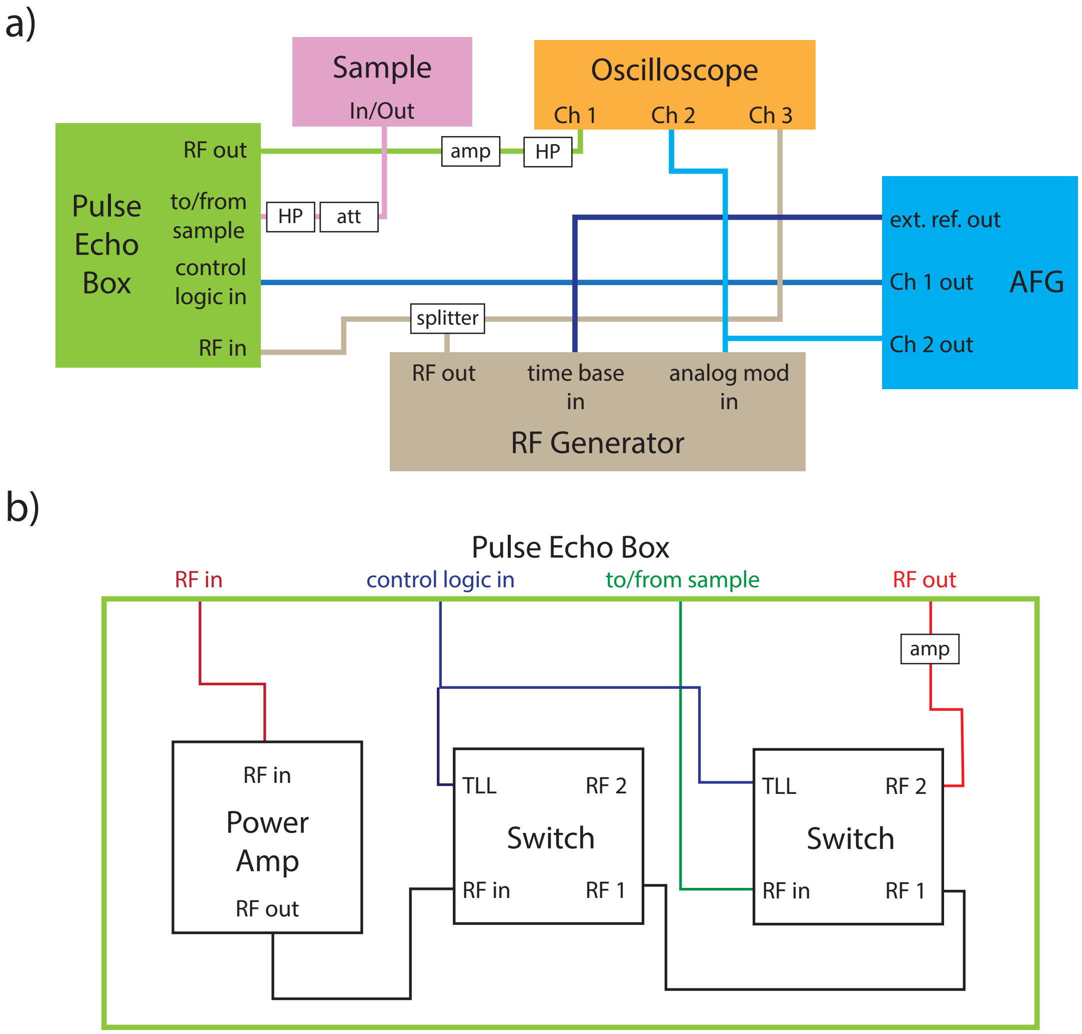

Figure 3.10: **Pulse-echo ultrasound measurement electronics.** Shown is a schematic of the measurement electronics circuit of our pulse-echo setup. The power amplifier and switch array is grouped as the *pulse-echo box* in panel a) and shown in more detail in panel b). HP, att, amp stand for the high pass filters, fixed attenuators, low noise amplifiers described in the main text, respectively. Where appropriate, lines connecting different devices are colored according to the device from which they originate.

3.2.4 Sample Preparation and Constraints

In order to achieve echo patterns like the ones shown in Figure 3.7 or Figure 3.8, the sound wave excited at the transducer at one end of the sample has to travel through the entire sample volume, reflect off the far face of the sample, and come back to the transducer several times. For that to be possible, two flat, parallel faces (to better than 1°) need to be prepared on the sample. We prepare the samples by polishing with Thor Labs diamond lapping films with a grid size of maximum 1 μm.

A constraint on the cross-sectional area of the sample is given by the transducer beam spread. The sound wave generated by the transducer is in practice not a plane wave, but disperses slightly. This dispersion is often characterized by the angle θ between the centerline of the acoustic beam and the point at which the pressure of the sound wave is reduced by one half. It is given by [55]

$$\sin\frac{\theta}{2} = 0.514\frac{v}{df}, \tag{3.19}$$

where v is the sound velocity of the sample in which the sound wave travels, d is the diameter of a cylindrical transducer, and f is the frequency of the sound wave. Assuming a sound velocity of 5000 $\frac{\mathrm{m}}{\mathrm{s}}$, a frequency of 500 MHz, and a transducer diameter of 200 μm, we obtain a spread angle of about 3°. Thus, if we further assume a sample thickness of 500 μm, the beam diameter will increase by about 100 μm every time the sound wave travels from the transducer through the sample and back. Of course the amount of beam spread can be lowered by increasing the frequency, or making the sample thinner. We want the cross-sectional area of the sample to be large enough such that even after several passes through the sample, no part of the sound wave will reach the sample boundary. Otherwise, sound can be reflected off the sample walls and interfere with the straight part of the beam, leading to a distorted echo pattern.

A constraint on the sample thickness is given by the minimum width of sound pulses we can produce. The sample needs to be thick enough such that successive echoes do not overlap. However, we cannot make our sound pulses arbitrarily narrow. Since we analyze the measured echo patterns with a digital lock-in method, we need at least a few oscillations per echo (more echoes usually means less noise due to the lock-in). For frequencies of about 1 GHz, this minimum echo width is on the order of 50 ns. For a sample with sound velocity 5000 $\frac{\mathrm{m}}{\mathrm{s}}$ a sound wave travels 250 μm in 50 ns. Therefore, in this scenario the sample has to be at least 125 μm thick for successive echoes to not overlap, putting a rough lower bound on the thickness of a sample we can measure with our current setup.

One of the failure modes of the sputter deposition is dirt or scratches on the sample surface. In the worst case scenario, these impurities are large enough such that the ZnO doesn't form a continuous layer and the top and bottom electrodes short. To achieve smooth surfaces, we polish the face of the sample on which the transducer is sputtered with Thor Labs diamond lapping films with a final grid size of 20 nm. We also clean our samples in high purity acetone, methanol, and isopropanol successively.

CHAPTER 4

NUMERICAL CALCULATION OF RUS RESONANCE SPECTRA

In section 3.1, we have discussed the technique of resonant ultrasound spectroscopy (RUS). How we measure mechanical resonance frequencies, as well as the fitting algorithm we use to extract the elastic tensor (subsection 3.1.3). The only missing piece in the analysis of RUS measurements is the forward calculation: how do we calculate resonance frequencies from a given set of elastic moduli? This forward calculation is explained below. It was commonly only possible for regularly-shaped samples but as part of this thesis we have extended it to irregularly-shaped samples.

In the following, we first rephrase the problem of the elastic wave equation (Equation 3.3) into a generalized eigenvalue equation (see section 4.1). We then demonstrate how this eigenvalue problem is solved for irregularly-shaped samples (see section 4.2)—the case of samples in the shape of rectangular prisms is discussed in Appendix D. The mathematical framework for the calculation of resonance spectra of irregularly-shaped samples was developed mainly by Avi Shragai [56]. The main contribution of this thesis was the implementation of this new forward solver into a fitting algorithm [43]. This fitting algorithm is analyzed in section 4.3, by fitting elastic moduli to resonance spectra of regularly and irregularly-shaped samples of $SrTiO_3$ and Mn_3Ge.

4.1 Numerical Implementation of the Elastic Wave Equation

As we have already discussed in section 3.1, the vibrational spectrum of a three-dimensional solid is given by the linear elastic Lagrangian $\mathcal{L}$ in Equation 3.2 [35, 36]. Assuming a periodic time dependence of the displacement field $\vec{u}(\vec{x},t) = \vec{u}(\vec{x})e^{i\omega t}$, Equation 3.2 becomes

$$\mathcal{L} = \frac{1}{2}\int \left(\sum_i \rho\omega^2 u_i^2(\vec{x}) - \sum_{ijkl} c_{ijkl} \frac{\partial u_i(\vec{x})}{\partial x_j} \frac{\partial u_k(\vec{x})}{\partial x_l} \right) dV, \tag{4.1}$$

where the deformations $\vec{u}$ for which $\mathcal{L}$ is stationary are also solutions to the elastic wave equation (Equation 3.3). To make this a numerically tractable problem, we expand the deformation vector in a basis of Cartesian polynomials up to order N

$$u_i(\vec{x}) = \sum_\lambda a_{i\lambda}\phi_\lambda(\vec{x}), \tag{4.2}$$

where λ is a particular combination of $l,\ m,\ n$, such that $\phi_\lambda = x^l y^m z^n$, and the sum is over all such combinations with $l + m + n \leq N$. For a given N, there are $R = (N+1)(N+2)(N+3)/6$ different basis polynomials. $a_{i\lambda}$ is therefore a $3 \times R$ matrix. The Lagrangian then becomes

$$\mathcal{L} = \frac{1}{2}\omega^2 \sum_{ii'\lambda\lambda'} a_{i\lambda} E_{\lambda i \lambda' i'} a_{i'\lambda'} - \frac{1}{2} \sum_{ii'\lambda\lambda'} a_{i\lambda} \Gamma_{\lambda i \lambda' i'} a_{i'\lambda'}, \tag{4.3}$$

where we have defined kinetic energy ($E_{\lambda i \lambda' i'}$) and potential energy ($\Gamma_{\lambda i \lambda' i'}$) tensors as

$$E_{\lambda i \lambda' i'} = \delta_{ii'} \int \phi_\lambda \rho \phi_{\lambda'} dV, \tag{4.4}$$

$$\Gamma_{\lambda i \lambda' i'} = \int \sum_{jj'} c_{iji'j'} \frac{\partial \phi_\lambda}{\partial x_j} \frac{\partial \phi_{\lambda'}}{\partial x_{j'}} dV. \tag{4.5}$$

Both $E_{\lambda i \lambda' i'}$ and $\Gamma_{\lambda i \lambda' i'}$ are rank-4 tensors with shape $R \times 3 \times R \times 3$. The Lagrangian in Equation 4.3 is stationary for $\partial \mathcal{L} / \partial a_{i\lambda} = 0$, leading to

$$\omega^2 \sum_{i\lambda} a_{i\lambda} E_{\lambda i \lambda' i'} = \sum_{i\lambda} a_{i\lambda} \Gamma_{\lambda i \lambda' i'}. \tag{4.6}$$

Since the indices i and λ describe entirely independent parameters—$i = 1, 2, 3$ is the spatial component of the deformation and $\lambda = l,\ m,\ n$ is the order of the basis polynomial—we can reshape the $a_{i\lambda}$ matrix into a $3R$-dimensional vector a_α, and the kinetic and potential tensors into $3R \times 3R$ matrices ($E_{\alpha\beta}$ and $\Gamma_{\alpha\beta}$). Equation 4.6 then becomes the generalized eigenvalue problem

$$\omega^2 E_{\alpha\beta} a_\beta = \Gamma_{\alpha\beta} a_\beta, \tag{4.7}$$

where summation over repeated indices is implied. This eigenvalue problem can be solved with standard numerical eigenvalue solvers like *scipy.linalg.eigh* in Python (note that both $E_{\alpha\beta}$ and $\Gamma_{\alpha\beta}$ are real and symmetric). The eigenvalues are the resonance frequencies and the eigenvectors describe the corresponding deformations.

The crucial step in this calculation of vibrational resonance frequencies is the creation of the kinetic and potential energy matrices in Equation 4.4 and Equation 4.5. This step is significantly different for regularly-shaped (in particular rectangular prisms) and irregularly-shaped samples. These two cases are the subjects of Appendix D (rectangular prisms) and section 4.2 (irregularly-shaped samples).

4.2 Irregularly Shaped Samples

Assuming a constant density throughout the sample, each non-zero element of the kinetic energy matrix in Equation 4.4 is of the form

$$E_{\lambda i \lambda' i} \sim \int \phi_\lambda \phi_{\lambda'} dV = \int x^{l+l'} y^{m+m'} z^{n+n'} dV, \tag{4.8}$$

where we have taken $\lambda = l,\ m,\ n$ and $\lambda' = l',\ m',\ n'$. Similarly, assuming constant elastic moduli throughout the sample, we can rewrite the potential energy tensor in Equation 4.5 as

$$\Gamma_{\lambda i \lambda' i'} = \sum_{jj'} c_{iji'j'} G_{\lambda j \lambda' j'}, \tag{4.9}$$

where

$$G_{\lambda j \lambda' j'} = \int \frac{\partial \phi_\lambda}{\partial x_j} \frac{\partial \phi_{\lambda'}}{\partial x_{j'}} dV, \tag{4.10}$$

$$= \int x^\alpha y^\beta z^\gamma dV, \tag{4.11}$$

where, we have summarized $\alpha = l+l'-\delta_{1j}-\delta_{1j'}$, $\beta = m+m'-\delta_{2j}-\delta_{2j'}$, $\gamma = n+n'-\delta_{3j}-\delta_{3j'}$.

The expressions in Equation 4.9 and Equation 4.11 are both integrals of polynomials over the volume of the sample. They take straightforward closed-form solutions if the measured sample can be prepared in the shape of a rectangular prism. This can be, however, difficult for various reasons. Cutting or polishing samples can be tedious for brittle materials, or samples which are already small to begin with. Furthermore, there are potential health hazards associated with polishing certain materials, like uranium based compounds, as would be required for measurements on UTe_2 in chapter 5.

In the case of such irregularly shaped samples, the integrals in Equation 4.9 and Equation 4.11 need to evaluated numerically. A natural first step is to divide the geometry of the irregularly shaped sample into tetrahedra, such that the relevant integrals are reduced to integrals of polynomials over tetrahedra. Existing methods for the evaluation of these volume integrals include recursive, closed-form solutions [57] or quadrature integration [58]. However, the former method is too slow to perform fits and the latter lacks the required precision. In order to calculate the first roughly 100 resonances, basis polynomials with highest order of 15 or above are required (fits in this thesis are mainly performed with order 18 bases). That means that we need to evaluate integrals of polynomials up to order 30 in Equation 4.9 and Equation 4.11. However, quadrature rules only exist for polynomials of order 20 or below [58]. In Shragai et al. [56], we developed a new method where we convert the volume integrals in the kinetic and potential energy tensors to surface integrals using Gauss' theorem. This method, as outlined below, offers a computationally fast and precise way to calculate mechanical resonance spectra of irregularly shaped samples, which is compatible with performing RUS fits.

We have already established that the elements of both the kinetic and potential energy tensors eventually reduce to integrals of a polynomial of $x^l y^m z^n$ over the volume of the sample, where we now have that $l + m + n \leq 2N$. We can then write this polynomial as the gradient of a vector

$$x^l y^m z^n = \frac{1}{n+1} \nabla \cdot \left(0, 0, x^l y^m z^{n+1}\right). \tag{4.12}$$

We find no significant difference in the final resonance spectrum if equivalent vectors $\frac{1}{l+1}\left(x^{l+1} y^m z^n, 0, 0\right)$ or $\frac{1}{m+1}\left(0, x^l y^{m+1} z^n, 0\right)$ are chosen. The integral over the volume of the sample therefore becomes

$$\int_V x^l y^m z^n dV = \frac{1}{n+1} \int_V \nabla \cdot \left(0, 0, x^l y^m z^{n+1}\right) dV, \tag{4.13}$$

$$= \frac{1}{n+1} \int_A d\vec{A} \cdot \left(0, 0, x^l y^m z^{n+1}\right), \tag{4.14}$$

$$= \frac{1}{n+1} \sum_i \int_A d\vec{A}_i \cdot \left(0, 0, x^l y^m z^{n+1}\right), \tag{4.15}$$

$$= \frac{1}{n+1} \sum_i \int_A dA_{z,i} x^l y^m z^{n+1}, \tag{4.16}$$

where in the first step, we have used Gauss' law to convert the volume integral into an integral over the surface of the sample. From the second to the third line, we have then introduced the discretization of the surface of the sample into a triangular surface mesh, where $d\vec{A}_i$ is the area of the i-th triangular mesh element. In the last step, we have evaluated the scalar product $d\vec{A}_i \cdot \left(0, 0, x^l y^m z^{n+1}\right)$ such that the remaining integral is over the area of the i-th mesh element projected onto the $x - y$ plane.

Note that the projection of the individual mesh elements onto the $x - y$ plane is not unique and different vectors introduced to describe the original polynomial (see Equation 4.12 and the discussion below) lead to projections onto the $x - z$ or $y - z$ planes. We do not observe significant differences in the computed resonance spectra for different projections [56].

4.3 Experimental Proof of Concept

Here we demonstrate in two steps that the above method of computing RUS resonance frequencies via surface mesh integration gives enough precision to be used in fits of elastic moduli: first, we prepare a sample in the shape of a rectangular prism and measure its resonance frequencies. Fits are then performed with the genetic algorithm described in subsection 3.1.3, using three different forward calculation methods: the method developed by Visscher et al. [35] (as discussed in Appendix D; fits with this method are labeled *RPR*), the method using surface mesh integration developed by Shragai et al. [56] (as discussed in section 4.2; fits with this method are labeled *SMI*), and lastly we use a commercially available finite element software—Comsol—as the third forward solver (fits with this method are labeled *FEM*). In the second step, we prepare irregularly shaped samples of the same material and perform fits using the SMI and FEM forward solvers (the RPR method is not available for irregularly shaped samples). This entire procedure is repeated twice, once for samples of $SrTiO_3$ and once for samples of Mn_3Ge. The experimental resonance spectra and calculated frequencies corresponding to all fits discussed below are shown in Appendix E.

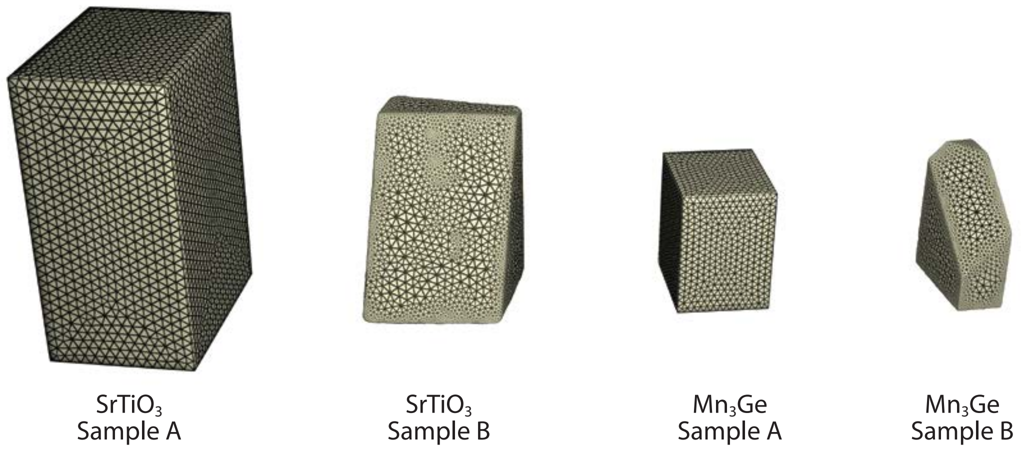

Figure 4.1: **Sample meshes.** Shown are 3D models of the samples used in the RUS fits described in the main text. Samples are from left to right: $SrTiO_3$ sample A (in the shape of a rectangular prism), $SrTiO_3$ sample B (irregularly shaped), Mn_3Ge sample A (in the shape of a rectangular prism), Mn_3Ge sample B (irregularly shaped). The meshes shown here are the ones we used for fits with the FEM forward solver. Fits using the SMI method allow for a much finer mesh, which cannot be resolved on the scale of the figure. Samples are shown with accurate relative scale. $SrTiO_3$ sample A has dimensions $(1.49 \times 2.035 \times 3.02)$ mm^3 and Mn_3Ge sample A has dimensions $(0.87 \times 1.01 \times 1.19)$ mm^3. Figure adapted from [43].

Method	$SrTiO_3$ sample A	$SrTiO_3$ sample B	Mn_3Ge sample A	Mn_3Ge sample B
FEM	103	40	63	30
SMI	60	5	23	5

Table 4.1: **Mesh size.** Average distance between two vertices (in μm) in the meshes we used in the RUS fits. Smaller meshes are possible for the SMI method than the FEM method. For the FEM method, smaller meshes slow down each forward calculation of resonance frequencies, significantly slowing down the total fit time. For the SMI method, the computationally expensive part is the creation of the kinetic and potential energy tensors, which only has to be done once at the beginning of the fit. While smaller mesh sizes slow down this part, once these tensors are created, the speed of each forward calculation is unaffected. Table adapted from [43].

We obtain the surface meshes required for the SMI method for the samples in the shapes of rectangular prisms by creating a model in Comsol and exporting the surface mesh. Meshes for the irregularly shaped samples are obtained via CT-scans with a Zeiss Xradia Versa XRM-520 X-ray nano-CT. 3D models of the samples, as well as representative meshes are shown in Figure 4.1. The average mesh sizes for all samples are quantified in Table 4.1.

Sample	Fit Method	c_{11}	c_{12}	c_{44}
$SrTiO_3$ A	RPR	321.9 ± 0.5	103.6 ± 0.6	125.0 ± 0.3
	FEM	321.9 ± 0.5	103.6 ± 0.6	125.0 ± 0.3
	SMI	321.9 ± 0.5	103.6 ± 0.6	125.0 ± 0.3
$SrTiO_3$ B	FEM	316.7 ± 0.5	103.1 ± 0.6	121.9 ± 0.3
	SMI	316.7 ± 0.5	102.9 ± 0.6	122.0 ± 0.3
Bell and Rupprecht [60]		317	102	123
Poindexter and Giardini [59]		348	101	119
Lüthi and Moran [61]		331	105	126
Migliori et al. [44]		315 ± 0.6	102 ± 0.7	122 ± 0.01

Table 4.2: **Elastic moduli of $SrTiO_3$ in GPa.** The elastic moduli for $SrTiO_3$ samples A (in the shape of a rectangular prism) and B (irregularly shaped) obtained with fits using various forward solvers. The uncertainties are from a 2 % increase in the RMS (see subsection 3.1.3). Literature values are provided in the bottom rows. Table adapted from [43].

4.3.1 $SrTiO_3$

$SrTiO_3$ is an ideal starting point for our demonstration. It is cubic—i.e. the crystal structure belongs to the O_h point group—meaning it only has three independent elastic moduli: c_{11}, c_{12}, and c_{44}. Values for the elastic moduli have also been reported previously [44, 59–61].

First, we polished a $SrTiO_3$ sample into a rectangular prism with dimensions $(1.49 \times 2.035 \times 3.02)$ mm^3 ($SrTiO_3$ sample A) and the corners aligned along the crystallographic axes. Fit results to the first 70 measured resonance frequencies are shown in Table 4.2. For this sample, all three forward solvers are available. The uncertainties to the elastic moduli are defined by a 2 % increase in the RMS as discussed in subsection 3.1.3. Next, we prepared an irregularly-shaped $SrTiO_3$ sample ($SrTiO_3$ sample B, see Figure 4.1) and again used the first 70 resonances for a fit of the elastic moduli. For the irregularly-shaped sample only the SMI and FEM methods are available.

Comparing different methods within each sample, we find that the different forward solvers give identical elastic moduli within uncertainties. Comparing the fit results between sample A (rectangular prism) and sample B (irregularly shaped), we find deviations of less than 2.5 % for all elastic moduli. These deviations are slightly larger than our statistical uncertainties. We attribute them to systematic uncertainties, like deviations of sample A from a perfect rectangular prism, uncertainties in the densities, or uncertainties due to sample loading. We analyze these systematic uncertainties in section 4.4.

Sample	Fit Method	c_{11}	c_{12}	c_{13}	c_{33}	c_{44}
Mn_3Ge A	RPR	130.0 ± 0.3	43.9 ± 0.4	13 ± 2	202 ± 2	48.3 ± 0.2
	FEM	130.0 ± 0.3	43.9 ± 0.3	13 ± 2	202 ± 2	48.3 ± 0.2
	SMI	130.0 ± 0.3	43.9 ± 0.4	13 ± 2	202 ± 2	48.3 ± 0.2
Mn_3Ge B	FEM	126.8 ± 0.3	40.3 ± 0.4	14 ± 4	203 ± 2	48.7 ± 0.2
	SMI	126.8 ± 0.3	40.2 ± 0.4	14 ± 4	203 ± 2	48.7 ± 0.2

Table 4.3: **Elastic moduli of Mn_3Ge in GPa.** The elastic moduli for both Mn_3Ge samples A (rectangular prism) and B (irregularly shaped). The uncertainties are from a 2 % increase in the RMS (see subsection 3.1.3). Table adapted from [43].

Comparing our fit results to previous studies, we find that none of our elastic moduli are significantly different from those reported in Bell and Rupprecht [60] and Migliori et al. [44]. Particularly for c_{11}, however, we find values nearly 10 % smaller than those reported in Poindexter and Giardini [59] and Lüthi and Moran [61]. While this difference is significantly beyond our uncertainties, it is within typical error bars for the absolute values of elastic moduli obtained with pulse-echo ultrasound (see section 3.2), which is the technique used in [61].

Table 4.2 also shows identical statistical uncertainties for both samples and all forward solvers. They are additionally consistent with the uncertainties reported in [44]. We thus conclude, that using our novel SMI forward solver, results in reliable fits of elastic moduli, even for irregularly shaped samples.

While this study shows that SMI and FEM methods result in the same fits for elastic moduli, using the SMI solver is about $50 - 100$ times faster than the FEM solver. There is no significant speedup from the SMI to the RPR solver, since the computationally expensive step—the creating of kinetic and potential energy tensor—only needs to be done once at the beginning of a fit. Every subsequent step in the calculation of resonance spectra is identical between SMI and RPR methods.

4.3.2 Mn_3Ge

Mn_3Ge is a hexagonal crystal (i.e. it belongs to the D_{6h} point group), which means it has five independent elastic moduli: c_{11}, c_{12}, c_{33}, c_{13}, and c_{44}. It is therefore a natural next test for the SMI method due to the increased complexity of additional free parameters in the RUS fits. Similarly to the case of $SrTiO_3$, we prepared one sample in the shape of a rectangular prism (Mn_3Ge sample A) and one irregularly shaped sample (Mn_3Ge sample B). See Figure 4.1 for models of the samples. Sample A has dimensions $(0.87 \times 1.01 \times 1.19)$ mm^3, where the first two dimensions are perpendicular, and the last dimension is parallel to the c axis. We measured 84 resonances for both samples and the fit results are shown in Table 4.3.

Sample	Arrangement	c_{11}	c_{33}	c_{12}	c_{13}	c_{44}
$SrTiO_3$ B	1	313.8	-	100.3	-	122.62
	2	316.7±0.5	-	102.9±0.7	-	121.95±0.05
	3	315.8	-	100.2	-	122.30
Mn_3Ge B	1	126	200	38	12	48.7
	2	127±1	203±2	40±2	14±5	48.7±0.5
	3	129	196	42	18	49.6

Table 4.4: **RUS uncertainty analysis.** Elastic moduli fit results are shown for $SrTiO_3$ and Mn_3Ge samples B. The arrangement number refers to the way the sample was mounted in the RUS setup and corresponds to the same column in Figure 4.2. The uncertainties for arrangement 2 are due to a 1° misalignment between crystal axes and sample mesh. All fits are performed with the SEM method. Table adapted from [43].

We find that as for $SrTiO_3$, fits for the same sample give equivalent elastic moduli and uncertainties, even when different forward solvers are used. This is true for both the regularly (Mn_3Ge sample A) and irregularly-shaped (Mn_3Ge sample B) samples. Comparing samples A and B, the elastic moduli differ by less than 4 GPa, which is analogous to what we observed for $SrTiO_3$ samples A and B. We therefore attribute this difference to similar systematic uncertainties as in the $SrTiO_3$ case, which we discuss in section 4.4.

4.4 Systematic Uncertainties

In subsection 3.1.3 we identify three sources of systematic uncertainties: small deviations from a nearly-free oscillator, uncertainties in the alignment of the crystallographic axes to the macroscopic sample shape, and an uncertainty in the sample densities.

Deviations from a nearly-free oscillator are caused by the weight of the top lever or transducer rod on the sample. $SrTiO_3$ and Mn_3Ge samples were measured in the same setup, with a top transducer rod which weighs about 5 g. This weight causes the measured resonance frequencies to slightly depend on how the sample is mounted between the transducers. To investigate the resulting effect on the elastic moduli, we mounted both the $SrTiO_3$ and Mn_3Ge samples B (i.e. the irregularly shaped samples) in three different ways in the RUS setup and fit elastic moduli to the resulting resonance spectra. Figure 4.2 shows the different arrangements in which the samples were mounted in the RUS setup and Table 4.4 shows the corresponding fit results. The average systematic uncertainty for $SrTiO_3$ (Mn_3Ge) sample B is 1.7 GPa (2.3 GPa).

We aligned the crystallographic axes to the sample mesh by performing Laue back-reflection diffractometry, with an uncertainty of up to 1°. We investigated the resulting uncertainty in the elastic moduli by refitting the RUS spectra with sample meshes rotated by 1° around the x, y, and z axes, respectively. The resulting average uncertainties are

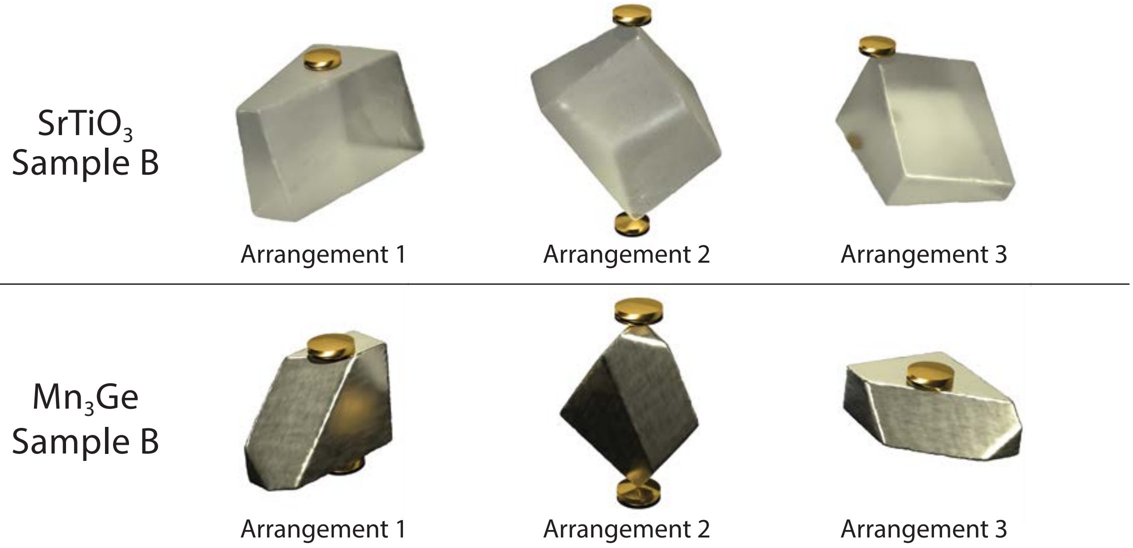

Figure 4.2: **RUS sample arrangements.** 3D models of SrTiO$_3$ sample B (top row) and Mn$_3$Ge B (bottom row) are shown in different arrangements between two piezoelectric transducers (gold cylinders). The different arrangements represent the different ways the samples were mounted in the RUS setup to estimate the uncertainty arising from the weight of the top transducer rod on the samples. Arrangement 2 is the one chosen for the fits in Table 4.2 and Table 4.3. Figure adapted from [43].

0.4 GPa for SrTiO$_3$ sample B, and 2 GPa for Mn$_3$Ge sample B. Uncertainties for each individual elastic modulus are given in Table 4.4.

To estimate the uncertainty in the densities of our samples, we measured their masses using a Fisher Scientific accu-225D analytical scale and extracted their volumes from the CT scans. We find about a 1 % discrepancy between our measured densities and reported literature values. This 1 % uncertainty in the sample density directly translates to a 1 % uncertainty in the elastic moduli.

4.5 Conclusion & Outlook

We have presented a novel method to compute mechanical resonance frequencies via surface mesh integration. We have shown on the examples of SrTiO$_3$ and Mn$_3$Ge that fits using this new method yield the same elastic moduli as fits performed with the standard forward solver presented by Visscher et al. [35] or with commercially available finite element solvers. In contrast to the method used in Visscher et al. [35], however, our new forward solver allows for the analysis of RUS spectra of irregularly-shaped samples. It thus extends the applicability of RUS to a much broader range of quantum materials, which cannot be polished into rectangular prisms.

One caveat is that while our new method is able to calculate resonances for irregularly-shaped samples, it does not necessarily work for any arbitrary shape. The kinetic energy matrix E is very close to being singular. Furthermore, the likelihood of E being singular increases with its size, i.e. with the highest order of the basis polynomials used in the expansion of the displacement. We find that forcing as many elements of E as possible to be zero (or at least small) reduces the chance of it being singular. This can be achieved by translating the sample mesh such that its center of mass is at the origin and rotating it such that its moment of inertia tensor is diagonal (note that translations and rotations don't affect the resonance spectrum).

We also recommend avoiding samples with large aspect ratios, since the measured resonance spectra for such samples can often exhibit many missing resonances and resonances are particularly broad at room temperature and atmospheric pressure.

CHAPTER 5

SUPERCONDUCTING ORDER PARAMETER IN $\mathrm{UTe_2}$

Understanding the driving mechanisms behind unconventional superconductivity is one of the primary challenges in condensed matter physics. Ultrasound plays a pivotal role in this endeavor, as it can constrain the symmetry of the superconducting order parameter and offer critical insights into the microscopic pairing mechanism. Heavy-fermion metals provide an ideal class of materials for this research, as they are characterized by strong electron-electron interactions leading to an abundance of collective phenomena, including unconventional superconductivity. In this chapter, we discuss our RUS and pulse-echo ultrasound measurements on the heavy-fermion spin-triplet superconductor $\mathrm{UTe_2}$. Despite earlier claims of a two-component superconducting order parameter, our main conclusion is that the order parameter in $\mathrm{UTe_2}$ has only one component, possibly transforming according to the B_{2u} irreducible representation of the D_{2h} point group.

5.1 Introduction to Superconductivity in $\mathrm{UTe_2}$

Superconductivity in uranium ditelluride with a critical temperature of about 1.6 K was first reported in 2019 [62]. Large upper critical fields implied spin-triplet pairing, even in the absence of magnetic order. Since then, complex phase diagrams with multiple superconducting and magnetic phases have been discovered under externally applied magnetic fields and hydrostatic pressure (see Figure 5.1).

The upper critical fields for fields along the crystallographic directions as determined by heat capacity measurements are shown in Figure 5.1a. The unconventional behavior of superconductivity in $\mathrm{UTe_2}$ is most pronounced for fields along the b axis. Here, field-reinforced superconductivity is observed until it is interrupted by a first-order transition to a magnetic state at about 35 T [62, 65]. Recent NMR and specific heat measurements even imply a transition into a distinct superconducting state for fields of about 15 T along the b axis [64, 66]. An additional superconducting phase has been conjectured to exist for fields starting above 40 T and persisting up to more than 60 T, if applied roughly along the [011] direction [67, 68].

Similarly to magnetic fields applied along the b axis, hydrostatic pressure induces a splitting of the critical temperature T_c at about 0.3 GPa [69, 70] (see Figure 5.1 b). Superconductivity is only interrupted by a first-order phase transition at about 1.7 GPa, followed by a magnetic state.

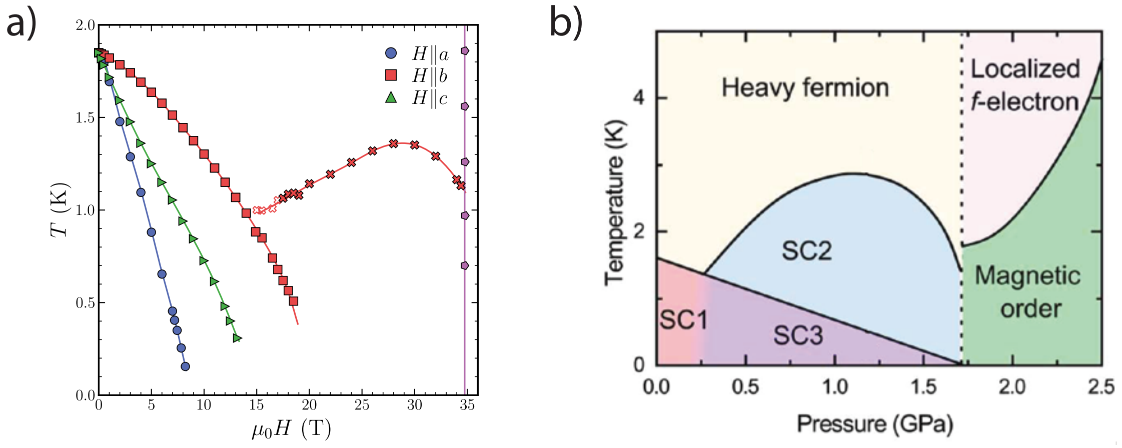

Figure 5.1: **UTe$_2$ phase diagrams.** a) Upper critical fields for fields along the crystallographic axes as determined by heat capacity measurements. b) Schematic phase diagram as a function hydrostatic pressure. Multiple superconducting phases appear as a function of b-axis magnetic field (a) and hydrostatic pressure (b). Additionally, fields along the b axis or hydrostatic pressures above about 1.7 GPa induce a magnetic state through a first-order transition. The low temperature superconducting state (SC1 in panel b) is conjectured to change its ground state properties as a function of pressure (SC3 in panel b), however, no phase transition has been observed yet [63]. Panels a) and b) are adapted from [64] and [63], respectively.

The general outlines of these phase diagrams are quite robust against changes in sample quality. However, the details of the superconducting state, in particular at zero field and ambient pressure, have been shown to depend significantly on the growth method that was used. Samples are grown with chemical vapor transport (VPT) or molten salt flux (MSF) growth methods. T_c varies between about 1.6 and 2.1 K with the highest T_c's seen in MSF grown samples [71–74]. Even more drastically, some VPT grown samples exhibit two superconducting phase transitions [75, 76] (even at ambient pressure and zero applied magnetic field).

Small changes in the Knight shift at T_c [77–79] together with the large upper critical fields [62, 65] imply spin-triplet pairing in all measured samples. Evidence for the particular nodal structure of the superconducting gap, however, seems to vary significantly between samples of different quality. NMR [80] and thermal conductivity [81] measurements on MSF grown samples imply a fully gapped state, whereas most measurements on CVT grown samples indicate the presence of point nodes, irrespective of T_c. These measurements include thermal conductivity [82, 83], penetration depth [84], NMR Knight shift [77–79], and specific heat measurements [85].

Furthermore, a finite Kerr rotation has been observed in samples with two transitions, indicative of time-reversal symmetry breaking (TRSB) in the superconducting state [76, 86]. This interpretation is supported by the observation of chiral surface states by scanning tunneling microscopy (STM) [87] and microwave surface impedance [88] measurements. Similar Kerr effect measurements on samples with one transition, on the other hand, find no evidence for TRSB [89].

Lastly, STM also observes the formation of a charge density wave (CDW) between 10 and 12 K [90–92], which has been interpreted as the parent phase of a pair density wave state below T_c [93]. Thermodynamic evidence of a phase transition in this temperature range, however, is lacking to date.

In this thesis we performed RUS and pulse-echo ultrasound measurements on UTe_2 to shed light on some of the open questions posed above. Elastic moduli are thermodynamic quantities which are very sensitive to second-order phase transitions. They should be able to detect a bulk CDW phase if present. Furthermore, TRSB in the superconducting state is only possible for a two-component order parameter. The question regarding the presence or absence of TRSB is therefore intimately linked to the dimensionality of the superconducting order parameter. Ultrasound measurements are uniquely qualified to determine this order-parameter dimensionality (see subsection 2.4.5) and thus to address the question of TRSB in UTe_2.

5.2 Normal State Elastic Moduli

Elastic Tensor at 4 and 300 K. UTe_2 crystallizes in an orthorhombic lattice, belonging to the D_{2h} point group/$Immm$ space group (see Figure 5.2a for an image of the crystal structure). It thus has nine independent elastic moduli. Due to potential health hazards associated with polishing uranium based compounds, we performed RUS measurements on two as-grown irregularly-shaped samples (see Figure 5.2 for 3D models of the samples) using the SMI forward method[1] (see chapter 4 for details).

The resulting elastic moduli for both samples at 300 K and at 4 K are shown in the top four rows of Table 5.1. The uncertainties are statistical uncertainties due to a 2 % increase in RMS. An analysis of systematic uncertainties similar to that in section 4.4, as well as all experimental and calculated resonance frequencies corresponding to the fit results shown here are given in Appendix F. The fit results for both UTe_2 samples A and B are in excellent agreement, at 4 and at 300 K. They are also remarkably consistent with density functional theory (DFT) calculations (bottom row of Table 5.1; details about the DFT calculations are given in Appendix G). We also performed pulse-echo measurements, which give elastic moduli in perfect agreement with the RUS and DFT results.

Low Temperatures Up To 20 K. The temperature dependence of the relative changes of the compressional moduli (i.e. c_{11}, c_{22}, and c_{33}) as well as the off-diagonal elastic

---

[1] The large number of free parameters in the RUS fit due nine independent elastic moduli, as well as smaller features in the 3D sample models make fits with the FEM method prohibitively slow.

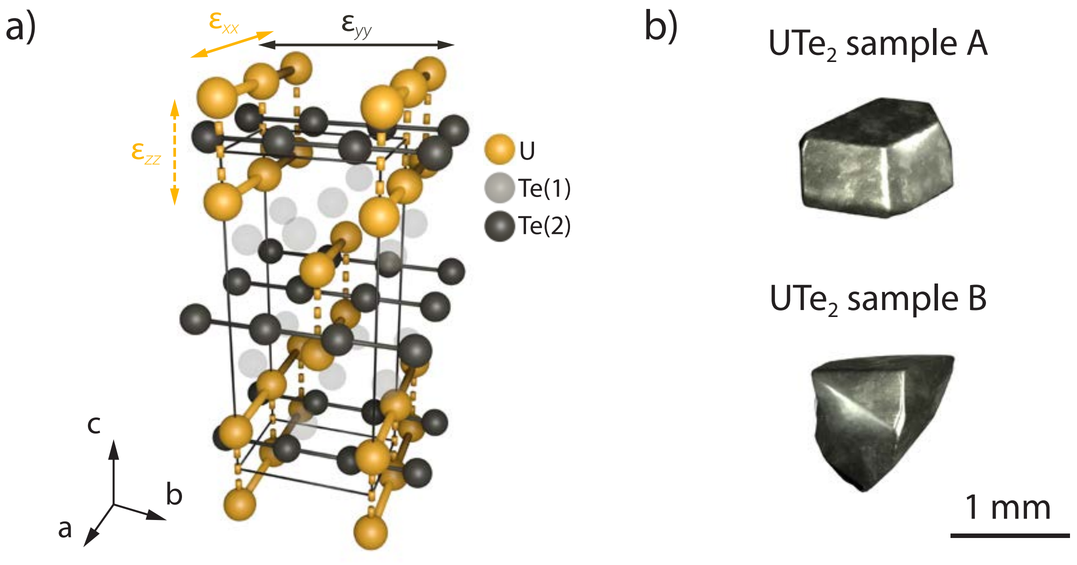

Figure 5.2: **UTe$_2$ crystal structure.** Crystal structure of UTe$_2$. Uranium atoms are shown in yellow and tellurium atoms in gray. There are two inequivalent tellurium sites (Te(1) and Te(2)). The Te(1) site is shown to not significantly contribute to the electronic structure of UTe$_2$ [94], which is why we are only displaying it faintly in the image. Uranium atoms forming dimers are connected by a dashed line, and uranium and tellurium atoms are connected with solid lines within their respective chains. Arrows indicate that the U-U dimer distance is most affected by ϵ_{zz} strain, whereas the intra-chain uranium/tellurium distances are most affected by $\epsilon_{xx}/\epsilon_{yy}$ strains. 3D models of the samples used for RUS measurements are shown in panel b). The scale bar represents 1 mm. Panels a) and b) are adapted from [33] and [43], respectively.

moduli c_{12}, c_{13}, and c_{23} obtained from our RUS measurements are shown in Figure 5.3. The measured temperature ranges from about 4 K to 20 K. All elastic moduli shown here stiffen upon cooling in the measured temperature range. This hardening amounts to roughly 0.5 % for all compressional moduli and 1 to 2 % for all off-diagonal moduli.

All of the shown elastic moduli correspond to strains transforming as the trivial A_g irreducible representation of the D_{2h} point group. They are therefore all allowed to show a step discontinuity at any second order phase transition (see subsection 2.3.3). This includes the proposed charge density wave order below $T_{CDW} \approx 10 - 12$ K [91], which is well within our measured temperature range. However, we do not observe any discontinuity in our measured elastic moduli.

The absence of a discontinuity in the compressional moduli can already be inferred from the temperature dependence of the raw resonance frequencies. In Figure 5.4, we compare selected resonances of CsV$_3$Sb$_5$ with selected resonances of UTe$_2$. CsV$_3$Sb$_5$ is known to exhibit a charge density wave around 94 K [95] (roughly marked by the vertical gray bar in Figure 5.4a). This phase transition leads to features on the order of 1 %

	T (K)	c_{11}	c_{22}	c_{33}	c_{12}	c_{13}	c_{23}	c_{44}	c_{55}	c_{66}
UTe_2 A	4	90.3	144.1	95.9	25.7	41.3	31.9	28.05	53.2	30.43
		±0.2	±0.6	±0.2	±0.8	±0.2	±0.5	±0.08	±0.2	±0.08
	300	84.7	139.5	91.1	26.8	38.1	31.6	26.93	52.4	29.65
		±0.2	±0.5	±0.2	±0.6	±0.2	±0.5	±0.07	±0.2	±0.08
UTe_2 B	4	89.2	146.9	94.0	28	40.4	31.4	28.2	52.5	30.3
		±0.3	±0.9	±0.3	±1	±0.2	±0.9	±0.1	±0.3	±0.1
	300	82.8	141.8	89.9	26	36.7	32.7	27.18	51.5	29.0
		±0.3	±0.8	±0.3	±1	±0.2	±0.7	±0.09	±0.3	±0.1
Pulse Echo	280	81	141	91	—	—	—	27	52	30
		±8	±15	±11	—	—	—	±3	±5	±3
DFT		96	136	90	28	46	26	28	57	31

Table 5.1: **Elastic moduli of UTe_2 in GPa.** We give the elastic moduli of UTe_2 samples A and B at 300 K and at 4 K. The shown uncertainties are due to a 2 % increase in RMS. Systematic uncertainties which are on the order of 1 GPa are discussed in Appendix F. All RUS fits were performed using the SMI forward solver with order 18 basis polynomials. Also shown are the elastic moduli obtained with pulse-echo ultrasound measurements and DFT calculations. Pulse-echo measurements were performed on three different samples. The elastic moduli c_{12}, c_{13}, and c_{23} were inaccessible with our samples. The uncertainties for the elastic moduli measured with pulse-echo ultrasound are due to uncertainties in the sample thicknesses. Details of the samples, pulse-echo carrier frequencies, and transducer configurations are given in Appendix I. Table adapted from [43].

in the relative changes of the measured resonance frequencies. No feature of remotely similar scale can be observed in the resonances measured in UTe_2 (see Figure 5.4b). Note the much smaller scale on the y axis for the UTe_2 panel in Figure 5.4 compared to the CsV_3Sb_5 panel.

In conclusion, we find no signs of a thermodynamic bulk second order phase transition in UTe_2, close to the proposed charge density wave ordering temperature. This implies that the charge density wave (and the proposed pair-density wave) observed in UTe_2 in STM measurements [90, 91, 93] is most likely a surface effect.

High Temperatures Up To 280 K. We now turn to a wider temperature range and show the relative changes of compressional and shear moduli from 2 to 280 K in figure Figure 5.5. All data for these curves have been measured with pulse-echo ultrasound. The temperature dependencies of c_{33}, c_{44}, and c_{55} have been previously published in [96] and are quantitatively consistent with our data.

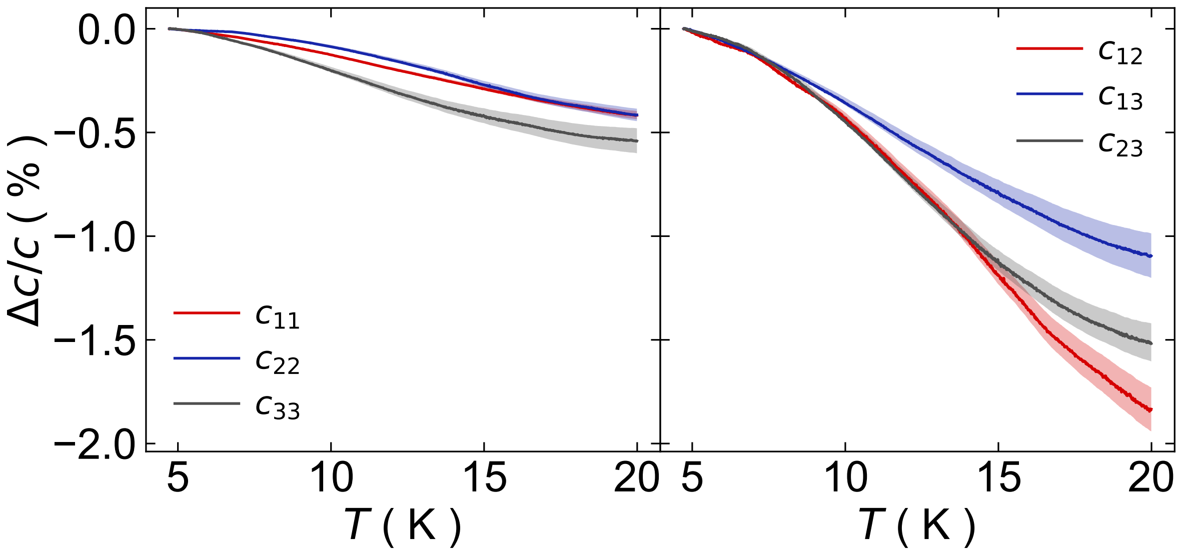

Figure 5.3: **UTe_2 RUS compressional moduli.** Shown are the relative changes in the compressional moduli (i.e. c_{11}, c_{22}, c_{33}—left panel) and the off-diagonal elements of the elastic tensor (i.e. c_{12}, c_{13}, c_{23}—right panel) from 4 to 20 K. These are all elastic moduli in UTe_2 which correspond to strains transforming according to the A_g irreducible representation of the D_{2h} point group. The elastic moduli were obtained from RUS measurements on UTe_2 sample B (see Figure 5.2b for a 3D model of the sample). The resonances used for this decomposition are marked in bold font in Table F.3. The uncertainties marked by colored shaded regions about the data are due to the statistical uncertainties of our fit results in Table 5.1.

All measured elastic moduli harden upon cooling until about 60 K, which is the expected behavior if the temperature dependence is purely due to the anharmonicity of the lattice [98]. For all compressional moduli (left panel in Figure 5.5), however, this hardening, slows down around 60 K, where they are mostly flat, until they significantly increase again below about 20 K. This shoulder-like feature is common in many heavy-fermion compounds [99–101], and is often explained with a two-band model arising from hybridization of conduction electrons with local f-electrons [102–105]. In Figure 5.5, we also show the a-axis resistivity taken from [97]. Its Kondo coherence peak coincides with the shoulder-like feature in the elastic moduli, further corroborating its origin due to f-electron hybridization.

The relative changes of the shear moduli are shown in the right panel of Figure 5.5. Both c_{55} and c_{66} soften significantly below about 60 K. Similarly to the shoulder in the compressional moduli, this softening can be qualitatively described with a two-band model, and we attribute it to Kondo coherence [100]. This is again corroborated by a Kondo peak of the a-axis resistivity at the same temperature at which c_{55} and c_{66} exhibit their maxima. c_{44} on the other hand increases monotonically upon cooling, without a pronounced feature near the Kondo temperature. This observation suggests that Kondo

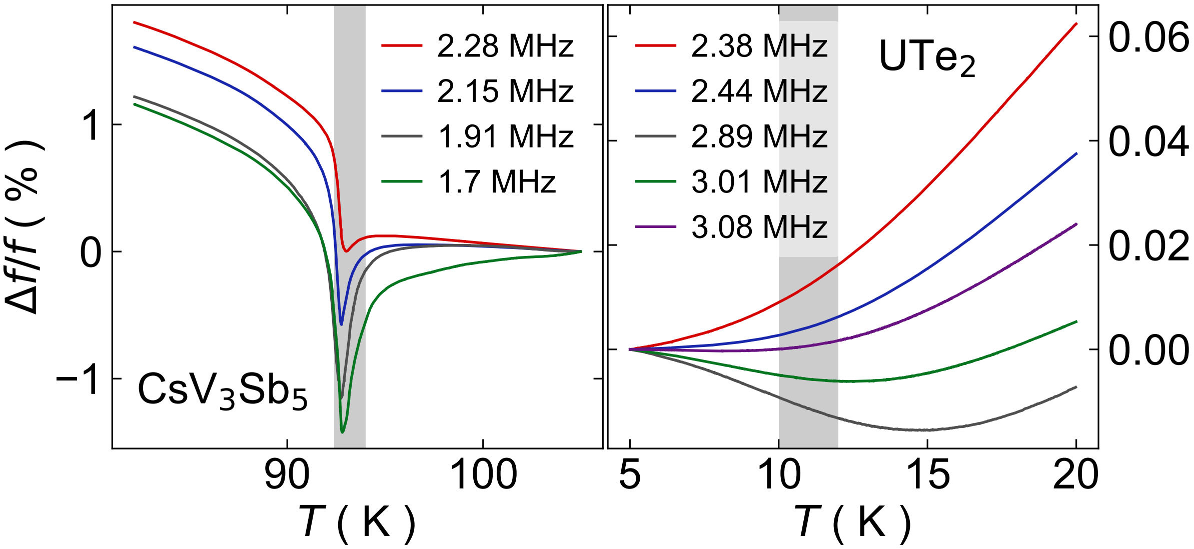

Figure 5.4: **Selected RUS resonances in CsV_3Sb_5 and UTe_2.** Temperature dependence of the relative changes of selected RUS resonance frequencies of a sample of CsV_3Sb_5 (left panel) and UTe_2 sample B (right panel). CsV_3Sb_5 exhibits a charge density wave (CDW) around 94 K [95], which is clearly visible in the resonance frequencies. The transition region is marked by a gray vertical bar. Similarly, a gray region in the right panel indicates the temperature range in which the CDW in UTe_2 is believed to start [90, 91]. No feature indicative of a thermodynamic bulk phase transition is observed in the resonance frequencies in UTe_2. Note the difference in scale between the left and right panel. Changes in the resonances of CsV_3Sb_5 at the phase transition are on the order of 1 %, whereas the total change of the resonances in UTe_2 are at most 0.06 % over the entire temperature range shown here.

physics in UTe_2 is insensitive to yz strain[2]. The origin of this insensitivity, however, is currently still an open question.

5.3 Superconducting Order Parameter in UTe_2

5.3.1 Possible Representations

Since UTe_2 crystallizes in an orthorhombic lattice, the superconducting order parameter must transform according to a representation of the D_{2h} point group. In particular, the order parameter is generally expected to transform as one of the irreducible representa-

---

[2] In [96], the softening in c_{55} was interpreted as a lattice instability related to zx strain. However, after observing the same softening in c_{66}, we believe that the behavior of both elastic moduli is due to Kondo hybridization.

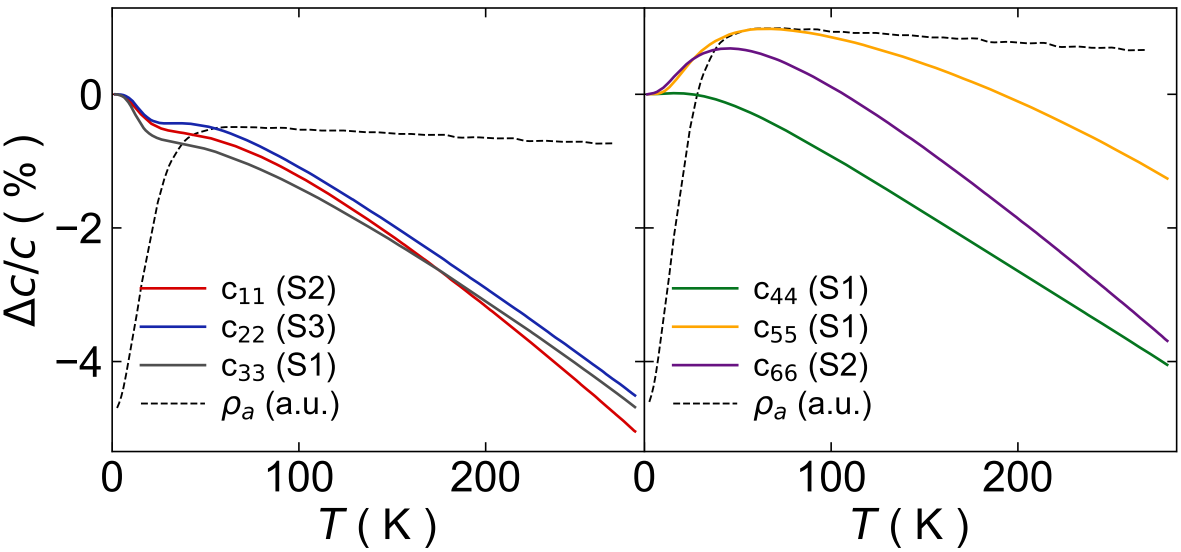

Figure 5.5: **UTe$_2$ high temperature elastic moduli.** Shown are the relative changes of all compressional (i.e. c_{11}, c_{22}, c_{33}; left panel) and shear (i.e. c_{44}, c_{55}, c_{66}; right panel) moduli from about 2 to 280 K. The legend indicates which sample was used for each curve. c_{33}, as well as all shear moduli were also measured on sample S3, but show no quantitative difference to the data shown in the figure. We also show the a-axis resistivity taken from [97]. The softening in the elastic moduli coincides roughly with the Kondo temperature as observed in the resistivity. Figure adapted from [33].

tions, which can be split into parity-even (A_g, B_{1g}, B_{2g}, B_{3g}) and parity-odd (A_u, B_{1u}, B_{2u}, B_{3u}) representations. All irreducible representations in the D_{2h} point group are, however, one-component representations. A possible two-component order parameter, as suggested for example by the observation of time-reversal symmetry breaking by Kerr effect measurements [76, 86], can only be generated by linear combinations of the one-component irreducible representation, i.e. $\varepsilon_{\Gamma_1}\Gamma_1 + \varepsilon_{\Gamma_2}\Gamma_2$, where Γ_i labels an irreducible representation and ε_{Γ_i} is a complex number. In other words, the two components of the two-component order parameter are not required to transform according to the same irreducible representation. Such a scenario is usually disregarded, because the two components of the order parameter are not required to be degenerate by symmetry and are generally expected to condense at different temperatures. In UTe$_2$, however, the existence of two distinct superconducting transitions in some samples is what makes this accidental two-component order parameter a plausible scenario.

Since UTe$_2$ is found to be a spin-triplet superconductor, the superconducting order parameter is required to be odd under inversion, and we are left with the possibilities of A_u, B_{1u}, B_{2u}, B_{3u}, or any two-component order parameter where each component transforms according to one of these parity-odd irreducible transformations. Table 5.2 shows a collection of suggested order parameter representations based on several experiments and theoretical proposals.

Dimensionality	Representation	Shear discontinuity?	Reference (E: experiment; T: theory)
One-Component	A_u	No	E: NMR [80] E: scanning SQUID [106]
	B_{2u}	No	E: Ultrasound (this thesis [33])
	B_{3u}	No	T: DFT [107] E: NMR[78, 79] E: scanning SQUID [106]
		No	E: specific heat [75, 108] E: uniaxial stress [109]
Two-Component	$\{B_{1u}, A_u\}$	c_{66}	E: microwave surface impedance [88] E: specific heat, Kerr effect [76]
	$\{B_{3u}, A_u\}$	c_{44}	E: penetration depth [84] E: NMR [110]
	$\{B_{1u}, B_{2u}\}$	c_{44}	T: ^{3}He A-phase-like pairing [111, 112] E: specific heat [85]
	$\{B_{1u}, B_{3u}\}$	c_{55}	T: phenomenology + DFT [113] T: DFT [114]
	$\{B_{2u}, B_{3u}\}$	c_{66}	T: DFT [115, 116] E: specific heat, Kerr effect [76, 86] T: emergent $D_{4\mathrm{h}}$ symmetry [117]
		Yes	E: STM [87] T: pair-Kondo effect [118] T: MFT of Kondo lattice [119]

Table 5.2: **Proposed order parameters for UTe$_2$.** Proposed order parameter representations for UTe$_2$. They are restricted to odd-parity order parameters, and include representations suggested by experiments or theoretical proposals. The order parameters are grouped by their dimensionality (i.e. one or two-component) and their irreducible representation. We also identify which shear modulus would exhibit a step discontinuity, if any. Some experimental and theoretical work is listed without a particular representation. These studies only address the dimensionality of the order parameter and are compatible with any type of one or two-component representations. In this thesis, we determine the order parameter to be one-component (see subsection 5.3.2). Furthermore, a quantitative analysis of the compressional moduli suggest it might transform according to the B_{2u} representation. Table adapted from [33].

In order to further narrow down the possible representations, it is instructive to visualize their respective gap functions on the Fermi surface of UTe$_2$. The UTe$_2$ Fermi surface is known from quantum oscillation measurements to consist of quasi two-dimensional cylinders [120–122]. We can gain intuitive understanding of this Fermi surface by considering a tight binding model for the crystal structure of UTe$_2$ (see Figure 5.2a for an image of the crystal structure). Uranium dimers along the c axis, which form chains along the a axis, and tellurium (2) chains along the b axis [94] (see Figure 5.2 for an image of the UTe$_2$ crystal structure) have been identified as the important structural motifs [94]. Tellurium (1) atoms have been found to not contribute significantly to the electronic structure. The uranium chains along the a axis lead to flat Fermi sheets along k_y, dominated by uranium $6d$ electrons (see Figure 5.6a). The chains of the tellurium (2) atoms along the b axis, on the other hand, lead to flat Fermi sheets along k_x, with predominantly tellurium (2) $5p$ character. By hybridizing these two sheets, as well as introducing small z axis and inter-chain hopping, we can reproduce the Fermi surface obtained from quantum oscillation measurements and DFT calculations (see Figure 5.6b for an image of the Fermi surface and Appendix G for details on our DFT calculations including an examination of the orbital character of the electronic states close to the Fermi energy). Details on the tight binding model can be found in Appendix H.

We can now examine characteristics of the superconducting gap functions particular to the UTe$_2$ Fermi surface. Functional forms of the gaps corresponding to the odd-parity irreducible representations of the D_{2h} point group (i.e. A_u, B_{1u}, B_{2u}, B_{3u}) in the strong spin-orbit coupling limit have already been discussed in Equations 2.51-2.54. They are plotted on a k_x-k_y slice of the UTe$_2$ Fermi surface (at $k_z = 0$) in Figure 5.7. As expected from the analysis in subsection 2.4.4, the A_u gap is fully gapped. However, we additionally find that on the UTe$_2$ Fermi surface—or generally, on any two-dimensional Fermi surface—the B_{1u} gap is also fully gapped[3]. The B_{2u} gap has point nodes along k_y, which is on tellurium dominated parts of the Fermi surface, whereas the B_{3u} gap has point nodes along k_x, which is on uranium dominated parts of the Fermi surface. Two-component order parameters, i.e. linear combinations of two of these four irreducible representations have nodes slightly off the high symmetry axes. A $\varepsilon_{B_{2u}} B_{2u} + i\varepsilon_{B_{3u}} B_{3u}$ order parameter (with $\varepsilon_{B_{2u}}$ and $\varepsilon_{B_{3u}}$ real numbers), for example, has point nodes close to the k_x-, k_z-, or k_y axis for $\varepsilon_{B_{2u}} \ll \varepsilon_{B_{3u}}$, $\varepsilon_{B_{2u}} \approx \varepsilon_{B_{3u}}$, or $\varepsilon_{B_{2u}} \gg \varepsilon_{B_{3u}}$, respectively. A full list of all possible odd-parity two-component order parameters for the D_{2h} point group and the position of their respective point nodes is given in [84].

Assuming the presence of nodes in the superconducting gap of UTe$_2$, as suggested by the majority of existing literature—performed on a wide range of samples, including

---

[3] There is one recent quantum oscillation study suggesting the presence of a small three-dimensional spherical Fermi surface at the Γ-point [123], which would lead to point nodes in the B_{1u} gap along k_z. However, oscillations at the frequencies corresponding to this Fermi surface have been interpreted as quantum interference orbits by [121]. Additionally, the mass observed for this potential pocket is almost a factor of ten smaller than for the quasi two-dimensional Fermi surfaces. It is therefore unlikely to contribute significantly to the thermodynamic behavior of UTe$_2$. For example, the quasi two-dimensional Fermi surfaces have been shown to fully account for the measured specific heat [120].

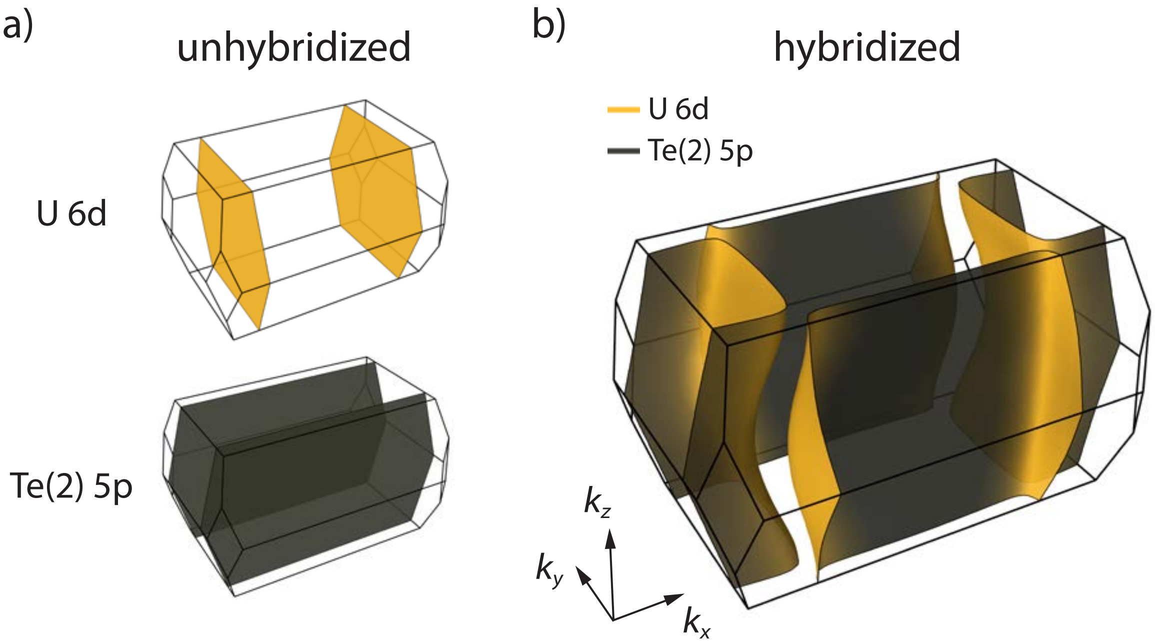

Figure 5.6: **UTe_2 Fermi surface.** Panel a) shows the Fermi sheets obtained from a tight binding model if only the uranium chains along the a axis (top panel) or the tellurium (2) chains along the b axis are considered. A Fermi surface which reproduces DFT calculations (see Appendix G) and quantum oscillation measurements [120] can be obtained by hybridizing these two sheets, as well as including hopping between chains in the plane and along the z axis. The resulting Fermi surface is shown in panel b). It is colored according to its original U $6d$ (yellow) and Te(2) $5p$ (gray) content. Figure adapted from [33].

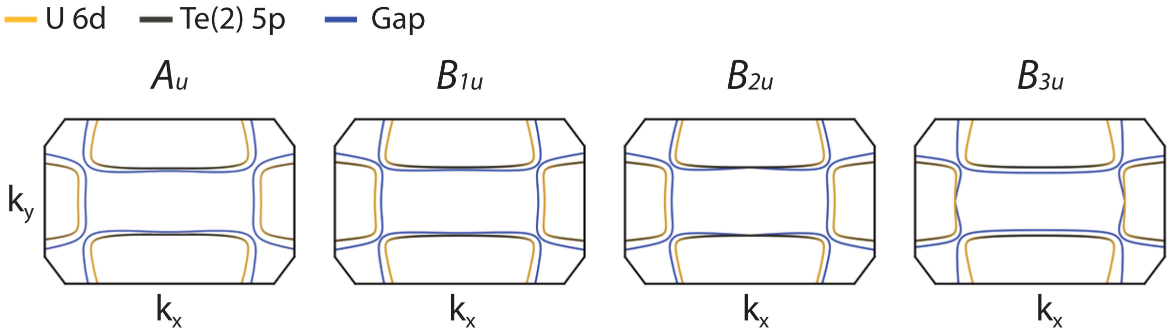

Figure 5.7: **UTe_2 single component gaps.** Shown are the gap magnitudes (blue) corresponding to the four odd-parity irreducible representations of the D_{2h} point group on the UTe_2 Fermi surface. The Fermi surface is plotted in the $k_x - k_y$ plane at $k_z = 0$. The colors represent a projection on the original U $6d$ (yellow)/Te(2) $5p$ (gray) bands. The distance between the Fermi surface and the blue line is proportional to the magnitude of the gap. Functional forms of the gap amplitudes in momentum space are given in Equations 2.51-2.54. Here, we have used $\alpha = \beta = \gamma$. Different values will change the detailed shape of the gaps, but not their nodal structure. Figure adapted from [33].

samples with T_c's above 2 K and samples grown with the CVT and MSF methods—we can rule out the single-component A_u and B_{1u} order parameters, since they are both fully gapped on the Fermi surface of UTe$_2$. The remaining one-component order parameters (i.e. B_{2u} and B_{3u}) both exhibit point nodes. Similarly, all two-component order parameters can in general have point nodes on the UTe$_2$ Fermi surface, depending on the relative size of the two components [84]. In the next two sections, we present our pulse-echo ultrasound data. We show that the shear moduli strongly imply that the superconducting order parameter in UTe$_2$ is one-component (subsection 5.3.2). The compressional moduli further suggest that the order parameter transforms as the B_{2u} irreducible representation (subsection 5.3.3).

5.3.2 One-Component Order Parameter from Shear Elastic Moduli

Figure 5.8 shows the relative changes in the compressional elastic modulus c_{33} and all shear moduli (i.e. c_{44}, c_{55}, c_{66}) in single-transition samples of UTe$_2$ across the superconducting phase transition. The data was measured with the pulse-echo ultrasound technique (see section 3.2) on two single-T_c samples: S1 with a transition temperature of about 1.63 K and S2 with $T_c \approx 1.70$ K. Details on the sample dimensions, as well as the transducer configurations, pulse-echo frequencies, and absolute elastic moduli are discussed in Appendix I. c_{33} exhibits a roughly 85 mK wide step discontinuity at T_c of about 40 parts per million. Such a jump in elastic modulus is allowed for all compressional moduli at any second order phase transition (see subsection 2.3.3 and subsection 2.4.5). c_{55}, on the other hand, exhibits an upward change in slope at T_c, and c_{66} a downward change in slope. c_{44} shows no discernible feature at T_c at all, which is notable since c_{44} is also the only elastic modulus which seems to be unaffected by Kondo physics in the normal state (see Figure 5.5). Most importantly, however, none of the shear moduli show a step discontinuity at T_c to within our resolution, which is a few parts in 10^7 (see section 3.2 for details). Based on this observation, combined with our discussion in subsection 2.4.5, we conclude that the superconducting order parameter in single-T_c samples of UTe$_2$ has only one component.

In Figure 5.9, we show the relative changes of c_{33} and all shear moduli in one double-T_c sample (sample S3). The data of the single-T_c samples from Figure 5.8 are repeated for comparison. c_{33} shows two distinct step discontinuities separated by about 40 mK. These jumps are consistent with two transitions in the specific heat measured on the same sample (see Figure 5.10). Similar to the single-T_c samples, none of the shear moduli in the two-T_c sample show a step discontinuity within our resolution. We thus conclude that even in double-transition samples of UTe$_2$, the superconducting order parameter is of the single-component type.

Figure 5.9 further shows a strong quantitative resemblance between the relative changes in elastic moduli between single- and double-T_c samples. We observe the same

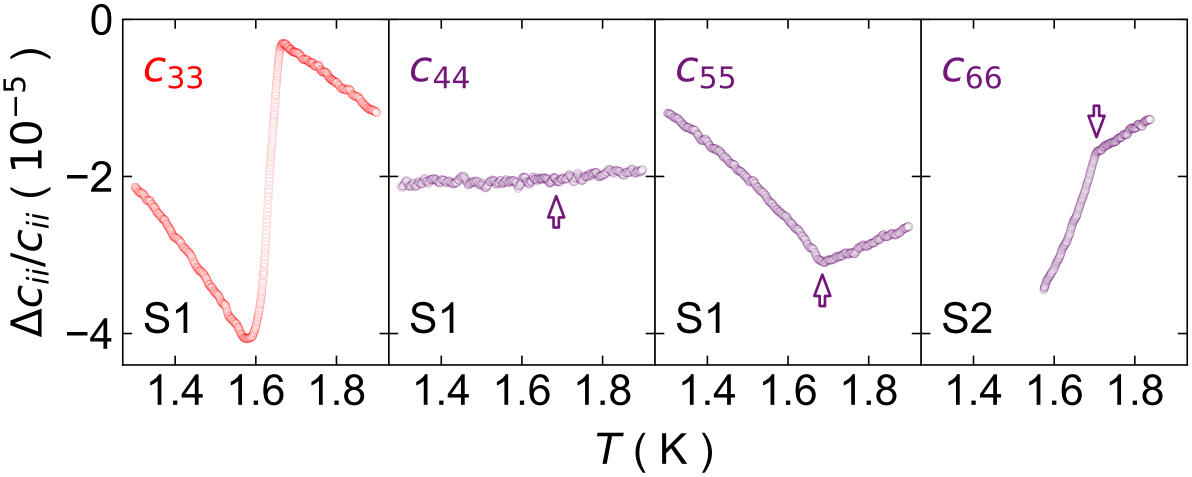

Figure 5.8: **UTe_2 single T_c shear moduli.** Relative changes of the compressional modulus c_{33} and all shear moduli (c_{44}, c_{55}, c_{66}) in single-T_c samples across the superconducting phase transition. The arrows mark the transition temperatures. c_{33} shows a step discontinuity at T_c, whereas all shear moduli only show changes in slopes implying the single-component nature of the superconducting order parameter in UTe_2. Figure adapted from [33].

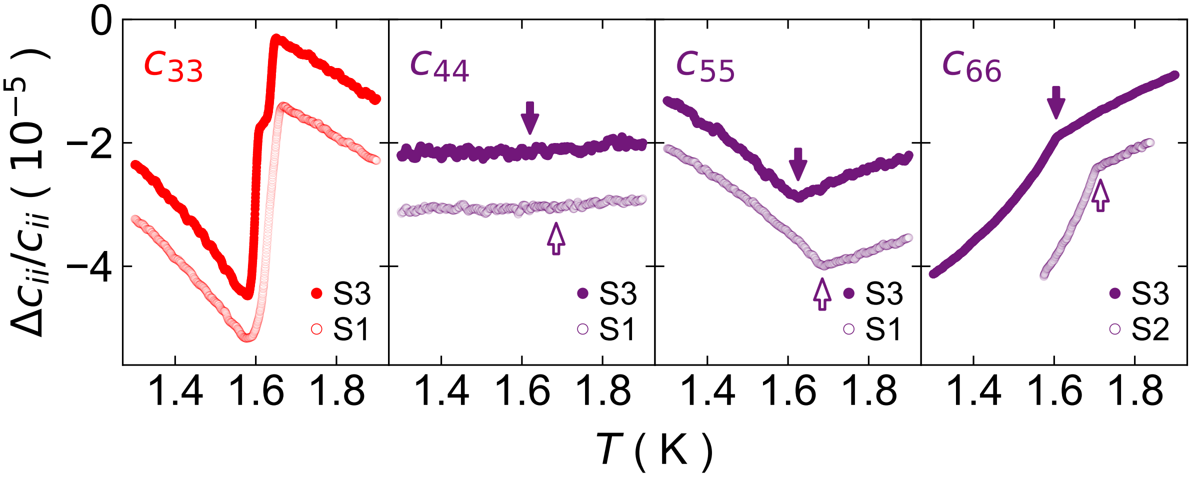

Figure 5.9: **UTe_2 double T_c shear moduli.** Relative changes of the compressional modulus c_{33} and all shear moduli (c_{44}, c_{55}, c_{66}) in double-T_c samples (filled symbols) across the superconducting phase transition. Elastic moduli for the single-T_c samples from Figure 5.8 are repeated here with empty symbols. c_{33} for the double-T_c sample shows two step discontinuities, consistent with two transitions measured in the specific heat. The shear moduli are quantitatively similar to those for the single-T_c samples. Filled (empty) arrows mark the transition temperatures for double-T_c (single-T_c) samples and the curves have been offset for clarity. Figure adapted from [33].

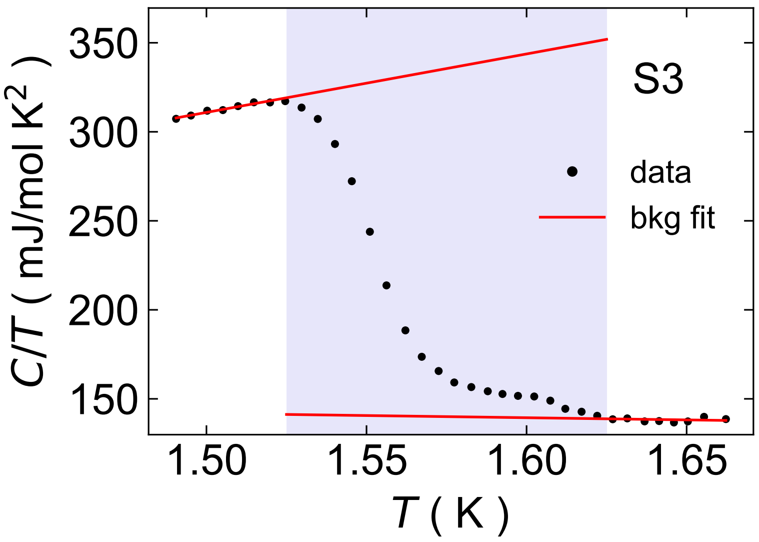

Figure 5.10: **UTe$_2$ double T_c specific heat.** Specific heat of the double-transition sample S3. Two superconducting transitions are observed with a similar double peak as measured in other two-T_c samples [76]. By fitting straight lines to the data below and above the transitions (see red lines), we extract the total specific heat jump to be (196 ± 18) mJ/(mol K^2). The uncertainty is due to the finite temperature range close to the transitions, in which the fits deviate significantly from the data. Specific heat measurements were performed in a ^{3}He cryostat, using the quasi-adiabatic method. Figure adapted from [33].

changes in slopes for all shear moduli between the two sample types. Additionally, the sum of the two step discontinuities in the two-T_c sample amount to roughly the same size as the discontinuity in the single-T_c samples. These quantitative similarities imply that both the single- and double-T_c samples are in the same thermodynamic ground state once they have gone through their successive phase transitions.

To summarize, the lack of a step discontinuity in any shear modulus and the similarity between single- and double-T_c samples lead us to conclude that both sample types exhibit the same single-component superconductivity. This observation rules out all proposed two-component scenarios and leaves only the A_u, B_{1u}, B_{2u}, and B_{3u} irreducible representations as possible superconducting order parameters in UTe$_2$. Based on our discussion in the previous section (subsection 5.3.1), these options are further reduced to only the B_{2u} and B_{3u} order parameters if we assume the presence of nodes in the gap function of UTe$_2$. In the following section (subsection 5.3.3), we will argue that the behavior of all compressional moduli through the superconducting transition favor the B_{2u} over the B_{3u} order parameter.

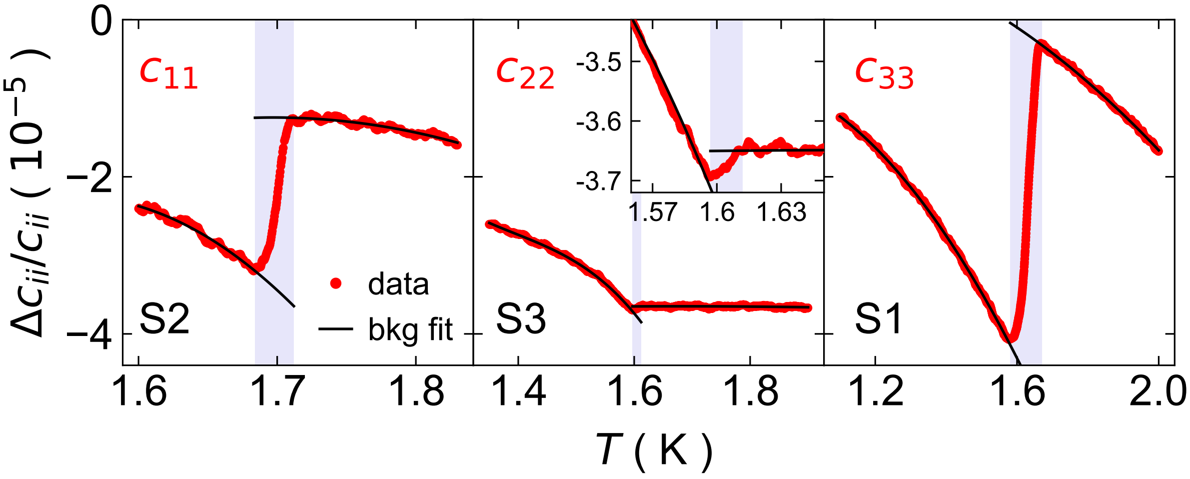

Figure 5.11: **UTe$_2$ compressional moduli.** Relative changes of all compressional moduli (c_{11}, c_{22}, c_{33}) across the superconducting phase transition. c_{33} is reproduced from the single-T_c sample in Figure 5.9. All compressional moduli jump at T_c, as expected by group theoretical arguments. A zoomed in view of c_{22} close to T_c is shown in the inset of the middle panel. Background polynomials (black lines) are fitted to all data below and above the phase transition. The sizes of the elastic moduli jumps (and their uncertainties) are extracted as the differences between these background fits over a temperature range close to T_c (blue shaded region) in which the data significantly deviates from the fits. Figure adapted from [33].

5.3.3 B_{2u} Order Parameter from Compressional Elastic Moduli

In Figure 5.11, we show the relative changes of all compressional moduli (c_{11}, c_{22}, c_{33}) in UTe$_2$. c_{33} is the same as for the single-transition sample in Figure 5.9. All compressional moduli show a jump at T_c, as expected to for any second order phase transition. The sizes of these jumps, however, vary significantly for the different moduli: it is smallest for c_{22} and largest for c_{33}. We quantify the sizes of these discontinuities by fitting second order polynomials[4] to the data above and below T_c (see black lines in Figure 5.11) and taking the difference of the fits in a small region close to the transition. This region is chosen as the temperature range in which the fits significantly deviate from the data. The resulting jump sizes are shown in Table 5.3 and we find that the discontinuity in $\Delta c/c$ for c_{22} is more than a factor of fifteen smaller than in c_{11}, which in turn is only half that of c_{33}.

As discussed in Equation 2.18, the jump δc in elastic modulus at T_c is directly proportional to the jump in the heat capacity ΔC via an Ehrenfest relation, if the corresponding strain couples linearly to the square of the order parameter (see subsection 2.3.3). This

---

[4] Only for the fit for c_{22} below T_c did we use a third-order polynomial.

Elastic Modulus	Step in $\frac{\Delta c}{c}$	$\frac{dT_c}{d\epsilon_{ii}}$ $\left(\frac{\mathrm{K}}{\%\,\mathrm{strain}}\right)$	$\frac{dT_c}{d\sigma_{ii}}$ $\left(\frac{\mathrm{K}}{\mathrm{GPa}}\right)$	$\frac{dT_c}{d\sigma_{ii}}$ $\left(\frac{\mathrm{K}}{\mathrm{GPa}}\right)$
c_{11} $(1T_c)$	$-(2.2 \pm 0.2) \times 10^{-5}$	-0.23 ± 0.02	-0.50 ± 0.03	-0.87
c_{22} $(2T_c)$	$-(0.13 \pm 0.07) \times 10^{-5}$	-0.07 ± 0.02	-0.09 ± 0.02	—
c_{33} $(1T_c)$	$-(4.4 \pm 0.3) \times 10^{-5}$	0.34 ± 0.02	0.60 ± 0.03	0.56

Table 5.3: **Ehrenfest analysis.** We show the magnitudes of the jumps in $\Delta c/c$ of all compressional moduli extracted from Figure 5.11. Together with the elastic tensor from Table 5.1 and the jump in the specific heat from Figure 5.10, we calculate the derivatives of the critical temperature with respect to ϵ_{xx}, ϵ_{yy}, and ϵ_{zz} strain via Ehrenfest relations. We use the same elastic tensor to convert these values to derivatives of the critical temperature with respect to stress $dT_c/d\sigma_{ii}$. In the last column, we compare our values of $dT_c/d\sigma_{ii}$ to those from uniaxial stress experiments [109]. Table adapted from [33].

is always the case for compressional moduli and in the case of UTe$_2$, Equation 2.18 reads

$$\delta c_{ii} = -\frac{\Delta C}{T}\left(\frac{dT_c}{d\epsilon_{ii}}\right)^2, \tag{5.1}$$

where $c_{ii} = c_{11}, c_{22}, c_{33}$. The proportionality constant is the square of the derivative of the critical temperature with respect to strain $dT_c/d\epsilon_{ii}$. The strains corresponding to c_{11}, c_{22}, and c_{33} are ϵ_{xx}, ϵ_{yy}, and ϵ_{zz}, respectively. Using the values of the relative jumps in the compressional moduli (see Figure 5.11), the absolute values of the elastic moduli obtained from RUS measurements[5] (see Table 5.1), and the size of the jump in the heat capacity divided by temperature (see Figure 5.10), we extract the absolute values of $dT_c/d\epsilon$ (see Table 5.3). We further use the values of the elastic tensor in Table 5.1 to calculate the derivatives of the critical temperature with respect to stress from the derivatives with respect to strain via

$$\begin{pmatrix} dT_c/d\sigma_{xx} \\ dT_c/d\sigma_{yy} \\ dT_c/d\sigma_{zz} \end{pmatrix} = \begin{pmatrix} c11 & c12 & c13 \\ c12 & c22 & c23 \\ c13 & c23 & c33 \end{pmatrix}^{-1} \begin{pmatrix} dT_c/d\epsilon_{xx} \\ dT_c/d\epsilon_{yy} \\ dT_c/d\epsilon_{zz} \end{pmatrix}. \tag{5.2}$$

The resulting values are given in Table 5.3. We also report the values measured in uniaxial stress experiments [109] and find rough agreement between the two measurements. It is important to note that for the correct calculation of $dT_c/d\sigma$ in Equation 5.2, we need to know the sign of $dT_c/d\epsilon$. Since our measurement only give the absolute values, however, we used the signs measured in [109].

From the values in Table 5.3 we see that the derivative of the critical temperature with respect to ϵ_{yy} is significantly smaller than for compressional strains along xx or zz, i.e.

$$\left|\frac{dT_c}{d\epsilon_{yy}}\right| \ll \left|\frac{dT_c}{d\epsilon_{xx}}\right| \lesssim \left|\frac{dT_c}{d\epsilon_{zz}}\right|. \tag{5.3}$$

---

[5] We used the elastic moduli from fits to the spectrum of sample A at 4 K, since the pulse-echo ultrasound sample S3 is the same sample as RUS sample A, except that it has been polished further as preparation for the pulse-echo ultrasound measurements.

In other words, we find that superconductivity is insensitive to strains along the b axis, but sensitive to strains along the a and c axes. This observation is quite surprising at first, considering that the Fermi surface of UTe_2 is quasi two-dimensional [120] (see Figure 5.6) with cylindrical Fermi surfaces along k_z. If anything, we would expect strains along the c axis to stand out one way or another. A different perspective, however, is provided by the crystal structure of UTe_2 (see Figure 5.2), where we have already discussed that the important structural motifs are uranium dimers along the c axis, forming chains along the a axis, and tellurium (2) chains along the b axis. The insensitivity of T_c to b-axis strain therefore suggests that superconducting pairing is insensitive to Te(2)-Te(2) distances along the tellurium chains. Superconductivity seems to be very sensitive, on the other hand, to U-U distances within the uranium dimers and chains. This observation implies that the superconducting gap is smaller on tellurium-dominated parts of the Fermi surface than on uranium-dominated parts.

Based on the discussion in the previous sections, the only remaining options for the superconducting order-parameter representations in UTe_2 are B_{2u} and B_{3u}. The B_{2u} order parameter has nodes along k_y which is on tellurium-dominated parts of the Fermi surface, and the B_{3u} order parameter has nodes along k_x which is on uranium-dominated parts of the Fermi surface. Since our analysis above indicates the superconducting gap to be smaller on tellurium compared to uranium-dominated parts of the Fermi surface, we conclude that the jumps in our compressional moduli are most consistent with a B_{2u} superconducting order parameter in UTe_2.

5.4 Open Questions

In addition to the pulse-echo ultrasound measurements presented above, we also performed RUS and high-energy X-ray diffraction microscopy (HEDM) measurements on two-transition samples of UTe_2. While these measurements are not yet fully conclusive, they still provide important insight into the superconducting and structural properties of UTe_2, and are presented below.

5.4.1 Resonant Ultrasound Spectroscopy

Here we show temperature dependent RUS data taken on UTe_2 sample A (see Figure 5.2 for a 3D model of the sample and Table 5.1 for RUS fit results at 300 and 4 K). Importantly, UTe_2 sample A from these RUS measurements is the same as sample S3 in our pulse-echo measurements, with the only difference that after the RUS measurements, two flat, parallel faces were polished on the sample in preparation for our pulse-echo ultrasound measurements.

In the left panel of Figure 5.12 we show the relative changes of selected resonance frequencies through the superconducting phase transitions from about 1 to almost 5 MHz.

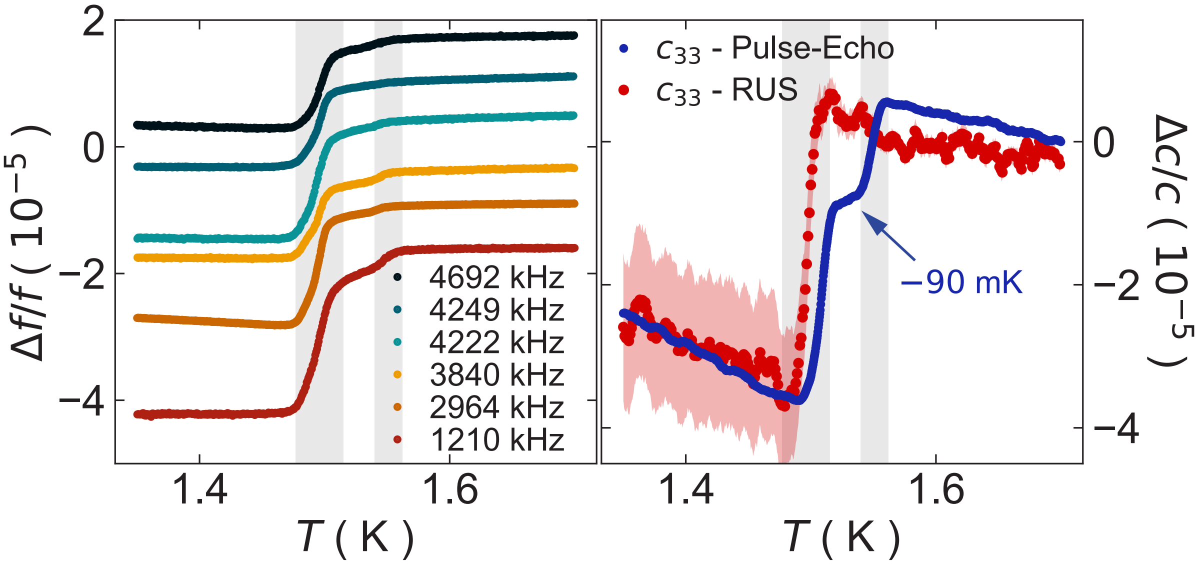

Figure 5.12: **RUS selected resonances and c_{33}.** Relative changes of selected resonance frequencies through the superconducting transitions of RUS sample A (left panel). Two jumps, each indicating a superconducting transition, can be observed, which are marked with gray vertical bars. The right panel shows the relative changes of c_{33}. In red is c_{33} as obtained from our RUS measurements. Blue is our pulse-echo data on sample S3, reproduced from Figure 5.9. Both RUS and pulse-echo ultrasound measurements were performed on the same sample, which has only been additionally polished between the two measurements. Note that the blue data is shifted to the left by 90 mK. We attribute this shift in temperature between the two samples to slightly differently calibrated thermometers. Uncertainties in our RUS elastic moduli are due to a 1° misalignment between the sample mesh and crystal axes.

All resonances are almost temperature independent immediately above T_c, followed by two successive jumps at $T_{c,1} \approx 1.55$ K and $T_{c,2} \approx 1.50$ K (marked by the gray vertical bars in Figure 5.12). These jumps mark the two superconducting transitions in this sample. After going through both successive transitions, the temperature dependence of the resonances becomes mostly flat again. Interestingly, the jump at $T_{c,1}$ is only a small fraction of the jump at $T_{c,2}$ for all measured resonances.

We measured the temperature dependence of 110 resonance frequencies (they are displayed in bold font in Table F.2), which we use to obtain the temperature dependence of the full elastic tensor. The relative change of c_{33} from our RUS measurements is shown in the right panel of Figure 5.12. The uncertainty indicated by the shaded region about the data points is calculated based on a 1° misalignment between the sample mesh and crystal axes. An uncertainty of the temperature dependence of $\Delta c/c$ based on the statistical uncertainties in our fit—as done for example in Figure 5.3—is orders of magnitude smaller. The right panel of Figure 5.12 also displays two vertical gray bars indicating the temperatures $T_{c,1}$ and $T_{c,2}$ at which the resonance frequencies in the left panel of Figure 5.3 jump.

The small jumps we observe at $T_{c,1}$ in the raw resonances disappear in the noise of c_{33} after the decomposition. c_{33} does, however, jump at $T_{c,2}$ by about 40 parts per million. We also reproduce c_{33} from our pulse-echo measurements (note that it is shifted by 90 mK to the left in Figure 5.3b). Comparing both c_{33} curves from RUS and pulse-echo ultrasound measurements we make two observations: the total size of both discontinuities are the same between the two data. Our pulse-echo ultrasound data, however, exhibit two clearly separated jumps, with the first one about half as large as the second one, whereas our RUS data only exhibits one jump at $T_{c,2}$ with the first one at $T_{c,1}$ being smaller than the noise in our data. These drastically different ratios of first to second jump is surprising, considering that both measurements were performed on the same sample.

While not fully conclusive, we speculate that this observation indicates that the two superconducting transitions in UTe_2 are due to sample inhomogeneity, i.e. part of the sample becoming superconducting at $T_{c,1}$ and the other part at $T_{c,2}$. If that is the case, the ratios of the two jumps in the elastic moduli are determined by the ratio of the two volume fractions of the probed part of the sample which become superconducting at different temperatures. Since RUS probes the entire sample, whereas pulse-echo ultrasound only probes a small cross-sectional area roughly the size of the transducer (i.e. a circle with about 100 μm diameter), it is possible that the relative volume fractions with $T_{c,1}$ and $T_{c,2}$ are different for the different techniques resulting in different ratios of first to second jump in the elastic moduli.

In Figure 5.13, we extend the comparison between RUS and pulse-echo ultrasound to all compressional moduli (i.e. c_{11}, c_{22}, c_{33}). We again indicate the two superconducting transitions with gray vertical bars at the temperatures at which the raw resonances jump (see Figure 5.12a). Pulse-echo ultrasound data are reproduced from Figure 5.9 and Figure 5.11 and have been measured on multiple samples with various T_c's. We find rough quantitative agreement between the two techniques. Similar to c_{33} as discussed above, none of the other compressional moduli show a jump at $T_{c,1}$. c_{11} shows a jump at $T_{c,2}$ which is of similar size as the jump from pulse echo measurements. c_{22} only shows a change in slope, just as in the pulse-echo data. The only difference we find between RUS and pulse-echo is a slight difference in the overall slope in the respective c_{22} data.

The relative changes in shear moduli (i.e. c_{44}, c_{55}, c_{66}) through the superconducting transitions are shown in Figure 5.14 (RUS/pulse-echo data in the left/right panel; pulse-ehco data is reproduced from Figure 5.9). c_{55} shows an upward change in slope at $T_{c,2}$, similar to the pulse-echo data. c_{66} shows kinks at both $T_{c,1}$ and $T_{c,2}$, in contrast to only one change in slope seen in pulse-echo measurements. However, besides the temperature range close to the superconducting transitions, there is qualitative consistency between RUS and pulse-echo. For c_{44}, however, we find qualitative deviations between the two techniques. Our RUS decomposition results in a small jump in c_{44} at $T_{c,2}$ in contrast to the absence of any feature in the pulse-echo data.

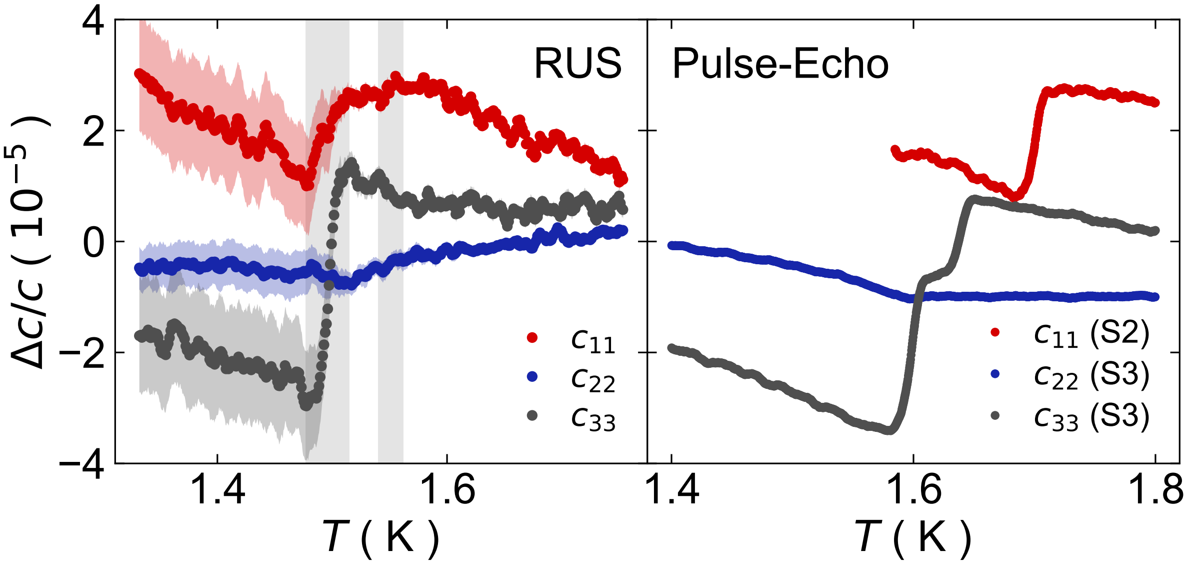

Figure 5.13: **RUS compressional moduli.** Relative changes of the compressional moduli (c_{11}, c_{22}, c_{33}) through the superconducting phase transitions. Shown are the elastic moduli obtained from our RUS measurements (left panel) and those obtained from our pulse-echo measurements (right panel; elastic moduli are reproduced from Figure 5.9). We find good agreement between the two techniques. The superconducting transitions in the left panel are marked with gray vertical bars. Uncertainties in our RUS elastic moduli are due to a 1° misalignment between the sample mesh and crystal axes.

The relative changes of the off-diagonal terms of the elastic tensor (i.e. c_{12}, c_{13}, c_{23}) are shown in the left panel of Figure 5.15. These elastic moduli were inaccessible with the available samples for our pulse-echo measurements, highlighting one of the advantages of the RUS technique, which gives the full elastic tensor on a single sample. c_{12} and c_{13} show large (≈ 7 and 10×10^{-5}) upward jumps at $T_{c,2}$. Similar to the compressional elastic moduli, no jumps are observed at $T_{c,1}$. c_{23}, on the other hand, stays mostly flat through both superconducting phase transitions.

Knowledge of the full elastic tensor as provided by RUS measurements allows us to calculate the bulk modulus B for UTe$_2$, which is given by

$$B = \frac{c_{13}^2 c_{22} - 2c_{12}c_{13}c_{23} + c_{12}^2 c_{33} + c_{11}(c_{23}^2 - c_{22}c_{33})}{c_{12}^2 + c_{13}^2 - c_{11}c_{22} + 2c_{13}(c_{22} - c_{23}) + 2c_{11}c_{23} + c_{23}^2 - 2c_{12}(c_{13} + c_{23} - c_{33}) - (c_{11} + c_{22})c_{33}}, \tag{5.4}$$

and shown in the right panel of Figure 5.15. No significant jump at either of the superconducting transition temperatures can be observed. Similar to the Ehrenfest relations relating the jump in compressional elastic moduli to the jump in the heat capacity through the derivative of the critical temperature with respect to strain (see Equation 5.1), a jump at T_c in the bulk modulus can be related to the jump in the heat capacity through the

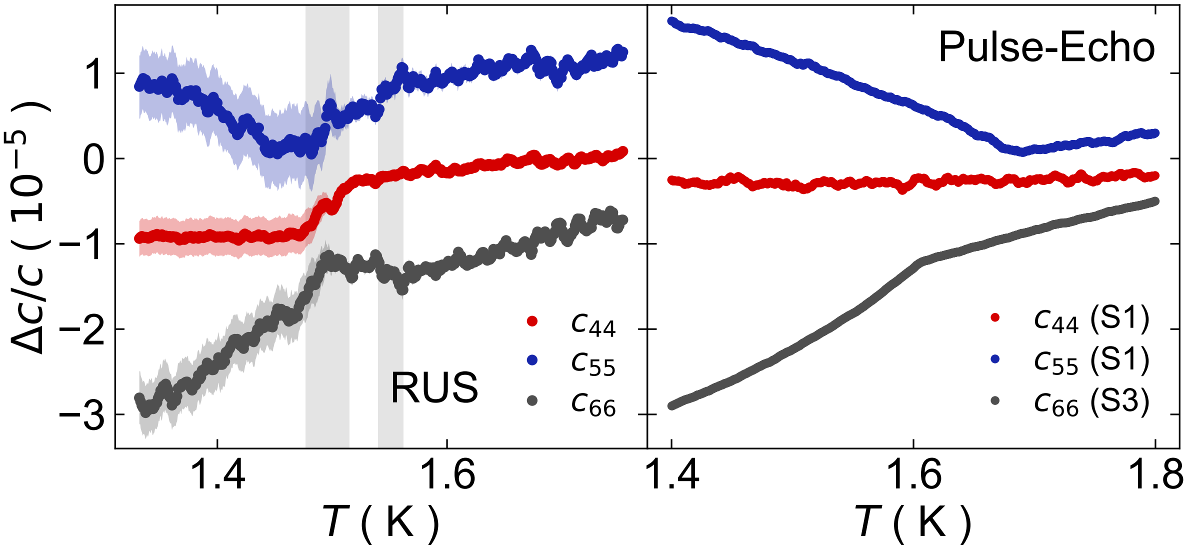

Figure 5.14: **RUS shear moduli.** Relative changes of the shear moduli (c_{44}, c_{55}, c_{66}) through the superconducting phase transitions. Shown are the elastic moduli obtained from our RUS measurements (left panel) and those obtained from our pulse-echo measurements (right panel; elastic moduli are reproduced from Figure 5.9). Rough agreement between the two techniques can be observed away from T_c. Close to the phase transitions, however, the RUS decomposition is quite noisy and inconsistent with pulse-echo ultrasound. The superconducting transitions in the left panel are marked with gray vertical bars. Uncertainties in our RUS elastic moduli are due to a 1° misalignment between the sample mesh and crystal axes.

derivative of the critical temperature with respect to hydrostatic pressure dT_c/dp. Importantly, the Ehrenfest relations consider the derivatives of the critical temperature at zero applied stress/pressure. The absence of a jump in the bulk modulus in UTe_2 implies that $dT_c/dp|_{p=0} = 0$.

Many phase diagrams of UTe_2 as a function of hydrostatic pressure exist, but they do not all agree on the same slope of the critical temperature at zero pressure. Some suggest a large slope of over 0.8 K/GPa for the superconducting transition existing at ambient pressure [69, 70], which is in contrast to our data. Other phase diagrams, however, suggest that the superconducting phase boundary flattens below the critical pressure at which the second transition emerges [108, 124]. The data in [108], for example, is consistent with $|dT_c/dp| \leq 0.2$ K/GPa close to ambient pressure. Since the bulk modulus is related to symmetry conserving strains, there is no symmetry based reason dT_c/dp is expected to change towards zero pressure. It is possible, however, that competition with the second superconducting phase emerging at low pressures of about 0.4 GPa can cause the phase boundary to change slope close to ambient pressure. More experiments, including more ultrasound measurements, will be necessary to confirm this conclusion, though.

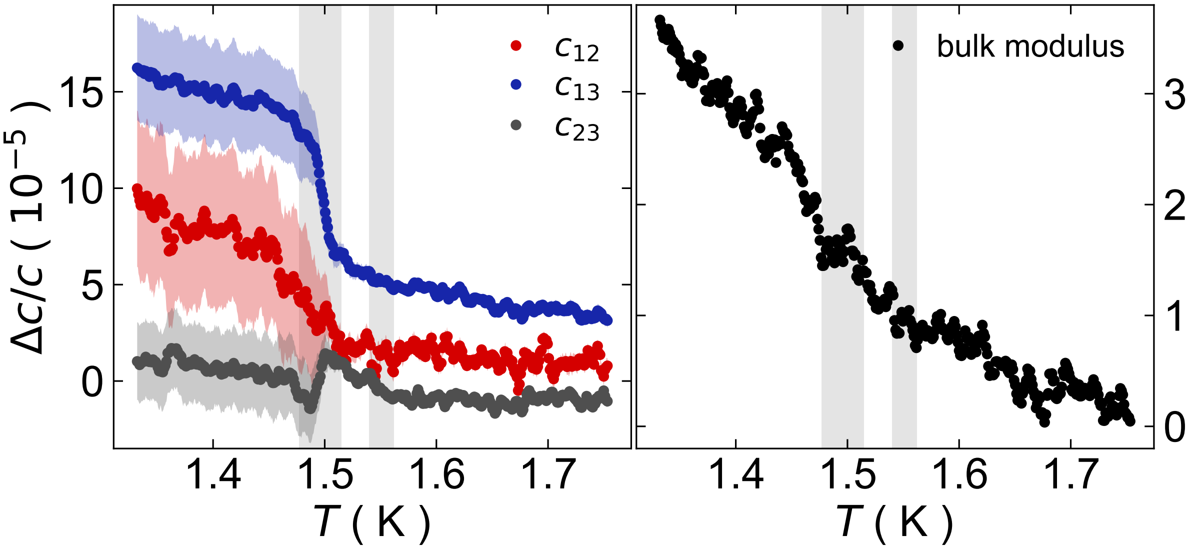

Figure 5.15: **RUS off-diagonal elastic tensor and bulk modulus.** Relative changes of the off-diagonal elements of the elastic tensor (c_{12}, c_{13}, c_{23}) through the superconducting phase transitions (left panel). These elastic moduli, which were inaccessible with pulse-echo ultrasound, show large upward jumps at T_c. The relative change of the bulk modulus, calculated from c_{11}, c_{22}, c_{33}, c_{12}, c_{13}, and c_{23}, is shown in the right panel. No jump is observed at the phase transitions indicating a vanishing derivative of the critical temperature with respect to hydrostatic pressure. The superconducting transitions are marked with gray vertical bars. Uncertainties in our RUS elastic moduli are due to a 1° misalignment between the sample mesh and crystal axes.

In summary, we compare the relative changes in elastic moduli as obtained from RUS and pulse-echo ultrasound measurements. The RUS data is mostly consistent with pulse-echo data, showing quantitative agreement between the jump sizes of the compressional moduli at the superconducting transitions. However, the results for the shear moduli, in particular c_{44}, are be slightly off. A possible explanation is that while our fit results shown in Table 5.1 are accurate enough to within a percent, they may lack precision on a 10^{-5} accuracy level required to investigate superconducting phase transitions. A reason for a slightly inaccurate fit could be the low crystal symmetry of UTe_2, leading to nine independent elastic moduli, which makes fitting them harder. Also possible, however, is that our sample is inhomogenous, containing for example impurity phases with different elastic moduli. In this case, the model in our RUS fits, which assumes a perfect single crystal, does not give us the right answer. This possibility of sample inhomogeneity is supported by the observation that the ratio of first to second jump is much smaller in our RUS measurements than in pulse-echo measurements, even if performed on the same sample.

5.4.2 High Energy X-Ray Diffraction Microscopy

Sample inhomogeneity, as indicated by our RUS measurements above, is indeed one of the proposed reasons for the existence of two superconducting transitions in some samples of UTe_2 [108]. Here, we investigate this possibility further, by performing high-energy X-ray diffraction microscopy (HEDM) measurements on a two-transition sample of UTe_2. A model of the sample is shown in Figure 5.16 (note that this sample is different from any of the previously measured samples). The existence of two superconducting transitions in this particular sample were confirmed by measuring selected mechanical resonance frequencies through both transitions (see Figure 5.16a).

HEDM measurements were performed at the Cornell High Energy Synchrotron Source (CHESS). A 90 keV monochromatic X-ray beam was shined on the sample and the resulting diffraction peaks were recorded with an area detector. An exemplary diffraction pattern is shown in Figure 5.16b. The sample was then rotated by 360° in steps of 0.25°, resulting in 1440 diffraction images. Using these diffraction images and the known crystal structure of UTe_2, we can fit the crystal orientation of the sample. The high resolution of the detectors allows us to additionally extract distributions of different orientations within the measured volume of the sample, along with their relative volume fractions. The orientation is measured relative to the lab coordinate frame, where the z axis is defined to be parallel to the beam direction, the x axis is perpendicular to the z direction in the horizontal plane, and the y axis is perpendicular to the z direction in the vertical plane (see Figure 5.16b). The different orientation distributions are then given in Euler angles, which are defined such that ψ is the rotation angle about the z axis, θ is the rotation angle about the new y axis, and finally ϕ is the rotation angle about the new x axis.

The distributions of orientations within the entire sample are shown in a 3D plot in Figure 5.17b. The figure also shows projections onto the planes corresponding to two Euler angles each. The colors used for these projections indicate the volume fraction occupied by a given orientation, with the maximum being purple and the minimum yellow. The color of the three-dimensional part of the plot has no specific meaning, but its transparency is again related to the volume fraction. The figure shows that among all different crystal orientations in the sample, three major orientations can be distinguished, all separated by a rotation of more than 2°. The three different sets of orientations are most easily identified in the $\phi - \theta$ projection, where they are roughly located at $12°-(-35°)$, $12°-(-38°)$, and $14°-(-40°)$.

In addition to the distribution of orientations in the entire sample, our measurements allow for a small degree of spatial resolution: the height of the X-ray beam (i.e. its dimension along the y axis as indicated in Figure 5.16b) was about one thirteenth of the dimension of our sample in the same direction. In order to scan the full sample volume, we therefore repeated our measurement thirteen times, each time probing a different slice of the sample (see Figure 5.17a for an illustration of the different slices). We can therefore investigate the distribution of orientations for these thirteen slices individually. Figure 5.18 shows examples of slices 1 and 6, i.e. at the narrow tip at the bottom and near

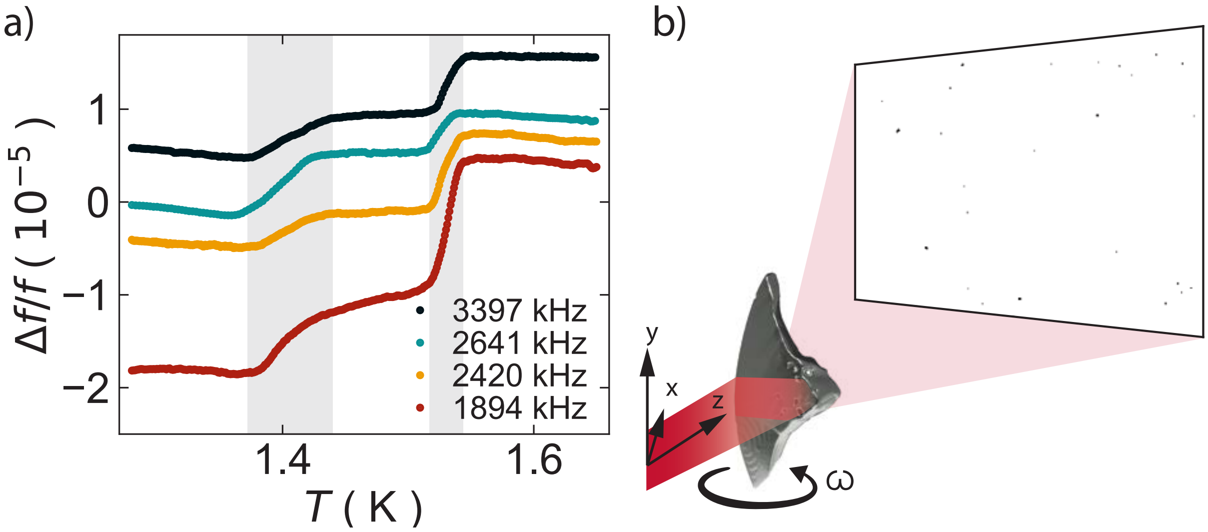

Figure 5.16: **RUS resonances and HEDM sketch.** a) The relative changes of selected RUS resonance frequencies show two superconducting transitions around 1.53 and 1.40 K. b) Sketch of a HEDM measurement. An X-ray beam is shined on the sample and the resulting diffraction pattern is recorded with an area detector. Conventionally, the lab coordinate frame is chosen relative to the X-ray beam. The sample used in this sketch is a 3D model of the measured sample.

the widest part of the sample. We can see that while the distribution of Euler angles in slice 1 is centered around one orientation, slice 6 exhibits two distinct set of orientations, separated by about 2° along θ.

The distributions of Euler angles for all thirteen slices are discussed in Appendix J. Figure J.1, Figure J.2, and Figure J.3 show projections onto the $\phi - \theta$, $\phi - \psi$, and $\theta - \psi$ planes, respectively. Particularly from Figure J.1, we see that the three distinct sets of orientations we observe in Figure 5.17b are separated in space along the y direction. Slices 1-9, 10-11, and 12-13 each make up a different of the three major sets of Euler angles.

While this observation does not directly explain the existence of two superconducting phase transitions, it is a curious feature. Such a distinct spatial separation of different orientations is for example hard to explain with random strains or other sources of random inhomogeneity in the sample. If it is a common feature among all double-transition samples (including the one used for our RUS measurements), it is a likely reason why the decomposition of our RUS elastic moduli above (see subsection 5.4.1) was unable to reproduce our results from pulse-echo ultrasound measurements.

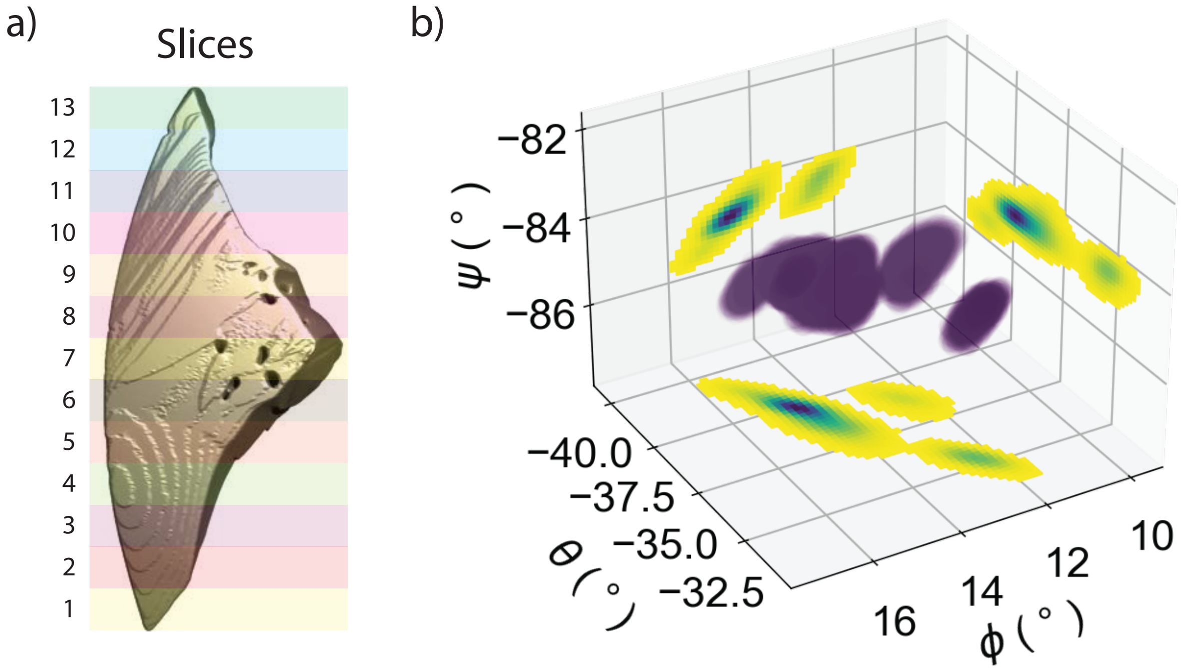

Figure 5.17: **Distribution of orientations.** a) 3D model of the sample divided into 13 slices. Each slice corresponds to a different volume of the sample which was probed in a separate experiment. b) Distributions of crystal orientations within the entire volume of the sample. The colors of the projections indicate the relative volume fraction occupied by a given orientation (purple is maximum and yellow is minimum).

5.5 Conclusion

In this chapter we discussed our ultrasound measurements on UTe_2. The absence of a jump in any of the shear moduli in both single and double-transition samples implies that the superconducting order parameter for both samples has only one component. This is the strongest statement extracted from our measurements since it is a purely symmetry based argument. Furthermore, since a one-component order parameter cannot break time-reversal symmetry, this suggests that the interpretation of time-reversal symmetry breaking in Kerr effect measurements [76, 86], as well as of chiral surface states in STM [117] and microwave surface impedance [88] measurements need to be revisited.

The quantitatively similar behavior of all shear moduli between single- and double-transition samples implies that both types of samples exhibit the same superconducting ground state. However, why c_{44} does not even exhibit a significant change in slope at T_c and a possible connection to the observation that c_{44} is also unaffected by Kondo physics is unsolved to date.

The small jump of c_{22} compared to c_{11} and c_{33} at T_c, in combination with the assumption of point nodes in the superconducting gap of UTe_2, further suggests that the

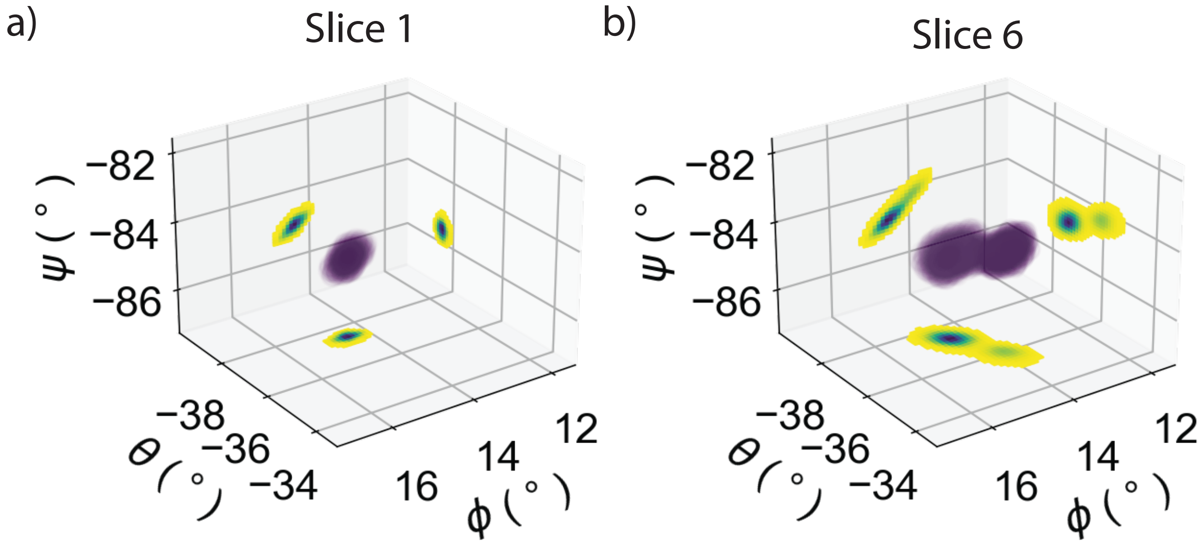

Figure 5.18: **Distribution of orientations with y-resolution.** Distributions of crystal orientations in slices 1 (a) and (6). Different slices indicate a different part of the sample which was probed by the X-ray beam as indicated in Figure 5.17a. The colors of the projections indicate the relative volume fraction occupied by a given orientation (purple is maximum and yellow is minimum).

superconducting order parameter in UTe$_2$ transforms according the B_{2u} irreducible representation of the D_{2h} point group.

The different ratios between the two jumps in c_{33} in a double-transition sample as measured by RUS and pulse-echo ultrasound suggest that volume fractions with different T_c's are inhomogeneously distributed within the sample, similar to the conclusion of specific heat measurements in successively cut samples [108]. This interpretation is supported by high-energy X-ray diffraction microscopy measurements on a two-transition sample, finding three different crystallographic orientations, each occupying distinct volume fractions in one sample. All different orientations are separated by more than 2° and up to 5°.

CHAPTER 6

STRONG MAGNETOELASTIC COUPLING IN Mn_3X

Piezomagnetism is exceptionally rare magnetic behavior where the total magnetization depends linearly on applied strain, akin to electric fields in piezoelectric materials. Our ultrasound studies presented in this chapter combined with subsequent magnetization measurements under applied uniaxial strain [125] lead us to indentify a piezomagnetic phase in Mn_3X (X = Ge, Sn), a family of topological antiferromagnets. This discovery not only advanced our understanding of the interplay between elasticity and magnetism but also opened new avenues for innovative applications in spintronics. Most of this chapter has been adapted from a paper published in Physical Review B [126], with Sayak Ghosh, Taishi Chen, Oleg Tchernyshyov, Satoru Nakatsuji, and B. J. Ramshaw.

6.1 Introduction to Mn_3X

Elastic strains offer a fast, local, and reversible way to manipulate the magnetic properties of solids. On a microscopic level, strains alter bond distances and the angles between magnetic ions, leading to changes in magnetic exchange coupling and magnetic anisotropy [127]. On a phenomenological level, these effects can lead to a strain dependence of the critical temperature and of the total magnetic moment. In the most extreme case, externally applied strains can break the crystal symmetry and drive magnetic phase transitions. The strain dependence of the magnetization most commonly comes in the form of magnetostriction, piezomagnetism, or flexomagnetism. All of these effects find useful applications in the recently-emerging field of straintronics [128, 129]. This necessitates the search for materials with large magnetoelastic coupling.

In this regard, the noncollinear antiferromagnets Mn_3X (X = Ge, Sn) are promising candidates. These compounds crystallize in a hexagonal lattice (D_{6h} point group), with lattice parameters $a = 5.3\,\text{Å}$ and $c = 4.3\,\text{Å}$ for Mn_3Ge [130], and $a = 5.7\,\text{Å}$ and $c = 4.5\,\text{Å}$ for Mn_3Sn [131]. In both compounds, magnetic Mn atoms arrange in Kagome networks in the $a - b$ plane and form 120° triangular magnetic order well above room temperature [132, 133] (see Figure 6.1 for images of the crystal structure and magnetic order). This magnetic order is the source of several anomalous transport properties including giant anomalous Hall, Nernst, and thermal Hall effects [134–141]. These quantities were shown to be strongly strain dependent. For example, hydrostatic pressure was demonstrated to change the sign of the Hall angle in Mn_3Ge [142], and in [125], the authors switched the

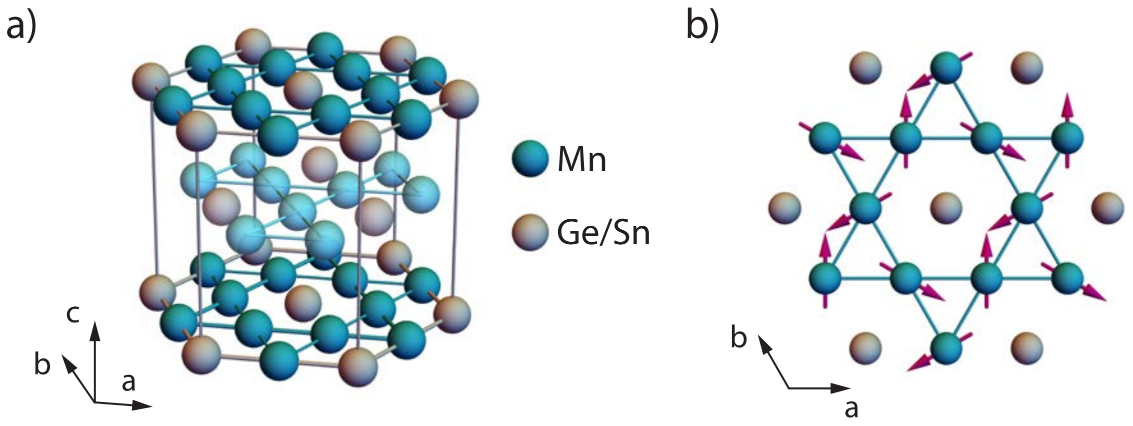

Figure 6.1: **$\mathbf{Mn_3X}$ crystal structure and antiferromagnetic order.** a) Mn_3X crystallizes in a hexagonal lattice, belonging to the D_{6h} point group. Mn atoms form an AB-stacked Kagome lattice in the $a-b$ plane. Ge/Sn atoms are located in the center of the Kagome hexagons. Different shades of the same color indicate different Kagome layers and are only for visual purposes. b) Top view of one Kagome layer. Local spins (purple arrows) on the Mn sites form 120° triangular magnetic order. Shown is one possible spin configuration for Mn_3Ge, but configurations rotated by multiples of 60° are equivalent. Spin configurations for Mn_3Sn are rotated by 30°. Figure adapted from [126].

sign of the Hall coefficient in Mn_3Sn by applying uniaxial strain. Additional evidence for large magnetoelastic coupling has been found in neutron diffraction studies [143], as well as in spontaneous magnetostriction at T_N [144] in Mn_3Ge. Additionally, Mn_3Sn was found to exhibit an extraordinarily large piezomagnetic effect [125]. These findings reveal an intimate connection between magnetism, anomalous transport properties, and elastic strain in Mn_3X, making it a prime candidate for applications in straintronics.

In this thesis, we directly investigated the magnetoelastic coupling in Mn_3X by measuring the full elastic tensors of Mn_3Ge and Mn_3Sn through their respective magnetic phase transitions using resonant ultrasound spectroscopy (RUS) and pulse-echo ultrasound. We find large discontinuities at T_N in the compressional elastic moduli and, using Ehrenfest relations, relate them to large derivatives of the Néel temperature with respect to hydrostatic pressure. We calculate dT_N/dP to be roughly 39 K/GPa in Mn_3Ge and 14.3 K/GPa in Mn_3Sn—some of the largest values ever reported for itinerant antiferromagnets. We measure $\frac{c_{11}-c_{12}}{2}$—corresponding to the strain that switches the sign of the anomalous Hall coefficient [125]—in magnetic fields up to 18 tesla. We find that, while the elastic moduli of Mn_3Ge and Mn_3Sn exhibit large quantitative differences in zero field, their magnetic field dependencies are quite similar.

In section 6.2, we discuss the magnetic order parameter in Mn_3X and the associated Landau free energy, including the coupling between order parameter and strain. We continue to show our RUS fit results in section 6.3, before analyzing the temperature dependencies of the compressional (see section 6.4) and shear moduli (see section 6.5), respectively.

6.2 Magnetic Order Parameter And Landau Free Energy

6.2.1 Magnetic Order Parameter

Various neutron diffraction studies find that local moments on the Mn sites of the Kagome lattice order in a chiral antiferromagnetic structure (Figure 6.1 b) [132, 133], with a small in-plane magnetic moment due to spin canting [145]. The Néel temperature (T_N) for Mn_3Ge is 370 K. For Mn_3Sn, T_N depends strongly on the exact stochiometry: here we investigated $Mn_{3.019}Sn_{0.981}$ with a critical temperature of 415 K. This composition of Mn_3Sn features an additional phase transition to spiral spin order below about 270 K [146, 147], which is however not topic of this thesis. For simplicity, we will refer to $Mn_{3.019}Sn_{0.981}$ as Mn_3Sn for the remainder of this chapter.

The magnetic order parameter associated with the high-temperature chiral antiferromagnetic order transforms according to the E_{1g} representation in the D_{6h} point group [133, 148]. It is therefore a two-component order parameter that can be written as $\boldsymbol{\eta} = \{\eta_x, \eta_y\}$. Up to fourth order in $\boldsymbol{\eta}$, the Landau free energy is

$$\mathcal{F}_{OP} = \alpha \left(T - T_N\right) |\boldsymbol{\eta}|^2 + b_1 |\boldsymbol{\eta}|^4 + b_2 \left(\eta_x^2 - \eta_y^2\right) + b_3 \eta_x^2 \eta_y^2. \tag{6.1}$$

Hexagonal crystal symmetry requires $b_3 = 4b_2$, which simplifies the free energy to

$$\mathcal{F}_{OP} = \alpha \left(T - T_N\right) \eta^2 + b\eta^4, \tag{6.2}$$

with $b = b_1 + b_2$. Here, we have also parametrized the order parameter as $\boldsymbol{\eta} = \eta \left\{\cos\left(\phi_\eta\right), \sin\left(\phi_\eta\right)\right\}$. Note that this free energy is fully isotropic—sixth-order is the lowest order at which anisotropy appears.

At zero applied strain, this order parameter is proportional to the total magnetization $\boldsymbol{M}$:

$$\boldsymbol{M} = \delta \boldsymbol{\eta}, \tag{6.3}$$

where δ is a constant. The Zeeman term in the free energy in the presence of an in-plane magnetic field, $\boldsymbol{H} = h \left\{\cos\left(\phi_h\right), \sin\left(\phi_h\right)\right\}$, is then given by

$$\begin{aligned} \mathcal{F}_{Zeeman} &= -\delta \boldsymbol{\eta} \boldsymbol{H} && (6.4) \\ &= -\delta \eta h \cos\left(\phi_\eta - \phi_h\right). && (6.5) \end{aligned}$$

Before we continue with the elastic free energy and its coupling to magnetism in subsection 6.2.2 and subsection 6.2.3, we need to note that the magnetic transition in Mn_3X is not purely mean-field. As we will discuss in section 6.4 the elastic moduli exhibit

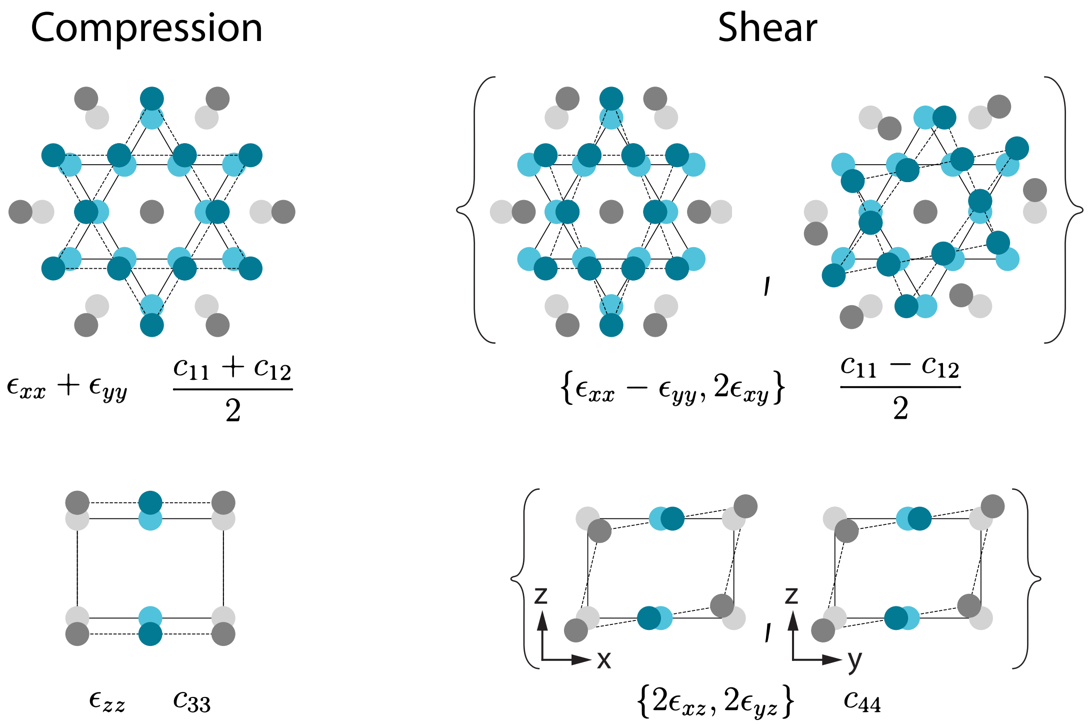

Figure 6.2: **Mn$_3$X irreducible strains.** Shown are the irreducible strains in Mn$_3$X and the corresponding elastic moduli. The strains are grouped by compression and shear strains. Compression strains transform as the trivial A_{1g} irreducible representation. Shear strains transform as the two-component E_{1g} ($\{2\epsilon_{xz}, 2\epsilon_{yz}\}$) and E_{2g} ($\{\epsilon_{xx} - \epsilon_{xy}, 2\epsilon_{xy}\}$) irreducible representations, respectively. Figure adapted from [126].

non-mean-field corrections near the phase transition. However, defining a Landau free energy is still useful to illustrate the symmetry of the coupling terms and the expected behavior of the moduli "not too close" to the phase transition.

6.2.2 Irreducible Strains and Elastic Free Energy

As discussed in subsection 2.3.2, the strain tensor for a crystal belonging to the D_{6h} point group contains only four independent elements. They can be split into compressional and shear strains. The compressional strains are in-plane compression $\epsilon_{A_{1g},1} = \epsilon_{xx} + \epsilon_{yy}$ and out-of-plane compression $\epsilon_{A_{1g},2} = \epsilon_{zz}$, both transforming according to the trivial A_{1g} irreducible representation. The shear strains are $\boldsymbol{\epsilon}_{E_{1g}} = \{2\epsilon_{xz}, 2\epsilon_{yz}\}$ and $\boldsymbol{\epsilon}_{E_{2g}} = \{\epsilon_{xx} - \epsilon_{xy}, 2\epsilon_{xy}\}$, transforming as the two-dimensional E_{1g} and E_{2g} irreducible representations, respectively.

The corresponding compressional elastic moduli are $\frac{c_{11}+c_{12}}{2}$ $(\epsilon_{xx} + \epsilon_{yy})$ and c_{33} (ϵ_{zz}). There is a third compressional modulus, c_{13}, which corresponds to the coupling of both

A_{1g} strains. The shear elastic moduli are c_{44} ($\{2\epsilon_{xz}, 2\epsilon_{yz}\}$) and $\frac{c_{11}+c_{12}}{2}$ ($\{\epsilon_{xx} - \epsilon_{xy}, 2\epsilon_{xy}\}$). These irreducible strains and corresponding elastic moduli are illustrated in Figure 6.2. The corresponding elastic free energy $\mathcal{F}_{el}$ is given in Equation 2.10.

6.2.3 Coupling Strain and Magnetism

Considering the E_{1g} magnetic order parameter (i.e. it breaks time-reversal symmetry in addition to the D_{6h} point group symmetry) and the irreducible strains above, the allowed coupling terms in the free energy are (see D_{6h} multiplication table in Table 2.1)

$$\mathcal{F}_{coupling} = \sum_{i=1}^{3} \gamma_{A_{1g},i}\epsilon_{A_{1g},i}\left|\boldsymbol{\eta}^2\right| + \gamma_{E_{1g}}\left|\boldsymbol{\epsilon}_{E_{1g}}^2\right|\left|\boldsymbol{\eta}^2\right| + \gamma_{E_{2g}}\left(\epsilon_{E_{2g},x}\left(\eta_x^2 - \eta_y^2\right) + 2\epsilon_{E_{2g},y}\eta_x\eta_y\right) \tag{6.6}$$

$$= \sum_{i=1}^{3} \gamma_{A_{1g},i}\epsilon_{A_{1g},i}\eta^2 + \gamma_{E_{1g}}\left|\boldsymbol{\epsilon}_{E_{1g}}^2\right|\eta^2 + \gamma_{E_{2g}}\eta^2\epsilon_{E_{2g}}\cos\left(2\left(\phi_\epsilon - \phi_\eta\right)\right), \tag{6.7}$$

where we have used the parametrization of the order parameter given above, as well as $\boldsymbol{\epsilon}_{E_{2g}} = \epsilon_{E_{2g}}\left\{\cos\left(2\phi_\epsilon\right), \sin\left(2\phi_\epsilon\right)\right\}$.

Since an in-plane magnetic field also transforms as the E_{1g} representation (and breaks time-reversal symmetry), certain additional terms in the free energy which are trilinear in order parameter, magnetic field, and A_{1g} or E_{2g} strain are also allowed in the free energy. These piezomagnetic terms are

$$\mathcal{F}_{piezo} = \sum_{i=1}^{2} \lambda_{A_{1g},i}\epsilon_{A_{1g},i}\eta h\cos\left(\phi_\eta - \phi_h\right) + \lambda\epsilon_{E_{2g}}\eta h\cos\left(\phi_\eta + \phi_h - 2\phi_\epsilon\right), \tag{6.8}$$

where we have used the same polar coordinates as above.

The total free energy is then given by the sum of Equation 2.10, Equation 6.2, Equation 6.6, Equation 6.4, and Equation 6.8

$$\mathcal{F} = \mathcal{F}_{el} + \mathcal{F}_{OP} + \mathcal{F}_{coupling} + \mathcal{F}_{Zeeman} + \mathcal{F}_{piezo}. \tag{6.9}$$

6.2.4 Elastic Moduli at the Magnetic Phase Transition

For our RUS measurements, we can make the assumptions of zero magnetic field and constant angles ϕ_h, ϕ_η, and ϕ_ϵ. These constraints lead to a simplified free energy

$$\begin{aligned}\mathcal{F} = \frac{1}{2}\left(\frac{c_{11}+c_{12}}{2}\epsilon_{A_{1g},1}^2 + c_{33}\epsilon_{A_{1g},2}^2 + 2c_{13}\epsilon_{A_{1g},1}\epsilon_{A_{1g},2} + c_{44}\left|\boldsymbol{\epsilon}_{E_{1g}}\right|^2 + \frac{c_{11}-c_{12}}{2}\left|\boldsymbol{\epsilon}_{E_{2g}}\right|^2\right) \\ + \alpha\left(T-T_N\right)\eta^2 + b\eta^4 + \sum_{i=1}^{3}\gamma_{A_{1g},i}\epsilon_{A_{1g},i}\eta^2 + \gamma_{E_{1g}}\left|\boldsymbol{\epsilon}_{E_{1g}}\right|^2\eta^2 + \gamma_{E_{2g}}\eta^2\epsilon_{E_{2g}} \\ - \sum_{i=1}^{2}\lambda_{A_{1g},i}\epsilon_{A_{1g},i}\eta h - \lambda\epsilon_{E_{2g}}\eta h,\end{aligned} \tag{6.10}$$

where the cosine terms originally appearing in Equation 6.9 are absorbed into the expansion coefficients. From this free energy and our discussion in subsection 2.3.3, we can read off that in addition to the compressional moduli (for which a jump is always allowed) $\frac{c_{11}-c_{12}}{2}$ is also allowed to jump at the magnetic phase transition, since the corresponding strain $\epsilon_{E_{2g}}$ couples linearly to the square of the order parameter. c_{44}, on the other hand, is only allowed to exhibit a change in slope at T_N.

The magnitudes of the jumps in the compressional moduli and $\frac{c_{11}-c_{12}}{2}$ can be calculated by finding the equilibrium order parameter η_{eq} defined by $\left.(d\mathcal{F}/d\eta)\right|_{\eta_{eq}} = 0$. The elastic moduli c_Γ are then defined through $\left.(\partial^2\mathcal{F}/\partial\epsilon_\Gamma^2)\right|_{\eta_{eq}}$, and we have for the jumps at T_N

$$\delta c_\Gamma = \left(c_\Gamma\left(T>T_N\right) - c_\Gamma\left(T<T_N\right)\right)_{T\to T_N} = \frac{2\gamma_\Gamma^2}{b}, \tag{6.11}$$

where Γ labels the irreducible representations A_{1g} or E_{2g}.

6.3 Elastic Tensors In The Normal And Ordered States

We measured RUS spectra for Mn_3Ge and Mn_3Sn at room temperature (i.e. 300 K) and at high temperatures above their respective antiferromagnetic phase transitions. All samples used in our measurements were cut from one large Mn_3Ge and one Mn_3Sn crystal. The final samples were polished into the shapes of rectangular prisms, with edges oriented along the high symmetry directions. For our Mn_3Ge RUS measurements, we used a $(911 \times 1020 \times 1305)$ μm^3 large sample for the RUS fit at 387 K and to measure the temperature dependence of the elastic moduli. For the fit at room temperature, this sample was further polished to $(869 \times 1010 \times 1193)$ μm^3[1]. All RUS measurements on

---

[1] This is the same sample as was used as a proof of concept for our SMI forward solver in chapter 4. The elastic moduli from this study are given in Table 4.3. The two fits are mostly identical. Minor deviations, which are well within the given uncertainties, are because we used basis polynomials up to order 18 in chapter 4, whereas here we only used polynomials up to order 16.

	Mn_3Ge		Mn_3Sn	
	300 K	387 K	300 K	438 K
$\frac{c_{11}+c_{12}}{2}$	87.0 ± 0.5	90.4 ± 0.2	85.8 ± 0.5	79.7 ± 0.2
c_{13}	13 ± 2	14.6 ± 0.6	18 ± 1	17.0 ± 0.6
c_{33}	202 ± 2	194.6 ± 0.5	165 ± 1	151.3 ± 0.5
c_{44}	48.4 ± 0.1	45.09 ± 0.05	52.0 ± 0.2	48.11 ± 0.08
$\frac{c_{11}-c_{12}}{2}$	43.0 ± 0.5	48.1 ± 0.2	50.8 ± 0.5	51.2 ± 0.2
B	65.9 ± 0.7	67.9 ± 0.3	64.5 ± 0.7	59.7 ± 0.3
ν_{xy}	0.334 ± 0.006	0.300 ± 0.002	0.246 ± 0.007	0.206 ± 0.003
ν_{zx}	0.041 ± 0.005	0.053 ± 0.002	0.083 ± 0.007	0.089 ± 0.003

Table 6.1: **Elastic properties of Mn_3X**. Listed are the elastic tensors of Mn_3X in GPa. We provide values at 387 K for Mn_3Ge and at 438 K for Mn_3Sn, where each compound is in the paramagnetic state, as well as at 300 K. Also given are the bulk moduli (in GPa) and the in-plane (ν_{xy}) and out-of-plane ($\nu_{xz} = \nu_{yz}$) Poisson ratios. Uncertainties are due to a 2 % increase in RMS. Table adapted from [126].

Mn_3Sn were performed on a $(743 \times 836 \times 1.136)\ \mu\text{m}^3$ piece cut out of the original crystal. The first two dimensions are in the plane of the hexagonal lattice and the last dimension is along the c axis. The measured resonance spectra and calculated resonances corresponding to our fits are given in Appendix K.

The resulting elastic moduli are listed in Table 6.1. In their respective paramagnetic states, the compresional elastic moduli, $(c_{11} + c_{12})/2$ and c_{33}, are 13 % and 28 % larger in Mn_3Ge than in Mn_3Sn. This implies tighter bonding in Mn_3Ge, which is consistent with its smaller unit cell.

Table 6.1 also lists the bulk moduli B, as well as the in-plane (ν_{xy}) and out-of-plane ($\nu_{xz} = \nu_{yz}$) Poisson ratios, which we calculate from the elastic tensors through

$$B = \frac{\frac{c_{11}+c_{12}}{2} c_{33} - c_{13}^2}{\frac{c_{11}+c_{12}}{2} + c_{33} - 2c_{13}}, \tag{6.12}$$

$$\nu_{xy} = \frac{c_{13}^2 - c_{12}c_{33}}{c_{13}^2 - c_{11}c_{33}}, \tag{6.13}$$

$$\nu_{zx} = \nu_{zy} = \frac{(c_{11} - c_{12})\, c_{13}}{-c_{13}^2 + c_{11}c_{33}}. \tag{6.14}$$

The value of the in-plane Poisson ratio, ν_{xy}, is consistent with what is found in most conventional metals [149]. ν_{zx} on the other hand, is anomalously small, even compared to other layered materials like Sr_2RuO_4 ($\nu_{zx} = 0.16$ [23]), URu_2Si_2 ($\nu_{zx} = 0.20$ [150]), $CeIrIn_5$ ($\nu_{zx} = 0.32$ [151]), and La_2CuO_4 ($\nu_{zx} = 0.21$ [152]), implying extremely weak elastic coupling between different planes in the hexagonal crystal structure of Mn_3X.

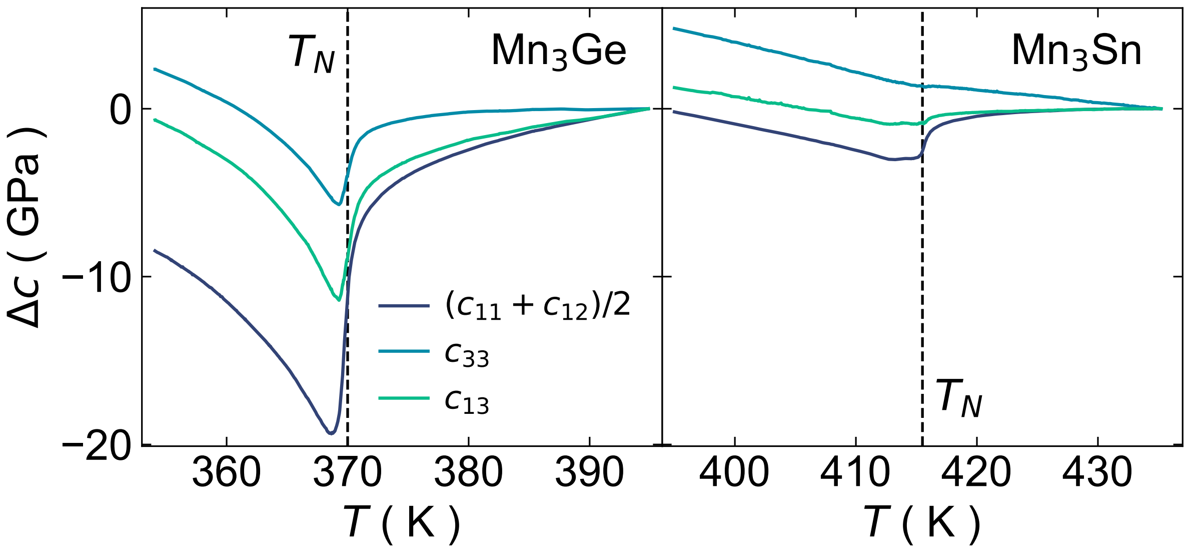

Figure 6.3: **Mn_3X compressional moduli.** Changes of the compressional moduli for Mn_3Ge (left panel) and Mn_3Sn (right panel) through their respective high-temperature antiferromagnetic transitions. The change is defined as $\Delta c(T) = c(T) - c(387\ K)$ for Mn_3Ge and $\Delta c(T) = c(T) - c(438\ K)$ for Mn_3Sn. Néel temperatures are indicated by vertical dashed lines. Figure adapted from [126].

To investigate the coupling between magnetism and elasticity in Mn_3X, we measured the elastic moduli as a function of temperature through their respective Néel temperatures T_N. The resonances used for these decompositions are displayed in bold font in Table K.1 and Table K.2. Their temperature dependencies were measured in our home-built high-temperature RUS setup (see subsection 3.1.2). The behavior of the compressional moduli is discussed in section 6.4 and the shear moduli, including the magnetic field dependence of $\frac{c_{11}-c_{12}}{2}$, are discussed in section 6.5.

6.4 Compressional Elastic Moduli

Data. The changes in compressional moduli for Mn_3Ge and Mn_3Sn through their respective high-temperature phase transitions are shown in Figure 6.3. Starting well above T_N, all three compressional moduli in Mn_3Ge (see left panel of Figure 6.3) decrease smoothly upon cooling towards the phase transition. This anomalous softening is in contrast to the conventional stiffening of elastic moduli when the temperature is lowered [98] (see for example Figure 5.5), and implies sizable antiferromagnetic fluctuations well above T_N. Anomalous softening of the elastic moduli approaching T_N also suggest a non-mean-field phase transition in Mn_3Ge. The softening of the compressional moduli above T_N is followed by a step-like feature at the phase transition.

Qualitatively similar behavior is seen in Mn_3Sn (see right panel of Figure 6.3), but with quantitative differences. In Mn_3Sn, c_{13} and $(c_{11} + c_{12})/2$ are almost temperature independent well above T_N, and c_{33} increases upon cooling. All compressional elastic moduli eventually soften above T_N, but much more weakly than in Mn_3Ge. Additionally, the absolute sizes of the steps at T_N are nearly a factor of 10 smaller in Mn_3Sn than in Mn_3Ge. Both the smaller precursor softening and the smaller steps at T_N suggest that the coupling between magnetism and the lattice is significantly stronger in Mn_3Ge than in Mn_3Sn.

Ehrenfest Relations. As discussed in subsection 2.3.3, the jump in the compressional moduli across T_N is directly proportional to the jump in the specific heat, via Ehrenfest relations. Since the bulk modulus (see Equation 6.12) is calculated from all compressional moduli, a similar expression exists, relating the jump of the bulk modulus at T_N to the jump in specific heat. Here, the proportionality constant is the square of the derivative of T_N with respect to hydrostatic pressure P_{hydro}. This Ehrenfest relation reads [23]

$$\left(\frac{dT_N}{dP_{\text{hydro}}}\right)^2 = -\frac{\delta B}{B^2}\left(\frac{\Delta C}{T_N}\right)^{-1}, \tag{6.15}$$

where δB and ΔC are the discontinuities in the bulk modulus and specific heat, respectively, and B is the absolute bulk modulus at T_N. Using the measured heat capacity and our measurements of the compressional moduli, we can then calculate the absolute value of dT_N/dP_{hydro}.

To extract the derivative of the Néel temperature with hydrostatic pressure from our data, we plot the bulk modulus $B/B\left(T_N\right)^2$ on the same scale as the specific heat scaled by dT_N/dP_{hydro}, i.e. $-\Delta C/T_N\left(dT_N/dP_{hydro}\right)^2$ (see Figure 6.4). We perform this scaling procedure because the non-mean field nature of the transition in Mn_3X makes it hard to accurately extract jump sizes. For mean-field transitions, this is easily done by fitting background polynomials above and below the transition and taking their differences (see Figure 5.11 for an example). The non-mean field "rounding" of the bulk moduli approaching T_N, however, creates ambiguity in the definition of these background fits. Assuming that this rounding is approximately the same in the specific heat and the bulk moduli, our scaling procedure still allows us to use the Ehrenfest relation to extract dT_N/dP_{hydro} from our data.

This analysis for Mn_3Ge, along with the specific heat data for Mn_3Ge from [133], is shown in the left panel of Figure 6.4. We obtain a derivative of T_N with respect to pressure of $dT_N/dP_{hydro} = 39\pm3$ K/GPa. Specific heat data are not available for Mn_3Sn through its high temperature phase transition. However, using the specific heat data for Mn_3Ge, we estimate $dT_N/dP_{\text{hydro}} \approx (14.3 \pm 2)$ K/GPa for Mn_3Sn (see right panel of Figure 6.4). This value is about a factor of three smaller than for Mn_3Ge. It is possible that the true heat capacity of Mn_3Sn is a factor of 9 larger than in Mn_3Ge. Either way—whether it is due to a factor of 9 difference in heat capacity or a factor of 3 difference in dT_N/dP_{hydro}—this observation is puzzling given that the two compounds share similar values of T_N, the

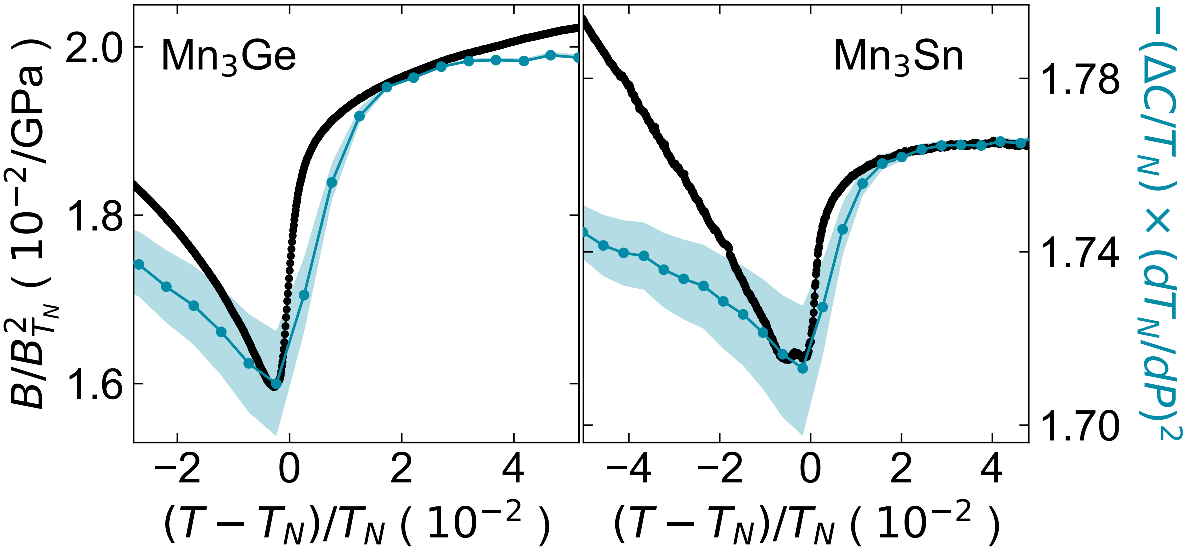

Figure 6.4: **Ehrenfest scaling.** Shown are the bulk moduli (black points) of Mn_3Ge (left panel) and Mn_3Sn (right panel) divided by their respective values at T_N squared, i.e. $B/B^2_{T_N}$. Also shown is the specific heat, divided by the Néel temperature and scaled by $(dT_N/dP_{\mathrm{hydro}})^2$ (blue points). Both quantities are plotted on the same scale and in $(\mathrm{K/GPa})^2$. The specific heat of Mn_3Ge is taken from [133] and used for both Mn_3Ge and Mn_3Sn. The scaling factors used in the figure correspond to values of $dT_N/dP \approx (39 \pm 3)$ K/GPa for Mn_3Ge and $dT_N/dP \approx (14.3 \pm 2)$ K/GPa for Mn_3Sn. The uncertainties correspond to the blue shaded regions in the figure. Figure adapted from [126].

same room-temperature magnetic structure, and the same crystal structure with only marginally different unit cell parameters.

Table 6.2 compares the size of dT_N/dP_{hydro} between several metallic antiferromagnets. Mn_3Ge and Mn_3Sn stand out with some of the largest pressure derivatives of their respective Néel temperatures. Only the alloy Mn_3Pt and elemental chromium have transition temperatures more sensitive to pressure than Mn_3Ge. Note that these compounds and Mn_3X are also the only materials with transitions above room temperature. These features, as well as their metallic conductivity, make Mn_3Ge and Mn_3Sn two of only a few materials exceptionally well suited for applications in straintronics.

Critical Exponent. In the paragraphs above, we have already noticed the pronounced softening of the bulk moduli in the disordered state, approaching T_N (see Figure 6.4). This softening is due to fluctuations of the order parameter not captured by mean-field theory. The bulk moduli are affected by these fluctuations in the same way as the specific heat. Both quantities therefore diverge towards the Néel temperature as $t^{-\alpha}$ with the same

Compound	$\frac{dT_N}{dP_{hydro}}$ (K/GPa)	T_N (K)	Reference
Mn_3Ge	39	370	This thesis
Mn_3Sn	14.3	415	This thesis
Mn_3Pt	70	475	[153]
Cr	51	312	[154]
α-Mn	17	95	[155]
UN	9.3	53	[156]
CuMnSb	4.7	50	[157]
$MnPd_3$	2.0	195	[158]
$UPtGa_5$	1.5	26	[156]
CrB_2	1.0	87	[159]
TiAu	0.6	33	[160]
UIrGe	0.11	16.5	[161]

Table 6.2: **Magnetoelastic coupling in various compounds.** The derivative of the Néel temperature with respect to hydrostatic pressure for selected metallic antiferromagnets. Table adapted from [126].

critical exponent α[2], where $t = (T - T_N)/T_N$ is the reduced temperature [53, 162]. We can therefore use our measured bulk moduli to determine the specific heat critical exponent α and determine the universality class of the high temperature magnetic transition in Mn_3X.

We determine the universality class by fitting the following function

$$B = At^{-\alpha} + C + DT, \tag{6.16}$$

to the bulk moduli of Mn_3X for temperatures above T_N (see Figure 6.5). $C + DT$ is a linear background capturing non-critical behavior. Data too close to the transition are also excluded from the fit to avoid experimental rounding effects. We performed several fits for different universality classes, where T_N was always fixed to 370.0 K for Mn_3Ge and 415.5 K for Mn_3Sn and α was fixed to the theoretical value of the respective universality class [163]. Only, the parameters A, C, and D were free parameters in the fits.

The results of this analysis are shown in Figure 6.5. We compare several universality classes, including the 3D XY, 3D Heisenberg, 3D Ising, and Chiral XY models. While all of them capture the bulk modulus of Mn_3Ge above $t \approx 3 \times 10^{-3}$ (see left panel of Figure 6.5), only the 3D XY model fits the entire included data range and even extrapolates well onto data not included in the fit. Our data is therefore most consistent with the high-temperature antiferromagnetic phase in Mn_3Ge belonging to the 3D XY universality class. Fits for Mn_3Sn, on the other hand, are less conclusive and don't allow for a distinction between the 3D XY and 3D Ising models (see right panel of Figure 6.5).

---

[2] The step discontinuities seen in the bulk modulus and specific heat at mean-field transitions can be described by $\alpha = 0$.

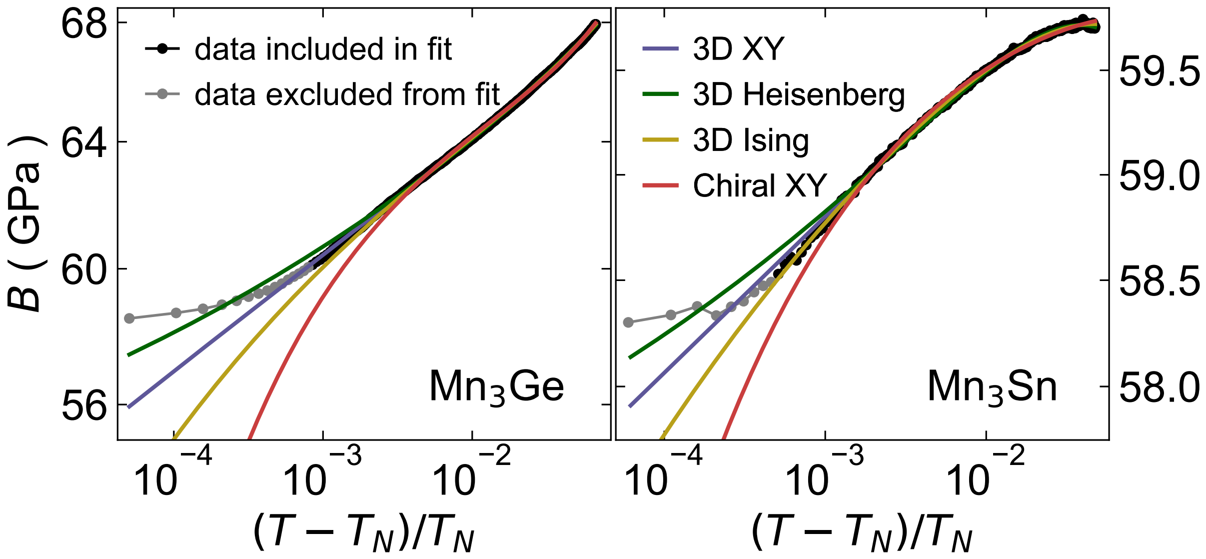

Figure 6.5: **Mn₃X critical exponent.** Shown are the bulk moduli of Mn_3Ge (left panel) and Mn_3Sn (right panel) as a function of reduced temperature $(T - T_N)/T_N$ for temperatures above T_N on a log–log scale. Black points are bulk moduli data included in the fits. Gray points are excluded since they are too close to T_N and therefore exhibit experimental rounding effects.

6.5 Shear Elastic Moduli

Data. The change in shear moduli for Mn_3Ge and Mn_3Sn through their respective high-temperature phase transitions are shown in the left and right panels of Figure 6.6, respectively. The behavior of c_{44} is relatively conventional, with no precursor softening and only a change in slope at T_N, which is as expected because the lowest order coupling in the free energy is quadratic in both the order parameter and the corresponding strain. $\frac{c_{11}-c_{12}}{2}$, on the other hand, softens towards the Néel temperature upon cooling, similar to the compressional modes. The much stronger signature in Mn_3Ge than in Mn_3Sn again indicates stronger magnetoelastic coupling in the former compound. While a jump in $\frac{c_{11}-c_{12}}{2}$ at T_N is allowed by symmetry for the chiral order in Mn_3X [125, 164, 165], no feature that is comparable in width to the steps in the compressional moduli is seen in $\frac{c_{11}-c_{12}}{2}$. The precursor softening in this channel again indicates the non-mean-field nature of the magnetic phase transition in Mn_3X.

$\frac{c_{11}-c_{12}}{2}$ In Magnetic Fields. $\frac{c_{11}-c_{12}}{2}$ plays a special role in Mn_3X, since the associated E_{2g} strain $\boldsymbol{\epsilon}_{E2g} = \{\epsilon_{xx} - \epsilon_{yy}, 2\epsilon_{xy}\}$ is the same strain that is responsible for the piezomagnetic effect and the switching of the anomalous Hall effect. Unlike most shear strains in magnetic systems, $\boldsymbol{\epsilon}_{E2g}$ can couple to the magnetic order parameter $\boldsymbol{\eta} = \{\eta_x, \eta_y\}$ as $((\epsilon_{xx} - \epsilon_{yy})(\eta_x^2 - \eta_y^2) + 4\epsilon_{xy}\eta_x\eta_y)$ within a Landau free energy (see Equation 6.6). Due

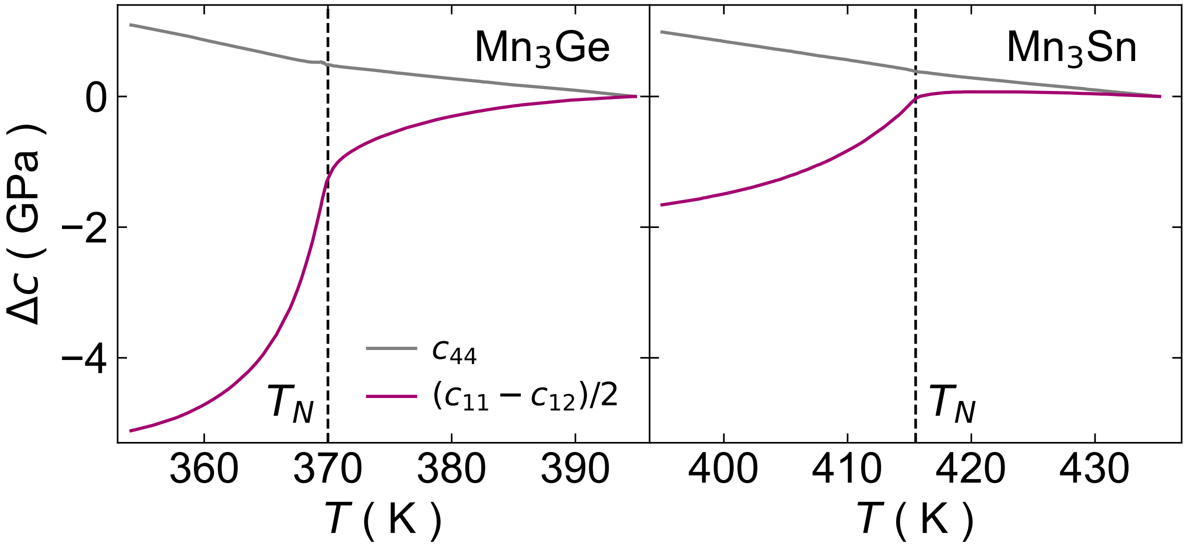

Figure 6.6: **Mn_3X shear moduli.** Changes of the shear moduli for Mn_3Ge (left panel) and Mn_3Sn (right panel) through their respective high-temperature antiferromagnetic transitions. The change is defined as $\Delta c(T) = c(T) - c(387\ K)$ for Mn_3Ge and $\Delta c(T) = c(T) - c(438\ K)$ for Mn_3Sn. Néel temperatures are indicated by vertical dashed lines. Figure adapted from [126].

to this type of coupling—linear in shear strain and quadratic in order parameter—finite E_{2g} shear strain breaks the six-fold order parameter degeneracy caused by the hexagonal lattice of Mn_3X. It can therefore reorient the magnetic moments on the Kagome lattice and align domains [125, 164] (see Figure 6.7). These domains have been demonstrated to work as magnetic memory [166], and $\boldsymbol{\epsilon}_{E2g}$ strain has been shown to change the sign of the Hall coefficient and to exhibit a large piezomagnetic effect in Mn_3Sn [125]. This motivates a measurement of the associated elastic modulus, $c_{E_{2g}} = \frac{c_{11}-c_{12}}{2}$, in external magnetic fields.

Elastic moduli in an externally applied magnetic field were measured with pulse-echo ultrasound in our custom-built high-temperature probe (see subsection 3.2.3), which was inserted into an Oxford Instruments variable temperature insert (VTI) in an Oxford Instruments 20 Tesla superconducting magnet system. We used commercially available $LiNbO_3$ shear transducers with fundamental frequency of 40 MHz, driven at 199 MHz for Mn_3Ge and at 175 MHz for Mn_3Sn. $c_{E_{2g}}$ was measured with both the propagation and polarization vectors of the excited sound pulse in the $a - b$ plane. In-plane magnetic field was applied parallel to the polarization vector of the sound wave (and perpendicular to the direction of sound propagation). The used samples were cut from the same original crystals as the RUS samples.

The resulting data is shown in Figure 6.7b. The inset shows the change in $c_{E_{2g}}$ as a function of temperature in zero magnetic field for Mn_3Ge (solid lines) and Mn_3Sn

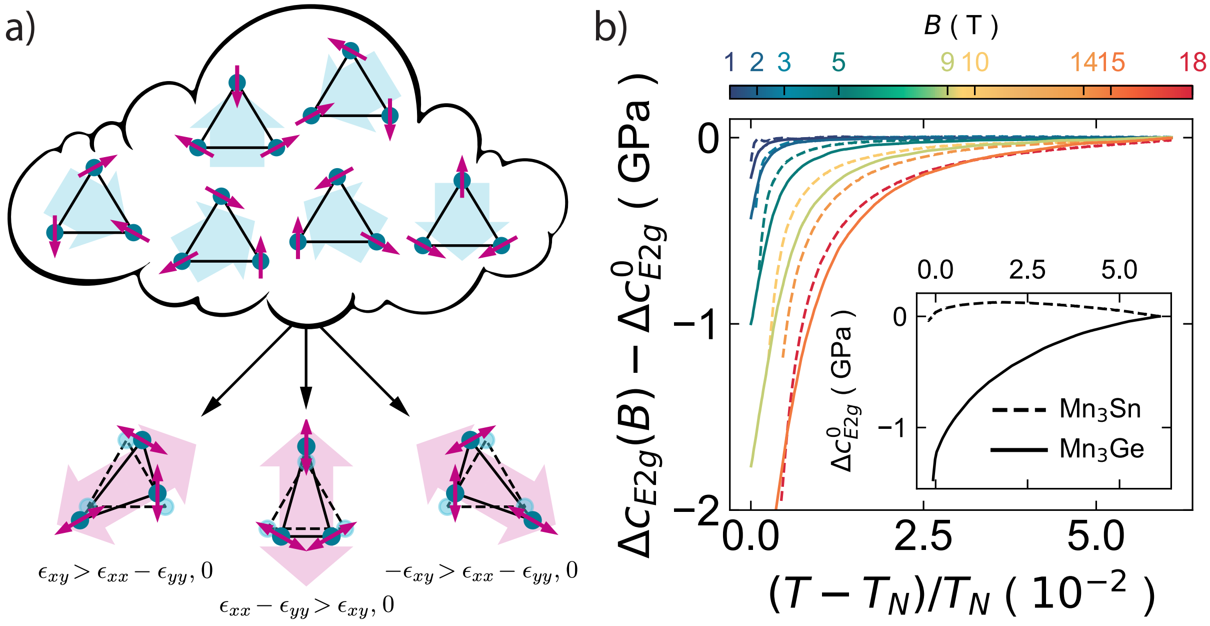

Figure 6.7: **OP under E_{2g} strain and $c_{E_{2g}}$ in magnetic fields.** a) The magnetic structure of the high-temperature antiferromagnetic phase in Mn_3X is unambiguously defined by the spin configuration (purple arrows) on a single triangle of Mn sites (turquoise circles) on the Kagome lattice. Six different domains of degenerate order parameter configurations exist, each rotated by 60°. The order parameter in the unstrained case is indicated by large blue arrows. Finite E_{2g} shear strain breaks this degeneracy and favors one of three different alignments, depending on the relative size of ϵ_{xy} to $\epsilon_{xx} - \epsilon_{yy}$. Shown are the spin configurations for Mn_3Ge. The spin configurations for Mn_3Sn are 30°. b) The changes in $c_{E_{2g}} = \frac{c_{11} - c_{12}}{2}$ for Mn_3Ge (solid lines) and Mn_3Sn (dashed lines) at different fields with respect to the zero-field elastic moduli are shown as a function of the reduced temperature $(T - T_N)/T_N$. The data were taken at 1, 2, 5, 9, and 15 T for Mn_3Ge and at 1, 2.7, 5, 10, 14, and 18 T for Mn_3Sn. The inset shows the zero-field data for both compounds. Panel b) adapted from [126].

(dashed lines). The main panel of Figure 6.7b shows this temperature dependence at different magnetic fields with the zero-field data subtracted from each curve. The data are shown as a function of the reduced temperature $(T - T_N)/T_N$ above their respective phase transitions. The data end at (or just before) T_N because the ultrasonic attenuation becomes too large to resolve a clear signal in the ordered phase.

As noted earlier, the temperature dependence of $c_{E_{2g}}$ in zero field shows much stronger precursor fluctuations in Mn_3Ge than in Mn_3Sn. However, once we account for this difference in the zero-field temperature dependence, the change with magnetic field is quite similar for the two compounds. With increasing magnetic field, the softening towards T_N becomes more pronounced. This behavior is reminiscent of ferromagnetic transitions and is indicative of the trilinear, piezomagnetic coupling allowed by symmetry between E_{2g}

shear strain, magnetic order parameter, and the external in-plane magnetic field in Mn_3X (see Equation 6.8).

6.6 Conclusion

In summary, we used resonant ultrasound spectroscopy and pulse-echo ultrasound to measure the elastic moduli of Mn_3Ge and Mn_3Sn. In addition to the full elastic tensor, we also provide the bulk moduli and Poisson's ratios. We find an anomalously small out-of-plane Poisson's ratio, ν_{zx}, in both materials, implying weak elastic coupling between different layers of the hexagonal crystal structure. By scaling the bulk modulus anomalies to match the heat capacity anomaly at T_N, we extract large derivatives of the Néel temperatures with respect to hydrostatic pressure: (39 ± 3) K/GPa and (14.3 ± 2.0) K/GPa in Mn_3Ge and Mn_3Sn, respectively. Finally, although the zero-field magneto-elastic coupling appears to be much larger in Mn_3Ge than in Mn_3Sn, we find that the field dependence of the in-plane shear modulus—associated with the strain that couples strongly to the magnetism in Mn_3X—is similar in the two compounds.

The Mn_3X family hold promise for straintronic applications because it combines metallic conductivity, robust room-temperature magnetism, a large anomalous Hall effect whose sign can be switched with strain, and strong piezomagnetism. The latter two properties—piezomagnetism and strain dependence of anomalous transport properties [125]—have only been performed on Mn_3Sn to date. Our measurements suggest that these effects may be even more dramatic in Mn_3Ge.

CHAPTER 7

CONCLUSION & OUTLOOK

In this thesis we investigated collective behavior of two correlated electron systems with resonant ultrasound spectroscopy (RUS) and pulse-echo ultrasound. These systems included unconventional superconductivity in UTe_2 and topological magnetism in Mn_3X ($X = Ge$, Sn). For our RUS measurements on UTe_2, we developed a novel algorithm to calculate mechanical resonances and fit elastic moduli of irregularly-shaped samples.

Mn_3X. Mn_3X is a family of above-room-temperature topological antiferromagnets, where the magnetic order parameter is associated with various anomalous transport properties. Our RUS measurements revealed strong coupling between elasticity and the magnetic order parameter, indicated by a large derivative of the Néel temperature T_N with respect to hydrostatic pressure: (39 ± 3) K/GPa in Mn_3Ge and (14.3 ± 2.0) K/GPa in Mn_3Sn. We also found that the bulk modulus of Mn_3Ge diverges towards T_N from above with a critical exponent belonging to the 3D XY universality class. A similar analysis for the bulk modulus of Mn_3Sn was less conclusive.

We found that the shear modulus $\frac{c_{11}-c_{12}}{2}$, corresponding to in-plane shear strain $\epsilon_{E_{2g}}$, also softens upon approaching T_N. This softening becomes more pronounced with an externally applied in-plane magnetic field, indicating that Mn_3X is piezomagnetic. The existence of this rare piezomagnetic phase has subsequently been corroborated by magnetization measurement under uniaxial strain [125].

The critical exponent we were able to extract from the bulk modulus of Mn_3Ge is the same critical exponent underlying the divergence of the specific heat. Access to all elastic moduli, however, generally allows us to also extract different critical exponents, which are not available to other techniques. Exciting examples are the nematic critical exponent of the quadrupolar susceptibility, which dominates the behavior of $\frac{c_{11}-c12}{2}$ close to T_N, or dynamical critical exponents describing the divergence of the sound attenuation. For a reliable determination of either, data in a larger temperature range than what we measured is required, though. A detailed analysis of the sound attenuation also requires measurements at additional frequencies.

UTe_2. UTe_2 is a strongly-correlated heavy-Fermion metal, exhibiting multiple superconducting and magnetic phases as functions of magnetic fields and hydrostatic pressure. Of particular interest is the zero-field, ambient-pressure spin-triplet superconducting phase, speculated to host topological quasiparticles. The characterization of this phase has been complicated by large variations between samples, some even exhibiting two successive superconducting transitions and signs of time-reversal symmetry breaking.

We performed pulse-echo ultrasound measurements on one and two-transition samples and found no jump in any of the shear moduli of either sample. This observation implies that the superconducting order parameter in both generations of samples has one component, further ruling out time-reversal symmetry breaking as an intrinsic property of superconductivity in UTe_2. Additionally, we found that the jump in the c_{22} compressional modulus is significantly smaller than in c_{11} or c_{33}, which suggests that the superconducting order parameter transforms as the B_{2u} irreducible representation of the D_{2h} point group.

We also performed RUS and high-energy X-ray diffraction microscopy (HEDM) measurements on two-transition samples. Both measurements, even though not entirely conclusive, suggest spatial inhomogeneity in two-transition samples. These measurements raise the possibility of spatially separated patches with different critical temperatures in a single sample of UTe_2. The origin behind the existence of exactly two superconducting transitions in some samples, however, is still an open question. Further analysis of our X-ray data (including near-field HEDM) has the potential to solve part of this puzzle.

Another exciting prospect is the direct determination of the nodal structure of the superconducting gap with ultrasound. A common technique used to determine the nodal structure in superconductors is thermal transport, where the rate of how fast the thermal conductivity decreases below T_c indicates the presence or absence of nodes. This determination, however, is not always unambiguous, because effects in thermal transport are averaged over the entire Fermi surface. In UTe_2, for example, different thermal conductivity studies give inconsistent results. Pulse-echo ultrasound, on the other hand, if performed at high enough frequencies only probes small parts of the Fermi surface with momentum perpendicular to the sound propagation. For this measurement, however, the sound wavelength needs to be shorter than the electron mean-free path, which is currently not accessible. Cleaner samples with higher mean-free paths or ultrasound at tens of gigahertz are required. While neither are available yet, they are also not entirely out of reach and present exciting possibilities for the advancement of pulse-echo ultrasound.

Besides superconductivity at zero field and ambient-pressure, additional superconducting phases in UTe_2 have been identified above 1.7 GPa hydrostatic pressure and above about 15 T magnetic field applied along the b axis. Characterizing these phases would give critical insights into the interplay between different superconducting states and guide our understanding of the underlying microscopic pairing mechanism. While both additional phases are in principle accessible with pulse-echo ultrasound, particularly a setup for controlled measurements under pressure still needs to be developed.

Lastly, ultrasound can be used to investigate the phase transition emerging for magnetic fields of 40 T applied along the [011] direction. This intriguing phase, which persists up to over 60 T and is characterized by zero resistance has been speculated to be another unconventional superconducting phase. Zero-resistance alone, however, is not sufficient to determine if a state is a superconductor and thermodynamic measurements are lacking to date. A drop in the ultrasonic attenuation at the phase transition could unambiguously distinguish a superconductor from a perfect metal, which would cause a dramatic rise in the sound attenuation.

APPENDIX A

INTRODUCTION TO GROUP THEORY

This section is intended as a short introduction of relevant terms and properties of groups and representations. Helpful references are [16, Chapters 12 and 13] and [17]. Some definitions and properties may already be discussed in the main text in chapter 2 but are repeated here for completeness.

A.1 Groups

A set G (denoted by capital italic letters) consisting of elements g_1, g_2, ... (denoted by lower case italic letters) forms a group if the following criteria are satisfied [17, Chapter 1]:

1. The product $g_i = g_j g_k$ of any two elements of the group G is also an element of G.
2. The product is associative, i.e. $g_i\left(g_j g_k\right) = \left(g_i g_j\right) g_k$.
3. There exists a *unit element* e of the group, such that $eg_i = g_i e = g_i$ for any element g_i in G.
4. For any element g_i in G, there exists an *inverse element* g_i^{-1} also in G, such that $g_i g_i^{-1} = g_i^{-1} g_i = e$.

In general, the product of two elements does not commute, i.e. $g_i g_j \neq g_j g_i$. A group for which all of its elements commute with each other is called *abelian*.

Important definitions/properties of groups include:

- **Subgroups:** A group H is a subgroup of G, if all elements of H are also elements of G.
- **Order of a group:** The total number of elements in a group is its order.
- **Conjugate Elements:** Two elements g_i, g_j of G are conjugate to each other if there exists another element g_k in G, such that $g_i = g_k g_j g_k^{-1}$. Importantly, if g_i is conjugate to g_j, and g_j is conjugate to g_l, then g_i is conjugate to g_l.
- **Classes:** A class of conjugate elements (or just *class*) is a set of all elements of a group which are conjugate to each other. Each set is completely defined by one of its elements g_i, since the rest of them can be found by forming the products Gg_iG^{-1}, where successively the product is performed over all remaining elements of

the group. Therefore, the whole group can be divided into classes and each element can only appear in one class. Since the unit element of a group commutes with all other elements, it always forms a class on its own. Importantly, classes are not groups themselves.

A.2 Representations

Definition of Representations. To illustrate the meaning of a representation of a group, it is instructive to discuss the effect of group transformations on some function f_1. By applying all transformations of the group G, we obtain n new functions, where n is the order of the group. We can expect that while some of these functions may be linearly dependent, a subset of $d \leq n$ functions f_1, f_2, ..., f_m are linearly independent. Thus, the function obtained by applying an arbitrary transformation g from G to one of the functions f_i will be a linear combination of all linearly independent f_i $(i = 1, ..., d)$, i.e.

$$g f_i = \sum_{j=1}^{d} G_{ji} f_j, \tag{A.1}$$

where the constants G_{ij} correspond to the group element g. The full matrix G_{ij} is called the *matrix* of the transformation g. The full set of matrices of all the elements in a group is called a *representation* of the group. The set of linearly independent functions f_i $(i = 1, ..., d)$ with respect to which these matrices are defined is called the *basis* of the representation, and the number d of these functions is called the *dimension* of the representation.

Characters. An important quantity characterizing a representation are its *characters*. A character is defined as the trace of a matrix representing an element g of a group G. It is therefore unique to the group element and a specific representation. We will refer to the character of g as $\chi(g)$. From this definition follows that the character of the unit element $\chi(e)$ is the dimension of the representation.

Irreducible Representations. Representations can be split into *reducible* and *irreducible* representations: Consider a representation of dimension d with basis f_1, f_2, ..., f_d. Assume there exists a linear transformation which divides the basis into several subsets, such that if any element of the group acts on a basis function of a given subset, the resulting function is a linear combination only of basis functions of the same subset and does not involve other subsets. A representation for which such a linear transformation exists is called reducible. On the other hand, if no such linear transformation (by which the number of basis functions that are transformed only into combinations of themselves is reduced) exists, the representation is called irreducible. Any reducible representation can always be decomposed into irreducible ones, meaning any function can be written as a sum of functions transforming according to irreducible representations. It is therefore sufficient to focus on the properties of irreducible representations:

- For a given representation, all matrices representing group elements belonging to the same class have the same characters.
- If and only if two irreducible representations have the same characters, they are *equivalent* (meaning there is a linear unitary transformation transforming one basis into the other).
- The number of irreducible representations is equal to the number of classes in a group.
- Among the irreducible representations of a group, there always exists a one-dimensional *identity representation* for which all characters are 1. In other words, the basis functions transforming according to the identity representation are invariant under all elements of the group.

Direct Product. Consider the bases f_1, ..., f_n, and h_1, ..., h_m of an n- and m-dimensional irreducible representation, respectively. Forming the products of all basis functions $f_i h_j$, we obtain $n \cdot m$ functions which can serve as the basis of a new representation. This new representation is the *direct product* of the original two irreducible representations, and it is in general a reducible representation. More precisely, the direct product of two irreducible representations is only another irreducible representation if one of the two original ones has dimension one.

A special case arises when the direct product of an irreducible representation is formed with itself. For an explicit construction, consider two different sets of basis functions f_1, ..., f_n, and f'_1, ..., f'_n of the same representation, with the direct product being the collection of functions created by $f_i f'_j$. We can divide these resulting functions into *symmetric* products $f_i f'_j + f_j f'_i$, and *antisymmetric* products $f_i f'_j - f_j f'_i$ $(i \neq j)$. Since f_i and f'_i are both basis functions of the same representation, symmetric (antisymmetric) products transform into linear combinations of only symmetric (antisymmetric) products. In other words, the sets of symmetric and antisymmetric product functions each form a basis for a different representation (note that neither of these new representations is required to be irreducible). The characters for the symmetric χ_{symm} and antisymmetric χ_{asymm} direct products of a given element g with itself are given by

$$\chi^2_{symm}(g) = \frac{1}{2}\left[\chi(g)^2 + \chi(g^2)\right], \tag{A.2}$$

$$\chi^2_{asymm}(g) = \frac{1}{2}\left[\chi(g)^2 - \chi(g^2)\right], \tag{A.3}$$

where $\chi(g)$ is the character of the element g in the original representation.

Real Representations. A representation is *real* if all matrices representing the group transformations are real. A set of complex functions can still be a basis for a real representation. Importantly, all irreducible representations of point groups (see section 2.2) are real. The direct product of a real representation with itself always contains the identity representation. Combining with the fact that the product of any two one-dimensional irreducible representations is also one-dimensional (the product of two irreducible representations of orders n and m is at most $n \cdot m$), we have that any product of a real one-dimensional representation with itself is always identical to the identity representation. The identity representation is, however, never present in the direct product of two different real representations.

APPENDIX B

POINT GROUPS

B.1 General Point Group Operations

Point groups contain symmetry operations which leave at least one point of the lattice fixed. These operations include:

- $\mathbf{C_n}$: Rotation of angle $2\pi/n$ about some axis. The notation C_n^k indicates the group element obtained by k successive rotations, i.e. a rotation of $k \cdot 2\pi/n$ about the axis of rotation (k is an integer).
- $\boldsymbol{\sigma}$ **:** Reflection off a plane. In general, mirror planes perpendicular to a given axis are denoted by σ_h, whereas mirror planes parallel to a given axis are denoted by σ_v.
- $\mathbf{S_n}$: Rotation of angle $2\pi/n$ about some axis, followed by a reflection off a plane perpendicular to the rotation axis.
- **I** : Inversion about a center of symmetry.

An important relation is given by

$$\sigma' = \sigma C_n^k, \tag{B.1}$$

where σ' and σ are mirror planes intersecting at an angle $(k \cdot 2\pi/n)/2$ and C_n^k is a rotation of angle $k \cdot 2\pi/n$ about the axis defined by the line of intersection between the two mirror planes.

A point group can only contain the above operations in a way such that all axes or planes of symmetry intersect in at least one point. Otherwise, successive application of symmetry operations can violate the requirement that one point needs to remain fixed at all times.

There are a total of 32 point groups describing the symmetries of crystal lattices [15, 16, 18]. Below we will discuss the groups O_h and D_{nh}. They describe the crystal lattices of highest symmetry, achieved by unit cells of higher or equivalent symmetry as the Bravais lattice.

B.2 D_{nh}

Symmetry Transformations of D_{nh}. The crystal structures described by the D_{nh} point groups are orthorhombic (D_{2h}), tetragonal (D_{4h}), and hexagonal (D_{6h}) lattices. When discussing the different classes in the D_{nh} point groups, one needs to differentiate even and odd n. Here we will restrict ourselves the case of even n, a full discussion on both cases can be found in [16, Chapter 12, subsection 93]. D_{nh} groups are generated by one n-fold axis of symmetry (C_n), one 2-fold axis of symmetry (C_2) perpendicular to it, and one horizontal mirror plane σ_h perpendicular to the n-fold rotation axis and passing through the 2-fold rotation axis. The remaining elements of the group are obtained by forming all possible products of the above elements. They include n vertical mirror planes σ_v parallel to the n fold rotation axis. A first one of these mirror planes can be thought of as the product of the horizontal mirror plane and the 2-fold rotation axis ($\sigma_v = \sigma_h C_2$ according to Equation B.1). The remaining vertical mirror planes are then created as the product of an existing vertical mirror plane and a rotation of angle $k \cdot 2\pi/n$ about the n-fold rotation axis ($\sigma_v' = \sigma_v C_n^k$, again according to Equation B.1). Using the relation in Equation B.1 one more time, each new vertical mirror plane can be associated with a 2-fold rotation axis through $C_2 = \sigma_v \sigma_h$. These rotation axes are the intersection lines between the vertical and horizontal mirror planes. These operations result in n 2-fold rotation axes in the plane of the horizontal mirror plane and each separated by an angle of $(2\pi/n)/2$, and n vertical mirror planes, each spanned by one 2-fold rotation axis and the n-fold rotation axis. Additional elements are n rotary-reflection transformations S_n ($S_n = C_n \sigma_h$), and the inversion operation i. However, the latter only exists for even n ($I = S_2 = S_n^{n/2} = C_n^{n/2} \sigma_h$ is only contained in D_{nh} if n is even, such that the n-fold rotation axis contains a rotation about π).

Classes of D_{nh}. As mentioned in section 2.1 we can organize group elements into classes, whereby group elements of the same class have the same character for a given representation. Furthermore, irreducible representations are uniquely identified by their sets of characters for each class. It is therefore instructive to find the different classes of the D_{nh} point groups. Notably, two rotations through the same angle belong to the same class, if their rotation axes can be transformed into each other by an element of the group. Equivalently, two reflections belong to the same class, if their mirror planes can be transformed into each other.

The identity element e always forms its own class, since it commutes with every other element of the group. Additionally, the mirror planes σ_v relate the rotations C_n^k and C_n^{-k}, such that they all form their own classes. Special cases arise for C_n^n and $C_n^{n/2}$. The former is identical to the identity representation and for the latter we have $C_n^{n/2} = C_n^{-n/2} = C_2$, which forms its own C_2 class. Thus, there are $(n-2)/2$ additional classes (each containing 2 elements) related to the n-fold rotational symmetry axis. Further, all 2-fold rotation axes separated by an angle of $k \cdot 2\pi/n$ belong to the same class. However, as mentioned

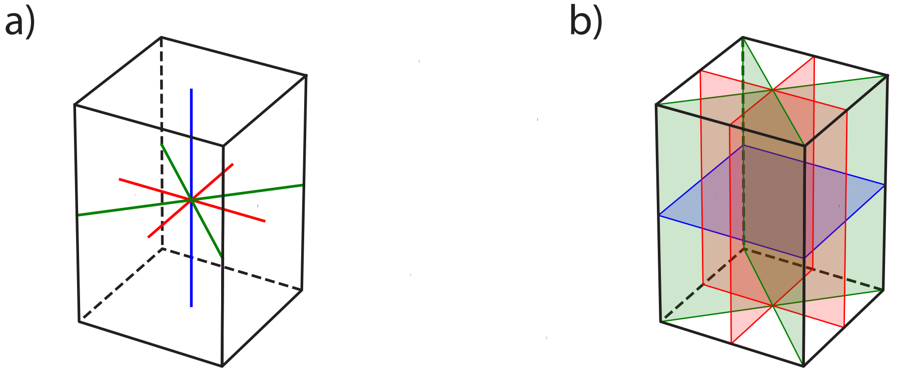

Figure B.1: **$\mathbf{D_{4h}}$ symmetry operations.** All rotational symmetry axes of the D_{4h} point group are shown in panel a). Axes with the same colors belong the same class. Blue is a 4-fold rotational symmetry axis, whereas red and green are 2-fold axes. The same axes are the basis of all rotary-reflection operations. b) shows all mirror planes. Different colors are again indicating different classes. Blue is σ_h, red is σ_v and green is σ_d.

above, for even n, 2-fold rotation axes exist every $(2\pi/n)/2$, such that there are two different classes, each containing $n/2$ rotation axes. Furthermore, since the horizontal mirror plane commutes with all other elements in the group, the remaining additional classes are obtained by multiplying the existing ones by σ_h. This results in a class only containing σ_h (by multiplying it with e), and $(n-2)/2$ classes of n-fold rotary-reflection axes, each containing 2 elements (S_n^k and S_n^{-k} obtained by $C_n^k\sigma_h$). The inverse element, given by $i = C_n^{n/2}\sigma_h$, forms its own class. Lastly, multiplying elements of the two classes containing the 2-fold rotation axes with σ_h gives two more classes each containing $(n/2)$ vertical mirror planes separated by an angle of $2\pi/n$ ($\sigma_v = C_2\sigma_h$).

D_{4h} **Example.** Let us consider the example of the tetragonal point group D_{4h}, describing the symmetries of a cuboid (see Figure B.1). Besides the identity e element, it is characterized by a 4-fold rotation axis C_4 along the z axis (including rotations by $\pi/2$ (C_4^1), π (C_4^2), and $3\pi/2$ (C_4^3)), a horizontal mirror plane σ_h in the $x-y$ plane at $z=0$. There is an additional 4-fold rotary-reflection axis along the z-direction (including three elements $S_4^i = C_4^i\sigma_h$, in analogy to the 4-fold rotation axis). Note that S_4^2 is the inverse element i. Furthermore, there are 4 2-fold rotation axes C_2, lying in the $x-y$ plane at $z=0$, separated by an angle of $\pi/4$. They are conventionally placed along the x and y axes, as well as along the diagonals $x+y$ and $x-y$. These 4 rotation axes each span one mirror plane σ_v with the 4-fold rotation axis, leading to an additional 4 more group elements, resulting in a total of 16 elements for D_{4h}. They can be grouped into 10 classes. From the discussion above, it becomes clear that the group elements e, i, and σ_h each form their own class. The three elements describing rotations about the z axis split into two classes: one class $2C_4$ contains the elements C_4^1 and $C_4^3 = C_4^{-1}$, and one class C_2 contains

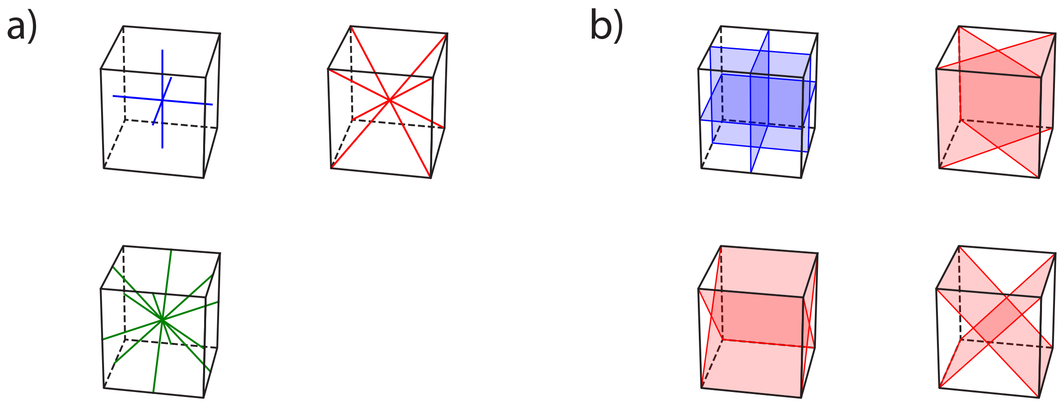

Figure B.2: **$\mathbf{O_h}$ symmetry operations.** a) shows all rotational symmetry axes: blue are 4-fold axes, red are 3-fold axes, and green are 2-fold axes. All axes of the same color can be related by a symmetry element of the O_h point group. b) shows all mirror planes. Planes of the same color belong to the same class. Blue is σ_h and red is σ_d.

the element $C_4^2 = C_2$. Besides the inversion element $i = S_4^2$, there are only two more rotary-reflection operations S_4^1 and $S_4^3 = S_4^-1$ which form one class $2S_4$. What remains are the group elements reflecting the 2-fold rotational symmetries and the vertical mirror planes. As mentioned above, all 2-fold symmetry operations fall into the same class if the rotation axes are separated by $\pi/2$. For D_{4h} there are thus 2 different classes $2C_2'$ and $2C_2''$, each containing 2 group elements. Conventionally, $2C_2'$ contains two-fold rotations about the x and y axes, whereas $2C_2''$ contains two-fold rotations about $x + y$ and $x - y$. The two remaining classes are usually labelled $2\sigma_v$ and $2\sigma_d$. $2\sigma_v$ contains the two vertical mirror planes along x and y axes, and $2\sigma_d$ contains the two vertical mirror planes along the diagonals $x + y$ and $x - y$.

B.3 O_h

The point group O_h describes the full symmetry of a cube. It contains 48 elements, which can be grouped into 10 classes (see Figure B.2).

Again, the identity e and inversion i elements each form their own class. The class $8C_3$ contains the eight rotations of $2\pi/3$ (C_3^1) and $4\pi/3$ (C_3^2) about each of the 4 body diagonals of the cube (i.e. the lines connecting opposite corners; those are 3-fold rotation axes). $6C_4$ is the class containing the six rotations of $\pi/2$ (C_4^1) and $3\pi/2$ (C_4^3) about each of the 3 axes connecting the midpoint of opposite faces (i.e. lines along the x, y, and z axes; they are 4-fold rotation axes). Each of these three rotation axes leads to one more element C_4^2 which form an additional class (usually labelled $3C_2$). There are also 6 equivalent 2-fold rotation axes connecting the midpoints of opposite edges, forming the

	e	C_2	C_2'	C_2''	i	σ_h	σ_v	σ_d
A_g	1	1	1	1	1	1	1	1
B_{1g}	1	1	-1	-1	1	1	-1	-1
B_{2g}	1	-1	-1	1	1	-1	1	-1
B_{3g}	1	-1	1	-1	1	-1	-1	1
A_u	1	1	1	1	-1	-1	-1	-1
B_{1u}	1	1	-1	-1	-1	-1	1	1
B_{2u}	1	-1	-1	1	-1	1	-1	1
B_{3u}	1	-1	1	-1	-1	1	1	-1

Table B.1: **$\mathbf{D_{2h}}$ character table.** Characters for all 8 irreducible representations and classes of the D_{2h} point group are shown. Table adapted from [20].

class $6C_2'$ with 6 elements. The remaining group elements and classes can be deduced by multiplying the existing ones with the inverse element. They are $8S_6$—a class of 8 6-fold rotary-reflection operations, obtained by multiplying the elements of the class $8C_3$ with i—and $6S_4$—6 4-fold rotary-reflection axes obtained by multiplying the elements in $6C_4$ with i. Multiplying the remaining two classes $3C_2$ and $6C_2'$ with i, we obtain $3\sigma_h$ and $6\sigma_d$, respectively. $3\sigma_h$ contains three horizontal mirror plane operations defined by the $x = 0$, $y = 0$, and $z = 0$ planes, respectively. $6\sigma_d$ contains the mirror planes connecting two opposite edges of the cube.

B.4 Character Tables for D_{2h} and D_{6h}

Shown are the character tables for the orthorhombic (D_{2h}, Table B.1) and hexagonal (D_{6h}, Table B.2) point groups.

	e	$2C_6$	$2C_3$	C_2	$3C_2'$	$3C_2''$	i	$2S_6$	$2S_3$	σ_h	$3\sigma_v$	$3\sigma_d$
A_{1g}	1	1	1	1	1	1	1	1	1	1	1	1
A_{2g}	1	1	1	1	-1	-1	1	1	1	1	-1	-1
B_{1g}	1	-1	1	-1	1	-1	1	1	-1	-1	-1	1
B_{2g}	1	-1	1	-1	-1	1	1	1	-1	-1	1	-1
E_{1g}	2	1	-1	-2	0	0	2	-1	1	-2	0	0
E_{2g}	2	-1	-1	2	0	0	2	-1	-1	2	0	0
A_{1u}	1	1	1	1	1	1	-1	-1	-1	-1	-1	-1
A_{2u}	1	1	1	1	-1	-1	-1	-1	-1	-1	1	1
B_{1u}	1	-1	1	-1	1	-1	-1	-1	1	1	1	-1
B_{2u}	1	-1	1	-1	-1	1	-1	-1	1	1	-1	1
E_{1u}	2	1	-1	-2	0	0	-2	1	-1	2	0	0
E_{2u}	2	-1	-1	2	0	0	-2	1	1	-2	0	0

Table B.2: **$\mathbf{D_{6h}}$ character table.** Characters for all 12 irreducible representations and classes of the D_{6h} point group are shown. Table adapted from [20].

APPENDIX C

SUM RULE FOR THE $\alpha_{i\mu}$ COEFFICIENTS

Here we want to derive the sum rule

$$\sum_{\mu} \alpha_{i\mu} = 1, \tag{C.1}$$

for the $\alpha_{i\mu}$ coefficients defined in Equation 3.7. Starting from the elastic wave equation in Equation 3.3 and expanding the displacement in basis functions, we can write (see chapter 4 for details)

$$\omega_i^2 E a_i = \Gamma a_i, \tag{C.2}$$

where E is the kinetic energy matrix, Γ is the potential energy matrix, ω_i are the resonance frequencies, and a_i are the eigenvectors representing the displacement of the corresponding eigenvalue ω_i expanded in the chosen basis. In the particular way we create E and Γ, we have that E is diagonal, $\Gamma^T = \Gamma$, and Γ is linear in elastic moduli, such that we can write $\Gamma = \sum_\mu c_\mu M_\mu$, where M_μ is independent of elastic moduli. Furthermore, the solutions to Equation C.2 are only defined up to a normalization factor. In the following we will choose a normalization, such that $a^T E a = 1$. With these prerequisites, taking a derivative of Equation C.2 with respect to c_μ we get

$$\frac{\partial}{\partial c_\mu}\left(\omega_i^2 E a_i\right) = \frac{\partial}{\partial c_\mu}\left(\Gamma a_i\right), \tag{C.3}$$

$$\Leftrightarrow \quad \frac{\partial \omega_i^2}{\partial c_\mu} E a_i + \omega_i^2 \frac{\partial E}{\partial c_\mu} a_i + \omega_i^2 E \frac{\partial a_i}{\partial c_\mu} = \frac{\partial \Gamma}{\partial c_\mu} a_i + \Gamma \frac{\partial a_i}{\partial c_\mu}. \tag{C.4}$$

Realizing that E is independent of c_μ and multiplying Equation C.4 with a_i^T on the left, we get

$$\frac{\partial \omega_i^2}{\partial c_\mu} a_i^T E a_i + \omega_i^2 a_i^T E \frac{\partial a_i}{\partial c_\mu} = a_i^T \frac{\partial \Gamma}{\partial c_\mu} a_i + a_i^T \Gamma \frac{\partial a_i}{\partial c_\mu}. \tag{C.5}$$

Transposing Equation C.2 and using $\Gamma^T = \Gamma$ we also have that $\omega_i^2 a_i^T E = a_i^T \Gamma$, such that Equation C.5 becomes

$$\frac{\partial \omega_i^2}{\partial c_\mu} a_i^T E a_i = a_i^T \frac{\partial \Gamma}{\partial c_\mu} a_i, \tag{C.6}$$

$$\Leftrightarrow \quad \frac{\partial \omega_i^2}{\partial c_\mu} = a_i^T \frac{\partial \Gamma}{\partial c_\mu} a_i, \tag{C.7}$$

where we have used that $a_i^T E a_i = 1$. Using $\Gamma = \sum_\mu c_\mu M_\mu$, Equation C.7 becomes

$$2\omega_i \frac{\partial \omega_i}{\partial c_\mu} = a_i^T M_\mu a_i, \tag{C.8}$$

$$\Rightarrow \sum_\mu 2 \frac{\partial \omega_i}{\partial c_\mu} \frac{c_\mu}{\omega_i} = a_i^T \left(\sum_\mu c_\mu M_\mu \right) a_i \frac{1}{\omega_i^2}, \tag{C.9}$$

$$\Leftrightarrow \sum_\mu \frac{\partial \ln \omega_i^2}{\partial \ln c_\mu} = a_i^T \omega_i^2 E a_i \frac{1}{\omega_i^2}, \tag{C.10}$$

$$\Leftrightarrow \sum_\mu \alpha_{i\mu} = a_i^T E a_i = 1, \tag{C.11}$$

where in the first step we have multiplied both sides by $\frac{c_\mu}{\omega_i^2}$ and summed both sides over μ.

APPENDIX D

RUS FORWARD CALCULATION FOR RECTANGULAR PRISMS

Here, we discuss the forward calculation of RUS resonance spectra for samples in the shape of rectangular prisms. This problem has been previously discussed in [35, 36].

Assuming a constant density throughout the sample, each non-zero element of the kinetic energy matrix in Equation 4.4 is of the form

$$E_{\lambda i \lambda' i} \sim \int \phi_\lambda \phi_{\lambda'} dV = \int x^{l+l'} y^{m+m'} z^{n+n'} dV, \tag{D.1}$$

where we have taken $\lambda = l,\ m,\ n$ and $\lambda' = l',\ m',\ n'$. Performing these integrals becomes straightforward for a sample in the shape of a rectangular prism with dimensions $(a \times b \times c)$. If we center the sample around the origin, Equation D.1 becomes

$$E_{\lambda i \lambda' i} \sim 8 \frac{(a/2)^{l+l'+1}}{l+l'+1} \frac{(b/2)^{m+m'+1}}{m+m'+1} \frac{(c/2)^{n+n'+1}}{n+n'+1}. \tag{D.2}$$

Similarly, assuming constant elastic moduli throughout the sample, we can rewrite the potential energy tensor in Equation 4.5 as

$$\Gamma_{\lambda i \lambda' i'} = \sum_{jj'} c_{iji'j'} G_{\lambda j \lambda' j'}, \tag{D.3}$$

where

$$\begin{aligned} G_{\lambda j \lambda' j'} &= \int \frac{\partial \phi_\lambda}{\partial x_j} \frac{\partial \phi_{\lambda'}}{\partial x_{j'}} dV, && \text{(D.4)} \\ &= \int x^\alpha y^\beta z^\gamma dV, && \text{(D.5)} \\ &= 8 \frac{(a/2)^{\alpha+1}}{\alpha+1} \frac{(b/2)^{\beta+1}}{\beta+1} \frac{(c/2)^{\gamma+1}}{\gamma+1}. && \text{(D.6)} \end{aligned}$$

In the first step, we have summarized $\alpha = l + l' - \delta_{1j} - \delta_{1j'}$, $\beta = m + m' - \delta_{2j} - \delta_{2j'}$, $\gamma = n + n' - \delta_{3j} - \delta_{3j'}$. In the second step, we have again assumed the sample shape to be a rectangular prism with dimensions $(a \times b \times c)$, centered around the origin.

Equation D.2 and Equation D.6 provide closed form expressions for each element of the kinetic and potential energy matrices for the case of a sample in the shape of a rectangular prism. Similarly straightforward expressions can be found for other regular shapes, like cylinders or spheres, or any shape which can be described by a functional form.

Centering the rectangular prism around the origin is not necessary to get the correct resonance frequencies. However, if the crystal symmetry of the material is additionally orthorhombic or higher, both $E_{\alpha\beta}$ and $\Gamma_{\alpha\beta}$ are block-diagonal, with eight blocks [35], significantly increasing the speed of the eigenvalue solver.

APPENDIX E

RUS FOR IRREGULARLY-SHAPED SAMPLES: RESONANCE SPECTRA AND FIT RESULTS

Here, we show the tables containing the experimental resonance frequencies f_{exp} (70 for $SrTiO_3$ and 84 for Mn_3Ge) as well as the calculated frequencies f_{calc} corresponding to the RUS fit results discussed in section 4.3. The tables also contain the difference between measured and calculated frequencies. No difference value is given for the first three resonances of each fit, since these were excluded from the fits. The data for the $SrTiO_3$ samples A (sample in the shape of a rectangular prism) and B (irregularly shaped sample) are shown in Table E.1 and Table E.2, respectively. The data for the Mn_3Ge samples A (sample in the shape of a rectangular prism) and B (irregularly shaped sample) are shown in Table E.3 and Table E.4, respectively. All tables are taken from [43].

Table E.1: **$SrTiO_3$ sample A (regular shape).**

		RPR		SMI		FEM	
Index	f_{exp} (MHz)	f_{calc} (MHz)	diff (%)	f_{calc} (MHz)	diff (%)	f_{calc} (MHz)	diff (%)
1	0.71037	0.70491	-	0.70491	-	0.70489	-
2	0.79197	0.79156	-	0.79156	-	0.79155	-
3	0.89772	0.90185	-	0.90185	-	0.90184	-
4	1.17353	1.17781	0.363	1.17781	0.363	1.17779	0.361
5	1.24570	1.24714	0.116	1.24714	0.116	1.24711	0.113
6	1.33132	1.32506	0.473	1.32506	0.473	1.32504	0.474
7	1.37709	1.38138	0.310	1.38138	0.310	1.38135	0.308
8	1.41735	1.40410	0.944	1.40410	0.944	1.40408	0.945
9	1.50363	1.49941	0.281	1.49941	0.281	1.49939	0.283
10	1.55724	1.55327	0.256	1.55327	0.256	1.55325	0.257
11	1.59727	1.58515	0.765	1.58515	0.765	1.58513	0.766
12	1.60045	1.58865	0.743	1.58865	0.743	1.58863	0.744
13	1.71219	1.71178	0.024	1.71178	0.024	1.71175	0.025
14	1.77642	1.77451	0.108	1.77451	0.108	1.77449	0.109
15	1.78574	1.79251	0.377	1.79251	0.377	1.79247	0.375
16	1.83710	1.84222	0.278	1.84222	0.277	1.84219	0.276
17	1.85498	1.85528	0.016	1.85528	0.016	1.85524	0.014
18	1.91594	1.92356	0.396	1.92356	0.396	1.92353	0.395

Table continued on next page.

Table continued.

		RPR		SMI		FEM	
Index	f_{exp} (MHz)	f_{calc} (MHz)	diff (%)	f_{calc} (MHz)	diff (%)	f_{calc} (MHz)	diff (%)
19	1.97811	1.97315	0.251	1.97315	0.251	1.97314	0.252
20	1.98353	1.98541	0.095	1.98541	0.095	1.98538	0.093
21	2.03547	2.04563	0.496	2.04563	0.496	2.04559	0.495
22	2.07281	2.07985	0.338	2.07985	0.338	2.07982	0.337
23	2.16306	2.17696	0.638	2.17696	0.639	2.17695	0.638
24	2.17570	2.17867	0.136	2.17867	0.136	2.17864	0.135
25	2.20327	2.21156	0.375	2.21156	0.375	2.21154	0.374
26	2.20830	2.21607	0.350	2.21607	0.350	2.21606	0.350
27	2.22903	2.22728	0.078	2.22728	0.078	2.22727	0.079
28	2.23226	2.23763	0.240	2.23763	0.240	2.23761	0.239
29	2.23351	2.23846	0.221	2.23846	0.221	2.23845	0.221
30	2.28139	2.27258	0.388	2.27258	0.388	2.27258	0.388
31	2.32126	2.31051	0.465	2.31051	0.465	2.31052	0.465
32	2.33100	2.32182	0.395	2.32182	0.395	2.32180	0.396
33	2.34719	2.34083	0.272	2.34083	0.272	2.34082	0.272
34	2.44146	2.44675	0.216	2.44675	0.216	2.44674	0.216
35	2.46013	2.45143	0.355	2.45142	0.355	2.45144	0.355
36	2.50210	2.50958	0.298	2.50958	0.298	2.50956	0.297
37	2.50662	2.50968	0.122	2.50968	0.122	2.50965	0.121
38	2.53756	2.53887	0.051	2.53887	0.051	2.53889	0.052
39	2.57650	2.57679	0.011	2.57679	0.011	2.57680	0.012
40	2.58500	2.59496	0.384	2.59496	0.384	2.59496	0.384
41	2.59850	2.59922	0.028	2.59922	0.028	2.59920	0.027
42	2.62865	2.63115	0.095	2.63116	0.095	2.63117	0.096
43	2.65167	2.65229	0.023	2.65229	0.023	2.65226	0.022
44	2.68309	2.68338	0.011	2.68338	0.011	2.68338	0.011
45	2.70518	2.70901	0.141	2.70901	0.141	2.70898	0.140
46	2.74782	2.74881	0.036	2.74881	0.036	2.74883	0.037
47	2.75176	2.75107	0.025	2.75107	0.025	2.75107	0.025
48	2.75392	2.76091	0.253	2.76091	0.253	2.76092	0.254
49	2.78789	2.79403	0.220	2.79403	0.220	2.79408	0.221
50	2.80071	2.79544	0.189	2.79545	0.188	2.79545	0.188
51	2.82197	2.82346	0.053	2.82346	0.053	2.82352	0.055
52	2.84439	2.85166	0.255	2.85167	0.255	2.85166	0.255
53	2.91635	2.91928	0.101	2.91928	0.101	2.91931	0.102
54	2.92322	2.92473	0.051	2.92473	0.051	2.92478	0.053
55	2.94885	2.92904	0.677	2.92904	0.677	2.92902	0.677
56	3.00333	2.99929	0.135	2.99929	0.135	2.99940	0.131
57	3.01642	3.01070	0.190	3.01070	0.190	3.01074	0.189
58	3.03353	3.03246	0.035	3.03246	0.036	3.03254	0.033

Table continued on next page.

Table continued.

		RPR		SMI		FEM	
Index	f_{exp} (MHz)	f_{calc} (MHz)	diff (%)	f_{calc} (MHz)	diff (%)	f_{calc} (MHz)	diff (%)
59	3.03869	3.04328	0.151	3.04328	0.151	3.04332	0.152
60	3.06889	3.06572	0.103	3.06572	0.103	3.06574	0.103
61	3.13815	3.14283	0.149	3.14283	0.149	3.14288	0.151
62	3.15099	3.15332	0.074	3.15332	0.074	3.15339	0.076
63	3.15918	3.16111	0.061	3.16111	0.061	3.16112	0.062
64	3.16664	3.16975	0.098	3.16975	0.098	3.16985	0.101
65	3.22486	3.22895	0.127	3.22895	0.127	3.22893	0.126
66	3.22600	3.23110	0.158	3.23110	0.158	3.23107	0.157
67	3.25102	3.24020	0.334	3.24020	0.334	3.24033	0.330
68	3.25333	3.24905	0.132	3.24905	0.132	3.24915	0.129
69	3.26656	3.25129	0.470	3.25129	0.470	3.25141	0.466
70	3.27348	3.28127	0.237	3.28127	0.237	3.28131	0.239

Table E.2: **$SrTiO_3$ sample B (irregular shape).**

		SMI		FEM	
Index	f_{exp} (MHz)	f_{calc} (MHz)	diff (%)	f_{calc} (MHz)	diff (%)
1	1.10869	1.09168	-	1.09156	-
2	1.20480	1.19121	-	1.19112	-
3	1.52331	1.50347	-	1.50341	-
4	1.88059	1.86636	0.762	1.86620	0.771
5	1.97243	1.97144	0.050	1.97135	0.055
6	1.98450	1.98777	0.164	1.98756	0.154
7	2.07997	2.07118	0.424	2.07100	0.433
8	2.15054	2.14467	0.274	2.14453	0.280
9	2.23955	2.23207	0.335	2.23186	0.344
10	2.37823	2.36840	0.415	2.36833	0.418
11	2.43553	2.44027	0.194	2.44001	0.184
12	2.58487	2.57275	0.471	2.57258	0.478
13	2.72511	2.71927	0.215	2.71912	0.220
14	2.80098	2.79093	0.360	2.79078	0.366
15	2.83415	2.83210	0.072	2.83199	0.077
16	2.87280	2.86311	0.339	2.86304	0.341
17	2.92701	2.91494	0.414	2.91473	0.421
18	3.07796	3.07446	0.114	3.07432	0.118
19	3.13235	3.14863	0.517	3.14864	0.517
20	3.16734	3.16494	0.076	3.16486	0.079
21	3.18282	3.18195	0.027	3.18191	0.029
22	3.25382	3.24307	0.331	3.24298	0.334

Table continued on next page.

Table continued.

		SMI		FEM	
Index	f_{exp} (MHz)	f_{calc} (MHz)	diff (%)	f_{calc} (MHz)	diff (%)
23	3.29615	3.29027	0.179	3.29022	0.180
24	3.31731	3.33535	0.541	3.33524	0.538
25	3.48056	3.50474	0.690	3.50469	0.688
26	3.51006	3.52415	0.400	3.52412	0.399
27	3.65645	3.66182	0.147	3.66178	0.145
28	3.78318	3.79193	0.231	3.79191	0.230
29	3.84523	3.84207	0.082	3.84198	0.085
30	3.89894	3.90375	0.123	3.90368	0.122
31	3.98772	3.99729	0.239	3.99727	0.239
32	4.00064	4.00409	0.086	4.00407	0.086
33	4.06006	4.04985	0.252	4.04979	0.254
34	4.10005	4.10447	0.108	4.10444	0.107
35	4.15255	4.14028	0.296	4.14022	0.298
36	4.18979	4.20182	0.286	4.20174	0.284
37	4.23696	4.22814	0.209	4.22819	0.207
38	4.27449	4.28863	0.330	4.28857	0.328
39	4.30861	4.31115	0.059	4.31124	0.061
40	4.34986	4.35327	0.078	4.35335	0.080
41	4.39819	4.39097	0.165	4.39113	0.161
42	4.46403	4.46713	0.069	4.46719	0.071
43	4.48597	4.47481	0.249	4.47493	0.247
44	4.63845	4.62951	0.193	4.62957	0.192
45	4.68243	4.69013	0.164	4.69022	0.166
46	4.74359	4.74395	0.008	4.74417	0.012
47	4.75697	4.76987	0.270	4.76996	0.272
48	4.80223	4.79540	0.142	4.79552	0.140
49	4.82394	4.84266	0.387	4.84274	0.388
50	4.89389	4.90448	0.216	4.90445	0.215
51	4.93746	4.93653	0.019	4.93677	0.014
52	4.98372	4.98686	0.063	4.98700	0.066
53	5.00140	5.00252	0.022	5.00247	0.021
54	5.03260	5.03444	0.037	5.03457	0.039
55	5.06065	5.06660	0.117	5.06673	0.120
56	5.10892	5.10434	0.090	5.10460	0.085
57	5.12704	5.12970	0.052	5.12991	0.056
58	5.16940	5.18029	0.210	5.18061	0.216
59	5.20187	5.23093	0.556	5.23130	0.562
60	5.25259	5.25272	0.002	5.25278	0.004
61	5.27776	5.27884	0.020	5.27913	0.026
62	5.28863	5.29927	0.201	5.29969	0.209

Table continued on next page.

Table continued.

Index	f_{exp} (MHz)	SMI		FEM	
		f_{calc} (MHz)	diff (%)	f_{calc} (MHz)	diff (%)
63	5.33266	5.33158	0.020	5.33170	0.018
64	5.37012	5.35725	0.240	5.35743	0.237
65	5.40014	5.39589	0.079	5.39627	0.072
66	5.43224	5.43571	0.064	5.43599	0.069
67	5.45845	5.45699	0.027	5.45728	0.021
68	5.49232	5.49778	0.099	5.49816	0.106
69	5.54920	5.55358	0.079	5.55405	0.087
70	5.58061	5.58871	0.145	5.58914	0.153

Table E.3: **Mn_3Ge sample A (regular shape).**

Index	f_{exp} (MHz)	RPR		SMI		FEM	
		f_{calc} (MHz)	diff (%)	f_{calc} (MHz)	diff (%)	f_{calc} (MHz)	diff (%)
1	0.96469	0.95542	-	0.95544	-	0.95531	-
2	1.31011	1.31762	-	1.31764	-	1.31751	-
3	1.46748	1.46874	-	1.46876	-	1.46855	-
4	1.50955	1.50952	0.002	1.50951	0.002	1.50947	0.005
5	1.56402	1.56137	0.169	1.56136	0.170	1.56127	0.176
6	1.57830	1.57952	0.077	1.57951	0.077	1.57945	0.073
7	1.58425	1.60049	1.015	1.60051	1.016	1.60029	1.002
8	1.60141	1.61340	0.743	1.61340	0.743	1.61327	0.735
9	1.60582	1.61949	0.845	1.61951	0.846	1.61938	0.838
10	1.78631	1.80175	0.857	1.80177	0.858	1.80162	0.850
11	1.82036	1.81183	0.471	1.81182	0.471	1.81169	0.478
12	1.87303	1.87322	0.010	1.87322	0.010	1.87313	0.005
13	1.94132	1.93235	0.464	1.93233	0.465	1.93222	0.471
14	1.95112	1.95456	0.176	1.95455	0.175	1.95451	0.173
15	2.03329	2.02996	0.164	2.02997	0.164	2.02986	0.169
16	2.09609	2.08355	0.602	2.08353	0.603	2.08339	0.610
17	2.10555	2.10872	0.150	2.10867	0.148	2.10854	0.142
18	2.14587	2.12376	1.041	2.12373	1.043	2.12363	1.047
19	2.16239	2.17045	0.371	2.17041	0.369	2.17050	0.374
20	2.16541	2.17570	0.473	2.17572	0.474	2.17548	0.463
21	2.25310	2.26434	0.496	2.26437	0.497	2.26423	0.491
22	2.32002	2.30809	0.517	2.30807	0.518	2.30797	0.522
23	2.37049	2.35061	0.846	2.35060	0.846	2.35052	0.849
24	2.38275	2.38340	0.027	2.38330	0.023	2.38334	0.024
25	2.43586	2.41898	0.698	2.41896	0.699	2.41890	0.701
26	2.46256	2.47420	0.471	2.47422	0.471	2.47413	0.468

Table continued on next page.

Table continued.

		RPR		SMI		FEM	
Index	f_{exp} (MHz)	f_{calc} (MHz)	diff (%)	f_{calc} (MHz)	diff (%)	f_{calc} (MHz)	diff (%)
27	2.47301	2.47498	0.080	2.47498	0.080	2.47483	0.073
28	2.52384	2.55083	1.058	2.55069	1.053	2.55063	1.051
29	2.55464	2.57203	0.676	2.57205	0.677	2.57190	0.671
30	2.57758	2.59117	0.524	2.59118	0.525	2.59105	0.520
31	2.61331	2.62284	0.363	2.62282	0.363	2.62273	0.359
32	2.65457	2.64939	0.196	2.64940	0.195	2.64940	0.195
33	2.71919	2.72259	0.125	2.72258	0.124	2.72248	0.121
34	2.75160	2.74615	0.198	2.74616	0.198	2.74602	0.203
35	2.78098	2.77733	0.131	2.77734	0.131	2.77722	0.135
36	2.84224	2.83905	0.112	2.83904	0.113	2.83904	0.113
37	2.86041	2.86306	0.092	2.86298	0.090	2.86289	0.086
38	2.87166	2.86844	0.112	2.86847	0.111	2.86843	0.113
39	2.91103	2.92610	0.515	2.92611	0.516	2.92617	0.518
40	2.93140	2.92769	0.127	2.92770	0.126	2.92756	0.131
41	2.93455	2.93191	0.090	2.93190	0.090	2.93189	0.091
42	2.94156	2.94237	0.027	2.94237	0.028	2.94228	0.024
43	3.04438	3.05124	0.225	3.05123	0.224	3.05109	0.220
44	3.10644	3.09616	0.332	3.09616	0.332	3.09622	0.330
45	3.12912	3.13303	0.125	3.13303	0.125	3.13297	0.123
46	3.19343	3.17795	0.487	3.17796	0.487	3.17801	0.485
47	3.21141	3.21040	0.031	3.21041	0.031	3.21032	0.034
48	3.28658	3.28210	0.136	3.28212	0.136	3.28219	0.134
49	3.30955	3.29828	0.342	3.29828	0.342	3.29851	0.335
50	3.31565	3.32261	0.209	3.32261	0.209	3.32258	0.209
51	3.35754	3.37386	0.484	3.37387	0.484	3.37382	0.482
52	3.38287	3.37789	0.147	3.37786	0.148	3.37795	0.146
53	3.44121	3.45795	0.484	3.45795	0.484	3.45796	0.484
54	3.47190	3.46067	0.324	3.46069	0.324	3.46107	0.313
55	3.49421	3.48695	0.208	3.48694	0.208	3.48696	0.208
56	3.49812	3.50059	0.071	3.50057	0.070	3.50061	0.071
57	3.49964	3.51232	0.361	3.51236	0.362	3.51229	0.360
58	3.54746	3.53238	0.427	3.53237	0.427	3.53259	0.421
59	3.57278	3.56487	0.222	3.56488	0.222	3.56526	0.211
60	3.58496	3.57191	0.365	3.57191	0.365	3.57200	0.363
61	3.58767	3.59720	0.265	3.59714	0.263	3.59709	0.262
62	3.60231	3.60308	0.022	3.60311	0.022	3.60304	0.020
63	3.60760	3.60521	0.066	3.60521	0.066	3.60540	0.061
64	3.61308	3.60655	0.181	3.60655	0.181	3.60663	0.179
65	3.61436	3.61431	0.001	3.61432	0.001	3.61455	0.005
66	3.61865	3.62068	0.056	3.62069	0.057	3.62084	0.060

Table continued on next page.

Table continued.

		RPR		SMI		FEM	
Index	f_{exp} (MHz)	f_{calc} (MHz)	diff (%)	f_{calc} (MHz)	diff (%)	f_{calc} (MHz)	diff (%)
67	3.64765	3.64158	0.167	3.64152	0.168	3.64153	0.168
68	3.67018	3.64580	0.669	3.64580	0.669	3.64602	0.663
69	3.71718	3.70179	0.416	3.70179	0.416	3.70203	0.409
70	3.72327	3.72386	0.016	3.72386	0.016	3.72412	0.023
71	3.78761	3.79633	0.230	3.79635	0.230	3.79659	0.237
72	3.81140	3.80554	0.154	3.80556	0.153	3.80579	0.147
73	3.84430	3.82293	0.559	3.82295	0.559	3.82310	0.554
74	3.86988	3.84886	0.546	3.84885	0.546	3.84915	0.539
75	3.91723	3.91340	0.098	3.91339	0.098	3.91352	0.095
76	3.94563	3.92345	0.565	3.92345	0.565	3.92395	0.552
77	3.97908	3.97784	0.031	3.97787	0.030	3.97802	0.027
78	3.99942	3.99986	0.011	3.99985	0.011	4.00031	0.022
79	4.01915	4.00900	0.253	4.00903	0.252	4.00943	0.242
80	4.03495	4.02355	0.284	4.02355	0.283	4.02443	0.262
81	4.04595	4.06045	0.357	4.06046	0.357	4.06074	0.364
82	4.05758	4.06567	0.199	4.06558	0.197	4.06568	0.199
83	4.06491	4.08637	0.525	4.08631	0.524	4.08631	0.524
84	4.0780	4.09008	0.295	4.09004	0.294	4.09015	0.297

Table E.4: **Mn_3Ge sample B (irregular shape).**

		SMI		FEM	
Index	f_{exp} (MHz)	f_{calc} (MHz)	diff (%)	f_{calc} (MHz)	diff (%)
1	0.77100	0.72927	-	0.72932	-
2	1.08478	1.06421	-	1.06356	-
3	1.22382	1.21029	-	1.21031	-
4	1.33437	1.32618	0.618	1.32623	0.614
5	1.44953	1.43028	1.346	1.43030	1.344
6	1.60718	1.59563	0.723	1.59565	0.722
7	1.86078	1.84572	0.816	1.84544	0.831
8	1.88524	1.88848	0.172	1.88804	0.148
9	2.02059	2.01970	0.044	2.01929	0.064
10	2.06617	2.03724	1.420	2.03660	1.452
11	2.12700	2.11597	0.521	2.11593	0.523
12	2.30712	2.29890	0.358	2.29885	0.360
13	2.33951	2.33223	0.312	2.33215	0.316
14	2.44134	2.43977	0.064	2.43948	0.076
15	2.48376	2.48460	0.034	2.48477	0.040
16	2.66501	2.66902	0.150	2.66862	0.135

Table continued on next page.

Table continued.

		SMI		FEM	
Index	f_{exp} (MHz)	f_{calc} (MHz)	diff (%)	f_{calc} (MHz)	diff (%)
17	2.75780	2.74510	0.463	2.74453	0.484
18	2.78254	2.78677	0.152	2.78699	0.160
19	2.83647	2.82217	0.507	2.82196	0.514
20	2.97943	2.99342	0.467	2.99356	0.472
21	3.01159	3.01770	0.203	3.01823	0.220
22	3.07402	3.09174	0.573	3.09132	0.560
23	3.13148	3.13824	0.215	3.13768	0.198
24	3.16311	3.17632	0.416	3.17606	0.408
25	3.24362	3.25436	0.330	3.25461	0.338
26	3.25447	3.27058	0.492	3.27034	0.485
27	3.30929	3.30305	0.189	3.30309	0.188
28	3.40908	3.42759	0.540	3.42754	0.539
29	3.46136	3.46796	0.190	3.46799	0.191
30	3.53828	3.52248	0.449	3.52213	0.459
31	3.58063	3.59778	0.477	3.59745	0.468
32	3.64885	3.64490	0.108	3.64495	0.107
33	3.70451	3.68606	0.500	3.68572	0.510
34	3.73124	3.74476	0.361	3.74458	0.356
35	3.77514	3.78817	0.344	3.78828	0.347
36	3.81664	3.81972	0.081	3.82010	0.091
37	3.84659	3.86236	0.408	3.86303	0.426
38	3.89301	3.90315	0.260	3.90408	0.283
39	3.92147	3.92013	0.034	3.92011	0.035
40	4.00155	4.01985	0.455	4.01957	0.448
41	4.05232	4.04810	0.104	4.04792	0.109
42	4.07279	4.07673	0.096	4.07692	0.101
43	4.11185	4.10555	0.154	4.10515	0.163
44	4.16568	4.12779	0.918	4.12750	0.925
45	4.17169	4.15185	0.478	4.15181	0.479
46	4.23171	4.23428	0.061	4.23422	0.059
47	4.25632	4.26175	0.127	4.26195	0.132
48	4.28696	4.29318	0.145	4.29333	0.148
49	4.33501	4.33233	0.062	4.33252	0.057
50	4.39232	4.39776	0.124	4.39806	0.131
51	4.44617	4.44492	0.028	4.44480	0.031
52	4.45932	4.45990	0.013	4.45953	0.005
53	4.47269	4.48323	0.235	4.48383	0.248
54	4.50973	4.51226	0.056	4.51274	0.067
55	4.54993	4.53911	0.239	4.53896	0.242
56	4.57564	4.59124	0.340	4.59160	0.348

Table continued on next page.

Table continued.

		SMI		FEM	
Index	f_{exp} (MHz)	f_{calc} (MHz)	diff (%)	f_{calc} (MHz)	diff (%)
57	4.61763	4.59924	0.400	4.59942	0.396
58	4.64177	4.63850	0.070	4.63892	0.061
59	4.67340	4.67170	0.036	4.67168	0.037
60	4.67725	4.71140	0.725	4.71268	0.752
61	4.74328	4.72813	0.320	4.72823	0.318
62	4.75405	4.76937	0.321	4.76985	0.331
63	4.78548	4.79885	0.279	4.79964	0.295
64	4.83816	4.84783	0.199	4.84855	0.214
65	4.87454	4.89056	0.328	4.89094	0.335
66	4.89770	4.89955	0.038	4.89976	0.042
67	4.91976	4.92224	0.050	4.92262	0.058
68	4.94198	4.93395	0.163	4.93404	0.161
69	4.97544	4.95930	0.326	4.95855	0.341
70	5.00234	4.98595	0.329	4.98635	0.321
71	5.05521	5.05121	0.079	5.05153	0.073
72	5.06222	5.07826	0.316	5.07871	0.325
73	5.10734	5.10605	0.025	5.10572	0.032
74	5.14001	5.15663	0.322	5.15649	0.320
75	5.17375	5.18850	0.284	5.18928	0.299
76	5.20031	5.19720	0.060	5.19750	0.054
77	5.22839	5.23149	0.059	5.23154	0.060
78	5.24876	5.27701	0.535	5.27763	0.547
79	5.31483	5.33671	0.410	5.33550	0.387
80	5.35238	5.35144	0.018	5.35154	0.016
81	5.36938	5.36972	0.006	5.36912	0.005
82	5.37790	5.40947	0.584	5.40967	0.587
83	5.41390	5.42943	0.286	5.42989	0.295
84	5.43467	5.44317	0.156	5.44304	0.154

APPENDIX F

UTe_2 RUS ANALYSIS

F.1 Systematic Uncertainty Analysis

Here we analyze the systematic uncertainties of the RUS fits of UTe_2 from section 5.2. This discussion is in analogy to the uncertainties in $SrTiO_3$ and Mn_3Ge discussed in section 4.4.

The uncertainty due to the finite weight of the top cantilever of the RUS setup on the sample is estimated by mounting UTe_2 sample A in three different arrangements (see Figure F.1). Fit results for the different arrangements are shown in Table F.1. The resulting average uncertainty is about 0.5 GPa, which is about a factor of 4 smaller than for $SrTiO_3$ and Mn_3Ge. This difference is because we used our low-temperature RUS setup to measure the UTe_2 samples, where the top lever resting on the sample weighs only about 0.5 g, which is in contrast to the 5 g heavy transducer rod in the setup used for $SrTiO_3$ and Mn_3Ge samples.

Furthermore, we repeated our fits for arrangement 2 with a sample mesh rotated by 1° around the x, y, and z axes respectively. The uncertainty due to this 1° misalignment between sample mesh and crystallographic axes is given by the error bars in the middle column in Table F.1.

We also estimate a 1 % uncertainty on all elastic moduli caused by a 1 % uncertainty in the sample density.

F.2 Resonance Spectra and Fit Results

Here we give all experimental resonance frequencies f_{exp} for the RUS measurements of UTe_2 samples A and B at 300 K and 4 K. We also show the calculated resonances f_{calc} corresponding to the fits shown in section 5.2. Additionally, we give the difference between experimental and calculated frequencies. We included the first 140/150 resonances in the fit for UTe_2 sample A at 300/4 K, and the first 114/118 resonances in the fit for UTe_2 sample B at 300/4 K. The first three resonances were excluded from all fits. All fits were performed with the SMI forward solver. Resonances displayed in bold font

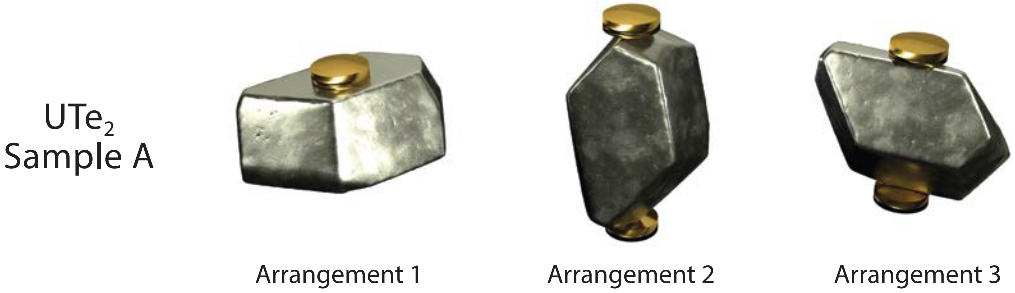

Figure F.1: **UTe_2 sample A arrangements.** The 3D model of UTe_2 sample A is shown in different arrangements between two piezoelectric transducers (gold). These different arrangements represent different ways we mounted the sample in the RUS setup to estimate the uncertainty due to the weight of the top lever on the sample. Arrangement 2 is the one chosen for the fit results in the main text in section 5.2. Figure adapted from [43].

	Arrangement		
	1	2	3
c_{11}	84.4	84.7±0.44	83.8
c_{22}	139.0	139.5±0.8	140.3
c_{33}	92.0	91.1±1.1	90.6
c_{12}	25.6	26.8±1.0	25.5
c_{13}	38.1	38.1±0.5	37.2
c_{23}	32.0	31.6±0.4	31.6
c_{44}	26.9	26.9±0.2	27.1
c_{55}	52.3	52.4±0.2	52.3
c_{66}	29.4	29.7±0.2	29.4

Table F.1: **UTe_2 sample A RUS uncertainty analysis.** Elastic moduli fit results are shown for UTe_2 sample A at 300 K. The different columns correspond to different arrangements of the sample in the RUS setup according to Figure F.1. The additional uncertainties given for arrangement 2 are due to a 1° misalignment between the crystallographic axes and the sample mesh. Table adapted from [43].

correspond to the resonances used for the temperature dependences of the elastic moduli in subsection 5.4.1. All tables are taken from [43].

Table F.2: **UTe$_2$ sample A SMI fit results.**

	300 K			4 K		
Index	f_{exp} (MHz)	f_{calc} (MHz)	diff (%)	f_{exp} (MHz)	f_{calc} (MHz)	diff (%)
1	0.64645	0.64254	-	0.66344	0.65765	-
2	0.80333	0.80092	-	0.81724	0.81425	-
3	0.86443	0.85869	-	**0.87702**	**0.87984**	**-**
4	1.09564	1.09407	0.143	**1.11952**	**1.12080**	**0.114**
5	1.18679	1.18992	0.263	**1.21970**	**1.21818**	**0.125**
6	1.32441	1.32471	0.023	**1.34208**	**1.34680**	**0.350**
7	1.34023	1.33357	0.499	**1.36327**	**1.35737**	**0.435**
8	1.49544	1.49019	0.353	**1.51789**	**1.51792**	**0.002**
9	1.56441	1.57149	0.450	**1.59618**	**1.60073**	**0.284**
10	1.64031	1.64096	0.040	**1.67269**	**1.67216**	**0.032**
11	1.67848	1.67996	0.088	**1.71445**	**1.71359**	**0.050**
12	1.71675	1.71182	0.288	**1.75060**	**1.74551**	**0.291**
13	1.77448	1.77473	0.014	**1.80806**	**1.80856**	**0.028**
14	1.83771	1.83767	0.002	**1.87151**	**1.87196**	**0.024**
15	1.86861	1.86685	0.094	**1.90573**	**1.90183**	**0.205**
16	1.93964	1.93352	0.317	**1.97323**	**1.97067**	**0.130**
17	2.02902	2.02240	0.327	**2.06927**	**2.06282**	**0.313**
18	2.06086	2.06388	0.146	**2.09666**	**2.10371**	**0.335**
19	2.13401	2.13646	0.115	**2.17374**	**2.17693**	**0.147**
20	2.18310	2.17778	0.244	**2.23096**	**2.22600**	**0.223**
21	2.21720	2.21601	0.054	**2.26583**	**2.25830**	**0.334**
22	2.25887	2.25321	0.251	**2.30249**	**2.29602**	**0.282**
23	2.27636	2.28024	0.170	**2.32310**	**2.32435**	**0.054**
24	2.33423	2.33367	0.024	**2.37609**	**2.37215**	**0.166**
25	2.35896	2.35370	0.223	**2.40235**	**2.40166**	**0.029**
26	2.37195	2.37131	0.027	**2.41002**	**2.41040**	**0.016**
27	2.40361	2.39962	0.166	**2.46079**	**2.45405**	**0.275**
28	2.45741	2.45189	0.225	**2.50592**	**2.50395**	**0.079**
29	2.47653	2.47529	0.050	**2.51386**	**2.52139**	**0.299**
30	2.49726	2.49516	0.085	**2.55527**	**2.55033**	**0.194**
31	2.53119	2.53407	0.113	**2.58793**	**2.58510**	**0.109**
32	2.56841	2.57293	0.176	**2.61987**	**2.62518**	**0.202**
33	2.58945	2.58640	0.118	**2.64506**	**2.64006**	**0.189**
34	2.67652	2.67401	0.094	**2.72662**	**2.72716**	**0.020**
35	2.69934	2.70106	0.064	**2.75414**	**2.75458**	**0.016**
36	2.70867	2.71641	0.285	**2.76160**	**2.76697**	**0.194**

Table continued on next page.

Table continued.

	300 K			4 K		
Index	f_{exp} (MHz)	f_{calc} (MHz)	diff (%)	f_{exp} (MHz)	f_{calc} (MHz)	diff (%)
37	2.75772	2.76163	0.142	**2.81381**	**2.81674**	**0.104**
38	2.80315	2.80522	0.073	**2.85929**	**2.86408**	**0.167**
39	2.83790	2.83401	0.137	**2.88995**	**2.88518**	**0.165**
40	2.84413	2.84397	0.006	**2.89806**	**2.89733**	**0.025**
41	2.85740	2.85678	0.022	**2.91031**	**2.91158**	**0.044**
42	2.89809	2.90021	0.073	**2.95404**	**2.95353**	**0.017**
43	2.91204	2.90687	0.178	**2.96297**	**2.95926**	**0.125**
44	2.93294	2.93629	0.114	**2.98892**	**2.98868**	**0.008**
45	2.97064	2.96887	0.060	**3.03454**	**3.03881**	**0.140**
46	2.98750	2.98376	0.125	**3.04986**	**3.04773**	**0.070**
47	3.04099	3.04359	0.086	**3.10384**	**3.10431**	**0.015**
48	3.05451	3.05513	0.020	**3.11878**	**3.11603**	**0.088**
49	3.07129	3.06617	0.167	**3.12869**	**3.12381**	**0.156**
50	3.11543	3.11631	0.028	**3.17516**	**3.18070**	**0.174**
51	3.14348	3.14681	0.106	**3.21205**	**3.20841**	**0.113**
52	3.16609	3.16333	0.087	**3.23373**	**3.23001**	**0.115**
53	3.19312	3.19392	0.025	**3.25821**	**3.25521**	**0.092**
54	3.21950	3.22107	0.049	**3.28885**	**3.29187**	**0.092**
55	3.26064	3.26213	0.046	**3.32549**	**3.32873**	**0.097**
56	3.27367	3.27710	0.105	**3.33381**	**3.33748**	**0.110**
57	3.28431	3.28793	0.110	**3.35277**	**3.35414**	**0.041**
58	3.33902	3.33560	0.103	**3.39969**	**3.39764**	**0.060**
59	3.37665	3.38210	0.161	**3.44137**	**3.44067**	**0.020**
60	3.38263	3.38841	0.171	**3.44466**	**3.45563**	**0.317**
61	3.40724	3.40264	0.135	**3.47399**	**3.46879**	**0.150**
62	3.42588	3.41984	0.176	**3.48688**	**3.48075**	**0.176**
63	3.46878	3.46450	0.123	**3.52655**	**3.52462**	**0.055**
64	3.48772	3.48306	0.134	**3.55491**	**3.55194**	**0.084**
65	3.49884	3.50575	0.197	**3.56459**	**3.57159**	**0.196**
66	3.51096	3.51080	0.005	3.58054	3.57953	0.028
67	3.54860	3.55098	0.067	3.61868	3.62048	0.050
68	3.56768	3.57417	0.182	**3.64321**	**3.64728**	**0.112**
69	3.57963	3.58351	0.108	**3.65177**	**3.65702**	**0.144**
70	3.59151	3.59154	0.001	**3.66315**	**3.66157**	**0.043**
71	3.63037	3.63146	0.030	**3.70535**	**3.70318**	**0.059**
72	3.66135	3.66185	0.014	**3.73498**	**3.73249**	**0.067**
73	3.67686	3.67367	0.087	**3.75129**	**3.74617**	**0.137**
74	3.70093	3.69729	0.098	3.77215	3.77270	0.015
75	3.72551	3.71979	0.154	**3.79478**	**3.78954**	**0.138**
76	3.74072	3.74038	0.009	**3.81853**	**3.81297**	**0.146**

Table continued on next page.

Table continued.

	300 K			4 K		
Index	f_{exp} (MHz)	f_{calc} (MHz)	diff (%)	f_{exp} (MHz)	f_{calc} (MHz)	diff (%)
77	3.75135	3.75430	0.079	**3.82596**	**3.82515**	**0.021**
78	3.76556	3.76595	0.010	**3.83940**	**3.83786**	**0.040**
79	3.77374	3.77640	0.071	**3.84028**	**3.84954**	**0.240**
80	3.81529	3.81717	0.049	**3.89424**	**3.89363**	**0.016**
81	3.84139	3.83861	0.072	**3.91424**	**3.91245**	**0.046**
82	3.85843	3.85711	0.034	**3.93674**	**3.93303**	**0.094**
83	3.87490	3.88271	0.201	**3.94923**	**3.95735**	**0.205**
84	3.89786	3.89296	0.126	3.97082	3.96312	0.194
85	3.90314	3.90305	0.002	**3.98043**	**3.98563**	**0.130**
86	3.91220	3.92250	0.263	**3.98665**	**3.99710**	**0.261**
87	3.94153	3.93803	0.089	**4.01442**	**4.01238**	**0.051**
88	3.99297	3.98031	0.318	**4.06185**	**4.05116**	**0.264**
89	3.99436	3.99491	0.014	4.07113	4.06908	0.050
90	4.00126	4.01160	0.258	**4.07942**	**4.08544**	**0.147**
91	4.03760	4.03141	0.154	**4.11408**	**4.10575**	**0.203**
92	4.07137	4.07176	0.010	**4.15105**	**4.14854**	**0.061**
93	4.08673	4.08572	0.025	**4.16596**	**4.16925**	**0.079**
94	4.11792	4.11397	0.096	**4.19784**	**4.19441**	**0.082**
95	4.12896	4.13582	0.166	**4.20427**	**4.21294**	**0.206**
96	4.14529	4.15212	0.164	**4.22149**	**4.22953**	**0.190**
97	4.15242	4.15367	0.030	**4.23333**	**4.23415**	**0.019**
98	4.17297	4.17074	0.053	**4.24888**	**4.24690**	**0.047**
99	4.18994	4.18888	0.025	4.27899	4.27740	0.037
100	4.20373	4.21285	0.216	**4.28904**	**4.29176**	**0.064**
101	4.22958	4.23006	0.011	**4.30977**	**4.31112**	**0.031**
102	4.24199	4.24296	0.023	4.32438	4.32504	0.015
103	4.25360	4.25075	0.067	4.33687	4.33486	0.046
104	4.28642	4.28345	0.069	**4.36950**	**4.36567**	**0.088**
105	4.30657	4.30624	0.008	4.39228	4.39207	0.005
106	4.31547	4.31995	0.104	**4.40638**	**4.40694**	**0.013**
107	4.34118	4.34193	0.017	**4.42091**	**4.42370**	**0.063**
108	4.34935	4.35598	0.152	4.43621	4.44172	0.124
109	4.36295	4.36176	0.027	4.44922	4.44494	0.096
110	4.37974	4.37984	0.002	4.46691	4.46202	0.110
111	4.39652	4.38614	0.237	4.47881	4.46618	0.283
112	4.40482	4.41073	0.134	**4.48982**	**4.49513**	**0.118**
113	4.42003	4.41888	0.026	4.49809	4.50730	0.204
114	4.42672	4.42968	0.067	4.51862	4.51611	0.055
115	4.44940	4.46193	0.281	**4.53519**	**4.54067**	**0.121**
116	4.46937	4.47430	0.110	4.55608	4.55307	0.066

Table continued on next page.

Table continued.

	300 K			4 K		
Index	f_{exp} (MHz)	f_{calc} (MHz)	diff (%)	f_{exp} (MHz)	f_{calc} (MHz)	diff (%)
117	4.48235	4.48380	0.032	**4.56374**	**4.56785**	**0.090**
118	4.50482	4.50569	0.019	4.59148	4.59609	0.100
119	4.50733	4.51327	0.132	**4.59729**	**4.60078**	**0.076**
120	4.52413	4.52782	0.081	**4.60960**	**4.61562**	**0.131**
121	4.53911	4.54276	0.080	4.62762	4.63458	0.150
122	4.56333	4.56602	0.059	**4.64820**	**4.65923**	**0.237**
123	4.57367	4.57286	0.018	4.66121	4.66642	0.112
124	4.60540	4.60303	0.051	**4.69278**	**4.69228**	**0.011**
125	4.61532	4.62032	0.108	4.70740	4.71043	0.064
126	4.62818	4.62519	0.065	4.71517	4.71609	0.020
127	4.63514	4.63026	0.105	4.72725	4.71991	0.155
128	4.64194	4.64199	0.001	4.73331	4.73754	0.089
129	4.66690	4.66430	0.056	4.75924	4.75618	0.064
130	4.66790	4.66597	0.041	**4.76674**	**4.75845**	**0.174**
131	4.69246	4.68730	0.110	**4.78743**	**4.78038**	**0.147**
132	4.70527	4.71080	0.118	4.80128	4.80542	0.086
133	4.72046	4.73008	0.203	4.81305	4.82061	0.157
134	4.75051	4.75395	0.072	4.84664	4.84559	0.022
135	4.75900	4.76169	0.057	4.85021	4.85330	0.064
136	4.76976	4.77384	0.085	**4.86402**	**4.86321**	**0.017**
137	4.77918	4.77950	0.007	**4.87531**	**4.87473**	**0.012**
138	4.79086	4.79493	0.085	4.88149	4.88582	0.089
139	4.80450	4.80244	0.043	**4.89785**	**4.89637**	**0.030**
140	4.81875	4.81484	0.081	**4.91309**	**4.90863**	**0.091**
141				4.93822	4.94346	0.106
142				4.95627	4.95918	0.059
143				4.96168	4.96342	0.035
144				4.98300	4.98143	0.032
145				4.98846	4.99420	0.115
146				4.99438	5.00516	0.215
147				5.01215	5.01596	0.076
148				5.02882	5.03051	0.034
149				5.04591	5.05275	0.135
150				5.06142	5.06270	0.025

Table F.3: **UTe$_2$ sample B SMI fit results.**

	300 K			4 K		
Index	f_{exp} (MHz)	f_{calc} (MHz)	diff (%)	f_{exp} (MHz)	f_{calc} (MHz)	diff (%)
1	0.84871	0.84530	-	-	0.86336	-
2	0.85476	0.85964	-	0.87178	0.87760	-
3	0.95597	0.95934	-	0.97940	0.97664	-
4	1.06829	1.07054	0.211	1.09070	1.09144	0.068
5	1.11300	1.11809	0.455	1.14186	1.14466	0.245
6	1.20905	1.20671	0.194	1.23137	1.23157	0.017
7	1.27627	1.27098	0.417	1.29907	1.29403	0.389
8	1.30668	1.30995	0.249	**1.33148**	**1.33537**	**0.291**
9	1.33404	1.33004	0.301	1.36093	1.35854	0.176
10	1.42356	1.41859	0.350	1.45056	1.44869	0.129
11	1.46580	1.46271	0.211	1.49748	1.49177	0.383
12	1.50799	1.51040	0.160	**1.54068**	**1.53982**	**0.055**
13	1.56016	1.56319	0.194	**1.60017**	**1.59666**	**0.219**
14	1.60842	1.60909	0.042	**1.64060**	**1.64240**	**0.110**
15	1.74339	1.74654	0.180	1.77974	1.78031	0.032
16	1.78190	1.79245	0.589	**1.81928**	**1.82974**	**0.572**
17	1.80619	1.80062	0.309	**1.85079**	**1.84454**	**0.338**
18	1.87349	1.87715	0.195	**1.90804**	**1.91116**	**0.163**
19	1.90921	1.90783	0.072	**1.94151**	**1.94324**	**0.089**
20	1.94674	1.94192	0.249	**1.98817**	**1.98452**	**0.184**
21	2.00583	2.00390	0.096	2.04584	2.04287	0.145
22	2.03086	2.02432	0.323	**2.08163**	**2.06424**	**0.843**
23	2.07441	2.07694	0.122	2.11713	2.11986	0.129
24	2.11673	2.11636	0.018	**2.15876**	**2.15825**	**0.023**
25	2.16436	2.16975	0.248	2.20781	2.21144	0.164
26	2.18929	2.19732	0.366	2.23165	2.23803	0.285
27	2.22146	2.23034	0.398	2.26420	2.27408	0.434
28	2.24902	2.25516	0.272	2.29215	2.30158	0.409
29	2.30961	2.31141	0.078	2.35312	2.36037	0.307
30	2.32704	2.33105	0.172	**2.37484**	**2.38182**	**0.293**
31	2.35294	2.34928	0.156	2.40488	2.39906	0.243
32	2.39058	2.38243	0.342	**2.43754**	**2.43052**	**0.289**
33	2.45167	2.45230	0.026	2.50518	2.50352	0.066
34	2.48080	2.48028	0.021	**2.53395**	**2.53062**	**0.132**
35	2.50531	2.51258	0.289	2.56447	2.56033	0.162
36	2.53711	2.53137	0.227	2.58939	2.58027	0.353
37	2.55822	2.55799	0.009	2.61119	2.61444	0.124
38	2.57543	2.57151	0.153	2.62709	2.61993	0.273
39	2.62322	2.61786	0.205	2.67498	2.67047	0.169

Table continued on next page.

Table continued.

	300 K			4 K		
Index	f_{exp} (MHz)	f_{calc} (MHz)	diff (%)	f_{exp} (MHz)	f_{calc} (MHz)	diff (%)
40	2.63654	2.63938	0.107	2.69240	2.69640	0.148
41	2.70147	2.70243	0.036	2.75821	2.75649	0.062
42	2.75069	2.74791	0.101	2.80820	2.80488	0.119
43	2.77773	2.77670	0.037	**2.83486**	**2.83282**	**0.072**
44	2.80230	2.80822	0.211	2.85674	2.86124	0.157
45	2.81487	2.81788	0.107	2.87440	2.87460	0.007
46	2.83215	2.82934	0.099	**2.88578**	**2.88481**	**0.034**
47	2.84899	2.84838	0.021	2.90458	2.90969	0.176
48	2.88217	2.89120	0.312	2.94201	2.95391	0.403
49	2.90566	2.89877	0.238	**2.96333**	**2.95683**	**0.220**
50	2.91847	2.91501	0.119	2.98089	2.97713	0.126
51	2.92686	2.92827	0.048	**2.98623**	**2.98834**	**0.071**
52	2.95275	2.95268	0.002	**3.01343**	**3.01194**	**0.049**
53	3.00092	2.99982	0.037	**3.06884**	**3.06684**	**0.065**
54	3.02153	3.02916	0.252	**3.08283**	**3.08955**	**0.217**
55	3.05196	3.04553	0.211	**3.11517**	**3.10990**	**0.170**
56	3.08793	3.08125	0.217	3.14866	3.14128	0.235
57	3.11778	3.11646	0.042	3.17516	3.17388	0.040
58	3.14639	3.14909	0.085	**3.20090**	**3.21009**	**0.286**
59	3.16393	3.16218	0.055	**3.22399**	**3.22528**	**0.040**
60	3.19065	3.18964	0.032	3.25573	3.25409	0.050
61	3.19738	3.20093	0.111	3.25919	3.26248	0.101
62	3.20855	3.20654	0.063	**3.26893**	**3.27039**	**0.045**
63	3.23995	3.24651	0.202	3.30460	3.31243	0.236
64	3.27675	3.28070	0.120	3.34246	3.34638	0.117
65	3.29429	3.29614	0.056	3.35998	3.36766	0.228
66	3.30627	3.30639	0.004	**3.37335**	**3.37228**	**0.032**
67	3.31057	3.31439	0.115	3.37764	3.38353	0.174
68	3.36154	3.35425	0.217	**3.42970**	**3.42873**	**0.028**
69	3.38338	3.38541	0.060	**3.45002**	**3.45428**	**0.123**
70	3.39821	3.39330	0.145	3.47019	3.46476	0.157
71	3.41174	3.41505	0.097	3.48083	3.48357	0.079
72	3.45929	3.45902	0.008	**3.52382**	**3.53192**	**0.229**
73	3.47176	3.46545	0.182	3.54420	3.53371	0.297
74	3.48530	3.48412	0.034	3.54503	3.55265	0.215
75	3.49764	3.50499	0.210	**3.56748**	**3.57564**	**0.228**
76	3.53011	3.52311	0.199	3.60152	3.59743	0.114
77	3.54142	3.54333	0.054	**3.60770**	**3.61281**	**0.141**
78	3.57423	3.56654	0.216	**3.64468**	**3.63636**	**0.229**
79	3.59789	3.59154	0.177	3.67123	3.66223	0.246

Table continued on next page.

Table continued.

	300 K			4 K		
Index	f_{exp} (MHz)	f_{calc} (MHz)	diff (%)	f_{exp} (MHz)	f_{calc} (MHz)	diff (%)
80	3.61091	3.60483	0.169	3.68580	3.68020	0.152
81	3.61554	3.61654	0.028	3.69086	3.68809	0.075
82	3.64128	3.64220	0.025	3.71976	3.71920	0.015
83	3.65329	3.65013	0.087	3.72490	3.72397	0.025
84	3.67338	3.67530	0.052	3.74859	3.75135	0.074
85	3.68955	3.68592	0.099	3.76758	3.75922	0.222
86	3.70091	3.69442	0.176	3.77312	3.76937	0.099
87	3.70751	3.70096	0.177	3.78014	3.77801	0.056
88	3.72219	3.72029	0.051	3.80089	3.80091	0.001
89	3.74091	3.74401	0.083	3.81654	3.81771	0.030
90	3.78334	3.78100	0.062	3.85825	3.85286	0.140
91	3.79235	3.79414	0.047	3.86975	3.87632	0.169
92	3.82170	3.81175	0.261	3.89582	3.88778	0.207
93	3.83868	3.83761	0.028	3.91696	3.91147	0.140
94	3.84736	3.85549	0.211	3.92636	3.93085	0.114
95	3.86778	3.85859	0.238	3.94426	3.93995	0.109
96	3.87212	3.87332	0.031	3.94801	3.95067	0.067
97	3.87768	3.88691	0.237	**3.95793**	**3.96709**	**0.231**
98	3.91034	3.91012	0.006	3.99414	3.98805	0.153
99	3.94800	3.93730	0.272	4.02057	4.01300	0.189
100	3.96335	3.96620	0.072	4.04528	4.04773	0.060
101	3.96897	3.97227	0.083	4.05160	4.05507	0.086
102	3.98406	3.98991	0.147	4.06035	4.06586	0.135
103	4.00409	4.00748	0.085	4.08358	4.08793	0.106
104	4.02581	4.02391	0.047	4.10434	4.10784	0.085
105	4.02903	4.03805	0.223	4.10898	4.11773	0.213
106	4.06773	4.06629	0.035	4.14695	4.14959	0.063
107	4.08881	4.08893	0.003	4.17275	4.17261	0.003
108	4.09297	4.09859	0.137	4.17465	4.18384	0.220
109	4.10732	4.10027	0.172	4.19085	4.18721	0.087
110	4.11337	4.11117	0.053	4.19902	4.19819	0.020
111	4.12319	4.12322	0.001	4.20850	4.20670	0.043
112	4.13332	4.14047	0.173	4.21682	4.22095	0.098
113	4.14011	4.14630	0.149	4.22597	4.23065	0.111
114	4.17361	4.16635	0.174	4.25691	4.24756	0.220
115				4.28207	4.28041	0.039
116				4.29878	4.29524	0.082
117				4.31342	4.31466	0.029
118				4.32482	4.32771	0.067

APPENDIX G

UTe_2 DFT CALCULATIONS

We used density-functional theory (DFT) to calculate the elastic moduli of UTe_2 shown in section 5.2 and the band structure and Fermi surface of UTe_2 discussed in subsection 5.3.1. The details of these calculations outlined below are taken from [43] and [33].

The DFT calculations involved total energy calculations, following the procedure of Ravindran et al. [167]. The full-potential linearized augmented plane wave method [168] calculations employed the generalized gradient approximation [169] for the exchange correlation, wave function and potential energy cutoffs of 16 and 200 Ry, respectively, muffin-tin sphere radii of 1.35 Å. Spin-orbit coupling was fully taken into account in the assumed nonmagnetic state.

G.1 Elastic Tensor

Calculations for the elastic tensor were performed on a 8×8×8 k-point mesh and the elastic moduli were extracted from fits of the total energy variations around the experimental structure [170] to the energy-strain formula [167], including linear terms.

During these calculations, one needs to decide whether to keep the atomic coordinates frozen to the experimental values or to optimize their positions. Table G.1 shows the resulting values for both options, together with DFT calculations presented in [109]. The values we give in section 5.2 are calculations for which the atomic coordinates have been optimized.

Method	c_{11}	c_{22}	c_{33}	c_{12}	c_{13}	c_{23}	c_{44}	c_{55}	c_{66}
coordinates frozen	100.2	140.0	99.3	28.7	56.4	27.1	33.8	69.4	36.1
coordinates optimized	95.7	136.0	89.7	28.1	46.0	26.0	28.0	57.1	31.0
Girod et al. [109]	97.0	140.7	101.3	40.9	48.6	46.7	19.6	57.3	27.1

Table G.1: **UTe_2 DFT elastic tensor**. Shown are the elastic moduli obtained from DFT calculations, with frozen and optimized atomic coordinates (top two rows). Also shown are the DFT elastic moduli presented in [109]. Table taken from [43].

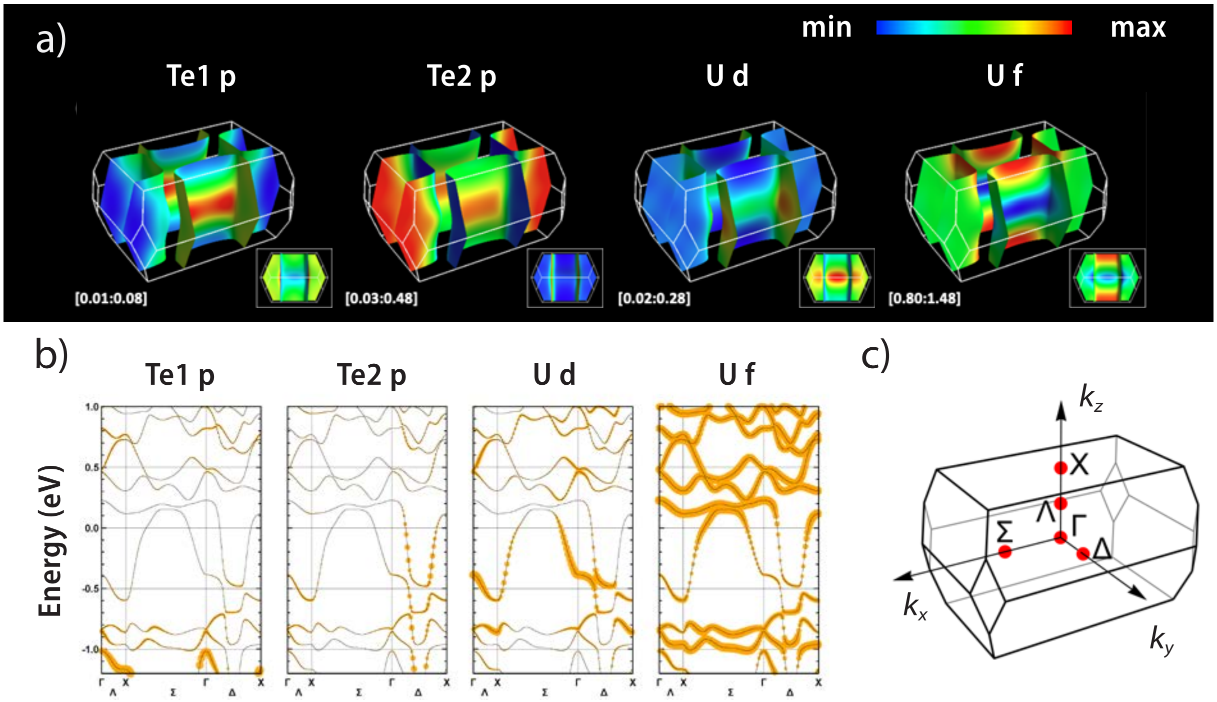

Figure G.1: **DFT Fermi surface and band structure.** a) The orbital content of tellurium and uranium states are plotted on the UTe_2 Fermi surface calculated with $U = 2$ eV. Color scales are rescaled between each plot, but respective minimum and maximum values are given to the bottom left of each panel. *FermiSurfer* [171] is used for the visualization of the Fermi surface. The content of the same orbitals is illustrated on the band structure in panel b), where the size of the orange circles is proportional to the Te(1) p, Te(2) p, U d, and U f orbital weight. Panel c) shows the UTe_2 Brillouin zone. Figure adapted from [33].

G.2 Band Structure and Fermi Surface

By additionally considering the Hubbard U for the uranium $5f$ electrons, DFT calculations allow us to examine the orbital character of the electronic states close to the chemical potential. The quasi 2D Fermi surface observed in experiments [114, 115], can be qualitatively reproduced with $U = 2$ eV.

The (Kramers degenerate) band dispersion and wave functions are then calculated along the high-symmetry directions in the UTe_2 Brillouin zone (Λ, Σ, and Δ lines, see Figure G.1c for an image of the Brillouin zone) and on a 50×50×50 k-point mesh. The orbital components of each degenerate band are calculated within the atom-centered spheres of radius 1.35 Å. Figure G.1a shows the orbital components of the tellurium p, uranium d, and uranium f electrons on the Fermi surface. Figure G.1b shows the orbital components along the band dispersion along high-symmetry directions.

We find that the orbital content from Te(1) electrons is about a factor of five smaller than for Te(2) and U. Te(2) p (U d) orbitals are dominant on parts of the Fermi surface with momentum along k_y (k_x).

While uranium f orbitals are a dominant influence on the orbital character on most parts of the Fermi surface, they don't contribute significantly to its shape. Our Fermi surface calculated with $U = 2$ eV is quite similar to that calculated for $ThTe_2$ [94], which has no f electrons. Thus, while the uranium f electrons hybridize strongly with uranium $6d$ and tellurium (2) $5p$ bands, they only enhance the cyclotron masses and shift the chemical potential, but don't significantly modify the shape of the Fermi surface.

APPENDIX H

UTe$_2$ TIGHT BINDING MODEL

Our DFT calculations in Appendix G (see Figure G.1 for an image of the Fermi surface), as well as quantum oscillation measurements (see [120]) imply that the shape UTe$_2$ Fermi surface can be captured by a tight binding model only considering quasi one-dimensional chains of U $6d$ orbitals along the a axis and of Te(2) $5p$ orbitals along the b axis. The description of our tight binding calculations below follows closely our publication in [33].

Our tight binding model is based on the crystal structure of UTe$_2$ shown in Figure 5.2. Two uranium atoms form a dimer (along the c axis) in the center of conventional unit cell. The dominant tight binding parameters will be:

- μ_{U}: the chemical potential.
- Δ_{U}: the intra-dimer overlap along the c axis.
- t_{U}: the hopping along the uranium chains along the a direction.
- t'_{U}: the hopping along the uranium chain direction, but to the other atom in the dimer.
- $t_{ch,\mathrm{U}}$: the hopping between chains in the $a-b$ plane (i.e. along the b direction).
- $t'_{ch,\mathrm{U}}$: the hopping between chains in the $a-b$ plane, but to the other atom in the dimer.
- $t_{z,\mathrm{U}}$: the hopping between chains along the c axis. This hopping is only to the other uranium atom in the dimer.

The two bands from the two uranium sites then come from diagonalizing the following matrix:

$$E_{\mathrm{U}} = \begin{bmatrix} E_{\mathrm{U}}^{11} & E_{\mathrm{U}}^{12} \\ (E_{\mathrm{U}}^{12})^* & E_{\mathrm{U}}^{11} \end{bmatrix}, \tag{H.1}$$

with

$$E_{\mathrm{U}}^{11} = \mu_{\mathrm{U}} - 2t_{\mathrm{U}} \cos k_x a - 2t_{ch,\mathrm{U}} \cos k_y b, \tag{H.2}$$

$$E_{\mathrm{U}}^{12} = -\Delta_{\mathrm{U}} - 2t'_{\mathrm{U}} \cos k_x a - 2t'_{ch,\mathrm{U}} \cos k_y b - 4t_{z,\mathrm{U}} e^{-ik_z c/2} \cos k_x \frac{a}{2} \cos k_y \frac{b}{2}. \tag{H.3}$$

By only including nearest-neighbor hopping between Te(2) atoms in the $a-b$ chain, we can reduce the problem of 4 Te(2) sites in the conventional unit cell to another 2×2 matrix. In this case, the two sites we consider are two neighboring Te(2) atoms within the same chain. The dominant tight binding parameters for the tellurium atoms will be:

- μ_{Te}: the chemical potential.
- Δ_{Te}: the intra-unit-cell overlap between the two Te(2) sites in the chain along the b direction.
- t_{Te}: the hopping along the chain in the b direction. This only includes hopping along one direction. Hopping to the nearest neighbor along the other direction is included in Δ_{Te}.
- $t_{ch,\mathrm{Te}}$: the hopping between chains along the a direction.
- $t_{z,\mathrm{Te}}$: the hopping between chains along the c direction.

The two Te(2) bands are then obtained by diagonalizing the following tight binding matrix:

$$E_{\mathrm{Te}} = \begin{bmatrix} E^{11}_{\mathrm{Te}} & E^{12}_{\mathrm{Te}} \\ (E^{12}_{\mathrm{Te}})^* & E^{11}_{\mathrm{Te}} \end{bmatrix}, \tag{H.4}$$

with

$$E^{11}_{\mathrm{Te}} = \mu_{\mathrm{Te}} - 2t_{ch,\mathrm{Te}} \cos k_x a, \tag{H.5}$$

$$E^{12}_{\mathrm{Te}} = -\Delta_{\mathrm{Te}} - t_{\mathrm{te}} e^{-ik_y b} - 2t_{z,\mathrm{Te}} \cos k_z \frac{c}{2} \cos k_x \frac{a}{2} \cos k_y \frac{b}{2}. \tag{H.6}$$

Diagonalizing Equation H.1 and Equation H.4 we obtain two U 6d and two Te(2) 5p bands which are plotted in Figure H.1a. We chose the values of our tight binding parameters (see Table H.1) to roughly match the band structure obtained from our DFT calculations (see Figure G.1).

In order to obtain a Fermi surface resembling that in Figure G.1, we hybridize the two bands which cross the Fermi energy with a hybridization parameter δ, which is momentum independent and whose value is chosen to match our DFT results. The resulting two hybridized bands which form the electron and hole pockets of the Fermi surface are shown in Figure H.1b. The resulting Fermi surface is plotted in Figure H.1c.

Comparing the Fermi surfaces calculated by DFT with $U = 2$ eV (see Figure G.1a) and the Fermi surface observed by quantum oscillation measurements [120], we find that the latter was chosen with an c-axis dispersion with opposite sign. We were also able to reproduce this Fermi surface with our tight binding model, with the parameters given in Table H.1 and the resulting Fermi surface plotted in Figure H.1d.

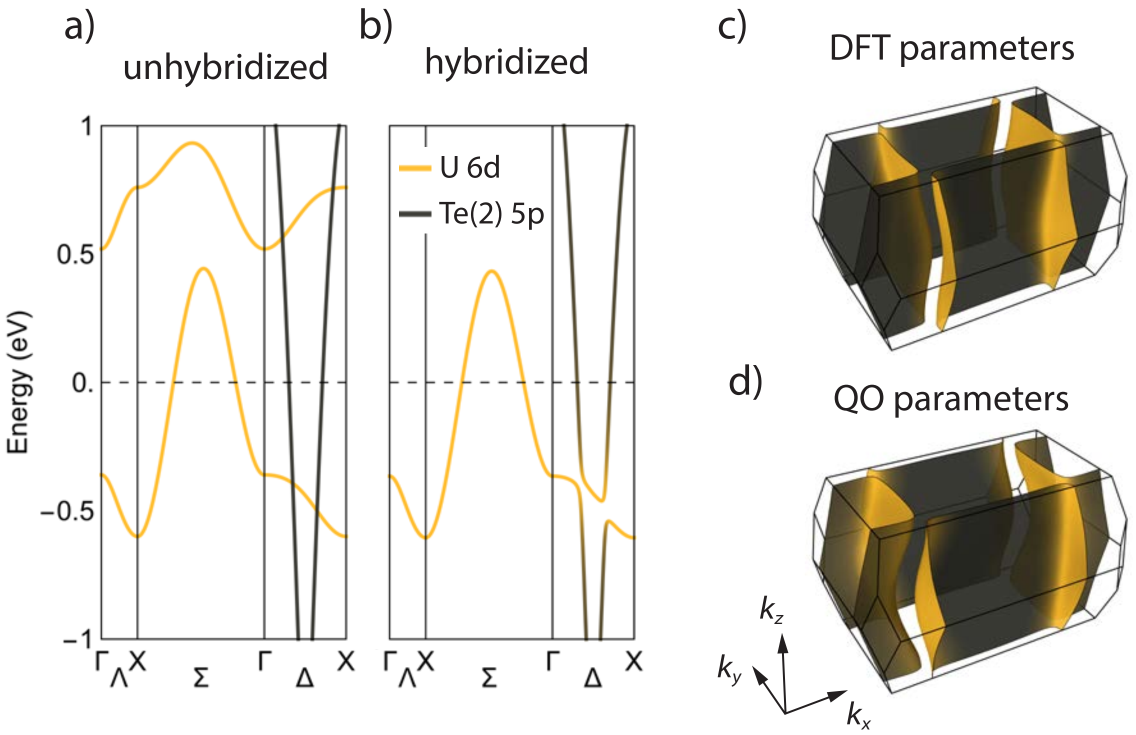

Figure H.1: **Tight binding model.** (a-c) Tight binding model with parameters to match DFT results. (a) Unhybridized bands formed by uranium 6*d* chains along the *a* axis (yellow) and tellurium (2) 5*p* chains along the *b* axis (gray). The two bands crossing the Fermi level are hybridized in (b) and form an electron and a hole pocket. The resulting Fermi surface is shown in (c). Colors represent a projection on original U/Te(2) bands. (d) The Fermi surface calculated with values for the tight binding model parameters to match the Fermi surface measured with quantum oscillations [120]. Figure adapted from [33].

	Δ_{U}	t_{U}	t'_{U}	$t_{ch,\mathrm{U}}$	$t'_{ch,\mathrm{U}}$	$t_{z,\mathrm{U}}$	μ_{Te}	Δ_{Te}	t_{Te}	$t_{ch,\mathrm{Te}}$	$t_{z,\mathrm{Te}}$	δ
DFT	0.40	0.15	0.08	0.01	0.00	-0.03	-1.80	-1.50	-1.50	0.00	-0.05	0.09
QO	0.05	0.10	0.08	0.01	0.00	0.04	-1.80	-1.50	-1.50	-0.03	-0.5	0.10

Table H.1: **Tight binding parameters.** Values for all parameters in our tight binding model used to reproduce the band structures and Fermi surfaces calculated by DFT (see Appendix G; top row) and measured by quantum oscillations [120] (bottom row). All parameters given in eV. Table adapted from [33].

APPENDIX I

UTe_2 PULSE ECHO ULTRASOUND TECHNICAL DETAILS

In this chapter, we give details on the samples, transducers, data reproducibility, and noise analysis regarding the pulse-echo ultrasound measurements on UTe_2 discussed in chapter 5. The following sections follow closely our publication in [33].

I.1 Measured Samples and Transducer Configurations

We measured a total of three different UTe_2 samples with pulse-echo ultrasound: S1, S2, and S3. Samples S1 and S2 exhibit one superconducting transition, whereas S3 exhibits two transitions. Table I.1 gives details on the samples and transducer configurations. They include the propagation $\vec{q}$ and the polarization $\vec{u}$ vector of the excited sound wave, and the elastic modulus which is consequently measured. The aim was to measure all shear moduli, i.e. c_{44}, c_{55}, and c_{66}, on both one and two-transition samples.

We also show the pulse-echo carrier frequencies which were used for the measurements through T_c (see section 5.3). As we will argue below in section I.2, however, measurements at different frequencies do not show any significant differences. Table I.1 also shows the thicknesses of the samples used in these measurements, with an uncertainty of 5 % as well as the absolute elastic moduli obtained from the distance between two echoes at 280 K.

I.2 Data Reproducibility

We address data reproducibility in three ways.

1. As discussed in subsection 3.2.2, our thin-film transducers exhibit both a longitudinal and shear response. Since we measured both c_{44} and c_{55} with transducer configurations such that the sound propagation was parallel to [001] (see Table I.1), the transducers for both measurements also detected c_{33}. We therefore have measurements of c_{33} from two different transducers, which differ by the polarization direction of their shear component. We compare the relative changes of c_{33} from these transducers on single- and double-transition samples in Figure I.1 and find no significant difference between them.

# T_c	Sample	$\vec{q}$	$\vec{u}$	c_{ij}	f (MHz)	d (μm)	c (GPa)
1	S1	[001]	[100]	c_{55}	1261	330 ± 17	51 ± 5
			[010]	c_{44}	1434	330 ± 17	27 ± 3
			[001]	c_{33}	2260	330 ± 17	91 ± 11
	S2	[100]	[100]	c_{11}	823	920 ± 46	81 ± 8
			[010]	c_{66}	1250	920 ± 46	28 ± 3
2	S3	[001]	[100]	c_{55}	1348	550 ± 28	52 ± 5
			[010]	c_{44}	1352	550 ± 28	28 ± 3
			[001]	c_{33}	1348	550 ± 28	88 ± 9
		[010]	[100]	c_{66}	1362	290 ± 15	30 ± 3
			[010]	c_{22}	1362	290 ± 15	141 ± 15

Table I.1: **Sample configurations.** We give the transducer configurations (i.e. propagation $\vec{q}$ and polarization $\vec{u}$ vectors of the excited sound wave) and the corresponding elastic moduli. Shown is also the pulse-echo frequency used for the data in section 5.3, as well as the sample thicknesses and absolute elastic moduli at 280 K. A subset of the elastic moduli values are also shown in Table 5.1. The thicknesses were obtained with an uncertainty of 5 %. Table taken from [33].

2. A single pulse-echo ultrasound measurement produces an echo pattern similar to that in Figure 3.7, with several echoes. However, only the phase difference between two echoes is necessary to obtain the relative change in sound velocity (see subsection 3.2.1). In Figure I.2 and Figure I.3 we compare the resulting relative changes in compressional and shear elastic moduli if different echoes are used. The red curves are the ones used in section 5.3. We find that using different echoes does not significantly affect the resulting elastic moduli.
3. The pulse-echo ultrasound data in section 5.3 were taken at the respective frequencies shown in Table I.1. In Figure I.4 and Figure I.5 we compare the relative changes in compressional and shear elastic moduli if different frequencies are used. The red curves are the ones used in section 5.3. We find no significant differences for any of the other frequencies we used.

I.3 Noise Analysis

In order to quantify the noise in our pulse echo measurements, we first subtract a background from the data shown in Figure 5.8, Figure 5.9, and Figure 5.11. This is done by first fitting a second-order polynomial to the normal state data, i.e. for temperatures greater than T_c (see Figure I.6). We then subtract this background from the data, which is shown in Figure I.7. The noise is eventually given by the RMS (root mean square) of this

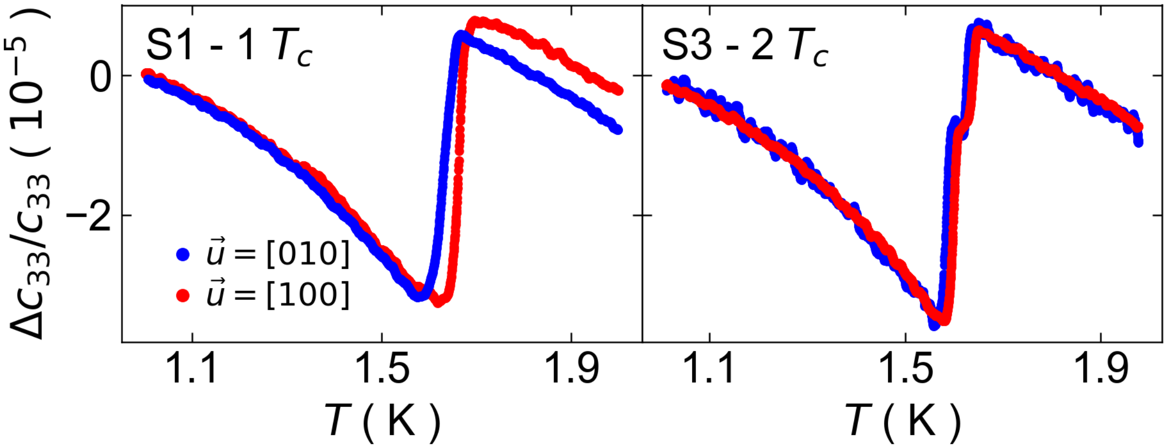

Figure I.1: **Transducer comparison.** The relative change of c_{33} is shown for both a single- and double-transition sample (left and right panel, respectively), for two different transducer configurations. For each sample, two transducers with sound propagation along [001], but polarization direction along [100] and [010] were deposited on the sample. Since all of our deposited transducers have a shear and longitudinal response, transducers with both polarization directions also measure c_{33}. No significant difference in c_{33} can be observed for the different transducer configurations. Figure adapted from [33].

background-subtracted data above the phase transition, i.e. over the same temperature range which was used to fit the background polynomial. The resulting RMS values lie between 0.04 and 0.41 parts per million, with an average below 1.9×10^{-7}.

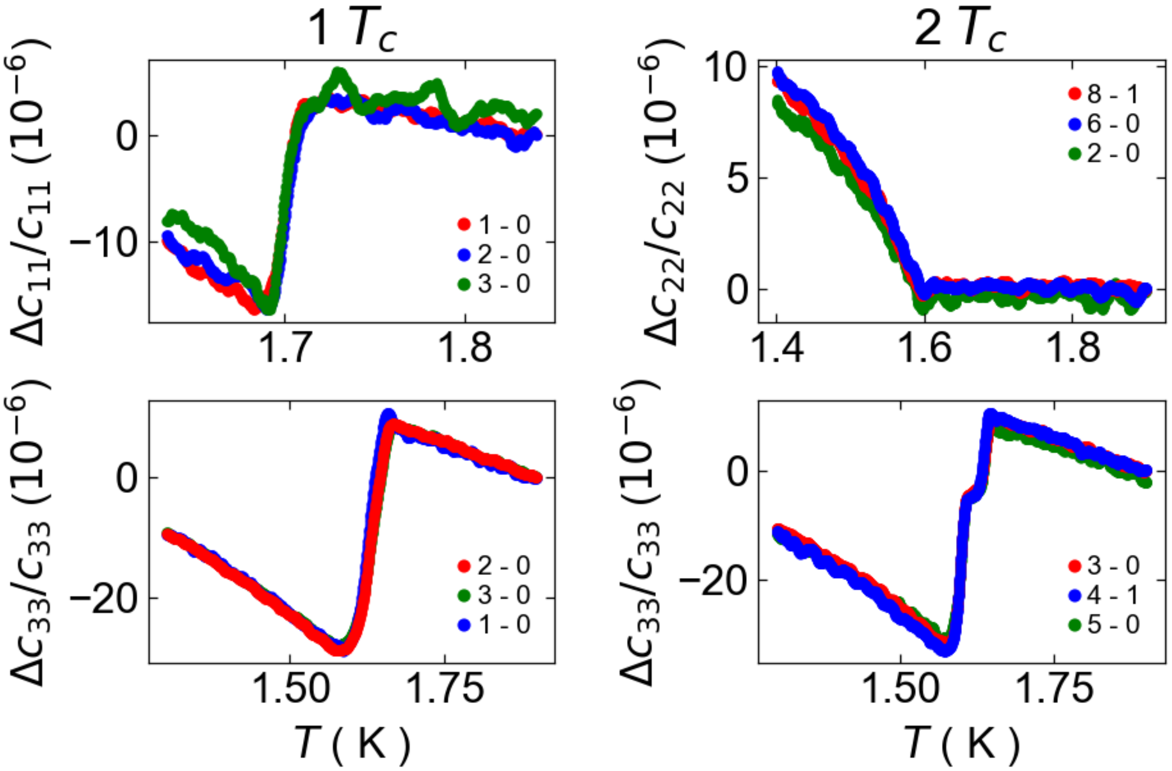

Figure I.2: **Echo dependence compressional moduli.** The relative changes in compressional moduli obtained from different echoes. Data from single- and double-transition samples are shown in the left and right panels, respectively. The curves shown in red are the data used in chapter 5. Figure adapted from [33].

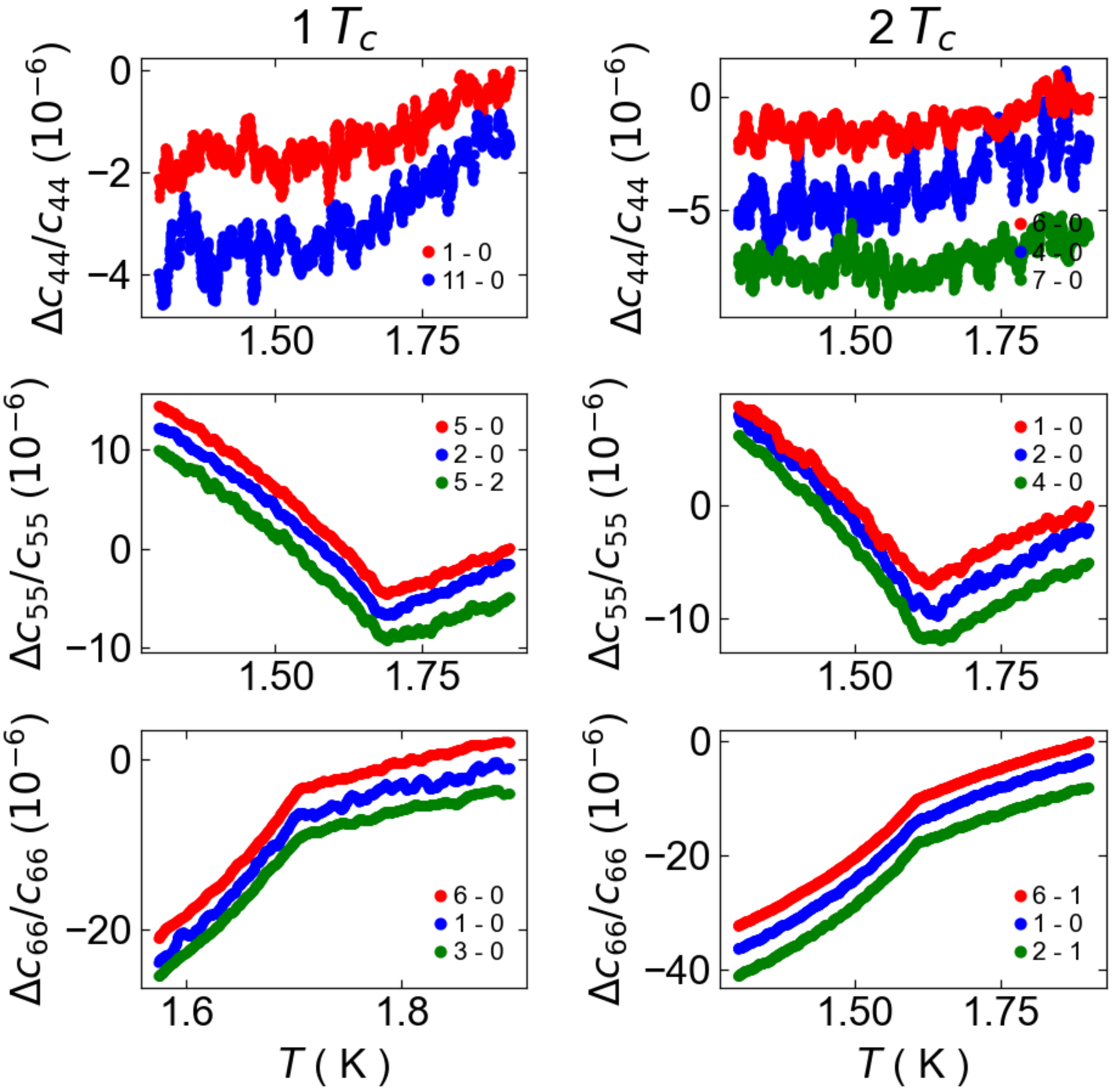

Figure I.3: **Echo dependence shear moduli.** The relative changes in shear moduli obtained from different echoes. Data from single- and double-transition samples are shown in the left and right panels, respectively. The curves shown in red are the data used in chapter 5. Figure adapted from [33].

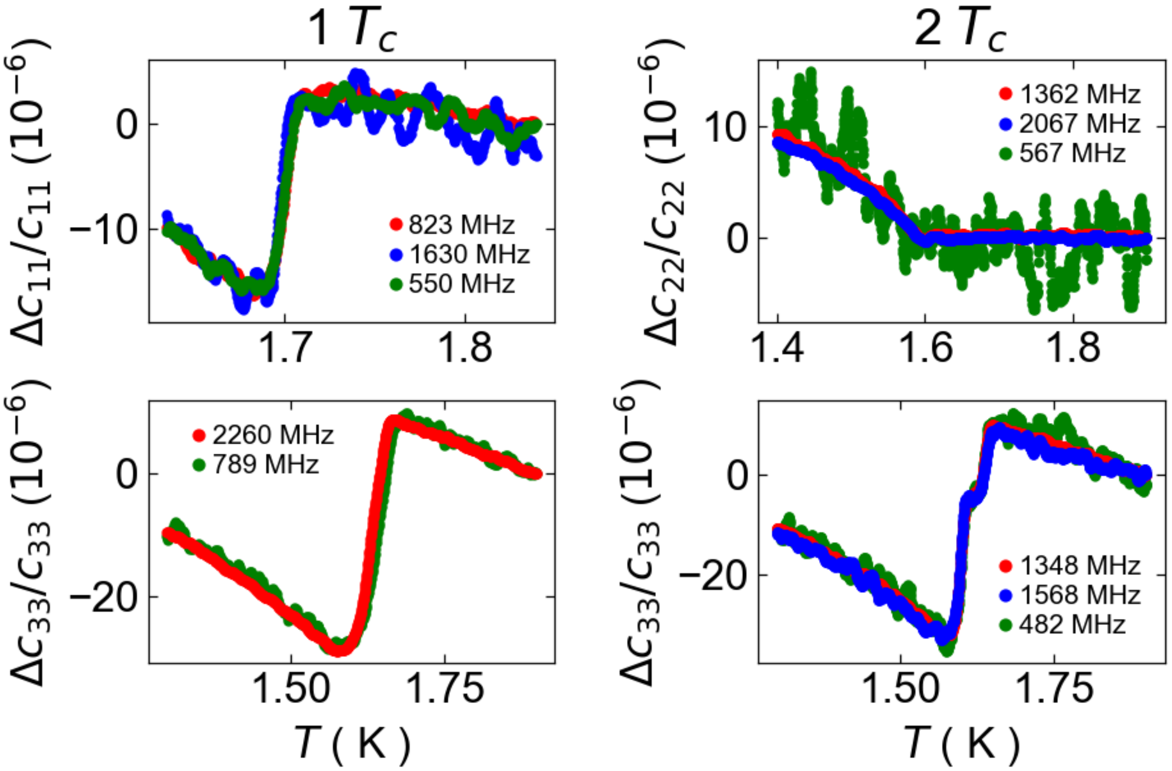

Figure I.4: **Frequency dependence compressional moduli.** The relative changes in compressional moduli at different frequencies. Data from single- and double-transition samples are shown in the left and right panels, respectively. The curves shown in red are the data used in chapter 5. Figure adapted from [33].

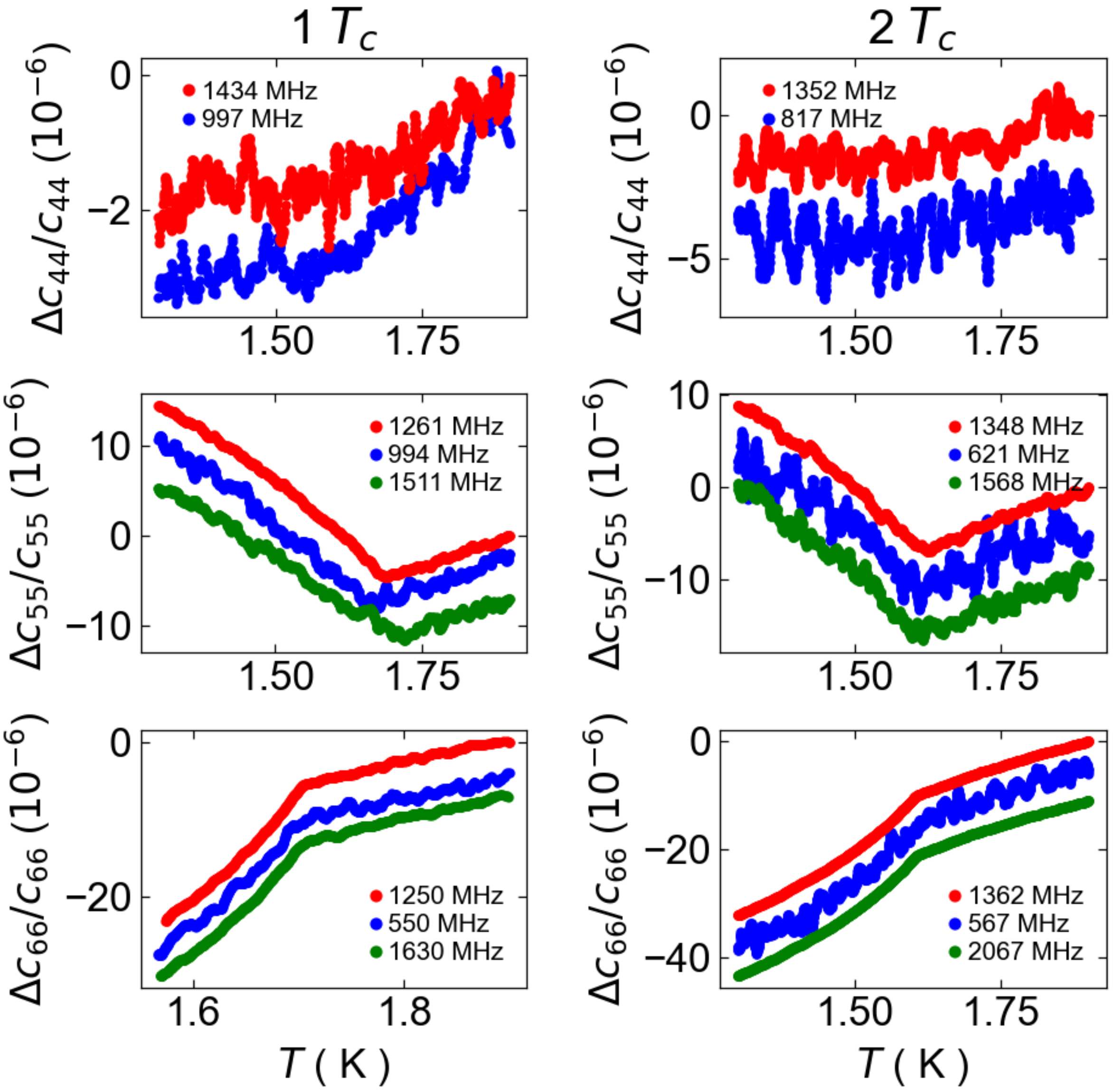

Figure I.5: **Frequency dependence shear moduli.** The relative changes in shear moduli at different frequencies. Data from single- and double-transition samples are shown in the left and right panels, respectively. The curves shown in red are the data used in chapter 5. Figure adapted from [33].

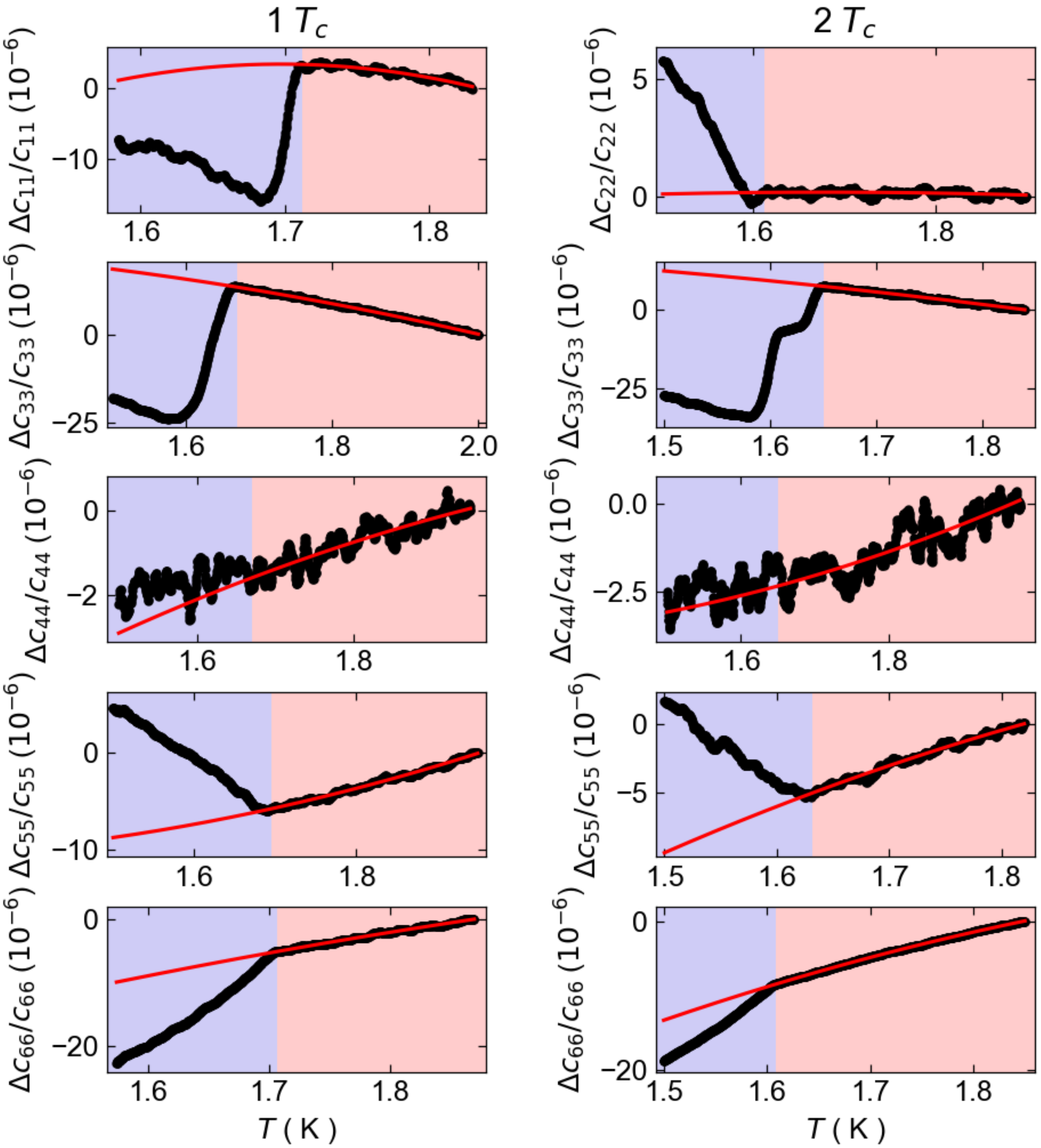

Figure I.6: **Background subtraction.** Relative changes of all elastic moduli shown in chapter 5. A second-order polynomial is fitted to all curves in the normal state, marked by the red shaded region. Figure adapted from [33].

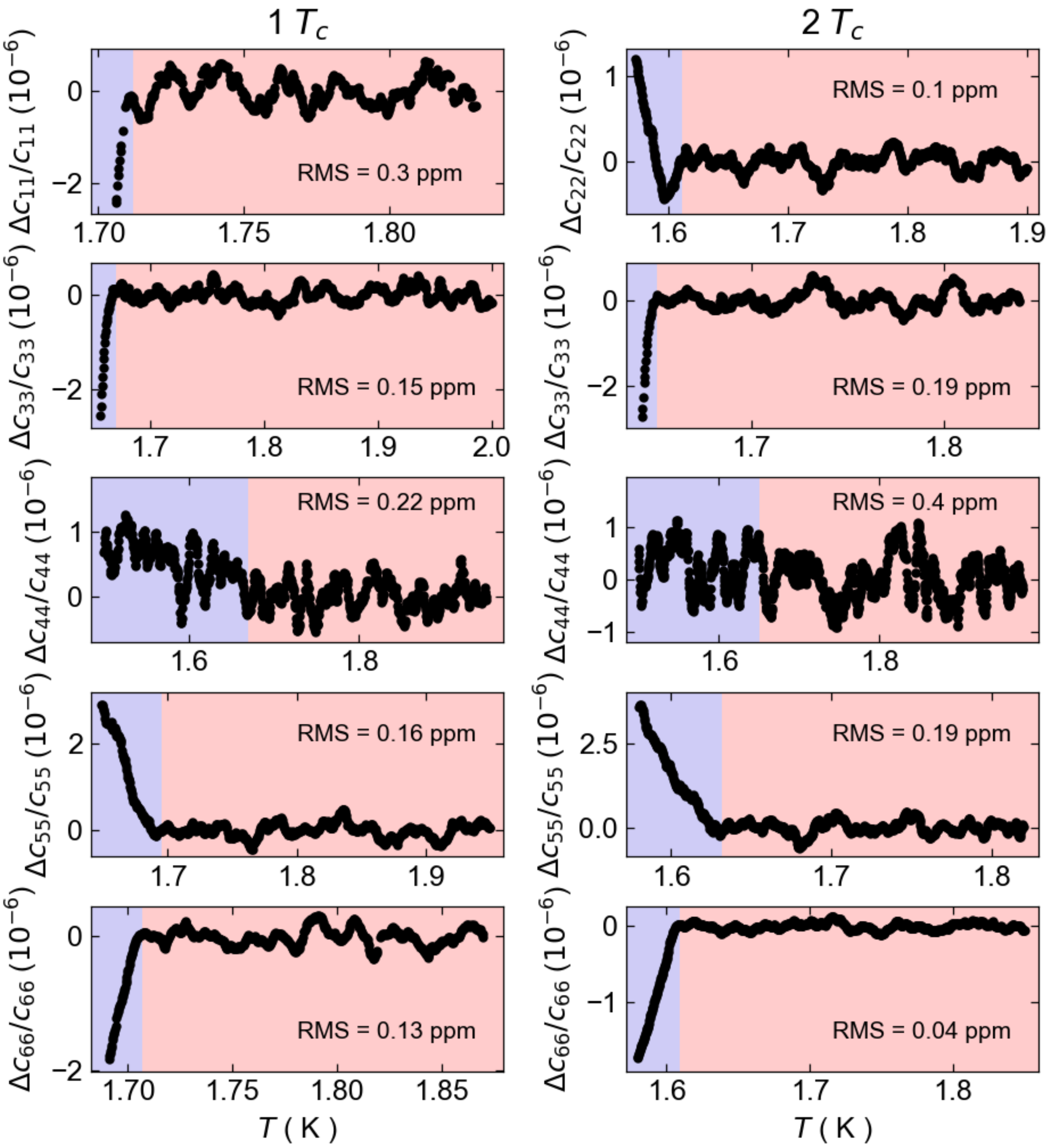

Figure I.7: **Noise estimate.** The background-subtracted data shown here are obtained by subtracting the background polynomial shown in Figure I.6 from the original data. The RMS is then calculated over the same temperature range which was used to fit these polynomials, i.e. the red shaded region. Figure adapted from [33].

APPENDIX J

UTe_2 HIGH ENERGY X-RAY DIFFRACTION MICROSCOPY

We performed high-energy X-ray diffraction microscopy (HEDM) on a double-transition UTe_2 sample at the Cornell High Energy Synchrotron Source (CHESS). Since the X-ray beam only covered about one thirteenth of the sample (see Figure 5.17a), we repeated the diffraction measurement thirteen times, each time focusing on a different slice of the sample.

From each measurement, we can extract the orientation of the crystal axes of the sample in terms of Euler angles relative to the lab coordinate frame. The lab frame is defined such that the z axis is parallel to the beam direction, the x axis is perpendicular to the z direction in the horizontal plane, and the y axis is perpendicular to the z direction in the vertical plane (see Figure 5.16b). The Euler angles are defined such that ψ is the rotation angle about the z axis, θ is the rotation angle about the new y axis, and ϕ is the rotation angle about the new x axis. Figure J.1, Figure J.2, and Figure J.3 show the distributions of orientations within each slice of the sample projected onto the $\phi - \theta$, $\phi - \psi$, and $\theta - \psi$ planes, respectively.

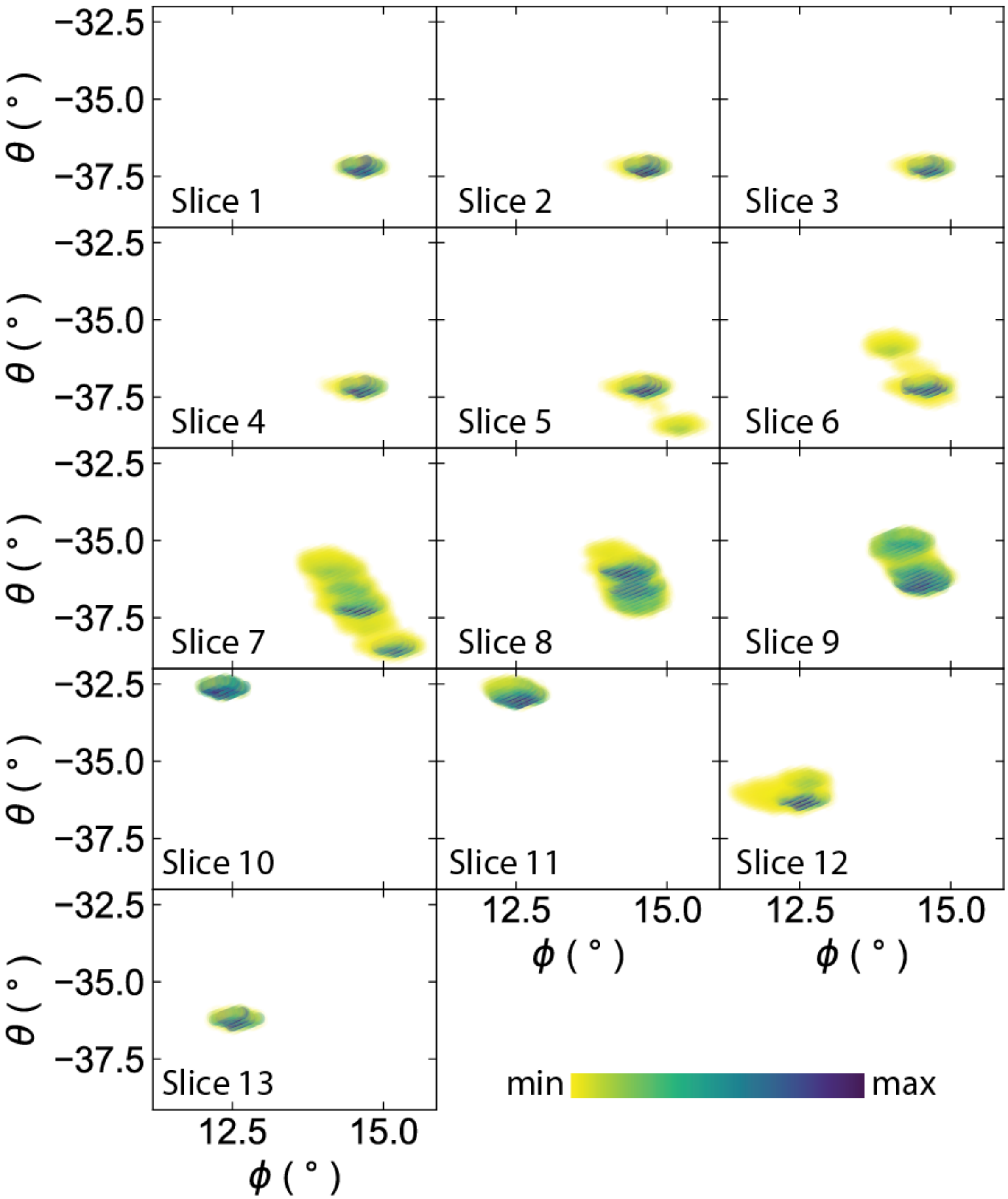

Figure J.1: **Orientation distributions in $\phi - \theta$ plane.** Distribution of orientations in terms of Euler angles projected onto the $\phi - \theta$ plane within each slice of the sample. The color scale indicates the volume fraction occupied by a given orientation. The volume fraction is normalized between each slice.

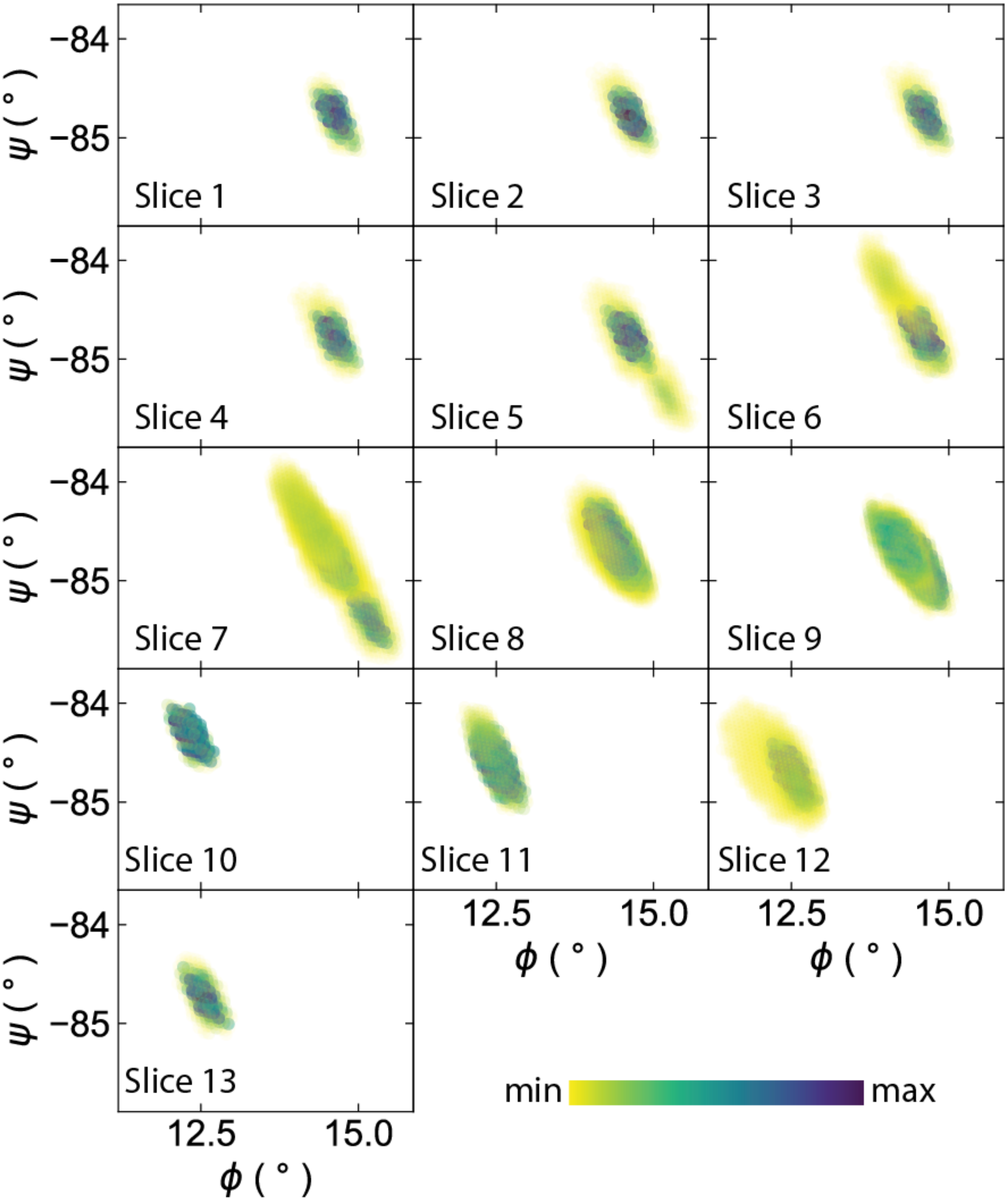

Figure J.2: **Orientation distributions in $\phi - \psi$ plane.** Distribution of orientations in terms of Euler angles projected onto the $\phi - \psi$ plane within each slice of the sample. The color scale indicates the volume fraction occupied by a given orientation. The volume fraction is normalized between each slice.

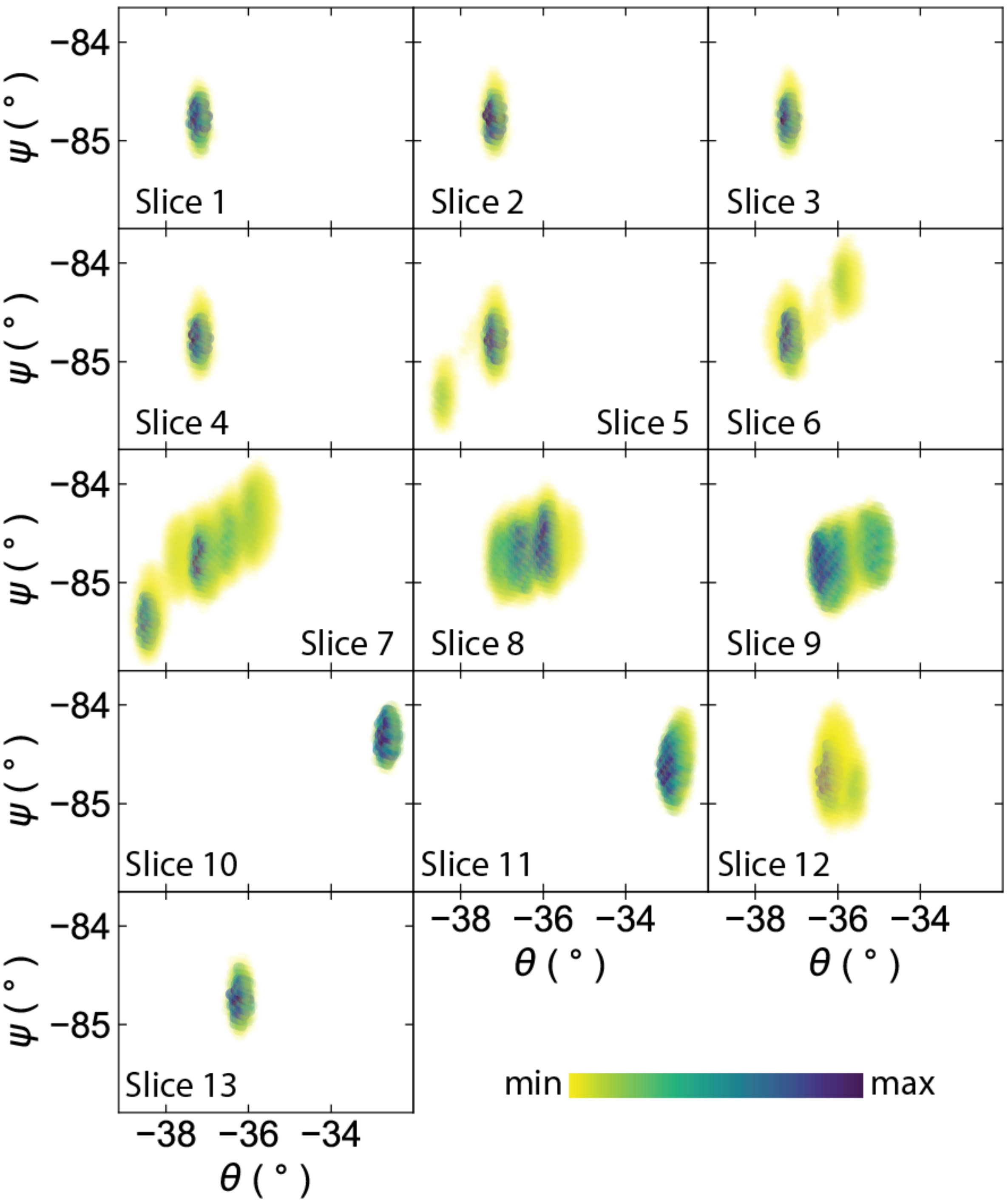

Figure J.3: **Orientation distributions in $\theta - \psi$ plane.** Distribution of orientations in terms of Euler angles projected onto the $\theta - \psi$ plane within each slice of the sample. The color scale indicates the volume fraction occupied by a given orientation. The volume fraction is normalized between each slice.

APPENDIX K

Mn_3X RUS SPECTRA AND FIT RESULTS

Here, we show tables of all experimental resonance frequencies (f_{exp}) included in our RUS fits, as well as the calculated resonance frequencies (f_{calc}) corresponding to the fit results presented in Table 6.1. Also shown is the difference between experimental and calculated frequencies $\frac{f_{exp}-f_{calc}}{f_{calc}}$ in %. We include fits for Mn_3Ge at 387 K and 300 K (Table K.1), and for Mn_3Sn at 438 K and 300 K (Table K.2). Fits at 387 K for Mn_3Ge and at 438 K for Mn_3Sn were used to obtain the temperature dependence of the elastic moduli. The resonances used in these decompositions are displayed in bold font in the tables below.

The Mn_3Ge sample used here for the fit at 300 K is the same sample used for the proof of concept regarding our novel SMI forward solver in chapter 4. The only difference is that basis polynomials of up to order 18 were used in chapter 4, whereas for this study on magnetoelasticity in Mn_3Ge, we used polynomials of up to order 16 to fit the RUS spectra. The resulting elastic moduli are almost identical between the two fits. Small deviations lie well within the given uncertainties.

Table K.1: **Mn_3Ge RUS spectra and calculated resonances at 387 K and 300 K.**

	387 K			300 K		
Index	f_{exp} (MHz)	f_{calc} (MHz)	diff (%)	f_{exp} (MHz)	f_{calc} (MHz)	diff (%)
1	0.86329	0.859066	0.492	0.964686	0.956224	0.885
2	**1.315918**	**1.312581**	**0.254**	1.310108	1.317659	0.573
3	1.337735	1.336578	0.087	1.467479	1.469985	0.17
4	**1.359745**	**1.360394**	**0.048**	1.509547	1.509463	0.006
5	**1.380895**	**1.380585**	**0.022**	1.564017	1.560709	0.212
6	**1.451318**	**1.453035**	**0.118**	1.578299	1.579394	0.069
7	**1.627631**	**1.625203**	**0.149**	1.584249	1.601805	1.096
8	**1.652097**	**1.659973**	**0.474**	1.601411	1.613058	0.722
9	**1.66751**	**1.663834**	**0.221**	1.605816	1.618775	0.801
10	**1.706839**	**1.70703**	**0.011**	1.786309	1.800976	0.814
11	**1.819579**	**1.815017**	**0.251**	1.820358	1.811905	0.467
12	**1.858302**	**1.858903**	**0.032**	1.87303	1.873366	0.018

Table continued on next page.

Table continued.

	387 K			300 K		
Index	f_{exp} (MHz)	f_{calc} (MHz)	diff (%)	f_{exp} (MHz)	f_{calc} (MHz)	diff (%)
13	**1.876659**	**1.872775**	**0.207**	1.941317	1.931709	0.497
14	**1.905238**	**1.903118**	**0.111**	1.951124	1.953711	0.132
15	1.914726	1.914616	0.006	2.033288	2.030126	0.156
16	**1.950258**	**1.950708**	**0.023**	2.096093	2.083367	0.611
17	**2.043762**	**2.039117**	**0.228**	2.105545	2.109193	0.173
18	2.056432	2.05242	0.195	2.145873	2.123002	1.077
19	2.073754	2.078511	0.229	2.162391	2.169167	0.312
20	2.154024	2.148777	0.244	2.165406	2.176431	0.507
21	2.259128	2.25193	0.32	2.253102	2.264518	0.504
22	2.267891	2.264419	0.153	2.320023	2.307887	0.526
23	2.2821	2.2756	0.286	2.370485	2.350548	0.848
24	2.28672	2.280567	0.27	2.382754	2.382635	0.005
25	2.331612	2.324629	0.3	2.435864	2.418329	0.725
26	2.353409	2.35653	0.132	2.462558	2.474235	0.472
27	2.397702	2.396495	0.05	2.473012	2.475588	0.104
28	2.405233	2.406206	0.04	2.523838	2.549998	1.026
29	2.452348	2.451764	0.024	2.554643	2.571023	0.637
30	2.481088	2.481642	0.022	2.577582	2.590433	0.496
31	2.495769	2.489697	0.244	2.61331	2.622595	0.354
32	2.510943	2.520272	0.37	2.654571	2.649171	0.204
33	2.573004	2.577864	0.189	2.719191	2.722728	0.13
34	2.587117	2.583748	0.13	2.751604	2.747202	0.16
35	2.645635	2.648888	0.123	2.780976	2.778539	0.088
36	2.660829	2.662691	0.07	2.842243	2.839749	0.088
37	**2.707036**	**2.714622**	**0.279**	2.860414	2.863792	0.118
38	2.718903	2.721322	0.089	2.871657	2.870075	0.055
39	2.787169	2.78735	0.007	2.911026	2.926243	0.52
40	2.819064	2.820408	0.048	2.931398	2.927636	0.128
41	**2.853757**	**2.853428**	**0.012**	2.93455	2.930862	0.126
42	**2.86775**	**2.868243**	**0.017**	2.941563	2.94228	0.024
43	**2.900467**	**2.899245**	**0.042**	3.044383	3.051906	0.246
44	3.004964	3.005587	0.021	3.10644	3.095465	0.355
45	3.027684	3.026964	0.024	3.12912	3.133605	0.143
46	3.055466	3.059585	0.135	3.193425	3.178438	0.472
47	3.075397	3.081272	0.191	3.211411	3.211541	0.004
48	3.12169	3.11315	0.274	3.28658	3.28379	0.085
49	3.153971	3.148271	0.181	3.309553	3.297572	0.363
50	3.180459	3.184064	0.113	3.315654	3.323133	0.225
51	3.195999	3.191377	0.145	3.357538	3.374973	0.517
52	3.236595	3.232265	0.134	3.38287	3.378185	0.139

Table continued on next page.

Table continued.

	387 K			300 K		
Index	f_{exp} (MHz)	f_{calc} (MHz)	diff (%)	f_{exp} (MHz)	f_{calc} (MHz)	diff (%)
53	3.302157	3.306776	0.14	3.441208	3.456592	0.445
54	3.30783	3.313241	0.163	3.471899	3.4604	0.332
55	3.311863	3.314773	0.088	3.494208	3.488521	0.163
56	3.326765	3.32714	0.011	3.498117	3.499481	0.039
57	3.338793	3.342154	0.101	3.499642	3.512645	0.37
58	3.350336	3.365099	0.439	3.547463	3.531192	0.461
59	3.406242	3.407761	0.045	3.572781	3.566142	0.186
60	3.418442	3.419212	0.023	3.584955	3.572166	0.358
61	3.445046	3.448244	0.093	3.587674	3.598522	0.301
62	3.453315	3.455402	0.06	3.602309	3.60153	0.022
63	3.503158	3.499268	0.111	3.607604	3.605513	0.058
64	3.533018	3.53394	0.026	3.613076	3.60711	0.165
65	3.547987	3.544604	0.095	3.614359	3.614274	0.002
66	3.580287	3.571457	0.247	3.618646	3.620746	0.058
67	3.590199	3.593931	0.104	3.647651	3.642217	0.149
68	3.596618	3.594777	0.051	3.670184	3.64649	0.65
69	3.648969	3.644795	0.115	3.717184	3.701586	0.421
70	3.669138	3.664341	0.131	3.72327	3.723366	0.003
71	3.688207	3.698064	0.267	3.787605	3.796285	0.229
72	3.698328	3.704204	0.159	3.811398	3.806552	0.127
73	3.713795	3.709839	0.107	3.8443	3.822001	0.583
74	3.73026	3.730008	0.007	3.869884	3.849273	0.535
75	3.743308	3.741472	0.049	3.917229	3.915088	0.055
76	3.750437	3.75735	0.184	3.945626	3.923404	0.566
77	3.76102	3.769173	0.216	3.979077	3.976995	0.052
78	3.763257	3.770313	0.187	3.999422	4.00085	0.036
79	3.811571	3.817756	0.162	4.01915	4.009941	0.23
80	3.860859	3.870459	0.248	4.034952	4.023893	0.275
81	3.869497	3.880479	0.283	4.045951	4.061753	0.389
82	3.898889	3.901128	0.057	4.057585	4.065825	0.203
83	3.942837	3.949442	0.167	4.064907	4.085995	0.516
84	3.953787	3.953558	0.006	4.078004	4.09122	0.323

Table K.2: **Mn$_3$Sn RUS spectra and calculated resonances at 438 K and 300 K.**

	438 K			300 K		
Index	f_{exp} (MHz)	f_{calc} (MHz)	diff (%)	f_{exp} (MHz)	f_{calc} (MHz)	diff (%)
1	0.956019	0.951489	0.476	0.994195	0.988336	0.593

Table continued on next page.

Table continued.

	438 K			300 K		
Index	f_{exp} (MHz)	f_{calc} (MHz)	diff (%)	f_{exp} (MHz)	f_{calc} (MHz)	diff (%)
2	**1.302051**	**1.303615**	**0.12**	1.355897	1.360526	0.34
3	**1.356757**	**1.356171**	**0.043**	1.416341	1.415183	0.082
4	1.545377	1.547471	0.135	1.597958	1.580247	1.121
5	**1.572799**	**1.559773**	**0.835**	1.603094	1.60859	0.342
6	**1.653398**	**1.652554**	**0.051**	1.714428	1.718097	0.214
7	1.826925	1.825464	0.080	1.870385	1.86784	0.136
8	**1.84124**	**1.842193**	**0.052**	1.90144	1.897641	0.2
9	**1.846365**	**1.850493**	**0.223**	1.903465	1.908627	0.27
10	**1.945893**	**1.947269**	**0.071**	1.918534	1.94585	1.404
11	1.951689	1.95092	0.039	1.97281	1.969372	0.175
12	**2.004886**	**2.004361**	**0.026**	2.057542	2.060389	0.138
13	2.045961	2.051807	0.285	2.092095	2.086459	0.27
14	**2.064675**	**2.056601**	**0.393**	2.104788	2.090323	0.692
15	**2.176206**	**2.183397**	**0.329**	2.159331	2.179086	0.907
16	**2.198152**	**2.193**	**0.235**	2.224686	2.214805	0.446
17	2.336228	2.326735	0.408	2.381973	2.362535	0.823
18	2.342467	2.331079	0.489	2.402662	2.401645	0.042
19	2.375163	2.376649	0.063	2.413194	2.426592	0.552
20	2.396917	2.385549	0.477	2.465173	2.46165	0.143
21	**2.448669**	**2.446057**	**0.107**	2.497626	2.47968	0.724
22	**2.477646**	**2.48024**	**0.105**	2.552512	2.540307	0.48
23	**2.489611**	**2.483812**	**0.233**	2.578463	2.572543	0.23
24	2.553737	2.562227	0.331	2.609505	2.621036	0.44
25	2.584251	2.584635	0.015	2.650515	2.639483	0.418
26	2.600278	2.59731	0.114	2.675979	2.664001	0.45
27	2.605038	2.598638	0.246	2.687564	2.677365	0.381
28	2.611152	2.61477	0.138	2.695202	2.690395	0.179
29	2.626227	2.625597	0.024	2.715151	2.719726	0.168
30	**2.66705**	**2.664576**	**0.093**	2.760339	2.759707	0.023
31	2.74096	2.749941	0.327	2.803317	2.832257	1.022
32	2.817082	2.804064	0.464	2.89555	2.868371	0.948
33	2.820105	2.826817	0.237	2.921852	2.929299	0.254
34	**2.85504**	**2.862191**	**0.25**	2.929966	2.938101	0.277
35	**2.887556**	**2.881883**	**0.197**	2.947121	2.965036	0.604
36	3.053394	3.05536	0.064	3.065267	3.090654	0.821
37	3.075785	3.077928	0.07	3.085791	3.104826	0.613
38	3.083823	3.091586	0.251	3.130633	3.121383	0.296
39	3.097191	3.100364	0.102	3.161843	3.176725	0.468
40	3.124406	3.129561	0.165	3.206676	3.200352	0.198
41	3.147232	3.142479	0.151	3.224375	3.226009	0.051

Table continued on next page.

Table continued.

	438 K			300 K		
Index	f_{exp} (MHz)	f_{calc} (MHz)	diff (%)	f_{exp} (MHz)	f_{calc} (MHz)	diff (%)
42	3.182915	3.188902	0.188	3.23735	3.240195	0.088
43	3.225322	3.226403	0.034	3.264707	3.267632	0.09
44	3.301824	3.312192	0.313	3.394271	3.414302	0.587
45	3.33583	3.343304	0.224	3.440456	3.454002	0.392
46	3.432684	3.434956	0.066	3.504948	3.504163	0.022
47	3.434088	3.444785	0.311	3.520484	3.534251	0.39
48	3.47998	3.484042	0.117	3.55844	3.555479	0.083
49	3.546648	3.556318	0.272	3.657986	3.642953	0.413
50	3.551306	3.559578	0.232	3.665025	3.67687	0.322
51	3.590234	3.590606	0.01	3.682794	3.684646	0.05
52	3.600708	3.603821	0.086	3.708454	3.693076	0.416
53	3.616276	3.613859	0.067	3.710922	3.703852	0.191
54	3.643436	3.638197	0.144	3.759539	3.71424	1.22
55	3.648954	3.648317	0.017	3.766532	3.754951	0.308
56	3.655188	3.653837	0.037	3.767296	3.789343	0.582
57	3.702148	3.710773	0.232	3.815364	3.832352	0.443
58	3.728572	3.73323	0.125	3.831993	3.839964	0.208
59	3.747068	3.746082	0.026	3.851426	3.85365	0.058
60	3.767859	3.770405	0.068	3.860065	3.870464	0.269
61	3.782426	3.781795	0.017	3.92407	3.911587	0.319
62	3.839776	3.84523	0.142	3.933947	3.942623	0.22
63	3.876186	3.8759	0.007	4.002253	4.005757	0.087
64	3.891183	3.882874	0.214	4.019562	4.021003	0.036
65	3.935088	3.93423	0.022	4.061745	4.046263	0.383
66	3.962969	3.960474	0.063	4.071424	4.068287	0.077
67	3.976983	3.979318	0.059	4.081862	4.075636	0.153
68	3.98941	3.99035	0.024	4.086442	4.089984	0.087

BIBLIOGRAPHY

[1] J. A. Mydosh, P. M. Oppeneer, and P. S. Riseborough, *Hidden order and beyond: An experimental—theoretical overview of the multifaceted behavior of URu_2Si_2*, Journal of Physics: Condensed Matter **32**, 143002 (2020).

[2] N. Lingg, D. Maurer, V. Müller, and K. A. McEwen, *Ultrasound investigations of orbital quadrupolar ordering in UPd_3*, Physical Review B **60**, R8430–R8433 (1999).

[3] R. M. Fernandes, L. H. VanBebber, S. Bhattacharya, P. Chandra, V. Keppens, D. Mandrus, M. A. McGuire, B. C. Sales, A. S. Sefat, and J. Schmalian, *Effects of nematic fluctuations on the elastic properties of iron arsenide superconductors*, Physical Review Letters **105**, 157003 (2010).

[4] A. S. Borovik-romanov, *Piezomagnetism, linear magnetostriction and magnetooptic effect*, Ferroelectrics **162**, 153–159 (1994).

[5] H. K. Onnes, *research notebooks 56, 57*, Kamerlingh Onnes Archive, Boerhaave Museum, Leiden, the Netherlands (1911).

[6] O. Gingras, M. Côté, and A.-M. S. Tremblay, *La supraconductivité non-conventionnelle du ruthénate de strontium : corrélations électroniques et couplage spin-orbite*, PhD thesis, Université de Montréal, Montreal, Canada (2022), available at `https://hdl.handle.net/1866/26832`.

[7] P. J. Ray, K. Lefmann, and L. Udby, *Structural investigation of $La_{2x}Sr_xCuO_{4+y}$—Following staging as a function of temperature*, Master's thesis, University of Copenhagen, Copenhagen, Denmark (2015), available at `10.6084/m9.figshare.2075680.v2`.

[8] P. Monthoux, D. Pines, and G. G. Lonzarich, *Superconductivity without phonons*, Nature **450**, 1177–1183 (2007).

[9] C. C. Tsuei and J. R. Kirtley, *Pairing symmetry in cuprate superconductors*, Reviews of Modern Physics **72**, 969–1016 (2000).

[10] A. P. Mackenzie and Y. Maeno, *Superconductivity of Sr_2RuO_4 and the physics of spin-triplet pairing*, Reviews of Modern Physics **75**, 657–712 (2003).

[11] S. A. Kivelson, A. C. Yuan, B. Ramshaw, and R. Thomale, *A proposal for reconciling diverse experiments on the superconducting state in Sr_2RuO_4*, npj Quantum Materials **5**, 43 (2020).

[12] M. Levy, *Ultrasonic attenuation in superconductors for ql<1*, Physical Review **131**, 1497–1500 (1963).

[13] R. Joynt and L. Taillefer, *The superconducting phases of UPt_3*, Reviews of Modern Physics **74**, 235–294 (2002).

[14] P. Hollister and B. Ramshaw, *Ultrasonic Studies of the Jahn-Teller Effect in a Model System*, PhD thesis, Cornell University, Ithaca, NY (2023), available at `https://doi.org/10.7298/bbbv-m183`.

[15] N. Ashcroft and N. Mermin, *Solid State Physics* (Saunders College Publishing, Philadelphia, 1976).

[16] L. D. Landau and E. M. Lifshitz, *Quantum mechanics: non-relativistic theory*, Vol. 3 (Elsevier, 2013).

[17] M. S. Dresselhaus, G. Dresselhaus, and A. Jorio, *Group theory: application to the physics of condensed matter* (Springer Science & Business Media, 2008).

[18] G. Katzer, Character and multiplication tables of point groups (accessed on 02/16/2024), `http://gernot-katzers-spice-pages.com/character_tables/`.

[19] R. S. Mulliken, *Report on notation for the spectra of polyatomic molecules*, The Journal of Chemical Physics **23**, 1997–2011 (1955).

[20] S. L. Altmann and P. Herzig, *Point-group theory tables*, 2nd ed. (Oxford University Press, 2011).

[21] L. D. Landau, E. M. Lifshitz, A. M. Kosevich, and L. P. Pitaevskii, *Theory of elasticity*, Vol. 7 (Elsevier, 1986).

[22] W. Rehwald, *The study of structural phase transitions by means of ultrasonic experiments*, Advances in Physics **22**, 721–755 (1973).

[23] S. Ghosh, A. Shekhter, F. Jerzembeck, N. Kikugawa, D. A. Sokolov, M. Brando, A. P. Mackenzie, C. W. Hicks, and B. J. Ramshaw, *Thermodynamic evidence for a two-component superconducting order parameter in* Sr_2RuO_4, Nature Physics **17**, 199–204 (2021).

[24] S. Ghosh and B. Ramshaw, *Resonant Ultrasound Investigations of Correlated Electron Systems*, PhD thesis, Cornell University, Ithaca, NY (2022), available at `http://doi.org/10.7298/pv4t-xf97`.

[25] The Nobel Prize in Physics 1913. NobelPrize.org. Nobel Prize Outreach AB 2024. Fri. 9 Feb 2024., `https://www.nobelprize.org/prizes/physics/1913/summary/`.

[26] J. Schmalian, *Failed theories of superconductivity*, Modern Physics Letters B **24**, 2679–2691 (2010).

[27] J. Bardeen, L. N. Cooper, and J. R. Schrieffer, *Microscopic theory of superconductivity*, Physical Review **106**, 162–164 (1957).

[28] M. Tinkham, *Introduction to Superconductivity* (Dover Publications, 2004).

[29] M. Sigrist, *Introduction to unconventional superconductivity*, AIP Conference Proceedings **789**, 165–243 (2005).

[30] J. F. Annett, *Symmetry of the order parameter for high-temperature superconductivity*, Advances in Physics **39**, 83–126 (1990).

[31] R. Balian and N. R. Werthamer, *Superconductivity with pairs in a relative p wave*, Physical Review **131**, 1553–1564 (1963).

[32] M. Sato and Y. Ando, *Topological superconductors: a review*, Reports on Progress in Physics **80**, 076501 (2017).

[33] F. Theuss, A. Shragai, G. Grissonnanche, I. M. Hayes, S. R. Saha, Y. S. Eo, A. Suarez, T. Shishidou, N. P. Butch, J. Paglione, and B. J. Ramshaw, *Single-component superconductivity in* UTe_2 *at ambient pressure*, arXiv:2307.10938 (2023).

[34] K. Brugger, *Pure modes for elastic waves in crystals*, Journal of Applied Physics **36**, 759–768 (1965).

[35] W. M. Visscher, A. Migliori, T. M. Bell, and R. A. Reinert, *On the normal modes of free vibration of inhomogeneous and anisotropic elastic objects*, The Journal of the Acoustical Society of America **90**, 2154–2162 (1991).

[36] F. F. Balakirev, S. M. Ennaceur, R. J. Migliori, B. Maiorov, and A. Migliori, *Resonant ultrasound spectroscopy: the essential toolbox*, Review of Scientific Instruments **90**, 121401 (2019).

[37] R. Storn and K. Price, *Differential evolution—a simple and efficient heuristic for global optimization over continuous spaces*, Journal of Global Optimization **11**, 341–359 (1997).

[38] P. Virtanen, R. Gommers, T. E. Oliphant, M. Haberland, T. Reddy, D. Cournapeau, E. Burovski, P. Peterson, W. Weckesser, J. Bright, S. J. van der Walt, M. Brett, J. Wilson, K. J. Millman, N. Mayorov, A. R. J. Nelson, E. Jones, R. Kern, E. Larson, C. J. Carey, İ. Polat, Y. Feng, E. W. Moore, J. VanderPlas, D. Laxalde, J. Perktold, R. Cimrman, I. Henriksen, E. A. Quintero, C. R. Harris, A. M. Archibald, A. H. Ribeiro, F. Pedregosa, P. van Mulbregt, and SciPy 1.0 Contributors, *Scipy 1.0: Fundamental algorithms for scientific computing in Python*, Nature Methods **17**, 261–272 (2020).

[39] B. J. Ramshaw, A. Shekhter, R. D. McDonald, J. B. Betts, J. N. Mitchell, P. H. Tobash, C. H. Mielke, E. D. Bauer, and A. Migliori, *Avoided valence transition in a plutonium superconductor*, Proceedings of the National Academy of Sciences of the United States of America **112**, 3285–3289 (2015).

[40] P. Demin, Red Pitaya Notes (accessed on 02/19/2024), `https://pavel-demin.github.io/red-pitaya-notes/`.

[41] A. W. Warner, M. Onoe, and G. A. Coquin, *Determination of elastic and piezoelectric constants for crystals in class (3m)*, The Journal of the Acoustical Society of America **42**, 1223–1231 (1967).

[42] B. P.-O. Inc., Material properties of lithium niobate transducers (accessed on 02/16/2024), `https://www.bostonpiezooptics.com/lithium-niobate`.

[43] F. Theuss, G. d. l. F. Simarro, A. Shragai, G. Grissonnanche, I. M. Hayes, S. Saha, T. Shishidou, T. Chen, S. Nakatsuji, S. Ran, M. Weinert, N. P. Butch, J. Paglione, and B. J. Ramshaw, *Resonant ultrasound spectroscopy for irregularly shaped samples and its application to uranium ditelluride*, Physical Review Letters **132**, 066003 (2024).

[44] A. Migliori, J. L. Sarrao, W. M. Visscher, T. M. Bell, M. Lei, Z. Fisk, and R. G. Leisure, *Resonant ultrasound spectroscopic techniques for measurement of the elastic moduli of solids*, Physica B: Condensed Matter **183**, 1–24 (1993).

[45] A. Bhatia, *Ultrasonic Absorption* (Monographs on the Physics and Chemistry of Materials. Oxford University Press, 1967).

[46] C. Lupien and L. Taillefer, *Ultrasound Attenuation in the Unconventional Superconductor Sr_2RuO_4*, PhD thesis, University of Toronto, Toronto (2002), available at `https://www.physique.usherbrooke.ca/lupien/papers/Lupien-phdSSbrth.pdf`.

[47] F. S. Khan and P. B. Allen, *Sound attenuation by electrons in metals*, Physical Review B **35**, 1002–1019 (1987).

[48] A. Pippard, *CXXII. Ultrasonic attenuation in metals*, The London, Edinburgh, and Dublin Philosophical Magazine and Journal of Science **46**, 1104–1114 (1955).

[49] A. B. Pippard, *Theory of ultrasonic attenuation in metals and magneto-acoustic oscillations*, Proceedings of the Royal Society of London. Series A. Mathematical and Physical Sciences **257**, 165–193 (1960).

[50] K. Miyake and C. M. Varma, *Landau-Khalatnikov damping of ultrasound in heavy-Fermion superconductors*, Physical Review Letters **57**, 1627–1630 (1986).

[51] J. Moreno and P. Coleman, *Ultrasound attenuation in gap-anisotropic systems*, Physical Review B **53**, R2995–R2998 (1996).

[52] L. Kadanoff and A. Pippard, *Ultrasonic attenuation in superconductors*, Proceedings of the Royal Society of London. Series A. Mathematical and Physical Sciences **292**, 299–313 (1966).

[53] B. Lüthi, T. J. Moran, and R. J. Pollina, *Sound propagation near magnetic phase transitions*, Journal of Physics and Chemistry of Solids **31**, 1741–1758 (1970).

[54] T. Abu Ali, J. Pilz, P. Schäffner, M. Kratzer, C. Teichert, B. Stadlober, and A. M. Coclite, *Piezoelectric properties of zinc oxide thin films grown by plasma-enhanced atomic layer deposition*, Physica Status Solidi A **217**, 2000319 (2020).

[55] Iowa State University, Center for Nondestructive Evaluation (`https://www.nde-ed.org/`), Transducer beam spread (accessed on 02/26/2024), `https://www.nde-ed.org/NDETechniques/Ultrasonics/EquipmentTrans/beamspread.xhtml`.

[56] A. Shragai, F. Theuss, G. Grissonnanche, and B. J. Ramshaw, *Rapid method for computing the mechanical resonances of irregular objects*, The Journal of the Acoustical Society of America **153**, 119–123 (2023).

[57] H. T. Rathod and H. S. G. Rao, *Integration of polynomials over an arbitrary tetrahedron in Euclidean three-dimensional space*, Computers & Structures **59**, 55–65 (1996).

[58] J. Jaśkowiec and N. Sukumar, *High-order cubature rules for tetrahedra*, International Journal for Numerical Methods in Engineering **121**, 2418–2436 (2020).

[59] E. Poindexter and A. A. Giardini, *Elastic constants of strontium titanate ($SrTiO_3$)*, Physical Review **110**, 1069 (1958).

[60] R. O. Bell and G. Rupprecht, *Elastic constants of strontium titanate*, Physical Review **129**, 90–94 (1963).

[61] B. Lüthi and T. J. Moran, *Sound propagation near the structural phase transition in strontium titanate*, Physical Review B **2**, 1211–1214 (1970).

[62] S. Ran, C. Eckberg, Q.-P. Ding, Y. Furukawa, T. Metz, S. R. Saha, I.-L. Liu, M. Zic, H. Kim, J. Paglione, and N. P. Butch, *Nearly ferromagnetic spin-triplet superconductivity*, Science **365**, 684–687 (2019).

[63] K. Kinjo, H. Fujibayashi, H. Matsumura, F. Hori, S. Kitagawa, K. Ishida, Y. Tokunaga, H. Sakai, S. Kambe, A. Nakamura, Y. Shimizu, Y. Homma, D. Li, F. Honda, and D. Aoki, *Superconducting spin reorientation in spin-triplet multiple superconducting phases of UTe_2*, Science Advances **9**, eadg2736 (2023).

[64] A. Rosuel, C. Marcenat, G. Knebel, T. Klein, A. Pourret, N. Marquardt, Q. Niu, S. Rousseau, A. Demuer, G. Seyfarth, G. Lapertot, D. Aoki, D. Braithwaite, J. Flouquet, and J. P. Brison, *Field-induced tuning of the pairing state in a superconductor*, Physical Review X **13**, 011022 (2023).

[65] D. Aoki, A. Nakamura, F. Honda, D. Li, Y. Homma, Y. Shimizu, Y. J. Sato, G. Knebel, J.-P. Brison, A. Pourret, D. Braithwaite, G. Lapertot, Q. Niu, M. Vališka, H. Harima, and J. Flouquet, *Unconventional superconductivity in heavy Fermion UTe_2*, Journal of the Physical Society of Japan **88**, 043702 (2019).

[66] K. Kinjo, H. Fujibayashi, S. Kitagawa, K. Ishida, Y. Tokunaga, H. Sakai, S. Kambe, A. Nakamura, Y. Shimizu, Y. Homma, D. X. Li, F. Honda, D. Aoki, K. Hiraki, M. Kimata, and T. Sasaki, *Change of superconducting character in* UTe_2 *induced by magnetic field*, Physical Review B **107**, L060502 (2023).

[67] S. Ran, I.-L. Liu, Y. S. Eo, D. J. Campbell, P. M. Neves, W. T. Fuhrman, S. R. Saha, C. Eckberg, H. Kim, D. Graf, F. Balakirev, J. Singleton, J. Paglione, and N. P. Butch, *Extreme magnetic field-boosted superconductivity*, Nature Physics **15**, 1250–1254 (2019).

[68] R. Schönemann, P. F. S. Rosa, S. M. Thomas, Y. Lai, D. N. Nguyen, J. Singleton, E. L. Brosha, R. D. McDonald, V. Zapf, B. Maiorov, and M. Jaime, *Sudden adiabaticity entering field-induced state in* UTe_2, arXiv:2206.06508 (2023).

[69] D. Aoki, F. Honda, G. Knebel, D. Braithwaite, A. Nakamura, D. X. Li, Y. Homma, Y. Shimizu, Y. J. Sato, J. P. Brison, and J. Flouquet, *Multiple superconducting phases and unusual enhancement of the upper critical field in* UTe_2, Journal of the Physical Society of Japan **89**, 053705 (2020).

[70] D. Braithwaite, M. Vališka, G. Knebel, G. Lapertot, J.-P. Brison, A. Pourret, M. E. Zhitomirsky, J. Flouquet, F. Honda, and D. Aoki, *Multiple superconducting phases in a nearly ferromagnetic system*, Communications Physics **2**, 147 (2019).

[71] S. Ran, I.-L. Liu, S. R. Saha, P. Saraf, J. Paglione, and N. P. Butch, *Comparison of two different synthesis methods of single crystals of superconducting uranium ditelluride*, Journal of Visualized Experiments **173**, e62563 (2021).

[72] D. Aoki, *Molten salt flux liquid transport method for ultra clean single crystals* UTe_2, Journal of the Physical Society of Japan **93**, 043703 (2024).

[73] L. P. Cairns, C. R. Stevens, C. D. O'Neill, and A. Huxley, *Composition dependence of the superconducting properties of* UTe_2, Journal of Physics: Condensed Matter **32**, 415602 (2020).

[74] H. Sakai, P. Opletal, Y. Tokiwa, E. Yamamoto, Y. Tokunaga, S. Kambe, and Y. Haga, *Single crystal growth of superconducting* UTe_2 *by molten salt flux method*, Physical Review Materials **6**, 073401 (2022).

[75] P. F. S. Rosa, A. Weiland, S. S. Fender, B. L. Scott, F. Ronning, J. D. Thompson, E. D. Bauer, and S. M. Thomas, *Single thermodynamic transition at 2 K in superconducting* UTe_2 *single crystals*, Communications Materials **3**, 33 (2022).

[76] I. M. Hayes, D. S. Wei, T. Metz, J. Zhang, Y. S. Eo, S. Ran, S. R. Saha, J. Collini, N. P. Butch, D. F. Agterberg, A. Kapitulnik, and J. Paglione, *Multicomponent superconducting order parameter in* UTe_2, Science **373**, 797–801 (2021).

[77] G. Nakamine, S. Kitagawa, K. Ishida, Y. Tokunaga, H. Sakai, S. Kambe, A. Nakamura, Y. Shimizu, Y. Homma, D. Li, *et al.*, *Superconducting properties of heavy Fermion* UTe_2 *revealed by* ^{125}*Te-nuclear magnetic resonance*, Journal of the Physical Society of Japan **88**, 113703 (2019).

[78] G. Nakamine, K. Kinjo, S. Kitagawa, K. Ishida, Y. Tokunaga, H. Sakai, S. Kambe, A. Nakamura, Y. Shimizu, Y. Homma, D. Li, F. Honda, and D. Aoki, *Anisotropic response of spin susceptibility in the superconducting state of* UTe_2 *probed with* ^{125}*Te-NMR measurement*, Physical Review B **103**, L100503 (2021).

[79] H. Fujibayashi, G. Nakamine, K. Kinjo, S. Kitagawa, K. Ishida, Y. Tokunaga, H. Sakai, S. Kambe, A. Nakamura, Y. Shimizu, Y. Homma, D. Li, F. Honda, and D. Aoki, *Superconducting order parameter in* UTe_2 *determined by knight shift measurement*, Journal of the Physical Society of Japan **91**, 043705 (2022).

[80] H. Matsumura, H. Fujibayashi, K. Kinjo, S. Kitagawa, K. Ishida, Y. Tokunaga, H. Sakai, S. Kambe, A. Nakamura, Y. Shimizu, Y. Homma, D. Li, F. Honda, and D. Aoki, *Large reduction in the a-axis Knight shift on* UTe_2 *with* $T_c = 2.1$ *K*, Journal of the Physical Society of Japan **92**, 063701 (2023).

[81] S. Suetsugu, M. Shimomura, M. Kamimura, T. Asaba, H. Asaeda, Y. Kosuge, Y. Sekino, S. Ikemori, Y. Kasahara, Y. Kohsaka, M. Lee, Y. Yanase, H. Sakai, P. Opletal, Y. Tokiwa, Y. Haga, and Y. Matsuda, *Fully gapped pairing state in spin-triplet superconductor* UTe_2, Science Advances **10**, eadk3772 (2024).

[82] T. Metz, S. Bae, S. Ran, I.-L. Liu, Y. S. Eo, W. T. Fuhrman, D. F. Agterberg, S. M. Anlage, N. P. Butch, and J. Paglione, *Point-node gap structure of the spin-triplet superconductor* UTe_2, Physical Review B **100**, 220504(R) (2019).

[83] I. M. Hayes, T. E. Metz, C. E. Frank, S. R. Saha, N. P. Butch, V. Mishra, P. J. Hirschfeld, and J. Paglione, *Robust nodal behavior in the thermal conductivity of superconducting* UTe_2, arXiv:2402.19353 (2024).

[84] K. Ishihara, M. Roppongi, M. Kobayashi, K. Imamura, Y. Mizukami, H. Sakai, P. Opletal, Y. Tokiwa, Y. Haga, K. Hashimoto, and T. Shibauchi, *Chiral superconductivity in* UTe_2 *probed by anisotropic low-energy excitations*, Nature Communications **14**, 2966 (2023).

[85] S. Kittaka, Y. Shimizu, T. Sakakibara, A. Nakamura, D. Li, Y. Homma, F. Honda, D. Aoki, and K. Machida, *Orientation of point nodes and nonunitary triplet pairing tuned by the easy-axis magnetization in* UTe_2, Physical Review Research **2**, 032014(R) (2020).

[86] D. S. Wei, D. Saykin, O. Y. Miller, S. Ran, S. R. Saha, D. F. Agterberg, J. Schmalian, N. P. Butch, J. Paglione, and A. Kapitulnik, *Interplay between magnetism and superconductivity in* UTe_2, Physical Review B **105**, 024521 (2022).

[87] L. Jiao, S. Howard, S. Ran, Z. Wang, J. O. Rodriguez, M. Sigrist, Z. Wang, N. P. Butch, and V. Madhavan, *Chiral superconductivity in heavy-Fermion metal UTe$_2$*, Nature **579**, 523–527 (2020).

[88] S. Bae, H. Kim, Y. S. Eo, S. Ran, I.-l. Liu, W. T. Fuhrman, J. Paglione, N. P. Butch, and S. M. Anlage, *Anomalous normal fluid response in a chiral superconductor UTe$_2$*, Nature Communications **12**, 2644 (2021).

[89] M. O. Ajeesh, M. Bordelon, C. Girod, S. Mishra, F. Ronning, E. D. Bauer, B. Maiorov, J. D. Thompson, P. F. S. Rosa, and S. M. Thomas, *Fate of time-reversal symmetry breaking in UTe$_2$*, Physical Review X **13**, 041019 (2023).

[90] A. Aishwarya, J. May-Mann, A. Raghavan, L. Nie, M. Romanelli, S. Ran, S. R. Saha, J. Paglione, N. P. Butch, E. Fradkin, and V. Madhavan, *Magnetic-field-sensitive charge density waves in the superconductor UTe$_2$*, Nature **618**, 928–933 (2023).

[91] A. LaFleur, H. Li, C. E. Frank, M. Xu, S. Cheng, Z. Wang, N. P. Butch, and I. Zeljkovic, *Inhomogeneous high temperature melting and decoupling of charge density waves in spin-triplet superconductor UTe$_2$*, Nature Communications **15**, 4456 (2024).

[92] A. Aishwarya, J. May-Mann, A. Almoalem, S. Ran, S. R. Saha, J. Paglione, N. P. Butch, E. Fradkin, and V. Madhavan, *Melting of the charge density wave by generation of pairs of topological defects in UTe$_2$*, Nature Physics (2024).

[93] Q. Gu, J. P. Carroll, S. Wang, S. Ran, C. Broyles, H. Siddiquee, N. P. Butch, S. R. Saha, J. Paglione, J. C. S. Davis, and X. Liu, *Detection of a pair density wave state in UTe$_2$*, Nature **618**, 921–927 (2023).

[94] L. Miao, S. Liu, Y. Xu, E. C. Kotta, C.-J. Kang, S. Ran, J. Paglione, G. Kotliar, N. P. Butch, J. D. Denlinger, and L. A. Wray, *Low energy band structure and symmetries of UTe$_2$ from angle-resolved photoemission spectroscopy*, Physical Review Letters **124**, 076401 (2020).

[95] B. R. Ortiz, S. M. L. Teicher, Y. Hu, J. L. Zuo, P. M. Sarte, E. C. Schueller, A. M. M. Abeykoon, M. J. Krogstad, S. Rosenkranz, R. Osborn, R. Seshadri, L. Balents, J. He, and S. D. Wilson, *CsV_3Sb_5 : A Z_2 topological Kagome metal with a superconducting ground state*, Physical Review Letters **125**, 247002 (2020).

[96] K. Ushida, T. Yanagisawa, R. Hibino, M. Matsuda, H. Hidaka, H. Amitsuka, G. Knebel, J. Flouquet, and D. Aoki, *Lattice instability of UTe$_2$ studied by ultrasonic measurements*, JPS Conference Proceedings **38**, 011021 (2023).

[97] Y. S. Eo, S. Liu, S. R. Saha, H. Kim, S. Ran, J. A. Horn, H. Hodovanets, J. Collini, T. Metz, W. T. Fuhrman, A. H. Nevidomskyy, J. D. Denlinger, N. P. Butch, M. S. Fuhrer, L. A. Wray, and J. Paglione, *c-axis transport in UTe$_2$: Evidence of three-dimensional conductivity component*, Physical Review B **106**, L060505 (2022).

[98] Y. P. Varshni, *Temperature dependence of the elastic constants*, Physical Review B **2**, 3952–3958 (1970).

[99] S. W. Lin, S. Adenwalla, J. B. Ketterson, M. Levy, and B. K. Sarma, *Ultrasonic studies of the heavy Fermion compounds*, Journal of Low Temperature Physics **89**, 217–228 (1992).

[100] B. Lüthi, G. Bruls, P. Thalmeier, B. Wolf, D. Finsterbusch, and I. Kouroudis, *Electron-phonon effects in heavy Fermion systems*, Journal of Low Temperature Physics **95**, 257–270 (1994).

[101] B. Wolf, W. Sixl, R. Graf, D. Finsterbusch, G. Bruls, B. Lüthi, E. A. Knetsch, A. A. Menovsky, and J. A. Mydosh, *Elastic properties of the heavy Fermion superconductor* URu_2Si_2, Journal of Low Temperature Physics **94**, 307–324 (1994).

[102] S. Nakamura, T. Goto, Y. Isikawa, S. Sakatsume, and M. Kasaya, *Elastic properties of dense Kondo compounds CeNiSn and CePdSn*, Journal of the Physical Society of Japan **60**, 2305–2310 (1991).

[103] Y. Pan, X. He, S. Zou, H. Zeng, Y. Zhao, Z. Li, Y. Li, and Y. Luo, *Ultrasonic investigation of the Kondo semimetal CeBi*, Physical Review B **108**, 165153 (2023).

[104] R. Kurihara, A. Miyake, M. Tokunaga, A. Ikeda, Y. H. Matsuda, A. Miyata, D. I. Gorbunov, T. Nomura, S. Zherlitsyn, J. Wosnitza, and F. Iga, *Field-induced valence fluctuations in* YbB_{12}, Physical Review B **103**, 115103 (2021).

[105] S. Nakamura, T. Goto, M. Kasaya, and S. Kunii, *Electron-strain interaction in valence fluctuation compound* SmB_6, Journal of the Physical Society of Japan **60**, 4311–4318 (1991).

[106] Y. Iguchi, H. Man, S. M. Thomas, F. Ronning, P. F. S. Rosa, and K. A. Moler, *Microscopic imaging homogeneous and single phase superfluid density in* UTe_2, Physical Review Letters **130**, 196003 (2023).

[107] Y. Xu, Y. Sheng, and Y.-f. Yang, *Quasi-two-dimensional Fermi surfaces and unitary spin-triplet pairing in the heavy Fermion superconductor* UTe_2, Physical Review Letters **123**, 217002 (2019).

[108] S. M. Thomas, C. Stevens, F. B. Santos, S. S. Fender, E. D. Bauer, F. Ronning, J. D. Thompson, A. Huxley, and P. F. S. Rosa, *Spatially inhomogeneous superconductivity in* UTe_2, Physical Review B **104**, 224501 (2021).

[109] C. Girod, C. R. Stevens, A. Huxley, E. D. Bauer, F. B. Santos, J. D. Thompson, R. M. Fernandes, J.-X. Zhu, F. Ronning, P. F. S. Rosa, and S. M. Thomas, *Thermodynamic and electrical transport properties of* UTe_2 *under uniaxial stress*, Physical Review B **106**, L121101 (2022).

[110] G. Nakamine, K. Kinjo, S. Kitagawa, K. Ishida, Y. Tokunaga, H. Sakai, S. Kambe, A. Nakamura, Y. Shimizu, Y. Homma, D. Li, F. Honda, and D. Aoki, *Inhomogeneous superconducting state probed by* ^{125}*Te NMR on UTe*$_2$, Journal of the Physical Society of Japan **90**, 064709 (2021).

[111] K. Machida, *Theory of spin-polarized superconductors—an analogue of superfluid* ^{3}*He A-phase*, Journal of the Physical Society of Japan **89**, 033702 (2020).

[112] K. Machida, *Nonunitary triplet superconductivity tuned by field-controlled magnetization: URhGe, UCoGe, and UTe*$_2$, Physical Review B **104**, 014514 (2021).

[113] A. H. Nevidomskyy, *Stability of a nonunitary triplet pairing on the border of magnetism in UTe*$_2$, arXiv:2001.02699 (2020).

[114] J. Ishizuka, S. Sumita, A. Daido, and Y. Yanase, *Insulator-metal transition and topological superconductivity in UTe*$_2$ *from a first-principles calculation*, Physical Review Letters **123**, 217001 (2019).

[115] T. Shishidou, H. G. Suh, P. M. R. Brydon, M. Weinert, and D. F. Agterberg, *Topological band and superconductivity in UTe*$_2$, Physical Review B **103**, 104504 (2021).

[116] H. C. Choi, S. H. Lee, and B.-J. Yang, *Correlated normal state fermiology and topological superconductivity in UTe*$_2$, arXiv:2206.04876 (2023).

[117] D. Shaffer and D. V. Chichinadze, *Chiral superconductivity in UTe*$_2$ *via emergent* C_4 *symmetry and spin-orbit coupling*, Physical Review B **106**, 014502 (2022).

[118] T. Hazra and P. A. Volkov, *Pair-Kondo effect: a mechanism for time-reversal broken superconductivity in UTe*$_2$, arXiv:2210.16293 (2023).

[119] Y.-Y. Chang, K. V. Nguyen, K.-L. Chen, Y.-W. Lu, C.-Y. Mou, and C.-H. Chung, *Topological Kondo superconductors*, arXiv:2301.00538 (2023).

[120] A. G. Eaton, T. I. Weinberger, N. J. M. Popiel, Z. Wu, A. J. Hickey, A. Cabala, J. Pospíšil, J. Prokleška, T. Haidamak, G. Bastien, P. Opletal, H. Sakai, Y. Haga, R. Nowell, S. M. Benjamin, V. Sechovský, G. G. Lonzarich, F. M. Grosche, and M. Vališka, *Quasi-2D Fermi surface in the anomalous superconductor UTe*$_2$, Nature Communications **15**, 223 (2024).

[121] T. I. Weinberger, Z. Wu, D. E. Graf, Y. Skourski, A. Cabala, J. Pospisil, J. Prokleska, T. Haidamak, G. Bastien, V. Sechovsky, G. G. Lonzarich, M. Valiska, F. M. Grosche, and A. G. Eaton, *Quantum interference between quasi-2D Fermi surface sheets in UTe*$_2$, arXiv:2307.00568 (2023).

[122] D. Aoki, H. Sakai, P. Opletal, Y. Tokiwa, J. Ishizuka, Y. Yanase, H. Harima, A. Nakamura, D. Li, Y. Homma, Y. Shimizu, G. Knebel, J. Flouquet, and Y. Haga,

First observation of the de Haas-van Alphen effect and Fermi surfaces in the unconventional superconductor UTe$_2$, Journal of the Physical Society of Japan **91**, 083704 (2022).

[123] C. Broyles, Z. Rehfuss, H. Siddiquee, J. A. Zhu, K. Zheng, M. Nikolo, D. Graf, J. Singleton, and S. Ran, *Revealing a 3D Fermi surface pocket and electron-hole tunneling in UTe$_2$ with quantum oscillations*, Physical Review Letters **131**, 036501 (2023).

[124] Z. Wu, J. Chen, T. I. Weinberger, A. Cabala, V. Sechovsky, M. Valiska, P. L. Alireza, A. G. Eaton, and F. M. Grosche, *Magnetic signatures of multicomponent superconductivity in pressurized UTe$_2$*, arXiv:2403.06650 (2024).

[125] M. Ikhlas, S. Dasgupta, F. Theuss, T. Higo, S. Kittaka, B. J. Ramshaw, O. Tchernyshyov, C. W. Hicks, and S. Nakatsuji, *Piezomagnetic switching of the anomalous Hall effect in an antiferromagnet at room temperature*, Nature Physics **18**, 1086–1093 (2022).

[126] F. Theuss, S. Ghosh, T. Chen, O. Tchernyshyov, S. Nakatsuji, and B. J. Ramshaw, *Strong magnetoelastic coupling in* Mn$_3X$ *(X =* Ge*, Sn)*, Physical Review B **105**, 174430 (2022).

[127] C. Song, Y. You, X. Chen, X. Zhou, Y. Wang, and F. Pan, *How to manipulate magnetic states of antiferromagnets*, Nanotechnology **29**, 112001 (2018).

[128] F. Miao, S.-J. Liang, and B. Cheng, *Straintronics with van der Waals materials*, npj Quantum Materials **6**, 59 (2021).

[129] A. A. Bukharaev, K. Zvezdin, A. P. Pyatakov, and Y. K. Fetisov, *Straintronics: a new trend in micro- and nanoelectronics and materials science*, Physics-Uspekhi **61**, 1175–1212 (2018).

[130] J. F. Qian, A. K. Nayak, G. Kreiner, W. Schnelle, and C. Felser, *Exchange bias up to room temperature in antiferromagnetic hexagonal Mn$_3$Ge*, Journal of Physics D: Applied Physics **47**, 305001 (2014).

[131] A. Markou, J. M. Taylor, A. Kalache, P. Werner, S. S. P. Parkin, and C. Felser, *Noncollinear antiferromagnetic Mn$_3$Sn films*, Physical Review Materials **2**, 051001(R) (2018).

[132] T. Nagamiya, S. Tomiyoshi, and Y. Yamaguchi, *Triangular spin configuration and weak ferromagnetism of Mn$_3$Sn and Mn$_3$Ge*, Solid State Communications **42**, 385–388 (1982).

[133] Y. Chen, J. Gaudet, S. Dasgupta, G. G. Marcus, J. Lin, T. Chen, T. Tomita, M. Ikhlas, Y. Zhao, W. C. Chen, M. B. Stone, O. Tchernyshyov, S. Nakatsuji, and C. Broholm, *Antichiral spin order, its soft modes, and their hybridization with phonons in the topological semimetal Mn$_3$Ge*, Physicsl Review B **102**, 054403 (2020).

[134] N. Kiyohara, T. Tomita, and S. Nakatsuji, *Giant anomalous Hall effect in the chiral antiferromagnet* Mn_3Ge, Physical Review Applied **5**, 064009 (2016).

[135] A. K. Nayak, J. E. Fischer, Y. Sun, B. Yan, J. Karel, A. C. Komarek, C. Shekhar, N. Kumar, W. Schnelle, J. Kuebler, C. Felser, and S. S. P. Parkin, *Large anomalous Hall effect driven by a nonvanishing Berry curvature in the noncolinear antiferromagnet* Mn_3Ge, Science Advances **2**, e1501870 (2016).

[136] M. Ikhlas, T. Tomita, T. Koretsune, M.-T. Suzuki, D. Nishio-Hamane, R. Arita, Y. Otani, and S. Nakatsuji, *Large anomalous Nernst effect at room temperature in a chiral antiferromagnet*, Nature Physics **13**, 1085–1090 (2017).

[137] G.-Y. Guo and T.-C. Wang, *Large anomalous Nernst and spin Nernst effects in the noncollinear antiferromagnets* Mn_3X *(X = Sn, Ge, Ga)*, Physical Review B **96**, 224415 (2017).

[138] C. Wuttke, F. Caglieris, S. Sykora, F. Scaravaggi, A. A. U. B. Wolter, K. Manna, V. Suess, C. Shekhar, C. Felser, B. Buechner, and C. Hess, *Berry curvature unravelled by the anomalous Nernst effect in* Mn_3Ge, Physical Review B **100**, 085111 (2019).

[139] S. Nakatsuji, N. Kiyohara, and T. Higo, *Large anomalous Hall effect in a noncollinear antiferromagnet at room temperature*, Nature **527**, 212–215 (2015).

[140] N. H. Sung, F. Ronning, J. D. Thompson, and E. D. Bauer, *Magnetic phase dependence of the anomalous Hall effect in* Mn_3Sn *single crystals*, Applied Physics Letters **112**, 132406 (2018).

[141] X. Li, L. Xu, L. Ding, J. Wang, M. Shen, X. Lu, Z. Zhu, and K. Behnia, *Anomalous Nernst and Righi-Leduc effects in* Mn_3Sn*: Berry curvature and entropy flow*, Physical Review Letters **119**, 056601 (2017).

[142] R. D. d. Reis, M. Ghorbani Zavareh, M. O. Ajeesh, L. O. Kutelak, A. S. Sukhanov, S. Singh, J. Noky, Y. Sun, J. E. Fischer, K. Manna, C. Felser, and M. Nicklas, *Pressure tuning of the anomalous Hall effect in the chiral antiferromagnet* Mn_3Ge, Physical Review Materials **4**, 051401(R) (2020).

[143] A. S. Sukhanov, M. S. Pavlovskii, P. Bourges, H. C. Walker, K. Manna, C. Felser, and D. S. Inosov, *Magnon-polaron excitations in the noncollinear antiferromagnet* Mn_3Ge, Physical Review B **99**, 214445 (2019).

[144] A. S. Sukhanov, S. Singh, L. Caron, T. Hansen, A. Hoser, V. Kumar, H. Borrmann, A. Fitch, P. Devi, K. Manna, C. Felser, and D. S. Inosov, *Gradual pressure-induced change in the magnetic structure of the noncollinear antiferromagnet* Mn_3Ge, Physical Review B **97**, 214402 (2018).

[145] S. Tomiyoshi, Y. Yamaguchi, and T. Nagamiya, *Triangular spin configuration and weak ferromagnetism of Mn_3Ge*, Journal of Magnetism and Magnetic Materials **31-34**, 629–630 (1983).

[146] E. Kren, J. Paitz, G. Zimmer, and E. Zsoldos, *Study of the magnetic phase transformation in the Mn_3Sn phase*, Physica B+C **80**, 226–230 (1975).

[147] J. W. Cable, N. Wakabayashi, and P. Radhakrishna, *A neutron study of the magnetic structure of Mn_3Sn*, Solid State Communications **88**, 161–166 (1993).

[148] J.-R. Soh, F. de Juan, N. Qureshi, H. Jacobsen, H.-Y. Wang, Y.-F. Guo, and A. T. Boothroyd, *Ground-state magnetic structure of Mn_3Ge*, Physical Review B **101**, 140411(R) (2020).

[149] J. R. Davis, *Metals Handbook Desk Edition, 2nd Edition* (1998).

[150] S. Ghosh, M. Matty, R. Baumbach, E. D. Bauer, K. A. Modic, A. Shekhter, J. A. Mydosh, E.-A. Kim, and B. J. Ramshaw, *One-component order parameter in URu_2Si_2 uncovered by resonant ultrasound spectroscopy and machine learning*, Science Advances **6**, eaaz4074 (2020).

[151] M. D. Bachmann, G. M. Ferguson, F. Theuss, T. Meng, C. Putzke, T. Helm, K. R. Shirer, Y.-S. Li, K. A. Modic, M. Nicklas, M. Koenig, D. Low, S. Ghosh, A. P. Mackenzie, F. Arnold, E. Hassinger, R. D. McDonald, L. E. Winter, E. D. Bauer, F. Ronning, B. J. Ramshaw, K. C. Nowack, and P. J. W. Moll, *Spatial control of heavy-Fermion superconductivity in $CeIrIn_5$*, Science **366**, 221–226 (2019).

[152] A. Migliori, W. M. Visscher, S. E. Brown, Z. Fisk, S.-W. Cheong, B. Alten, E. T. Ahrens, K. A. Kubat-Martin, J. D. Maynard, Y. Huang, D. R. Kirk, K. A. Gillis, H. K. Kim, and M. H. W. Chan, *Elastic constants and specific-heat measurements on single crystals of La_2CuO_4*, Physical Review B **41**, 2098–2102 (1990).

[153] H. Yasui, T. Kaneko, H. Yoshida, S. Abe, K. Kamigaki, and N. Mori, *Pressure dependence of magnetic transition temperatures and lattice parameters in an antiferromagnetic ordered alloy Mn_3Pt*, Journal of the Physical Society of Japan **56**, 4532–4539 (1987).

[154] D. B. McWhan and T. M. Rice, *Pressure dependence of itinerant antiferromagnetism in chromium*, Physical Review Letters **19**, 846–849 (1967).

[155] N. Môri and T. Mitsui, *Effect of hydrostatic pressure on Néel temperature and electrical residual resistivity of α-manganese*, Physics Letters A **39**, 413–414 (1972).

[156] M. Nakashima, Y. Haga, E. Yamamoto, Y. Tokiwa, M. Hedo, Y. Uwatoko, R. Settai, and Y. Onuki, *The high-pressure effect of an electronic state in uranium compounds: $UPtGa_5$ and UN*, Journal of Physics: Condensed Matter **15**, S2007 (2003).

[157] P. Malavi, J. Song, W. Bi, A. Regnat, L. Zhu, A. Bauer, A. Senyshyn, L. Yang, C. Pfleiderer, and J. S. Schilling, *High-pressure investigations on the semi-Heusler compound CuMnSb*, Physical Review B **98**, 054431 (2018).

[158] H. Yasui, T. Kaneko, S. Abe, H. Yoshida, and K. Kamigaki, *Pressure dependence of the Néel temperature and lattice parameters of an ordered alloy MnPd$_3$*, Journal de Physique Colloques **49**, C8–177–C8–178 (1988).

[159] G. E. Grechnev, A. S. Panfilov, A. V. Fedorchenko, V. B. Filippov, A. B. Lyashchenko, and A. N. Vasiliev, *Effect of pressure on the magnetic properties of CrB$_2$*, Low Temperature Physics **35**, 531–535 (2009).

[160] C. T. Wolowiec, Y. Fang, C. A. McElroy, J. R. Jeffries, R. L. Stillwell, E. Svanidze, J. M. Santiago, E. Morosan, S. T. Weir, Y. K. Vohra, and M. B. Maple, *Pressure effects in the itinerant antiferromagnetic metal TiAu*, Physical Review B **95**, 214403 (2017).

[161] J. Pospíšil, J. Gouchi, Y. Haga, F. Honda, Y. Uwatoko, N. Tateiwa, S. Kambe, S. Nagasaki, Y. Homma, and E. Yamamoto, *Effect of pressure on magnetism of UIrGe*, Journal of the Physical Society of Japan **86**, 044709 (2017).

[162] K. Balakrishnan and S. N. Kaul, *Determination of susceptibility and specific heat critical exponents for weak itinerant-electron ferromagnets from vibrating reed experiments*, Physical Review B **65**, 134412 (2002).

[163] J. Zinn-Justin, *Precise determination of critical exponents and equation of state by field theory methods*, Physics Reports **344**, 159–178 (2001).

[164] S. Dasgupta and O. Tchernyshyov, *Theory of spin waves in a hexagonal antiferromagnet*, Physical Review B **102**, 144417 (2020).

[165] S. Dasgupta and O. A. Tretiakov, *Tuning the Hall response of a noncollinear antiferromagnet via spin-transfer torques and oscillating magnetic fields*, Physical Review Research **4**, L042029 (2022).

[166] H. Reichlova, T. Janda, J. Godinho, A. Markou, D. Kriegner, R. Schlitz, J. Zelezny, Z. Soban, M. Bejarano, H. Schultheiss, P. Nemec, T. Jungwirth, C. Felser, J. Wunderlich, and S. T. B. Goennenwein, *Imaging and writing magnetic domains in the non-collinear antiferromagnet Mn$_3$Sn*, Nature Communications **10**, 5459 (2019).

[167] P. Ravindran, L. Fast, P. A. Korzhavyi, B. Johansson, J. Wills, and O. Eriksson, *Density functional theory for calculation of elastic properties of orthorhombic crystals: application to TiSi$_2$*, Journal of Applied Physics **84**, 4891–4904 (1998).

[168] M. Weinert, G. Schneider, R. Podloucky, and J. Redinger, *FLAPW: applications and implementations*, Journal of Physics: Condensed Matter **21**, 084201 (2009).

[169] J. P. Perdew, K. Burke, and M. Ernzerhof, *Generalized gradient approximation made simple*, Physical Review Letters **77**, 3865–3868 (1996).

[170] S. Ikeda, H. Sakai, D. Aoki, Y. Homma, E. Yamamoto, A. Nakamura, Y. Shiokawa, Y. Haga, and Y. Ōnuki, *Single crystal growth and magnetic properties of* UTe_2, Journal of the Physical Society of Japan **75**, 116–118 (2006).

[171] M. Kawamura, *FermiSurfer: Fermi-surface viewer providing multiple representation schemes*, Computer Physics Communications **239**, 197–203 (2019).